Energy-momentum conserving time-stepping algorithms for nonlinear dynamics of planar and spatial euler-bernoulli/timoshenko beams

Sophy Chhang

UNIVERSITE BRETAGNE SCIENCES LOIRE POUR L'INGENIEUR

INSA RENNES

THESE DE DOCTORAT DE

L'INSA RENNES
COMUE UNIVERSITE BRETAGNE LOIRE

ECOLE DOCTORALE N° 602
Sciences pour l'Ingénieur
Spécialité : « *Génie Civil* »

Par

« Sophy CHHANG »

« Energy-momentum conserving time-stepping algorithms for nonlinear dynamics of planar and spatial Euler-Bernoulli/Timoshenko beams »

Thèse présentée et soutenue à Rennes, le 11 Décembre 2018
Unité de recherche : LGCGM
Thèse N° : 18ISAR 36 / D18 - 36

Rapporteurs avant soutenance :

Reijo KOUHIA	Professor, Tampere University of Technology
Olivier BRÜLS	Professor, University of Liège
Anas BATOU	Professor, University of Liverpool

Composition du Jury :

Salima BOUVIER	Professor, Université de Technologie de Compiègne Président
Reijo KOUHIA	Professor, Tampere University of Technology
Olivier BRÜLS	Professor, University of Liège
Anas BATOU	Professor, University of Liverpool
Géry DE SAXCÉ	Professor, Université de Lille
Frédéric BOYER	Professor, IMT Atlantique / Ecole des Mines de Nantes
Jean-Marc BATTINI	Professor, KTH Royal Institute of Technology Directeur de thèse
Mohammed HJIAJ	Professor, INSA Rennes Directeur de thèse

Intitulé de la thèse :

Energy-momentum conserving time-stepping algorithms for nonlinear dynamics of planar and spatial Euler-Bernoulli/Timoshenko beams

Sophy CHHANG

En cotutelle avec :

KTH ROYAL INSTITUTE OF TECHNOLOGY

Abstract

Large deformations of flexible beams can be described using either the co-rotational approach or the total Lagrangian formalism. The co-rotational method is an attractive approach to derive highly nonlinear beam elements because it combines accuracy with numerical efficiency. On the other hand, the total Lagrangian formalism is the natural setting for the construction of geometrically exact beam theories. Classical time integration methods such as Newmark, standard midpoint rule or the trapezoidal rule do suffer severe shortcomings in nonlinear regimes. The construction of time integration schemes for highly nonlinear problems which conserve the total energy, the momentum and the angular momentum is addressed for planar co-rotational beams and for a geometrically exact spatial Euler-Bernoulli beam.

In the first part of the thesis, energy-momentum conserving algorithms are designed for planar co-rotational beams. Both Euler-Bernoulli and Timoshenko kinematics are addressed. These formulations provide us with highly complex non-linear expressions for the internal energy as well as for the kinetic energy which involve second derivatives of the displacement field. The main idea of the algorithm is to circumvent the complexities of the geometric non-linearities by resorting to strain velocities to provide, by means of integration, the expressions for the strain measures themselves. Similarly, the same strategy is applied to the highly nonlinear inertia terms. Several examples have been considered in which it was observed that energy, linear momentum and angular momentum are conserved for both formulations even when considering very large number of time-steps. Next, 2D elasto-(visco)-plastic fiber co-rotational beams element and a planar co-rotational beam with generalized elasto-(visco)-plastic hinges at beam ends have been developed and compared against each other for impact problems. Numerical examples show that strain rate effects influence substantially the structure response.

In the second part of this thesis, a geometrically exact 3D Euler-Bernoulli beam theory is developed. The main challenge in defining a three-dimensional Euler-Bernoulli beam theory lies in the fact that there is no natural way of defining a base system at the deformed configuration. A novel methodology to do so leading to the development of a spatial rod formulation which incorporates the Euler-Bernoulli assumption is provided. The approach makes use of Gram-Schmidt orthogonalisation process coupled to a one-parametric rotation to complete the description of the torsional cross sectional rotation and overcomes the non-uniqueness of the Gram-Schmidt procedure. Furthermore, the formulation is extended to the dynamical case and a stable, energy conserving time-stepping algorithm is developed as well. Many examples confirm the power of the formulation and the integration method presented.

Keywords: Nonlinear Dynamics, Energy-momentum conserving scheme, 2D co-rotational beam, Geometrically exact 3D Euler-Bernoulli beam, impact.

Résumé

Le mouvement des poutres flexibles peut être décrit à l'aide l'approche co-rotationnelle ou en adoptant le formalisme total lagrangien. La méthode co-rotationnelle est une approche intéressante pour développer des éléments de poutre fortement non-linéaires car elle allie précision et efficacité numérique. Par ailleurs, la formulation totale lagrangienne est une approche naturelle pour la construction de théories de poutre géométriquement exacte. Il est aujourd'hui reconnu que les méthodes de type Newmark, la méthode du point milieu classique ou la règle trapézoïdale posent des problèmes de stabilité en régime non-linéaire. La construction de schémas d'intégration temporelle qui conservent l'énergie totale, la quantité de mouvement et le moment cinétique est abordée pour les poutres co-rotationnelles planes et pour la poutre spatiale d'Euler-Bernoulli géométriquement exacte.

Dans la première partie de la thèse, les schémas d'intégration conservatifs sont appliqués aux poutres co-rotationnelles 2D. Les cinématiques d'Euler-Bernoulli et de Timoshenko sont abordées. Ces formulations produisent des expressions de l'énergie interne et l'énergie cinétique complexe et fortement non-linéaires. L'idée centrale de l'algorithme consiste à définir, par intégration, le champ des déformations en fin de pas à partir du champ de vitesses de déformations et non à partir du champ des déplacements au travers de la relation déplacement-déformation. La même technique est appliquée aux termes d'inerties. Ensuite, une poutre co-rotationnelle plane avec rotules généralisées élasto-(visco)-plastiques aux extrémités est développée et comparée au modèle fibre avec le même comportement pour des problèmes d'impact. Des exemples numériques montrent que les effets de la vitesse de déformation influencent sensiblement la réponse de la structure.

Dans la seconde partie de cette thèse, une théorie de poutre spatiale d'Euler-Bernoulli géométriquement exacte est développée. Le principal défi dans la construction d'une telle théorie réside dans le fait qu'il n'existe aucun moyen naturel de définir un trièdre orthonormé dans la configuration déformée. Une nouvelle méthodologie permettant de définir ce trièdre et par conséquent de développer une théorie de poutre spatiale en incorporant l'hypothèse d'Euler-Bernoulli est fournie. Cette approche utilise le processus d'orthogonalisation de Gram-Schmidt couplé avec un paramètre rotation qui complète la description cinématique et décrit la rotation associée à la torsion. Ce processus permet de surmonter le caractère non-unique de la procédure de Gram-Schmidt. La formulation est étendue au cas dynamique et un schéma intégration temporelle conservant l'énergie est également développé. De nombreux exemples démontrent l'efficacité de cette formulation.

Mot-clé : Dynamique non-linéaire, Schémas d'intégration conservatifs, Poutre co-rotationelle 2D, Poutre spatiale d'Euler-Bernoulli géométriquement exacte, Impact.

Preface

The research work reported in this thesis was carried out both at the laboratory LGCGM, INSA de Rennes (France) and at the Department of Civil and Architectural Engineering, KTH Royal Institute of Technology (Sweden).

This project was financed by the region of Brittany (France) through the ARED funding scheme and support by the European Commission (Research Fund for Coal and Steel) through the project RobustImpact, and by KTH Royal Institute of Technology. The work was conducted under direct supervision of Professor *Mohammed Hjiaj* (INSA de Rennes) and Professor *Jean-Marc Battini* (KTH).

First of all, I would like to express my gratitude to my two supervisors for their constant support, encouragement and valuable advices. Their dedication and professional guidance have helped me grow as a researcher. I feel privileged and have greatly enjoyed working with them. I also want to thank them for their help during the writing of this thesis and the papers as well as the preparation of the defense. I would like to thank Professor *Carlo Sansour* for his kind help and the fruitful discussion for the development of 3D beam formulation and the energy-momentum method.

I also wish to thank my colleagues and friends both at INSA de Rennes and KTH for the many useful discussions and for creating an enjoyable atmosphere for me. I would particularly like to thank *Piseth Heng*, *Theany To* and *Pisey Keo* for their friendship, inspiration and help during these years.

Finally, I would like to express my gratitude to *my grandparent*, *my parent* and *my two sisters* for their pure love and support.

Rennes, December 2018

Sophy Chhang

Publications

The current thesis is based on the research work presented in four journal papers.

Appended journal papers:

Paper I: **S. Chhang**, C. Sansour, M. Hjiaj, J.-M. Battini. An energy-momentum co-rotational formulation for nonlinear dynamics of planar beams. *Computers and Structures*, 187:50-63, 2017.

Paper II: **S. Chhang**, J.-M. Battini, M. Hjiaj. Energy-momentum method for co-rotational plane beams: A comparative study of shear flexible formulations. *Finite Elements in Analysis and Design*, 134:41-54, 2017.

Paper III: **S. Chhang**, P. Heng, J.-M. Battini, M. Hjiaj, S. Guezouli. Co-rotating flexible beam with generalized visco-plastic hinges for the nonlinear dynamics of frame structures under impacts. *Manuscript.*

Paper IV: **S. Chhang**, C. Sansour, M. Hjiaj, J.-M. Battini. Energy-conserving scheme of geometrically exact Euler-Bernoulli spatial beam in nonlinear dynamics. *Manuscript.*

I was responsible for the planning, the implementing of numerical models and the writing of Paper I, II, III and IV. All the authors participated in planning and writing the papers and contributed in the revision. All the typos found in the published version of the papers have been corrected in this thesis.

Other relevant publications:

- **S. Chhang**, M. Hjiaj, J.-M. Battini, C. Sansour (2018, June). Nonlinear dynamic analysis of framed structures with an energy-momentum conserving co-rotational formulation: generalized plastic hinge model versus distributed plasticity approach. *In 16th European conference on Earthquake Engineering.*
- **S. Chhang**, M. Hjiaj, J.-M. Battini, C. Sansour (2017, June). An energy-momentum formulation for nonlinear dynamics of planar co-rotating beams. *In 6th Computational Methods in Structural Dynamics and Earthquake Engineering*, COMPDYN 2017 (Vol. 2, p. 3682-3696).
- **S. Chhang**, M. Hjiaj, J. M. Battini, C. Sansour (2016, June). Energy-momentum

method for nonlinear dynamic of 2D corotational beams. *In 7th European Congress on Computational Methods in Applied Sciences and Engineering*, ECCOMAS Congress 2016 (Vol. 3, p. 5496-5066).

Contents

Chapter 1

Introduction

1.1 Background

Nonlinear dynamics of flexible beams is an active research topic in the field of engineering. Flexible beams can be found in many applications such as large deployable space structures, aircrafts, wind turbines propellers and offshore platforms. These structures may undergo large displacements and rotations which involves both geometrical and material nonlinearities. Consequently, the nonlinear dynamic behaviour may appear chaotic and unpredictable in contrast to much simpler systems. In this context, a successful simulation of these flexible beams requires two efficient numerical tools: a finite element beam formulation and a time integration method.

Firstly, there exist many approaches to derive the efficient beam formulations such as the Total Lagrangian approach [1, 2, 3, 4, 5], floating approach [6, 7, 8] and co-rotational approach [9, 10, 11, 12, 13, 14, 15, 16, 17, 18, 19, 20]. Whereas the total Lagrangian approach can be considered as the natural setting for geometrically exact dynamics, the co-rotational method is an attractive approach to derive highly nonlinear beam elements because it combines accuracy with numerical efficiency.

Secondly, response to extreme loadings, long term stability is a fundamental feature of a time integration method to capture extended responses over sufficiently long time intervals. The extended application of the traditional time integration scheme (i.e. Newmark family method [21]) from linear to nonlinear dynamic systems is not trivial and can lead to instabilities [1, 22]. Greenspan [23, 24] had demonstrated that the conservation of energy and momenta play a crucial role in stability of the time stepping algorithms. Simo [22] first discovered how to modify the 3D beam algorithms for the conservation of those properties which definitely improve the stability of the algorithms. While its formulation can only apply to the Saint-Venant Kirchhoff material, the energy momentum conserving scheme has been developed and enhanced in different area of applications.

Many research works on the finite element model in co-rotational [12, 25, 26, 27, 28, 29, 30, 31, 32, 33] and Total Lagrangian formulations [35, 36] have been done by the department of Civil and Architectural Engineering at KTH Royal Institute of Technology and by the laboratory LGCGM at INSA Rennes. Amongst those works, the co-rotational planar beam formulation proposed by Le et al. [12] is very efficient because the cubic interpolations have been adopted for deriving consistently both inertia and internal terms. However, the HHT-α [37] time integration scheme employed for solving the equation of motions

introduces artificial damping and a dissipation of the energy in the system. Sansour et al. [35] have proposed an energy-momentum method for a Total Lagrangian 2D Euler-Bernoulli beam. The extension of this approach to 2D corotational beams and 3D total Lagrangian beams appears to be an interesting challenge.

1.2 Aims and scope

In light of the above problems, the first objective of the research work is to extend the 2D co-rotational beam formulation by introducing an energy-momentum method. The energy-conserving scheme, proposed by Sansour et al. [38, 39], is applied to the co-rotational formulation for the first time. The aim of this formulation is to conserve the total energy as well as the linear and angular momentum. The main idea is to employ the strain velocity instead of the strain-displacement relationships directly. But, the task is not straight forward in the co-rotational method since the inertia terms are highly nonlinear. These inertia terms will be modified consistently with the help of the kinematic velocities. The work is presented in Paper I [40].

The second objective of the research work is to applied the methodology presented in Paper I to shear flexible formulations. Based on the same idea for the time integration scheme and on the same co-rotational framework, three different local formulations i.e. reduced integration method, Hellinger-Reissner mixed formulation and Interdependent Interpolation element (IIE) formulation are implemented and tested for a large number of time steps. Since the expression of the tangent dynamic matrix of IIE formulation may be complicated, a possible simplification is carefully studied. Finally, different predictors are tested along with the computational time. This is reported in paper II [41].

The third objective of the research work is to developed a 2D elasto-(visco)-plastic fiber co-rotational beam element and a planar co-rotational beam element with generalized elasto-(visco)-plastic hinges. For the generalized elasto-plastic hinges, the inelasticity of the structural members is considered through hinges which are modelled by combining axial and rotational springs. These hinges are placed at the end nodes of the beam element whereas the rest of the beam deforms elastically. The hinges remain uncoupled in the elastic range and the axial-bending interaction is considered in the plastic range. In addition, the strain rate effects have been considered by replacing the plastic flow rule with its visco-plastic counterpart. These beam formulations will be compared against each other for impact problems. This work is presented in paper III.

The fourth objective of the research work is to develop an energy-conserving time stepping algorithm for a three-dimensional geometrically exact Euler-Bernoulli beam. A novel methodology to the development of a spatial rod formulation which incorporates the Euler-Bernoulli assumption is provided. The approach makes use of Gram-Schmidt orthogonalisation process coupled to a one-parametric rotation. The latter completes the description of the torsional cross sectional rotation and overcomes the non-uniqueness of the Gram-Schmidt procedure. Furthermore, the formulation is extended to the dynamical case and a stable, energy conserving time-stepping algorithm is presented as well. Several examples involving large spatial deformations confirm the efficiency of both the proposed formulation and the integration method. This work is reported in paper IV.

1.3 Research contribution

The research work in this thesis has provided the following research contributions:

- An energy-momentum method for Bernoulli/Timoshenko co-rotational planar beams.
- A comparative study of three shear flexible co-rotational 2D beam formulations, i.e. Interdependent Interpolation Element (IIE), reduced integration and mixed formulations.
- A 2D elasto-(visco)-plastic fiber co-rotational beam element and a planar co-rotational beam element with generalized elasto-(visco)-plastic hinges. These formulations are especially interesting for steel frame structures subjected to impact with and without strain rate effect.
- A stable, energy-conserving integration scheme for a three-dimensional geometrically exact Euler-Bernoulli curved beam in a Total Lagrangian formulation.

The above contributions are discussed and presented in the thesis and in the appended papers.

1.4 Outline of thesis

The structure of this thesis is organized into two parts: an extended summary of the research work and appended papers. The first part provides readers with a general introduction and summary of the research work. This part consists of six chapters. The first chapter containing a background introduction, aims and research contributions has been presented. The rest of this part is organized as follows.

Chapter 2 presents a review of energy conserving/decaying integration schemes which are used to simulate the nonlinear dynamic of structures. A short conclusion regarding these schemes is given.

In Chapter 3, the planar beam co-rotational formulation is presented with different local strains for Bernoulli and Timoshenko elements. The beam kinematics, Hamilton's principle and the conserving properties are briefly presented.

In Chapiter 4, a new 3D Euler-Bernoulli beam formulation is presented in the total Lagrangian approach. The beam kinematics and the principle of virtual work for the dynamical analysis of beam are provided along with the conserving properties.

In Chapter 5, an extended summary of the research work is provided. Finally, Chapter 6 presents general conclusions and possible future research. The first part of the thesis is followed by the four appended papers.

Chapter 2

Energy-momentum method

Implicit time stepping methods are often used together with nonlinear finite elements to study linear and nonlinear dynamic problems. One of the most commonly employed implicit method is the Newmark family of algorithms [21] which includes average acceleration method as a special case. The average acceleration algorithm yields implicit, unconditionally stability and second-order accuracy in linear dynamics. However for general nonlinear dynamics, the Newmark method becomes unstable and often blows up, often due to convergence of the nonlinear Newton type iterations. In order to solve the instability problem, Hilber-Hughes-Taylor [37] proposed an extension algorithm of the Newmark method which enables to control dissipation to the damping, the stiffness and the external force. In this way, the algorithm presents second-order accuracy and unconditionally stability in the high frequency modes. Other time integration methods also include numerical dissipation in different ways i.e. Wood-Bossak-Zienkienwicz method [42], Wilson-θ method [43], Park method [44], the three parameter optimal χ-scheme [45], the Generalized-α method [46]. These algorithms are summarized in the Generalized single step solve (GSSSS) family of algorithms [47, 48, 49, 50]. One can notice that these methods affect the response for lower modes more or less depending on the dissipation parameter. Without introducing numerical dissipation, the direct extension from linear system to nonlinear one is not a trivial task. However, it is desirable to have an algorithm which fulfils the accuracy and stability without introducing any numerical dissipation.

With this motivation, Greenspan [23, 24] stressed out that the conserved properties (i.e. energy, linear and angular momenta) play an important role to develop stable time stepping algorithms. The satisfaction of these important conservation laws guarantees that the dynamic of the system remains at least qualitatively accurate and meaningful even in long term calculations. Moreover, numerical stability for the analysis of nonlinear systems is often defined through the requirement that the energy of the numerical solution has to remain bounded. Consequently, the conservation of energy may be regarded as a manifestation of unconditional numerical stability.

2.1 Energy-momentum conserving scheme

Simo and Tarnow [22] were the first authors to develop an energy-momentum method in nonlinear dynamics of three-dimensional elastic bodies. Their algorithm is based on the classical midpoint rule in which the equation of motion is defined at midpoint step. The geometrical nonlinearity arises only in the internal term which includes the 2nd Piola-Kirchhoff stress $\tilde{\mathbf{S}}$ or the right Cauchy-Green strain tensor $\mathbf{C}$. Moreover, Simo and

Tarnow [22] have shown that the algorithm with the classical midpoint rule, in which $\tilde{\mathbf{S}}$ or $\mathbf{C}$ are calculated directly from the nodal displacements and rotations, is clearly unstable. Therefore, Simo and Tarnow [22] proposed the following energy-momentum conserving algorithm:

$$\begin{aligned}
&\int_{\mathcal{B}} \rho_0 \frac{\mathbf{V}_{n+1} - \mathbf{V}_n}{\Delta t} \cdot \boldsymbol{\eta} \, \mathrm{d}V + \int_{\mathcal{B}} \mathbf{F}\left(\boldsymbol{\varphi}_{n+\frac{1}{2}}\right) \cdot \tilde{\mathbf{S}} : \partial \eta / \partial \boldsymbol{X} \, \mathrm{d}V \\
&= \int_{\mathcal{B}} \mathbf{B}_{n+\frac{1}{2}} \cdot \boldsymbol{\eta} \, \mathrm{d}V + \int_{\partial \mathcal{B}_\sigma} \bar{\mathbf{T}}_{n+\frac{1}{2}} \cdot \boldsymbol{\eta} \, \mathrm{d}A, \quad \forall \eta \in \mathcal{V} \qquad (2.1) \\
&\int_{\mathcal{B}} \frac{\boldsymbol{\varphi}_{n+1} - \boldsymbol{\varphi}_n}{\Delta t} \cdot \boldsymbol{\eta} \, \mathrm{d}V = \int_{\mathcal{B}} \mathbf{V}_{n+\frac{1}{2}} \cdot \boldsymbol{\eta} \, \mathrm{d}V \qquad (2.2)
\end{aligned}$$

where $\mathbf{V}$ denotes the material velocity fields, $\mathbf{F}$ the deformation gradient tensor. $\varphi(\boldsymbol{X}, t)$ represents the position in the Lagrangian description. η the test function. $\rho_0 : \mathcal{B} \to \mathbb{R}_+$ is the reference density. $\mathbf{B}$ is the body force per unit mass on the volume element $\mathcal{B}$ and $\bar{\mathbf{T}}$ denotes the surface traction on the surface $\partial \mathcal{B}_\sigma$.

There are two options for the 2nd Piola-Kirchhoff stress $\tilde{\mathbf{S}}$:

$$\text{Option 1} : \tilde{\mathbf{S}} = \tilde{\mathbf{S}}_1 := 2 \nabla \hat{W}\left(\mathbf{C}_{n+\beta}\right) \qquad (2.3)$$

$$\text{Option 2} : \tilde{\mathbf{S}} = \tilde{\mathbf{S}}_2 := \nabla \hat{W}\left(\mathbf{C}_{n+\beta}\right) + \nabla \hat{W}\left(\mathbf{C}_{n+(1-\beta)}\right) \qquad (2.4)$$

with $\beta \in (0, 1)$ such that

$$\hat{W}\left(\mathbf{C}_{n+1}\right) - \hat{W}\left(\mathbf{C}_n\right) = \tilde{\mathbf{S}} : \frac{1}{2}\left(\mathbf{C}_{n+1} - \mathbf{C}_n\right) \qquad (2.5)$$

In the proof of the energy-momentum scheme, the right Cauchy-Green strain tensor $\mathbf{C}_{n+\beta}$ is calculated by using a Taylor expansion. It yields

$$\mathbf{C}_{n+\beta} = \mathbf{C}_n + \beta \, \Delta t \, \dot{\mathbf{C}}_n + \mathcal{O}\left(\Delta t^2\right) \qquad (2.6)$$

One can observe carefully that in general, $\mathbf{C}_{n+\beta} \neq \mathbf{C}(\boldsymbol{\varphi}_{n+\beta})$ except for $\beta = 0$ and $\beta = 1$. They concluded that it is very important to use $\mathbf{C}_{n+\beta}$ instead of $\mathbf{C}(\boldsymbol{\varphi}_{n+\beta_0})$ to avoid non-physical couplings. With the help of expression (2.6), the second-order time accuracy is achieved for any $\beta \in (0, 1)$ in option 2.

However, for option 1, the second-order time accuracy is only obtained with $\beta = 1/2$, with $\beta \neq 1/2$ only the first-order time accuracy is obtained. Indeed, in order to enforce Eq. (2.5), a local Newton-Raphson method is used to solve for β at each quadratic point, with the values of $\boldsymbol{\varphi}_{n+1}$ necessary for Eq. (2.5). The values of β are then fixed to their values from the previous global equilibrium equation. With the values of β, the element force vectors and stiffness could then be determined for the next global equilibrium equation. However, the stiffness was calculated by neglecting the dependence of β on the deformation variables. It is then leading to an inconsistent stiffness matrix which may cause a convergence issue (see Laursen and Meng [51]). Besides, the nonlinear equation (2.5) degenerates to an equation with an explicit root when only a Saint Venant-Kirchhoff energy function is used. For that reason, this algorithm has been implemented only for Saint-Venant Kirchhoff material model. Nevertheless, the energy-momentum proposed by Simo and Tarnow gave the bases for future developments in nonlinear dynamics analysis.

Laursen and Meng [51] addressed the algorithm of Simo-Tarnow by correcting the coupling between the deformation variables and an algorithm parameter β which Simo and Tarnow

did not consider. They proposed two algorithms to solve that issue: one where the nonlinear equation for β is enforced at quadrature point and another where a single nonlinear equation for an element β is enforced at the element level. Consequently, the proposed algorithm presents an asymptotically quadratic rate of convergence and is applicable for general constitutive models in nonlinear elastodynamics. This work has then extended for transient impact problems [52] .

Besides, another improvement of the Simo-Tarnow framework was proposed by Simo and Gonzalez [53] and Gonzalez [54]. They applied a so-called discrete derivative for the evaluation of the stresses. The 2nd Piola-Kirchhoff stress $\tilde{\mathbf{S}}$ is given by Gonzalez-Simo framework:

$$\begin{aligned}\tilde{\mathbf{S}}\left(\boldsymbol{\varphi}_n, \boldsymbol{\varphi}_{n+1}\right) &:= 2\mathrm{d}\hat{W}\left(\mathbf{C}_n, \mathbf{C}_{n+1}\right) \\ &= 2D\hat{W}\left(\mathbf{C}_{n+1/2}\right) + 2\frac{\hat{W}\left(\mathbf{C}_{n+1}\right) - \hat{W}\left(\mathbf{C}_n\right) - D\hat{W}\left(\mathbf{C}_{n+1/2}\right) : \Delta\mathbf{C}}{\|\Delta\mathbf{C}\|^2}\Delta\mathbf{C} \end{aligned} \tag{2.7}$$

where

$$\Delta\mathbf{C} := \mathbf{C}_{n+1} - \mathbf{C}_n \quad \text{and} \|\Delta\mathbf{C}\| := \sqrt{\mathbf{C} : \mathbf{C}} \tag{2.8}$$

The stress $\tilde{\mathbf{S}}$ satisfies the directionality condition (Eq.(2.5)) and the consistency condition (Eq. 2.7). Moreover, it is symmetric. Therefore, the algorithm is second-order accurate, unconditionally stable and the conservation of energy and momenta is ensured. Furthermore, there is no singularity issue for any initial conditions due to Equation (2.7). The extra iteration needed for computing the parameter β in the implementation of the current formulation is not required.

Noels et al. [55] proposed an energy-momentum conserving scheme algorithm for nonlinear hypoelastic constitutive models. In elastic case, their algorithm is similar to Simo-Tarnow algorithm for a Saint-Venant Kirchhoff hyperelastic material and is also valid for general hyperelastic-based $J2$ plasticity models. However, the formulation of Simo et al. [35] did not consider the objectivity of the strain (see Crisfield and Jelenić [56]). For this reason, Romero and Armero claimed that the original algorithm of Simo et al. [22] does not exactly conserve the energy. Consequently, Romero and Armero [57] proposed an exact energy-momentum method for geometrically exact rods with an objective approximation of the strain measures of the rod involving finite rotations of the director frame. The improved stability due to the energy conservation property leads definitely to an improved performance of the algorithm.

Sansour et al. [39] developed an energy–momentum integration scheme and enhanced strain finite elements for the non-linear dynamics of shells with seven degree of freedom. The main idea is to use the midpoint rule but to calculate the strain field from the kinematical field differently without using directly the strain–displacement relations. Hence, the strain tensors $\mathbf{E}^0$ and $\mathbf{K}$ at midpoint time step are defined from the calculated these strain tensor velocities respectively. The following strain definition is given by

$$\mathbf{E}^0_{n+\xi} = \mathbf{E}^0_n + \xi\,\Delta t\,\dot{\mathbf{E}}^0_{n+\frac{1}{2}} \tag{2.9}$$

$$\mathbf{K}_{n+\xi} = \mathbf{K}_n + \xi\,\Delta t\,\dot{\mathbf{K}}_{n+\frac{1}{2}} \tag{2.10}$$

where $\xi \in (0,1)$ be a scalar defining any position within the time interval Δt. The choice of the midpoint in the expression is actually arbitrary. The expression would provide energy conservation for an arbitrary choice of ξ within the interval Δt.

The proposed algorithm guarantees the conservation of energy and momenta. However, this modification of the algorithms requires to store the previous right Cauchy-Green Strain E and tensor K at all the steps which are calculated by the midpoint rule. The ideas introduced in [38, 39] have been applied to develop Total Lagrangian formulations for Euler-Bernoulli [35] and Timoshenko [36] planar beams. One can notice that dealing with the nonlinearity in the kinematic terms is not an easy task. As an illustration, the equations for 2D Euler-Bernoulli beam are

$$\varepsilon_{n+\frac{1}{2}} = \varepsilon_n + \frac{1}{2}\,\Delta t\,\dot{\varepsilon}_{n+\frac{1}{2}} \tag{2.11}$$

$$\kappa_{n+\frac{1}{2}} = \kappa_n + \frac{1}{2}\,\Delta t\,\dot{\kappa}_{n+\frac{1}{2}} \tag{2.12}$$

$$\ddot{\boldsymbol{n}}_{n+\frac{1}{2}} = \frac{2}{\Delta t}\dot{\boldsymbol{n}}_{n+\frac{1}{2}} - \frac{2}{\Delta t}\dot{\boldsymbol{n}}_n \tag{2.13}$$

One can observe that midpoint velocity is not used only in the strain fields but also for the kinematic variables in order to ensure the conservation of energy and momenta. A similar idea, proposed by Gams et al. [58], is to use unconventional incremental strain updates to calculate the strains at midpoint. This approach was applied to the Reissner geometrically exact planar beam.

The energy conserving algorithms mentioned above were mostly based on the midpoint rule. Alternative methods to achieve the same objective have been proposed. Bathe [59] proposed a collocation method by combining the trapezoidal rule and the three-point backward Euler method in order to solve the second-order nonlinear dynamic equations. The method is second-order accurate, stable even for large deformations and gives accurate longtime response. Krenk [60] proposed another alternative way for energy conservation in nonlinear dynamics with general non-linear stiffness. The proposed algorithm works directly with the internal force and the stiffness matrix at the time integration interval end-points. The obtained algorithm is second-order accurate. In addition, it conserves energy and momenta which makes the algorithm unconditional stable.

While most of the energy conserving schemes addressed above are using implicit algorithms, Lim and Taylor [61] proposed an explicit-implicit conserving scheme for flexible-rigid multibody systems. An explicit integration scheme is adopted for the flexible body whereas an implicit conserving scheme is employed for the rigid body. Although the energy conservation is violated by the explicit scheme, in most cases the fluctuations of energy in the explicit scheme are negligible within the range of stable time steps. In a recent paper [62], Almonacid developed an explicit symplectic momentum-conserving scheme for the dynamics of geometrically exact rods. The characteristics of this algorithm are second-order accurate, conservation of the moment associated to the symmetries of the discrete Lagrangian, conservation of energy for long periods of times. The advantage of an explicit algorithm is that it is conditionally stable but does not require to solve nonlinear iterations at each time step. Therefore, alternative integration methods can be adopted according to the demand of specific applications.

In the past decades, energy conserving schemes or energy-momentum methods have been applied to various applications in nonlinear dynamics i.e. rigid body dynamic [63], multibody dynamics [61, 63, 64, 65], rod dynamics [18, 56, 66, 67] and shell dynamics [20, 68, 69, 70, 71, 73, 74]. However, many researchers have pointed out the issue related to spurious high frequencies in energy-momentum conserving methods. Jog and Motamarri [70] proposed an energy-momentum method for nonlinear analysis with the framework of

hybrid elements. When the hybrid stress element has been used, there is no need for an algorithmic modification for dissipating higher frequencies or due to the mesh refinement. On the other hand, Romero and Armero [57] claimed that their algorithm for geometrically exact rods should be extended to accommodate a controllable high frequency dissipation to handle the high numerical stiffness. The energy-momentum conserving algorithm proposed by Puso [65] for multibody dynamics still required small time steps to solve correctly the couple problems. Similarly, Brank et al. [69] suggested that an energy decaying scheme should be considered in order to dissipate higher order frequencies. Ibrahimbegović and Mamouri [67], who proposed an energy-momentum method for flexible beams in planar motion, had the same opinion. They clearly showed that even though the energy is preserved in the global sense and the method is unconditional stable, the beam axial force still presents high frequencies at the element level especially for stiff problems. Gams et al. [58] discussed about the size of time step for the axial, shear and bending strains and showed clearly that the local drift of strains is generally small and diminishes with a decreasing time step. However, the example proposed by Gams et al was only tested tested during one second.

2.2 Energy-momentum decaying scheme

In order to ensure that energy conserving algorithms produce reasonable and liable results regarding both the energy and internal forces for stiff problems or high-frequency problems, numerical dissipation is required. Kuhl and Ramm [75] proposed a generalized energy–momentum method for non-linear adaptive shell dynamics which guarantees either conservation of energy or decay of energy. Armero and Romero [76] developed an energy conserving/decaying algorithms for nonlinear elastodynamics that exhibits a controllable numerical dissipation in the high-frequency range. Unlike HHT dissipative numerical schemes, the proposed algorithms result in a correct qualitative picture of the exact dynamic behaviour for a fixed time step due to the conservation of the energy in the first place. Ibrahimbegović and Mamouri [77] proposed an extension of the energy conserving scheme for nonlinear dynamics of three-dimensional beams by introducing desirable properties to controll the energy decay, as well as numerical dissipation of the high-frequency contributions to the total response. The variation of strains and velocities over each time step are small and diminishes through the numerical dissipation. A similar idea was adopted by Mamouri et al. [78]. Another interesting idea adopted by Gams et al. [79] is to introduce the numerical damping in special locations, where and when it is needed.

2.3 Conclusion

The purpose of this chapter was to present a review of the energy-momentum conserving/dissipating algorithms. Most of the classical time integration methods have been derived by using Taylor's series expansions to approximate the variables such as displacement, velocity, and acceleration in the discretized equations of motion. However, the direct extended application of the traditional time integration scheme (i.e. Newmark family method [21]) from linear to nonlinear dynamic systems is not trivial and can lead to instabilities [1, 22]. Moreover, those methods could produce nonsense results with no obvious warning [80] if the solution converges to a spurious steady state. Yee et al. [81] suggested that the safety road is to understand of the dynamic behaviour of the numerical method being used.

The breakthrough of Simo-Tarnow energy-momentum method [22] gave the foundation for future development in nonlinear dynamics analysis. The stability of the algorithms is improved when the conservation of energy and momenta has been guaranteed. Most of the development of the energy conserving scheme is based on the classical midpoint rule. The main technique for energy conservation and momenta is to apply Taylor's series expansions to nonlinear kinematic and strain variables rather the directly calculate these quantities from the nodal displacements, velocities and accelerations. This idea is clearly emphasized in the papers of Sansour et al. [35, 38, 82]. In addition, the extension of energy conserving algorithms by introducing a controllable numerical dissipation in the high-frequency range is recommended for stiff problems.

Chapter 3

Co-rotational planar beam formulations

The co-rotational method is an attractive approach to derive highly nonlinear beam elements [9, 10, 11, 12, 13, 14, 15, 16, 17, 18, 19, 20, 25, 26, 27, 72, 73, 74]. The fundamental idea is to decompose the motion of the element into rigid body and pure deformational parts through the use of a local system which continuously rotates and translates with the element. The deformational response is captured at the level of the local reference frame, whereas the geometric non-linearity induced by the large rigid-body motion, is incorporated in the transformation matrices relating local and global quantities. The main interest is that the pure deformational parts can be assumed small and can be represented by a linear or a low order nonlinear theory. For a general account, we refer also to [28, 29, 30, 31, 32, 33, 34, 83, 84, 85].

One important issue in the co-rotational method is the choice of the local formulation. Whereas the Euler-Bernoulli beam theory is completely sufficient for the applications of slender beams, the Timoshenko beam theory takes into account shear deformation, making it suitable for describing the behaviour of short beams, composite beams, or beams subject to high-frequency excitation. The classical and simplest Timoshenko local element is obtained by using linear shape functions, a linear strain-displacement relation and a reduced integration [86, 87, 88]. Such a formulation requires a large number of elements in order to obtain accurate results. Several alternatives for the local part are possible in order to obtain a more efficient element: a mixed approach in which the displacements and the stress are interpolated independently [89, 90, 91, 92], an enhanced strain formulation [93, 94, 95, 96] or the Interdependent Interpolation element (IIE) formulation [97].

In the past decades, there have been many efforts to develop energy-momentum methods for co-rotational formulations. These efforts have been only partially successful. Examples of previous attempts are the ones of Crisfield and Shi [9] who developed a mid-point energy-conserving time integrator for corotating planar trusses. In their formulation, the time-integration strategy is closely linked to the co-rotational procedure which is "external" to the element. A similar approach was applied to the dynamic of co-rotational shell [20] and laminated composite shells [73]. Yang and Xia [74] proposed the energy-decaying and momentum-conserving algorithm in the context of thin-shell structures. Galvanetto and Crisfield [11] applied the previously developed energy-conserving time-integration procedure to implicit nonlinear dynamic analysis of planar beam structures. Various end- and mid-point time integration schemes for the nonlinear dynamic analysis of 3D

co-rotational beams are discussed in [17]. They concluded that the proposed mid-point scheme is an "approximately energy conserving algorithm". Salomon et al. [18] showed the conservation of energy and momenta in the 2D and 3D analyses for the simulation of elastodynamic problems. They mentioned that, for some cases, the angular momentum is asymptotically preserved and an a priori estimate is obtained. However, despite of all these works, the design of an effective time integration scheme for co-rotational elements that inherently fulfils the conservation properties of energy and momenta is still an open question.

In all the above examples energy conservation is either approximately achieved or enforced by means of constraint equations. Indeed, so far no method exists which inherently fulfills the conservation properties of energy and momenta in the context of co-rotational formulation. In this context, the main idea of Sansour et al. [39, 38] is applied to the co-rotational formulation for the first time. The fundamental idea of Sansour et al. [38, 39] is to derive strain rate quantities from the strain-displacement relations and to integrate the strains and the displacements by using the same schemes. However, this method is not as straightforward as it may seem. The choice of the correct strain rates is crucial since multiple nonlinear relations exist between the displacements and further quantities which constitute the strain field.

In this chapter, the beam kinematics and the various local strains for the co-rotational planar beam are presented. Hamilton's principle is used to derive the equation of motions. The conserving properties such as energy, linear and angular momenta for this beam model are given. The development of the energy-momentum method and numerical examples will be presented in Chapter 5 and in the appended papers I, II and III.

3.1 Beam kinematics

As shown in Figure 3.1, the motion of the element is decomposed in two parts. In a first step, a rigid body motion is defined by the global translation (u_1,w_1) of the node 1 as well as the rigid rotation α. This rigid motion defines a local coordinate system (x_l, z_l) which continuously translates and rotates with the element. In a second step, the element deformation is defined in the local coordinate system. Assuming that the length of the element is properly selected, the deformational part of the motion is always small relative to the local co-ordinate systems. Consequently, the local deformations can be expressed in a simplified manner. For a two node beam element, the global displacement vector is defined by

$$\boldsymbol{q} = \begin{bmatrix} u_1 & w_1 & \theta_1 & u_2 & w_2 & \theta_2 \end{bmatrix}^{\mathrm{T}}, \tag{3.1}$$

and the local displacement vector is defined by

$$\bar{\boldsymbol{q}} = \begin{bmatrix} \bar{u} & \bar{\theta}_1 & \bar{\theta}_2 \end{bmatrix}^{\mathrm{T}} \tag{3.2}$$

3.2 Strain measures

Bernoulli/IIE formulation

The Interdependent Interpolation Element(IIE), proposed in [97], is adopted for the local beam kinematic description. The development of this beam element is based on the

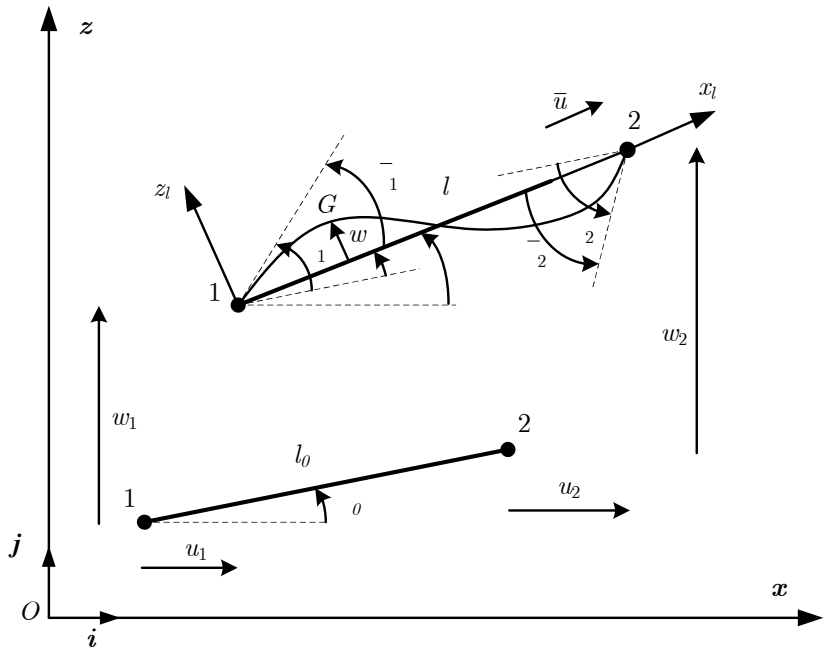

Figure 3.1: Beam kinematics.

exact solution of the homogeneous form of the equilibrium equations for a Timoshenko beam. Consequently, the IIE element retains not only the accuracy inherent to the cubic interpolation, but also includes the bending shear deformation. The shape functions of the IIE element are given by

$$\begin{aligned}
N_3 &= \mu\, x \left[6\,\Omega \left(1 - \frac{x}{l_0} \right) + \left(1 - \frac{x}{l_0} \right)^2 \right] \\
N_4 &= \mu\, x \left[6\,\Omega \left(\frac{x}{l_0} - 1 \right) - \frac{x}{l_0} + \frac{x^2}{l_0^2} \right] \\
N_5 &= \mu \left(1 + 12\,\Omega - \frac{12\,\Omega\, x}{l_0} - \frac{4\,x}{l_0} + \frac{3\,x^2}{l_0^2} \right) \\
N_6 &= \mu \left(\frac{12\,\Omega\, x}{l_0} - \frac{2\,x}{l_0} + \frac{3\,x^2}{l_0^2} \right)
\end{aligned} \tag{3.3}$$

where $\Omega = EI/(GA\,k_s\,l_0^2)$, $\mu = 1/(1+12\,\Omega)$ and k_s is the shear correction coefficient. For a rectangular cross-section, k_s is equal to 5/6. For the dynamic terms, Ω is taken to 0 since extensive numerical studies have shown that this simplification does not affect the numerical results (see [12]). It can be observed that with $\Omega = 0$, the Hermitian shape functions of the classical Bernoulli element are recovered.

The shape functions of the IIE are used together with a shallow arch beam theory. The shallow arch longitudinal and shear strains are given by

$$\varepsilon_{11} = \varepsilon - \kappa\, z \tag{3.4}$$

$$\gamma = \frac{\partial w}{\partial x} - \theta \tag{3.5}$$

in which the axial strain ε and the curvature κ are defined by

$$\varepsilon = \frac{1}{l_0}\int_{l_0}\left[\frac{\partial u}{\partial x} + \frac{1}{2}\left(\frac{\partial w}{\partial x}\right)^2\right]\mathrm{d}x \tag{3.6}$$

$$\kappa = \frac{\partial^2 w}{\partial x^2} \tag{3.7}$$

In Eq.(3.6), the axial strain is averaged over the element in order to avoid membrane locking. The purpose of introducing a mild geometrical non-linearity in the local formulation is to increase the accuracy of the formulation as compared to a purely linear strain definition, while still retaining the efficiency.

Reduced integration method

The reduced integration formulation (RIE) is the classical Timoshenko approach based on linear interpolations and one Gauss point integration in order to avoid shear locking. The curvature κ, shear deformation γ and strain ε are defined by

$$\kappa = \frac{\partial \theta}{\partial x} = \frac{\bar{\theta}_2 - \bar{\theta}_1}{l_0} \tag{3.8}$$

$$\gamma = \frac{\partial w}{\partial x} - \theta = -N_1\bar{\theta}_1 - N_2\bar{\theta}_2 \tag{3.9}$$

$$\varepsilon_{11} = \varepsilon - \kappa\, z = \frac{\bar{u}}{l_0} - \frac{\bar{\theta}_2 - \bar{\theta}_1}{l_0} z \tag{3.10}$$

The elastic potential energy for both IIE and reduced integration formulation is defined by

$$\mathsf{U}_{int} = \frac{1}{2}\int_{l_0} EA\,\varepsilon^2 \mathrm{d}x + \frac{1}{2}\int_{l_0} EI\,\kappa^2 \mathrm{d}x + \frac{1}{2}\int_{l_0} k_s GA\,\gamma^2 \mathrm{d}x \tag{3.11}$$

where E is the elastic modulus and G the shear modulus of the material.

Hellinger-Reissner mixed formulation

A two-field mixed formulation based on the Hellinger–Reissner variational principle is considered. Both displacements and internal forces along the element are approximated by independent linear interpolation functions. The elastic potential of the Hellinger-Reissner mixed formulation is written as

$$\mathsf{U}_{int} = \int_{l_0} \boldsymbol{S}^{\mathrm{T}}\left(\hat{\boldsymbol{e}} - \frac{1}{2}\boldsymbol{e}\right)\mathrm{d}x \tag{3.12}$$

The generalized stress resultant vector $\boldsymbol{S}$ is approximate by

$$\boldsymbol{S} = \begin{bmatrix} N \\ M \\ Q \end{bmatrix} = \mathbf{N}_s\,\boldsymbol{f}_l = \begin{bmatrix} 1 & 0 & 0 \\ 0 & -N_1 & N_2 \\ 0 & -1/l_0 & -1/l_0 \end{bmatrix}\begin{bmatrix} N \\ M_1 \\ M_2 \end{bmatrix} \tag{3.13}$$

where $\mathbf{N}_s$ is the matrix of shape functions satisfying local equilibrium.

From Eqs.(3.8),(3.9) and (3.10), the generalized strain vector $\hat{\mathbf{e}}$ is written as

$$\hat{\boldsymbol{e}} = \begin{bmatrix} \varepsilon \\ \kappa \\ \gamma \end{bmatrix} = \mathbf{N}_{\hat{e}}\,\bar{\boldsymbol{q}} = \begin{bmatrix} 1/l_0 & 0 & 0 \\ 0 & -1/l_0 & 1/l_0 \\ 0 & -N_1 & -N_2 \end{bmatrix}\begin{bmatrix} \bar{u} \\ \bar{\theta}_1 \\ \bar{\theta}_2 \end{bmatrix} \tag{3.14}$$

The cross-section deformation vector $\boldsymbol{e}$ is defined by

$$\boldsymbol{e} = \mathbf{N}_{s1}\, \boldsymbol{f}_l = \begin{bmatrix} 1/(EA) & 0 & 0 \\ 0 & -N_1/(EI) & N_2/(EI) \\ 0 & -1/(k_s G A\, l_0) & -1/(k_s G A\, l_0) \end{bmatrix} \begin{bmatrix} N \\ M_1 \\ M_2 \end{bmatrix} \tag{3.15}$$

3.3 Hamilton's principle and conserving properties

Hamilton's principle states that the integral of the Lagrangian between two specified time instants t_1 and t_2 of a conservative mechanical system is stationary

$$\delta \int_{t_1}^{t_2} \mathcal{L}\, \mathrm{d}t = \delta \int_{t_1}^{t_2} (\mathsf{K} - \mathsf{U}_{int} - \mathsf{U}_{ext})\, \mathrm{d}t = 0 \tag{3.16}$$

wihere K is the kinetic energy, and U_{ext} is the external potential. The body is a non-conducting linear elastic solid and thermodynamic effects are not included in the system. U_{int} are defined according to each formulation (see Eqs. (3.11) and (3.12)). The kinetic energy is the sum of the translational and rotational kinetic energies:

$$\mathsf{K} = \frac{1}{2} \int_{l_0} \rho A\, \dot{u}_G^2\, \mathrm{d}x + \frac{1}{2} \int_{l_0} \rho A\, \dot{w}_G^2\, \mathrm{d}x + \frac{1}{2} \int_{l_0} \rho I\, \dot{\theta}_G^2\, \mathrm{d}x \tag{3.17}$$

while the external potential is given as

$$\mathsf{U}_{ext} = -\int_{l_0} p_u u_G\, \mathrm{d}x - \int_{l_0} p_w w_G\, \mathrm{d}x - \int_{l_0} p_\theta \theta_G\, \mathrm{d}x - \sum_{i=1}^{6} P_i q_i \tag{3.18}$$

p_u and p_w are the distributed horizontal and vertical loads, p_θ is the distributed external moment, P_i is the i component (concentrated forces and moments at the nodes) of external force vector $\boldsymbol{P}$.

The above equations are the starting point for further developments. Further, the above Hamiltonian system exhibits the following conservation properties. If the external loads are conservative, the total energy of the beam element can be written as

$$\mathsf{K} + \mathsf{U}_{int} + \mathsf{U}_{ext} = \mathsf{constant} \tag{3.19}$$

The linear momentum is defined by

$$\mathsf{L} = \begin{bmatrix} \mathsf{L}_u \\ \mathsf{L}_w \end{bmatrix} = \int_{l_0} \rho A \begin{bmatrix} \dot{u}_G \\ \dot{w}_G \end{bmatrix} \mathrm{d}x \tag{3.20}$$

and the angular momentum by

$$\mathsf{J} = \int_{l_0} \rho A \begin{bmatrix} u_G \\ w_G \\ 0 \end{bmatrix} \times \begin{bmatrix} \dot{u}_G \\ \dot{w}_G \\ 0 \end{bmatrix} \mathrm{d}x + \int_{l_0} \rho I \begin{bmatrix} 0 \\ 0 \\ \dot{\theta}_G \end{bmatrix} \mathrm{d}x \tag{3.21}$$

The time derivative of the two momenta define the equations of motion:

$$\frac{\mathrm{d}}{\mathrm{d}t}\mathsf{L} = \begin{bmatrix} \int_{l_0} p_u\, \mathrm{d}x + P_1 + P_4 \\ \int_{l_0} p_w\, \mathrm{d}x + P_2 + P_5 \end{bmatrix} \tag{3.22}$$

and

$$\frac{\mathrm{d}}{\mathrm{d}t}\mathsf{J} = \int_{l_0} (u_G\, p_w - w_G\, p_u)\,\mathrm{d}x + (x_1 + u_1)P_2 - (z_1 + w_1)P_1 \\ + (x_2 + u_2)P_5 - (z_2 + w_2)P_4 + \int_{l_0} p_\theta\,\mathrm{d}x + P_3 + P_6 = M_{ext} \tag{3.23}$$

from which it can be seen that, with vanishing external load, the linear momentum is constant and, with vanishing external moments, the angular momentum is constant. It should be noted that the expression "external load" refers to all possible loading conditions including reactions forces.

Chapter 4

Geometrically exact Euler-Bernoulli spatial beam formulation

Flexible beam elements can be found in different areas of engineering practice. For some applications, such as large deployable space-structures, wind turbines propellers, offshore platforms or structures under extreme loading, beam structures could undergo large deformations as well. In addition to industrial applications, in many areas in biology and biomechanics researchers are resorting to slender beam theories as a powerful modelling tool as well.

While the linear beam theory is generally based on the Euler-Bernoulli hypothesis, which neglects shear deformations, a generalisation to the non-linear large deformation regime is usually based on the Timoshenko assumption which considers shear deformations. The main reason is that the kinematic description of the deformation of the beam cross section is straightforward under the latter assumption and very complex under the former. Indeed, the modelling of the non-linear static and dynamic behaviour of beams has been successfully carried out using concepts which incorporate three-parametric rotation tensors while exhibiting shear strains. The specific assumptions, details and parameterisations may differ but the outcomes are very much similar: Argyris et al. [98], Bathe and Balourchi [99], Simo and Vu-Quoc [100], Cardona and Géradin [101], Pimento and Yojo [102], Bauchau et al. [103] Ibrahimbegović [104, 105], Gruttmann et al. [106], Zupan and Saje [107], Sansour and Wagner [108], Kapania and Lie [109], Romero [110], Mata et al. [111], Zupan et al. [112], Zhong et al. [113]. and Li et al [114].

The extension of Euler-Bernoulli assumption to the non-linear large deformation regime is challenging. In the planar case, the desired extension has been successfully carried out for both the static and dynamic cases (Nanakorn and Vu [115], Armero and Valverde [116], Sansour et al. [35]). In contrast, the general three-dimensional case finds itself faced with multiple problems which prevented its development and so hindered possible applications. This is especially true within the context of dynamics. In this work, a three dimensional formulation for an Euler-Bernoulli-based beam theory is provided.

The main obstacle in defining a three-dimensional Euler-Bernoulli beam theory lies in the fact that there is no natural way of defining a base system at the deformed configuration. Such a system exists at the reference configuration by definition. The strain measures are

employed to characterise the deformation of these base vectors into the current configuration. Beam formulations, which consider shear, make use of a rotation tensor to define the current configuration of these vectors. In an Euler-Bernoulli beam, their final position can not be defined directly. Some recent attempts can be found in the literature where the problem has been successfully solved via different strategies which result in replacing two rotation parameters by expressions which relate to the displacements of the centre line resulting in 4 parametric beam formulations. Three of those parameters are either displacements or rotations, while the fourth parameter captures the cross sectional torsional rotation or the stretch of the centre line, respectively. The reader is referred to Pai [117], Zhoa and Ren [118], Greco and Cuomo [119], Bauer et al. [120], Meier [121] for a complete details on the issue. Besides, Shabana et al. [122, 123] proposed the absolute nodal position and slope degree of freedom instead of angles to define the orientation of the element.

In this work, an alternative and direct approach to realise the objective of developing an Euler-Bernoulli-based three-dimensional beam theory is presented. Based on the Euler-Bernoulli assumption, the only information available is that 1) the base vectors will stay normal to each other after the deformation and 2) the central line is well defined by means of a displacement vector and the only vector which changes length is that tangent to the central line. Two approaches to define the position of the deformed base system in a way consistent with the overarching Euler-Bernoulli assumption will be presented. In a first approach, the issue is resolved by resorting to the following idea. Given the tangent vector at the base line (centre line), which is available through a standard differentiating process, an orthogonal base system is constructed by means of a Gram-Schmidt process. This base system is then rotated to the final deformed one by means of a rotation tensor, the rotation vector of which is parallel to the tangent vector at the deformed configuration. Hence, this rotation is only one-parametric. The rotation defines an angle which is a degree of freedom of the system. Indeed, it contributes to the definition of the torsional motion of the cross section, though it does not describe it completely as parts of this torsional rotation are captured by means of the orthogonalisation process. However, since the orthogonal base system constructed by means of the Gram-Schmidt process is not unique, the rotation angle is not unique as well. Though, the final configuration of the base vectors is unique and so the resulting strain measures are unique and objective providing us with an access to a complete Euler-Bernoulli three-dimensional beam theory.

In a second approach, it will be shown as to how the rotation tensor can be defined based on first and second derivatives of the displacement vector of the centre line, together along a one parametric rotation. While this second approach is presented, it is not going to be implemented as the numerical implementation is restricted to the first approach.

The design of energy conservation is not straightforward and depends very much on the involved non-linearities in the formulation at hand. In fact the Euler-Bernoulli hypothesis, due to its coupling of the cross sectional deformation to the deformation of the central line, does provide us with highly complex non-linear expressions for bending as well as for the kinetic energy, which involve second derivatives of the displacement field. A general methodology for the systematic construction of energy-conserving schemes has been proposed by Sansour et al. [38, 39] and successfully applied to different shell and rod formulations in [82], [35]. The methodology is based on the realisation that geometric and material non-linearities have to be treated differently. The complexities of the geometric non-linearities can be circumvented by resorting to strain velocities to provide, by means of integration, the expressions for the strain measures themselves. The expressions for

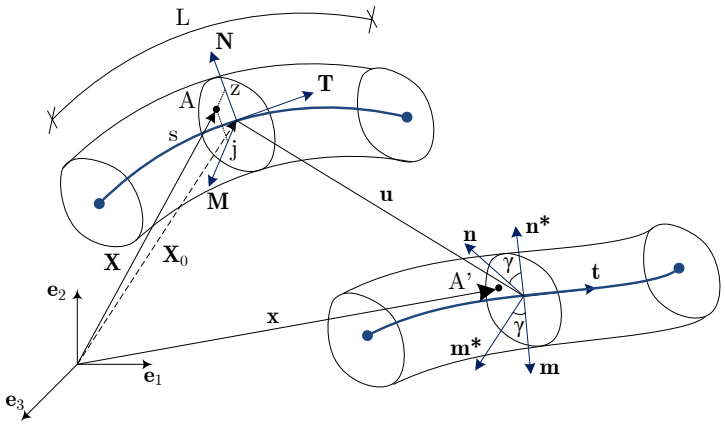

Figure 4.1: Beam kinematics.

the strain velocities, by definition, are linear in the velocities of the degrees of freedom of the system; the displacements as in the case of the present beam formulation. This is a powerful statement which makes energy-conservation accessible no matter how complex the geometric non-linearities, meaning the expressions of the strain-displacement relations, may be. This methodology will be applied to the present formulation and it proves itself again as powerful.

In this chapter, the beam kinematics and the implementation of Euler-Bernoulli assumption for the first approach are presented. An alternative approach to the same objective is presented as well. The principle of virtual work is given along with the conserving properties. The details for the development of energy-conserving scheme for this new formulation are discussed in Chapter 5 and the paper IV.

4.1 Beam kinematics

Let $\mathcal{B} \subset \mathbb{R}^3$, where $\mathcal{B}$ defines a reference configuration of a material body. The map $\varphi(t) : \mathcal{B} \to \mathbb{R}^3$ is an embedding depending on a time-like parameter $t \in \mathbb{R}$. Hence, $\varphi_0 = \varphi\,(t = t_0)$ defines a reference configuration which enables the identification of the material points. Then, for the reference position $\boldsymbol{X} \in \mathcal{B}$ and the deformed position $\boldsymbol{x} \in \mathcal{B}_t$, it gives: $\boldsymbol{x}(t) = \varphi(\boldsymbol{X}, t)$ and $\boldsymbol{X}(t) = \varphi^{-1}(\boldsymbol{x}, t)$. Furthermore, let $\boldsymbol{e}_i$, $i = 1, 2, 3$ be the Cartesian basis vectors. As shown in Figure 4.1, all the center points of the rod cross-sections defined the centre line, which assume to be smooth. An arc length parametrisation of this line with the arc length L at the reference configuration denoted as $s \in [0, L]$. Therefore, a curvilinear coordinate system, which is considered to be convected, is described by the triple (s, z, j) for any material point in the cross-section.

Let $\boldsymbol{X}_0$ be the position of the center line at the reference configuration and it gives:

$$\boldsymbol{X}(s, z, j) = \boldsymbol{X}_0(s) + z\,\boldsymbol{N}(s) + j\,\boldsymbol{M}(s) \tag{4.1}$$

The unit tangent vector is defined as $\boldsymbol{T} = \partial \boldsymbol{X}_0/\partial s|_{j=z=0}$. Similarly, the vectors $\boldsymbol{T}_1 = \partial \boldsymbol{X}/\partial s$, $\boldsymbol{N} = \partial \boldsymbol{X}/\partial z$ and $\boldsymbol{M} = \partial \boldsymbol{X}/\partial j$ are introduced. Hence, the triple $(\boldsymbol{T}_1, \boldsymbol{N}, \boldsymbol{M})$ defines a local curvilinear basis for the reference configuration. The corresponding contravariant-based vectors are then given by $\left(\boldsymbol{T}^1, \boldsymbol{N}, \boldsymbol{M}\right)$ with $\boldsymbol{T}^1 = \boldsymbol{T}_1/\left|\boldsymbol{T}_1\right|^2$. In a latter expression, $|\bullet|$ denotes the norm of a vector.

The corresponding tangent vectors at the deformed configuration are defined as $(\boldsymbol{g}, \boldsymbol{n}, \boldsymbol{m})$ with $\boldsymbol{g} = \partial \boldsymbol{x}/\partial s$ and both $\boldsymbol{n}$ and $\boldsymbol{m}$ are the normal vectors of the cross-section. From Figure 4.1, the position $\boldsymbol{x}$ of point A' at the deformed configuration is then defined as :

$$\boldsymbol{x}(s, z, j) = \boldsymbol{X}_0(s) + \boldsymbol{u}(s) + z\,\boldsymbol{n}(s) + j\,\boldsymbol{m}(s) \tag{4.2}$$

where $\boldsymbol{u}(s)$ is the displacement vector of the center line. From the above expression, it gives:

$$\boldsymbol{g} = \boldsymbol{x}_{,s} = \boldsymbol{X}_{0,s} + \boldsymbol{u}_{,s} + z\,\boldsymbol{n}_{,s} + j\,\boldsymbol{m}_{,s} \tag{4.3}$$

and the unit tangent vector $\boldsymbol{t}$ is given by

$$\boldsymbol{t} = \frac{\boldsymbol{X}_{0,s} + \boldsymbol{u}_{,s}}{|\boldsymbol{X}_{0,s} + \boldsymbol{u}_{,s}|} \tag{4.4}$$

where a comma denotes the derivative.

Two choices for the normal vectors of cross-sections in the deformed configuration are discussed in the following section.

First approach

By the definition of the Gram-Schmidt process, the deformed normal vector $\boldsymbol{n}^*$ can be constructed based on the deformed unit tangent vector $\boldsymbol{t}$ and one of the normal vectors ($\boldsymbol{N}$ or $\boldsymbol{M}$) in the reference configuration. By doing this, the $\boldsymbol{n}^*$ and $\boldsymbol{t}$ stay normal to each other. Therefore, the normal vector $\boldsymbol{n}^*$ is defined as:

$$\boldsymbol{n}^* = \frac{\boldsymbol{N} - (\boldsymbol{N}\cdot\boldsymbol{t})\,\boldsymbol{t}}{|\boldsymbol{N} - (\boldsymbol{N}\cdot\boldsymbol{t})\,\boldsymbol{t}|} \quad or \quad \boldsymbol{n}^* = \frac{\boldsymbol{M} - (\boldsymbol{M}\cdot\boldsymbol{t})\,\boldsymbol{t}}{|\boldsymbol{M} - (\boldsymbol{M}\cdot\boldsymbol{t})\,\boldsymbol{t}|} \tag{4.5}$$

where a dot denotes the scalar product of vectors.

This base system is then rotated to the final deformed one by means of a rotation tensor $\mathbf{R}_1$, this rotation vector is parallel to the tangent vector at the deformed configuration. Hence, this rotation has only one parameter γ. This parameter defines an angle which is taken as a degree of freedom of the element. Indeed, it contributes to the definition of the torsional motion of the cross section, though it does not describe it completely as parts of this torsional rotation are captured by means of the orthogonalisation process.

The rotation tensor $\mathbf{R}_1$ is defined with the help exponential map as follow (Choquet-Bruhat et al. [124]; Dubrovin et al. [125]).

$$\mathbf{R}_1 = \mathbf{I} + \sin\gamma\,\underline{\boldsymbol{\Gamma}}_t + (1 - \cos\gamma)\,\underline{\boldsymbol{\Gamma}}_t\,\underline{\boldsymbol{\Gamma}}_t \tag{4.6}$$

where $\underline{\boldsymbol{\Gamma}}_t$ denotes a skew-symmetric matrix of the vector $\boldsymbol{t}$:

$$\underline{\boldsymbol{\Gamma}}_t = \begin{bmatrix} 0 & -t(3) & t(2) \\ t(3) & 0 & -t(1) \\ -t(2) & t(1) & 0 \end{bmatrix} \tag{4.7}$$

Therefore, the final normal vector $\boldsymbol{n}$ in the deformed configuration is given as

$$\boldsymbol{n} = \mathbf{R}_1\,\boldsymbol{n}^* \tag{4.8}$$

Since the Euler-Bernoulli assumption is adopted, the remaining normal vector $\boldsymbol{m}$ stays normal to other vectors ($\boldsymbol{n}$, $\boldsymbol{t}$) after the deformation. It is defined by $\boldsymbol{m} = \boldsymbol{t} \times \boldsymbol{n}$ where $\times$ denotes the cross product of two vectors.

Second approach

In a second approach, the rotation tensor is defined based on first and second derivatives of the displacement vector of the centre line, together with one parametric rotation γ. The total rotation matrix is obtained by a multiplication of two rotation matrices:

$$\mathbf{R} = \mathbf{R}_1 (\gamma \boldsymbol{t}) \mathbf{R}_2 (\boldsymbol{w}) \tag{4.9}$$

where the rotation tensor $\mathbf{R}_1$ is already defined in the first approach. $\boldsymbol{w}$ is the rotation vector of $\mathbf{R}_2$ which is computed from the following expression:

$$\boldsymbol{T} \cdot \boldsymbol{t} = |\boldsymbol{T}||\boldsymbol{t}| \cos\alpha = \cos\alpha \tag{4.10}$$

$$\boldsymbol{T} \times \boldsymbol{t} = |\boldsymbol{T}||\boldsymbol{t}| \sin\alpha \frac{\boldsymbol{w}}{|\boldsymbol{w}|} = \frac{\sin\alpha}{\alpha} \boldsymbol{w} \tag{4.11}$$

with α being the angle between the vectors $\boldsymbol{T}$ and $\boldsymbol{t}$. It yields:

$$\boldsymbol{w} = \frac{\alpha}{\sin\alpha} (\boldsymbol{T} \times \boldsymbol{t}) \tag{4.12}$$

The rotation tensor $\mathbf{R}_2$ is given as:

$$\begin{aligned} \mathbf{R}_2 &= \mathbf{I} + \frac{\sin\alpha}{\alpha} \underline{\boldsymbol{\Gamma}}_w + \frac{1-\cos\alpha}{\alpha^2} \underline{\boldsymbol{\Gamma}}_w \underline{\boldsymbol{\Gamma}}_w \\ &= \mathbf{I} + \underline{\boldsymbol{\Gamma}}_v + \frac{1}{1+\boldsymbol{T}\cdot\boldsymbol{t}} \underline{\boldsymbol{\Gamma}}_v \underline{\boldsymbol{\Gamma}}_v \end{aligned} \tag{4.13}$$

where $\underline{\boldsymbol{\Gamma}}_w$ denotes a skew-symmetric matrix of the vector $\boldsymbol{w}$ and $\underline{\boldsymbol{\Gamma}}_v$ a skew-symmetric matrix of the vector $\boldsymbol{v} = \boldsymbol{T} \times \boldsymbol{t}$.

Finally, the normal vectors in the deformed configuration are then given by:

$$\boldsymbol{n} = \mathbf{R}\, \boldsymbol{N} \tag{4.14}$$

$$\boldsymbol{m} = \mathbf{R}\, \boldsymbol{M} \tag{4.15}$$

4.2 Strain measures

Based on the above beam kinematics, the deformation gradient can be written down in the curvilinear bases system as: $\mathbf{F} = \boldsymbol{g} \otimes \boldsymbol{T}^1 + \boldsymbol{n} \otimes \boldsymbol{N} + \boldsymbol{m} \otimes \boldsymbol{M}$. The right Cauchy deformation tensor is defined as $\mathbf{F}^{\mathrm{T}}\mathbf{F}$, which gives under the matrix form:

$$\mathbf{C} = \begin{bmatrix} \boldsymbol{g}\cdot\boldsymbol{g} & \boldsymbol{g}\cdot\boldsymbol{n} & \boldsymbol{g}\cdot\boldsymbol{m} \\ \boldsymbol{g}\cdot\boldsymbol{n} & 1 & 0 \\ \boldsymbol{g}\cdot\boldsymbol{m} & 0 & 1 \end{bmatrix} \tag{4.16}$$

Then, the Green stain tensor $\mathbf{E} = \frac{1}{2}(\mathbf{C} - \mathbf{I})$ is given as

$$\mathbf{E} = \begin{bmatrix} E_{11} & E_{12} & E_{13} \\ E_{12} & 0 & 0 \\ E_{13} & 0 & 0 \end{bmatrix} \tag{4.17}$$

The non-trivial components of the Green tensor are written as

$$E_{11} = \varepsilon_{11} + z\,\kappa_1 + j\,\kappa_2 \tag{4.18}$$

$$E_{12} = \frac{1}{2}\,j\,\kappa_{12} \tag{4.19}$$

$$E_{13} = \frac{1}{2}\,z\,\kappa_{13} \tag{4.20}$$

where ε_{11} denotes as the axial strain, κ_1, κ_2 as the curvature of the direction z and j respectively, κ_{12} and κ_{13} as the torsion of the cross-section. These strains are given after some algebraic manipulations:

$$\varepsilon_{11} \approx \boldsymbol{X}_{0,s} \cdot \boldsymbol{u}_{,s} + \frac{1}{2}\boldsymbol{u}_{,s} \cdot \boldsymbol{u}_{,s} \tag{4.21}$$

$$\kappa_1 = (\boldsymbol{X}_{0,s} + \boldsymbol{u}_{,s}) \cdot \boldsymbol{n}_{,s} - \boldsymbol{X}_{0,s} \cdot \boldsymbol{N}_{,s} \tag{4.22}$$

$$\kappa_2 = (\boldsymbol{X}_{0,s} + \boldsymbol{u}_{,s}) \cdot \boldsymbol{m}_{,s} - \boldsymbol{X}_{0,s} \cdot \boldsymbol{M}_{,s} \tag{4.23}$$

$$\kappa_{12} = \boldsymbol{n} \cdot \boldsymbol{m}_{,s} - \boldsymbol{N} \cdot \boldsymbol{M}_{,s} \tag{4.24}$$

$$\kappa_{13} = \boldsymbol{n}_{,s} \cdot \boldsymbol{m} - \boldsymbol{N}_{,s} \cdot \boldsymbol{M} \tag{4.25}$$

The axial strain is simplified by neglecting terms of z^2 and j^2 since the thickness of the beam is small compared to its length. Besides, $\kappa_{12} = -\kappa_{13}$ are equal to each other in magnitude because the following condition of normality is satisfied: $(\boldsymbol{m} \cdot \boldsymbol{n} - \boldsymbol{M} \cdot \boldsymbol{N})_{,s} = 0$.

4.3 Principle of virtual work and conserving properties

The principle of virtual work in dynamics is given by:

$$\int_{t_1}^{t_2} \left(\int_V \rho\, \ddot{\boldsymbol{x}} \cdot \delta \boldsymbol{x}\, \mathrm{d}V + \int_V E\, E_{11}\, \delta E_{11}\, \mathrm{d}V + \int_V \frac{2E}{1+\nu}\, E_{12}\, \delta E_{12}\, \mathrm{d}V \right.$$
$$\left. + \int_V \frac{2E}{1+\nu}\, E_{13}\, \delta E_{13}\, \mathrm{d}V - \int_L \boldsymbol{p}(s) \cdot \delta \boldsymbol{u}\, \mathrm{d}s - \sum_{i=1}^{N} \boldsymbol{P}_i \cdot \delta \boldsymbol{u}_i \right) \mathrm{d}t = 0 \tag{4.26}$$

Equation (4.26) is further developed to produce:

$$\int_{t_1}^{t_2} \left(\int_L \rho A\, \ddot{\boldsymbol{u}} \cdot \delta \boldsymbol{u}\, \mathrm{d}s + \int_L \rho I_z\, \ddot{\boldsymbol{n}} \cdot \delta \boldsymbol{n}\, \mathrm{d}s + \int_L \rho I_j\, \ddot{\boldsymbol{m}} \cdot \delta \boldsymbol{m}\, \mathrm{d}s \right.$$
$$+ \int_L EA\, \varepsilon_{11}\, \delta \varepsilon_{11}\, \mathrm{d}s + \int_L EI_z\, \kappa_1\, \delta \kappa_1\, \mathrm{d}s + \int_L EI_j\, \kappa_2\, \delta \kappa_2\, \mathrm{d}s$$
$$\left. + \int_L GI_j\, \kappa_{12}\, \delta \kappa_{12}\, \mathrm{d}s + \int_L GI_z\, \kappa_{13}\, \delta \kappa_{13}\, \mathrm{d}s - \int_L \boldsymbol{p}(s) \cdot \delta \boldsymbol{u}\, \mathrm{d}s - \sum_{i=1}^{N} \boldsymbol{P}_i \cdot \delta \boldsymbol{u}_i \right) \mathrm{d}t = 0 \tag{4.27}$$

where V is the volume of the beam, L the length, ρ the density of the material, A the area of the cross section, I_z and I_j moment of inertia. E is young module of the material and G shear modulus with the coefficient of Poisson ν. $\boldsymbol{P}_i$, $i = 1, 2, ..., N$ are concentrated force and $\boldsymbol{p}$ is a distributed external force.

Since $\kappa_{12} = -\kappa_{13}$, the terms related to torsion can be combined into a single term:

$$\int_L GI_j\, \kappa_{12}\, \delta \kappa_{12}\, \mathrm{d}s + \int_L GI_z\, \kappa_{13}\, \delta \kappa_{13}\, \mathrm{d}s = \int_L G\,(I_j + I_z)\, \kappa_{12}\, \delta \kappa_{12}\, \mathrm{d}s = \int_L GJ\, \kappa_{12}\, \delta \kappa_{12}\, \mathrm{d}s \tag{4.28}$$

Indeed, the torsional constant J equal to $I_j + I_z$ is only valid for circular section. However, for any arbitrary cross-section, the actual torsional constant J is adopted instead of the terms $I_j + I_z$.

Therefore, Equation (4.27) can be rewritten as

$$\begin{aligned}\int_{t_1}^{t_2} \Bigg(& \int_L \rho A\, \ddot{\boldsymbol{u}} \cdot \delta \boldsymbol{u}\, \mathrm{d}s + \int_L \rho I_z\, \ddot{\boldsymbol{n}} \cdot \delta \boldsymbol{n}\, \mathrm{d}s + \int_L \rho I_j\, \ddot{\boldsymbol{m}} \cdot \delta \boldsymbol{m}\, \mathrm{d}s \\ & + \int_L EA\ \varepsilon_{11}\, \delta\varepsilon_{11}\, \mathrm{d}s + \int_L EI_z\, \kappa_1\, \delta\kappa_1\, \mathrm{d}s + \int_L EI_j\, \kappa_2\, \delta\kappa_2\, \mathrm{d}s \\ & + \int_L GJ\, \kappa_{12}\, \delta\kappa_{12}\, \mathrm{d}s - \int_L \boldsymbol{p}(s) \cdot \delta \boldsymbol{u}\ \mathrm{d}s - \sum_{i=1}^{N} \boldsymbol{P}_i \cdot \delta \boldsymbol{u}_i \Bigg)\ \mathrm{d}t = 0 \end{aligned} \tag{4.29}$$

One can show that the aforementioned statement do entail certain conservation properties. The total energy is defined by:

$$\mathsf{E} = \mathsf{K} + \mathsf{U}_{int} + \mathsf{U}_{ext} \tag{4.30}$$

with:

$$\mathsf{K} = \frac{1}{2} \int_L \rho A\, \dot{\boldsymbol{u}} \cdot \dot{\boldsymbol{u}}\, \mathrm{d}s + \frac{1}{2} \int_L \rho I_z\, \dot{\boldsymbol{n}} \cdot \dot{\boldsymbol{n}}\, \mathrm{d}s + \frac{1}{2} \int_L \rho I_j\, \dot{\boldsymbol{m}} \cdot \dot{\boldsymbol{m}}\, \mathrm{d}s \tag{4.31}$$

$$\mathsf{U}_{int} = \frac{1}{2} \int_L EA\ \varepsilon_{11}^2\, \mathrm{d}s + \frac{1}{2} \int_L EI_z\, \kappa_1^2\, \mathrm{d}s + \frac{1}{2} \int_L EI_j\, \kappa_2^2 \mathrm{d}s + \frac{1}{2} \int_L GJ\, \kappa_{12}^2\, \mathrm{d}s \tag{4.32}$$

$$\mathcal{U}_{ext} = - \int_L \boldsymbol{p}(s) \cdot \boldsymbol{u}\, \mathrm{d}s - \sum_{i=1}^{N} \boldsymbol{P}_i \cdot \boldsymbol{u}_i \tag{4.33}$$

The linear momentum is defined by

$$\mathsf{L} = \int_V \rho\, \dot{\boldsymbol{x}}\, \mathrm{d}V = \int_L \int_A \rho\ (\dot{\boldsymbol{u}} + z\, \dot{\boldsymbol{n}} + j\, \dot{\boldsymbol{m}})\ \mathrm{d}A\, \mathrm{d}L = \int_L \rho A\, \dot{\boldsymbol{u}}\, \mathrm{d}s \tag{4.34}$$

and the angular momentum defined by

$$\begin{aligned} \mathsf{J} &= \int_V \rho\, \boldsymbol{x} \times \dot{\boldsymbol{x}}\, \mathrm{d}V \\ &= \int_L \rho A\ (\boldsymbol{X}_0 + \boldsymbol{u}) \times \dot{\boldsymbol{u}}\, \mathrm{d}s + \int_L \rho I_z\, (\boldsymbol{n} \times \dot{\boldsymbol{n}})\, \mathrm{d}s + \int_L \rho I_j\, (\boldsymbol{m} \times \dot{\boldsymbol{m}})\, \mathrm{d}s \end{aligned} \tag{4.35}$$

Functional (4.29) is equivalent to the statements:

$$\frac{D}{Dt}\mathsf{L} = \int_L \boldsymbol{p}(s) \cdot \delta \boldsymbol{u}\ \mathrm{d}s + \sum_{i=1}^{N} \boldsymbol{P}_i \tag{4.36}$$

$$\frac{D}{Dt}\mathsf{J} = \int_L \boldsymbol{x}_0 \times \boldsymbol{p}(s)\, \mathrm{d}s + \sum_{i=1}^{N} \boldsymbol{x}_0 \times \boldsymbol{P}_i \tag{4.37}$$

From the aforementioned equations, linear and angular momenta are conserved:

$$\mathsf{L} = \mathsf{constant}, \quad \text{for vanishing loading} \tag{4.38}$$

$$\mathsf{J} = \mathsf{constant}, \quad \text{for vanishing moments} \tag{4.39}$$

Likewise, one can derive that the total energy of the system $\mathsf{E} = \mathsf{K} + \mathsf{U}_{int} + \mathsf{U}_{ext}$, which coincides in most cases with the Hamiltonian, is constant if damping is disregarded. It gives: $\mathsf{E} = \mathsf{K} + \mathsf{U}_{int} + \mathsf{U}_{ext} = \mathsf{constant}$.

Chapter 5

Research work

In this thesis, the research work is divided into two main parts. The first part concerns the development of energy-momentum method for the co-rotational planar beam formulation. The work of this part produces three models with a specific application of steel structures subjected to seismic and impact loadings. This work is presented in papers I, II and III. The second part is devoted to the development of a 3D geometrically exact curved beam in the total Lagrangian approach. The detail of this formulation is presented in paper IV.

5.1 2D co-rotational Bernoulli beam (Paper I)

The dynamic co-rotational planar beam element proposed by Le et al. [12] is efficient: accurate results are obtained with only few elements. However, the HHT-α method [37] is used as time stepping method and consequently the energy and momenta of the system are not conserved. In order to tackle this problem, a so called energy-momentum method, that enhances the stability for long term analyses without introducing any numerical dissipation, is introduced. For that, the co-rotational formulation needs to be adapted.

The development of the energy-momentum method for the co-rotational formation is based on the following expression :

$$\begin{aligned}
&\int_{t_n}^{t_{n+1}} \Bigg(\int_{l_0} \rho A\, \ddot{u}_G\, \delta u_G \,\mathrm{d}x + \int_{l_0} \rho A\, \ddot{w}_G\, \delta w_G \,\mathrm{d}x + \int_{l_0} \rho I\, \ddot{\theta}_G\, \delta\theta_G \,\mathrm{d}x \\
&+ \int_{l_0} EA\, \varepsilon\, \delta\varepsilon \,\mathrm{d}x + \int_{l_0} EI\, \kappa\, \delta\kappa \,\mathrm{d}x - \int_{l_0} p_u\, \delta u_G \,\mathrm{d}x - \int_{l_0} p_w\, \delta w_G \,\mathrm{d}x \\
&- \int_{l_0} p_\theta\, \delta\theta_G \,\mathrm{d}x - \sum_{i=1}^{6} P_i\, \delta q_i \Bigg) \,\mathrm{d}t = 0
\end{aligned} \tag{5.1}$$

The previously developed time integration scheme [38, 39] is here adapted in the present context of the co-rotational formulation. Whereas the main idea of relating the strain fields to the strain velocity still applies, its specific realisation in the co-rotational context is not straightforward and is developed here for the first time. The midpoint velocities are applied to both the kinematic variables and strains. Formally, it takes the following generic form:

$$\int_{t_n}^{t_{n+1}} f(t)\,\mathrm{d}t \approx f(t_{n+\frac{1}{2}})\,\Delta t = f_{n+\frac{1}{2}}\,\Delta t \tag{5.2}$$

where the function f can represent either a kinematic variable or a deformational quantity.

Consequently, the application of the midpoint rule (Eq. (5.2)) to Eq. (5.1) gives the dynamical equation of motions at midpoint step:

$$\begin{aligned}
&\int_{l_0} \rho A\, \ddot{u}_{G,n+\frac{1}{2}} \left(\frac{\partial u_{G,n+\frac{1}{2}}}{\partial \boldsymbol{q}_{n+\frac{1}{2}}}\right)^{\mathrm{T}} \mathrm{d}x + \int_{l_0} \rho A\, \ddot{w}_{G,n+\frac{1}{2}} \left(\frac{\partial w_{G,n+\frac{1}{2}}}{\partial \boldsymbol{q}_{n+\frac{1}{2}}}\right)^{\mathrm{T}} \mathrm{d}x \\
&+ \int_{l_0} \rho I\, \ddot{\theta}_{G,n+\frac{1}{2}} \left(\frac{\partial \theta_{G,n+\frac{1}{2}}}{\partial \boldsymbol{q}_{n+\frac{1}{2}}}\right)^{\mathrm{T}} \mathrm{d}x + \int_{l_0} EA\, \varepsilon_{n+\frac{1}{2}} \left(\frac{\partial \varepsilon_{n+\frac{1}{2}}}{\partial \boldsymbol{q}_{n+\frac{1}{2}}}\right)^{\mathrm{T}} \mathrm{d}x \\
&+ \int_{l_0} EI\, \kappa_{n+\frac{1}{2}} \left(\frac{\partial \kappa_{n+\frac{1}{2}}}{\partial \boldsymbol{q}_{n+\frac{1}{2}}}\right)^{\mathrm{T}} \mathrm{d}x - \int_{l_0} p_{u,n+\frac{1}{2}} \left(\frac{\partial u_{G,n+\frac{1}{2}}}{\partial \boldsymbol{q}_{n+\frac{1}{2}}}\right)^{\mathrm{T}} \mathrm{d}x \\
&- \int_{l_0} p_{w,n+\frac{1}{2}} \left(\frac{\partial w_{G,n+\frac{1}{2}}}{\partial \boldsymbol{q}_{n+\frac{1}{2}}}\right)^{\mathrm{T}} \mathrm{d}x - \int_{l_0} p_{\theta,n+\frac{1}{2}} \left(\frac{\partial \theta_{G,n+\frac{1}{2}}}{\partial \boldsymbol{q}_{n+\frac{1}{2}}}\right)^{\mathrm{T}} \mathrm{d}x - \boldsymbol{P}_{n+\frac{1}{2}} = 0
\end{aligned} \tag{5.3}$$

The derivative of the kinematic and strain fields by respect to the global displacement $\boldsymbol{q}$ (the right side of each component) are calculated from the classical co-rotational equations. However, the accelerations ($\ddot{u}_{G,n+\frac{1}{2}}$, $\ddot{w}_{G,n+\frac{1}{2}}$, $\ddot{\theta}_{G,n+\frac{1}{2}}$) and the local strains ($\varepsilon_{n+\frac{1}{2}}$, $\kappa_{n+\frac{1}{2}}$) are not directly calculated from the nodal displacements, velocities and accelerations. In fact, since these variables are highly nonlinear, their coupling behavior can cause an instability [1, 22]. To see the matter clearly, one can show first how the nodal global displacement and the nodal global acceleration at midpoint are calculated:

$$\boldsymbol{q}_{n+\frac{1}{2}} = \boldsymbol{q}_n + \frac{\Delta t}{2} \dot{\boldsymbol{q}}_{n+\frac{1}{2}} \tag{5.4}$$

$$\ddot{\boldsymbol{q}}_{n+\frac{1}{2}} = \frac{2}{\Delta t} \dot{\boldsymbol{q}}_{n+\frac{1}{2}} - \frac{2}{\Delta t} \dot{\boldsymbol{q}}_n \tag{5.5}$$

One can see that both nodal displacement and acceleration depend mainly on the nodal velocity at $n + 1/2$ and the previous variable at step n. In order to solve the coupling problems, each kinematic relation has to apply the same procedure with the help of Eqs. (5.4) and (5.5). The accelerations are then obtained as:

$$\begin{aligned}
\ddot{u}_{G,n+\frac{1}{2}} &= \frac{2}{\Delta t}\, \dot{u}_{G,n+\frac{1}{2}} - \frac{2}{\Delta t}\, \dot{u}_{G,n} \\
\ddot{w}_{G,n+\frac{1}{2}} &= \frac{2}{\Delta t}\, \dot{w}_{G,n+\frac{1}{2}} - \frac{2}{\Delta t}\, \dot{w}_{G,n} \\
\ddot{\theta}_{G,n+\frac{1}{2}} &= \frac{2}{\Delta t} \dot{\theta}_{G,n+\frac{1}{2}} - \frac{2}{\Delta t} \dot{\theta}_{G,n}
\end{aligned} \tag{5.6}$$

In the same way, the local strains are obtained as:

$$\begin{aligned}
\varepsilon_{n+\frac{1}{2}} &= \varepsilon_n + \frac{\Delta t}{2}\, \dot{\varepsilon}_{n+\frac{1}{2}} \\
\kappa_{n+\frac{1}{2}} &= \dot{\kappa}_n + \frac{\Delta t}{2}\, \dot{\kappa}_{n+\frac{1}{2}}
\end{aligned} \tag{5.7}$$

It can be observed that the strains obtained by integrated the strain velocity using Eqs. (5.7) produces strains at $n + \frac{1}{2}$ that are not equal to the strains determined from the total displacements and rotations at $n + \frac{1}{2}$. In fact, both the strains and the displacements are updated using the mid-point rule and the strain field is accordingly consistent with the second order accuracy for single step method. The same concept is also applied to the computation of the accelerations as shown in Eqs. (5.6).

The proposed algorithm results in the conservation of energy and momenta. These properties can be shown theoretically. The details of those proofs are presented in Paper I. This indicates that the algorithm is unconditionally stable. Moreover, the expressions of the internal force vector and the tangent matrix can be obtained exactly without using any gauss point integration along the length of the element. These expressions have been derived by using MATLAB symbolic.

In paper I, four examples are tested in order to validate the proposed algorithm. The first example, see Figure 5.1, is a cantilever beam subjected to a concentrate load at its tip. The load induces large displacements to the beam. The results presented in Figure 5.2, show that the proposed energy-momentum scheme conserves the energy of the system and is stable during one million time steps. However, the Newmark method shows instabilities after some 24 s, see Figure 5.3. The HHT-α is stable but the energy is not conserved.

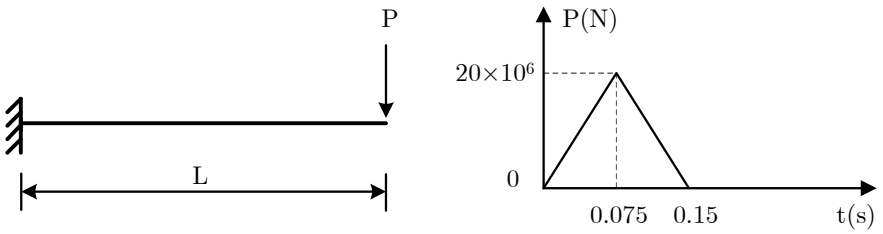

Figure 5.1: Geometry and load history of cantilever beam

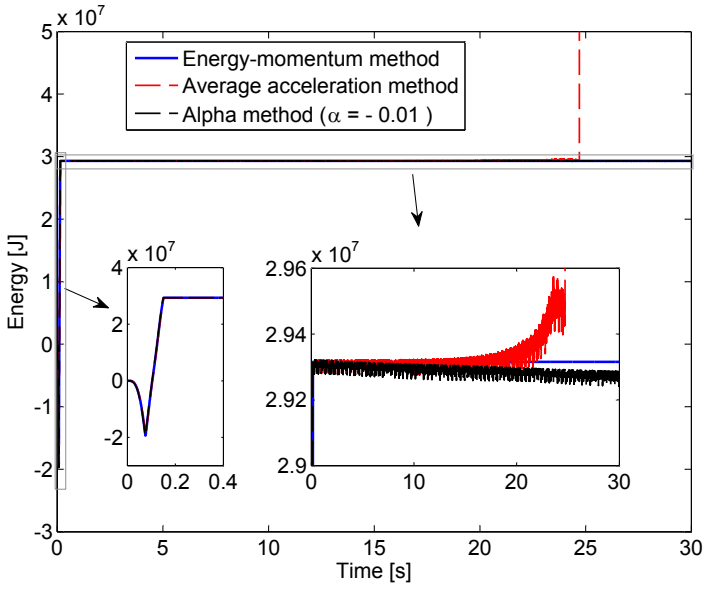

Figure 5.2: Comparison of energy from 0s to 30s

The last example is a free flying beam as shown in Figure 5.4. The length of the beam is $L = 3$ m, the cross-sectional area is $A = 0.002$ m^2 and the moment of inertia $I = 6.667 \times 10^{-8}$ m^4. The material properties are: elastic modulus $E = 210$ GPa and density $\rho = 7850$ kg/m^3. The number of element is 4 and the time step size is $\Delta t = 10^{-3}$ s.

This problem is suitable to study the conservation of the linear and angular momenta. Since only vertical loads are applied at the beginning, the linear momentum in the horizontal

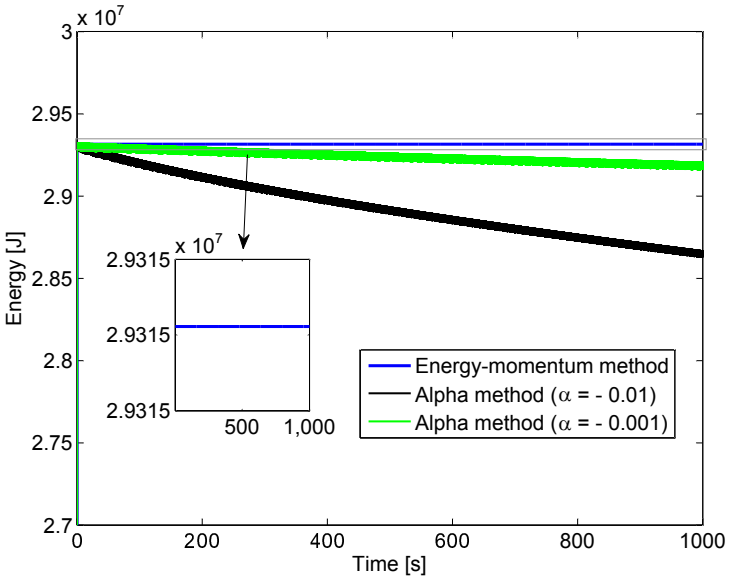

Figure 5.3: Comparison of energy from 0s to 1000s

direction should be zero. As shown in Figure 5.5(b), this linear momentum is almost zero with the maximum value of 3×10^{-7}. Figures 5.5(a), 5.5(b) and 5.6(a) show that the energy, the linear momentum in the vertical direction and the angular momentum are constant. This example has also been studied with the average acceleration and HHT-α ($\alpha = -0.01$) methods. As shown in Figure 5.6(b), the angular momentum is not conserved with these two methods.

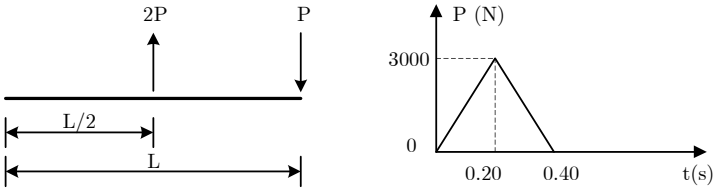

Figure 5.4: Geometry and load history of free flying beam

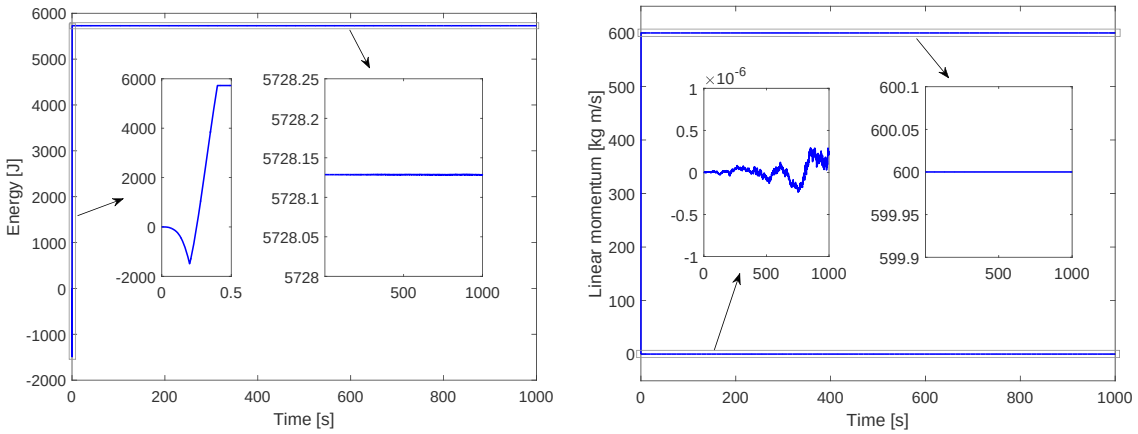

(a) (b)

Figure 5.5: (a). Energy of free flying beam, (b). Linear momentum.

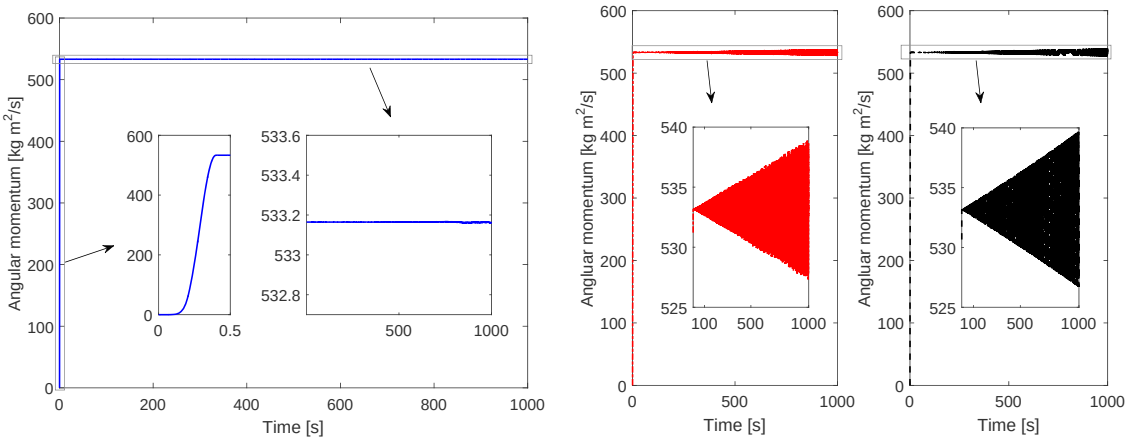

(a) (b)

Figure 5.6: (a). Angular momentum of Energy-Momentum method, (b). Angular momentum of Average acceleration method (left) and Alpha method $\alpha = -0.01$ (right).

5.2 2D co-rotational shear-flexible beam (Paper II)

In this work, the concept of energy-momentum method presented in paper I [40] is further developed to co-rotational shear flexible 2D beam elements. Based on the previous works of Sansour et al. [39, 38], the main idea is to apply the midpoint rule not only to nodal displacements, velocities and accelerations but also to the strain fields. The conservation of energy, linear and angular momentum is proved theoretically and also observed in the numerical applications.

Based on the same co-rotational framework, three different local formulations are implemented and tested for a large number of time steps. The respective shape functions and strain assumptions for each local formulation are presented in Table 5.1. The reduced integration method (RIE) is the classical Timoshenko approach based on linear interpolations and one Gauss point integration for the static terms. The Hellinger-Reissner mixed formulation (MX) is also based on linear interpolations but a mixed approach is used to derive the static terms. For the Interdependent Interpolation element (IIE) formulation, the IIE cubic shape functions [97] are used and a nonlinear shallow arch strain definition is adopted. For this last element, the expression of the tangent dynamic matrix is complicated and a possible simplification is carefully studied. For the three formulations, different predictors are tested.

Table 5.1: Formulations

Formulations	Shape function	Static term
RIE	Linear	Linear strain with reduced integration
MX	Linear	Linear strain with mixed formulation
IIE	Cubic	Shallow arch strain

For the reduced and mixed formulations, linear interpolations are taken for the local displacements u, w and local rotation θ. Consequently, a constant mass matrix is obtained. The tangent mass matrix is:

$$\mathbf{K}_k = \frac{2}{\Delta t^2}\,\mathbf{M} \tag{5.8}$$

where the constant mass matrix $\mathbf{M}$ is given by

$$\mathbf{M} = \rho\, l_0 \begin{bmatrix} A/3 & 0 & 0 & A/6 & 0 & 0 \\ 0 & A/3 & 0 & 0 & A/6 & 0 \\ 0 & 0 & I/3 & 0 & 0 & I/6 \\ A/6 & 0 & 0 & A/3 & 0 & 0 \\ 0 & A/6 & 0 & 0 & A/3 & 0 \\ 0 & 0 & I/6 & 0 & 0 & I/3 \end{bmatrix} \tag{5.9}$$

The development of the local IIE formulation [97] is based on the exact solution of the homogeneous form of the equilibrium equations for a Timoshenko beam. Consequently, the IIE element retains not only the accuracy inherent to the cubic interpolation, but also includes the bending shear deformation. However, due to the cubic shape functions, the exact expression of the tangent mass matrix is very complicated:

$$\begin{aligned} \mathbf{K}_k =& \frac{\partial \boldsymbol{f}_{k,n+\frac{1}{2}}}{\partial \boldsymbol{q}_{n+1}} \\ =& \frac{2}{\Delta t^2}\left[\mathbf{T}^{\mathrm{T}}\mathbf{M}_l\mathbf{T} + \frac{1}{2}\left(\mathbf{T}^{\mathrm{T}}\left(\boldsymbol{I}_1^{\mathrm{T}}\mathbf{M}_l + \mathbf{M}_l\boldsymbol{I}_1\right)\mathbf{T}\right)\left(\Delta\boldsymbol{q}\,\frac{\boldsymbol{z}^{\mathrm{T}}}{l_{n+\frac{1}{2}}}\right)\right. \\ &+ \frac{1}{2}\left(\mathbf{T}^{\mathrm{T}}\mathbf{M}_{l,l}\mathbf{T}\right)\left(\Delta\boldsymbol{q}\,\boldsymbol{r}^{\mathrm{T}}\right) + \left(\mathbf{T}^{\mathrm{T}}\mathbf{M}_{l,\bar{\theta}_1}\mathbf{T}\right)\left(\Delta\boldsymbol{q}\,\frac{\partial\bar{\theta}_{1,n+\frac{1}{2}}}{\partial\boldsymbol{q}_{n+1}}\right) \\ &\left. + \left(\mathbf{T}^{\mathrm{T}}\mathbf{M}_{l,\bar{\theta}_2}\mathbf{T}\right)\left(\Delta\boldsymbol{q}\,\frac{\partial\bar{\theta}_{2,n+\frac{1}{2}}}{\partial\boldsymbol{q}_{n+1}}\right)\right] - \frac{2}{\Delta t}\,\frac{\partial \boldsymbol{f}_{uw\theta}}{\partial \boldsymbol{q}_{n+1}} \end{aligned} \tag{5.10}$$

The expression of the tangent mass matrix is very long and its computation requires a lot of computational time. In order to reduce the computational time, Geradin and Cardona [101, 126] suggested to keep only the mass matrix and to neglect the gyroscopic and centrifugal matrices. Hence, a simplified tangent dynamic matrix is proposed:

$$\mathbf{K}_k = \frac{2}{\Delta t^2}\left(\mathbf{T}^{\mathrm{T}}\mathbf{M}_l\mathbf{T}\right) \tag{5.11}$$

where $\mathbf{T}$ is the rotation matrix:

$$\mathbf{T} = \begin{bmatrix} c_{n+\frac{1}{2}} & s_{n+\frac{1}{2}} & 0 & 0 & 0 & 0 \\ -s_{n+\frac{1}{2}} & c_{n+\frac{1}{2}} & 0 & 0 & 0 & 0 \\ 0 & 0 & 1 & 0 & 0 & 0 \\ 0 & 0 & 0 & c_{n+\frac{1}{2}} & s_{n+\frac{1}{2}} & 0 \\ 0 & 0 & 0 & -s_{n+\frac{1}{2}} & c_{n+\frac{1}{2}} & 0 \\ 0 & 0 & 0 & 0 & 0 & 1 \end{bmatrix} \tag{5.12}$$

The choice of an efficient predictor is also important. The predictor provides the initial value for the solution at time $n+1$. A poor predictor can increase the number of iterations and in some cases makes the procedure fail to converge. In this work, three predictors have

been implemented and tested:
• The first predictor (Pred.1), referred to as "Unchanged displacements", is used by Simo and Vu-Quoc [100].

$$\boldsymbol{q}_{n+1} = \boldsymbol{q}_n \tag{5.13}$$

• The second predictor (Pred.2), called as "Null accelerations", is proposed by Cardona and Geradin [101], Mäkinen [127], Chung and Hulbert [128]. Zero accelerations are taken as predictor for the solution at time $n+1$. In the case of midpoint rule the nodal accelerations at time $n+\frac{1}{2}$ are taken to zero, hence the new prediction for displacements is obtained as

$$\boldsymbol{q}_{n+1} = \boldsymbol{q}_n + \Delta t\, \dot{\boldsymbol{q}}_n \tag{5.14}$$

• The idea of the third predictor (Pred.3), proposed by de Borst et al. [129], is to assume that the system behaves linearly between steps $n-\frac{1}{2}$ and $n+\frac{1}{2}$. In the present case, Pred.3 can be written as

$$\left(\frac{2}{\Delta t^2}\,\mathbf{T}^{\mathrm{T}}\mathbf{M}_l\mathbf{T} + \mathbf{K}_g\right)_{n-\frac{1}{2}} \Delta\boldsymbol{q} = \frac{2}{\Delta t}\,\boldsymbol{f}_{uw\theta,n-\frac{1}{2}} - \boldsymbol{f}_{g,n-\frac{1}{2}} + \boldsymbol{f}_{ext,n+\frac{1}{2}} \tag{5.15}$$

In order to validate the proposed formulations, four numerical examples are presented in paper II. Four main features are discussed:
• Conservation of the total energy, linear and angular momentum.
• Stability of the algorithms for a large number of time steps (one million step).
• Efficiency of the three proposed formulations, both regarding the required number of elements and the computational time.
• Validation of the reference solution by taking a large number of elements against the three shear flexible formulations.

Only the shallow arch beam example is considered here. A shallow arch beam of span $L = 10$ m with clamped ends is depicted in Fig. 5.7. The radius R of the arch is 10 m and the height H is 1.3997 m. The shallow arch is subjected to a time-dependent concentrated load $P = P_0\, sin(\omega t)$ at mid-span. The amplitude of the load P_0 is 80 MN and its frequency ω is 1000 rad/s. The characteristics of the arch are: cross-sectional area $A = 0.087$ m^2, elastic modulus $E = 210$ GPa, moment of inertia $I = 3.562 \times 10^{-3}$ m^4, Poisson's ratio $\nu = 0.3$ and density $\rho = 7850$ kg/m^3. The size of time step is $\Delta t = 10^{-5}$ s.
For the presentation of the results, the following colors are used in Figure 5.8:

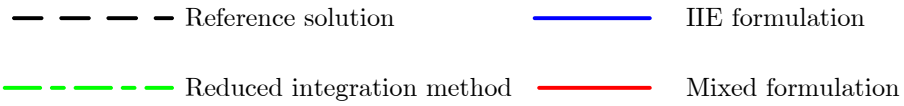

The following number of elements is used respectively for each formulation: 8 for IIE formulation, 16 for mixed formulation, 24 for Reduce integration method and 100 for the reference solution. Figure 5.8(a) shows the vertical displacement v at mid-span for the four analyses. With only 8 elements, the results obtained with IIE formulation are very close to the reference solution. However, large discrepancies can be observed between the results obtained with the mixed formulation (16 elements) and with the reduced integration method (24 elements) compared to the reference solution.

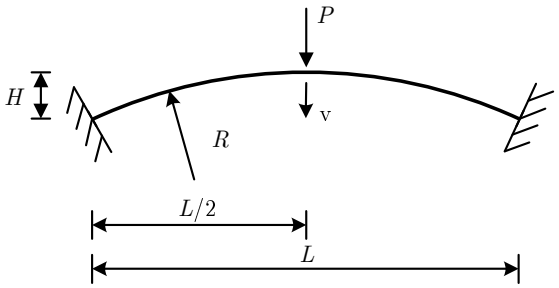

Figure 5.7: Shallow arch beam: geometry and loading history.

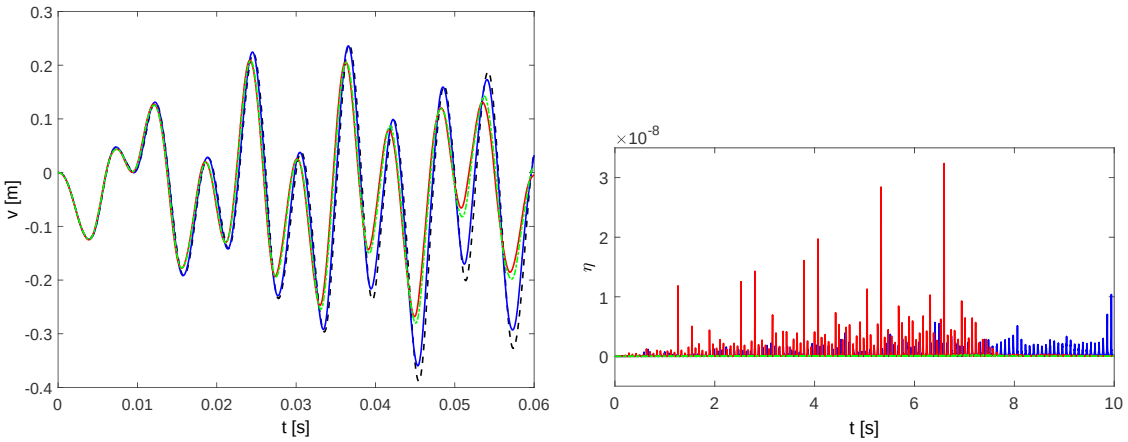

(a) (b)

Figure 5.8: (a). Vertical displacement v, (b). Relative energy error.

For the three formulations, the relative energy error is depicted in Fig. 5.8(b). The largest value is about 3×10^{-8} for a maximum external energy of 1.85×10^{8} J. These results proved the good stability of the proposed algorithm even for a large number of steps (one million).

The numerical performances of the three proposed formulations are presented in detail in Paper II. For each formulation, the three predictors described aboved have been tested. For the IIE approach, both the exact tangent dynamic matrix (Eq.(5.10)) and the simplified one (Eq. (5.11)) have been tested. For each example, the same number elements (corresponding to the number of elements for the MX approach in Table 2 of paper II) have been used in all analyses. In Table 5.2, the computational time and the total number of iterations (in parenthesis) are given for each case considering 5000 steps.

Table 5.2: Numerical performances for shallow arch beam

	RIE	MX	IIE-exact	IIE-simp.
Pred.1	38 (14999)	38 (14999)	138 (18569)	110 (22902)
Pred.2	38 (14999)	38 (14999)	114 (15000)	97 (19951)
Pred.3	38 (14997)	38 (14997)	115 (14999)	99 (19996)

The following conclusions can be drawn:
• For the RIE and MX approaches, all the predictors give almost the same computational

time. For the IIE formulation, Predictor 2 gives the lowest computational time, but the difference between Predictors 2 and 3 is not significant.
• The CPU time and number of iterations for the RIE and MX formulations are almost the same. This was expected since the only difference between these approaches resides in different constant local stiffness matrices. However, as shown previously in the examples, the RIE approach requires a larger number of elements in order to get an accurate solution.
• For the IIE formulation, it is better to use the simplified tangent stiffness matrix. The number of iterations increases but the CPU time decreases by 20% to 40% (Predictor 2).
• With Predictor 2, the IIE formulation (with simplified tangent dynamic matrix) requires about 2.0-2.6 times more CPU time than the MX formulation. On the other hand, the numerical examples have shown that with twice the number of elements, the MX formulation gives less accurate results that the IIE one. It is therefore difficult to conclude if one formulation is more efficient than another one.

5.3 A 2D elasto-(visco)-plastic fiber co-rotational beam element and a planar co-rotational beam element with generalized elasto-(visco)-plastic hinges (Paper III)

In this paper, 2D co-rotational beam element formulations for nonlinear dynamics of frame structures subjected to impact are developed. Based on the co-rotational framework, the inelastic behaviour of the frame structures is modelled by either distributed plasticity and generalized hinge approaches. Both Bernoulli and Timoshenko local beam formulations are employed for the distributed plasticity approach whereas Bernoulli formulation is associated with the generalized hinges element. For the latter, a condensation procedure is used to remove the internal degrees of freedom and to produce a two noded super-element that fits the standard co-rotational approach. For the three formulations, strain effects have been considered by replacing the plastic flow rule with its visco-plasticity counterpart. In addition, the dynamical equations of motion are solved by using a scheme that conserves the energy in case of elasticity. The responses of the three formulations have been compared against each other for impact problems.

Distributed plasticity models

For the Bernoulli model, the element is based on the classical linear beam theory, using a linear interpolation for the local axial displacement and a cubic one for the local transverse displacement. For the Timoshenko model, a reduced integration formulation based on linear interpolations and a single Gauss point is employed in order to avoid shear locking.

In these models, it is assumed that total strain rate is defined as the sum of elastic and plastic strain rates:

$$\dot{\boldsymbol{\Xi}} = \dot{\boldsymbol{\Xi}}^e + \dot{\boldsymbol{\Xi}}^p \tag{5.16}$$

The plastic strain rate is determined by the plastic flow rule:

$$\dot{\boldsymbol{\Xi}}^p = \dot{\lambda}\,\frac{\partial \Phi}{\partial \boldsymbol{\Sigma}} \tag{5.17}$$

where $\dot{\lambda}$ is the plastic multiplier and $\boldsymbol{\Sigma}$ is the stress-resultant vector. The yield function Φ for each formulation is defined by:
1/ For the Bernoulli formulation:

$$\Phi = |\sigma| - \sigma_y \tag{5.18}$$

where $\mathbf{\Sigma}$ is to equal to σ and σ_y is the yield stress.
2/ For the Timoshenko formulation, von Mises yield function is adopted:

$$\Phi = \left(\sigma^2 + 3\tau^2\right)^{1/2} - \sigma_y \tag{5.19}$$

with $\mathbf{\Sigma} = [\sigma \quad \tau]$.

The visco-plastic flow rule is introduced in order to study the strain rate effect of the structures subjected to impact. The plasticity flow rule is then defined by:

$$\dot{\lambda} = \begin{cases} D\left(\frac{\Phi}{\sigma_y}\right)^{\zeta} & \text{if} \quad \Phi \geq 0 \\ 0 & \text{if} \quad \Phi < 0 \end{cases} \tag{5.20}$$

where Φ is given by a power function of Cowper-Symonds-Bonder type [130, 131]. D and ζ are material constants; for mild steel, $\zeta = 5$ and $D = 40.4$ s^{-1} according to Cowper and Symonds [130] and for aluminum alloys, $\zeta = 4$ and $D = 6500$ s^{-1} according to Bonder and Symonds [131].

The details regarding the derivation of the consistent local tangent matrix are given in Paper III.

Generalized hinges

The structural member consists of three sub-elements: a standard flexible beam element and two generalized plastic hinges that are modeled by a combination of axial and rotational springs (see Figure 5.9). The elongation or shortening of the hinges occurs along the beam axis. The generalized hinges can be seen as finite elements with zero initial length. By assembling these hinges with the beam element and by performing static condensation, a two node super-element (see Figure 5.9) is obtained. This element is then incorporated into a co-rotational framework in order to introduce geometrical nonlinearities. Consequently, the local axial displacement $\bar{u}_1$ is equal to 0.

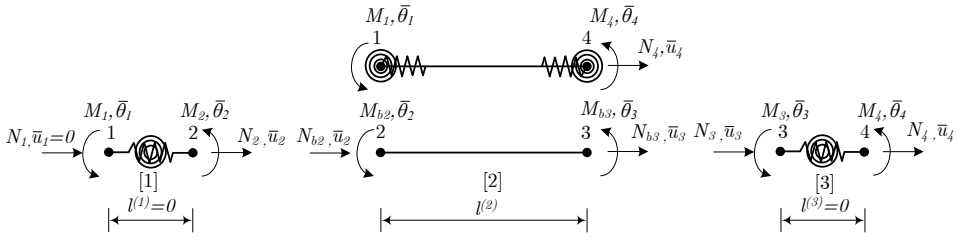

Figure 5.9: Local super-element.

The co-rotational kinematics of the element are shown in Figure 5.10. The motion of the element is decomposed in two parts. In a first step, a rigid body motion is defined by the global translation (u_1,w_1) of the node 1 and the rigid rotation α. This rigid motion defines a local coordinate system (x_l,z_l) which continuously translates and rotates with the element. In a second step, the element deformation is defined in the local coordinate system. The vectors of global, local and sub-element displacements are respectively defined

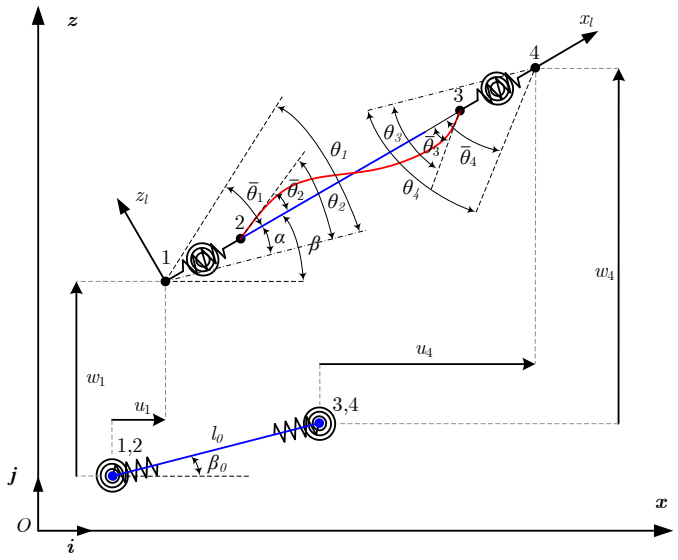

Figure 5.10: Beam kinematics.

by

$$\begin{aligned}
\boldsymbol{q} &= \begin{bmatrix} u_1 & w_1 & \theta_1 & u_4 & w_4 & \theta_4 \end{bmatrix}^{\mathrm{T}} \\
\bar{\boldsymbol{q}} &= \begin{bmatrix} \bar{u}_4 & \bar{\theta}_1 & \bar{\theta}_4 \end{bmatrix}^{\mathrm{T}} \\
\bar{\boldsymbol{q}}_{sub} &= \begin{bmatrix} \bar{u}_2 & \bar{\theta}_2 & \bar{u}_3 & \bar{\theta}_3 \end{bmatrix}^{\mathrm{T}}
\end{aligned} \tag{5.21}$$

The generalized plastic hinge model assumes that the plasticity is lumped into axial and rotational springs located at the end of the flexible beam element. The elastic behaviour of the generalized hinge is uncoupled whereas axial-moment interaction is considered in the plastic range. One adopts the total generalized strain rate decomposition into elastic and plastic parts which consists of the axial and rotational strain rate. For an associated flow rule, the direction of the generalized plastic strain rate vector is given by the gradient to the yield function, with its magnitude given by the plastic multiplier rate. The generalized stress vector containing the axial and bending forces in the hinge is denoted by $\boldsymbol{\Sigma} = [N \quad M]^{\mathrm{T}}$. The plastic multiplier $\dot{\lambda}$ is determined by the classical complementary conditions:

$$\dot{\lambda} \geq 0, \quad \Phi(N, M) \leq 0, \quad \dot{\lambda}\,\Phi(N, M) = 0 \tag{5.22}$$

In the case of visco-plasticity for the hinges, the visco-plasticity flow rule is defined by:

$$\dot{\lambda} = \begin{cases} D^*\,\Phi^{\zeta} & \text{if} \quad \Phi \geq 0 \\ 0 & \text{if} \quad \Phi < 0 \end{cases} \tag{5.23}$$

where D^* and ζ are material constants. The value D^* will be appropriately selected on the case study.

A family of symmetric and convex yield surfaces of generalized super-elliptic shape is considered:

$$\Phi(N, M) = \left(\left| \frac{M}{M^p} \right|^{\alpha} + \left| \frac{N}{N^p} \right|^{\beta} \right)^{\frac{1}{p}} - 1 \tag{5.24}$$

where α, β and p are the parameters of the yield surface shape.

Local tangent stiffness matrix for generalized hinges

The elastic stiffness matrix of the hinges is given by:

$$\mathbf{C}_e = \begin{bmatrix} k_{\bar{u}} & 0 \\ 0 & k_{\bar{\theta}} \end{bmatrix} \tag{5.25}$$

In (visco)-plasticity, the incremental stress-resultant for the first hinge (similar expression for the second hinge) is defined by

$$\begin{bmatrix} \Delta N_2 \\ \Delta M_2 \end{bmatrix} = \begin{bmatrix} C_{11} & C_{12} \\ C_{21} & C_{22} \end{bmatrix} \begin{bmatrix} \Delta \bar{u}_2 - \Delta \bar{u}_1 \\ \Delta \bar{\theta}_2 - \Delta \bar{\theta}_1 \end{bmatrix} \tag{5.26}$$

The details about the discrete governing equations of the generalized plastic hinges are described in [132, 133].

For the static condensation, the local internal force $\boldsymbol{f}_l$ and the local tangent stiffness matrix $\mathbf{k}_l$ of the super beam element are given as

$$\begin{aligned} \Delta \boldsymbol{f}_l &= \mathbf{k}_l \, \Delta \bar{\boldsymbol{q}} \\ \mathbf{k}_l &= \mathbf{k}_{hh} - \mathbf{k}_{bh}^{\mathrm{T}} \, \mathbf{k}_{bb}^{-1} \, \mathbf{k}_{bh} \end{aligned} \tag{5.27}$$

In elasticity, the equivalent local stiffness matrix $\mathbf{k}_{eq}$ should be the local stiffness of the Bernoulli beam element:

$$\begin{bmatrix} EA/l_0 & 0 & 0 \\ 0 & 4\,EI/l_0 & 2\,EI/l_0 \\ 0 & 2\,EI/l_0 & 4\,EI/l_0 \end{bmatrix} \tag{5.28}$$

To achieve that the elastic stiffness parameters of the hinges (see Eq.(5.25)) and the stiffness parameters of the elastic beam sub-element are taken as:

$$\begin{aligned} k_{\bar{u}} &= \varrho_n \, EA/l_0 \\ k_{\bar{\theta}} &= \varrho_m \, EI/l_0 \end{aligned} \tag{5.29}$$

$$\begin{aligned} k_{11} &= \varpi_1 \, EA/l_0 \\ k_{22} &= k_{33} = \varpi_2 \, EI/l_0 \\ k_{23} &= k_{32} = \varpi_3 \, EI/l_0 \end{aligned} \tag{5.30}$$

By introducing Eqs.(5.29) and (5.30) in the second expression of Eqs.(5.27), the following relations are obtained:

$$\begin{aligned} \varpi_1 &= \left(1 - 2\,\varrho_n^{-1}\right)^{-1} \\ \varpi_2 &= \frac{4\,\varrho_m(\varrho_m - 3)}{\varrho_m^2 - 8\,\varrho_m + 12} \\ \varpi_3 &= \frac{2\,\varrho_m^2}{\varrho_m^2 - 8\,\varrho_m + 12} \end{aligned} \tag{5.31}$$

Hence, the idea of the method is to choose the coefficients ϱ_n, ϱ_m of the hinges and then to calculate the coefficients $\varpi_1, \varpi_2, \varpi_3$ of the beam sub-element by using Eq.(5.31).

Related the impact analyses, the contact model is developed in a rigorous framework of non-smooth dynamics. The equations of motion are derived using a set of differential measures and convex analysis tools. Velocity jumps at impact instants are considered

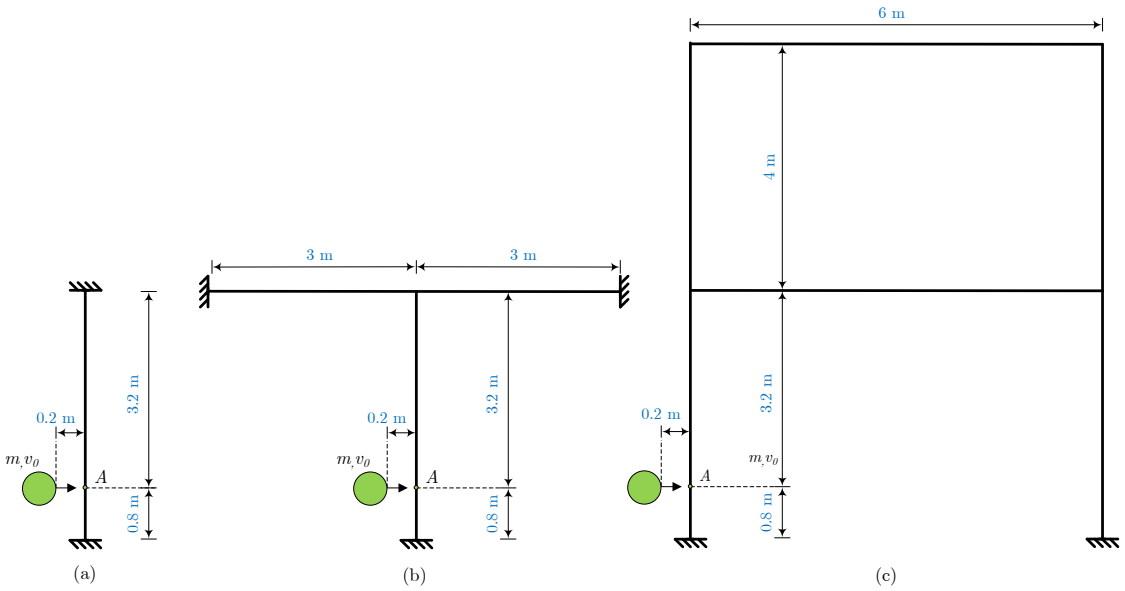

Figure 5.11: Geometry of the frames with the impact loadings

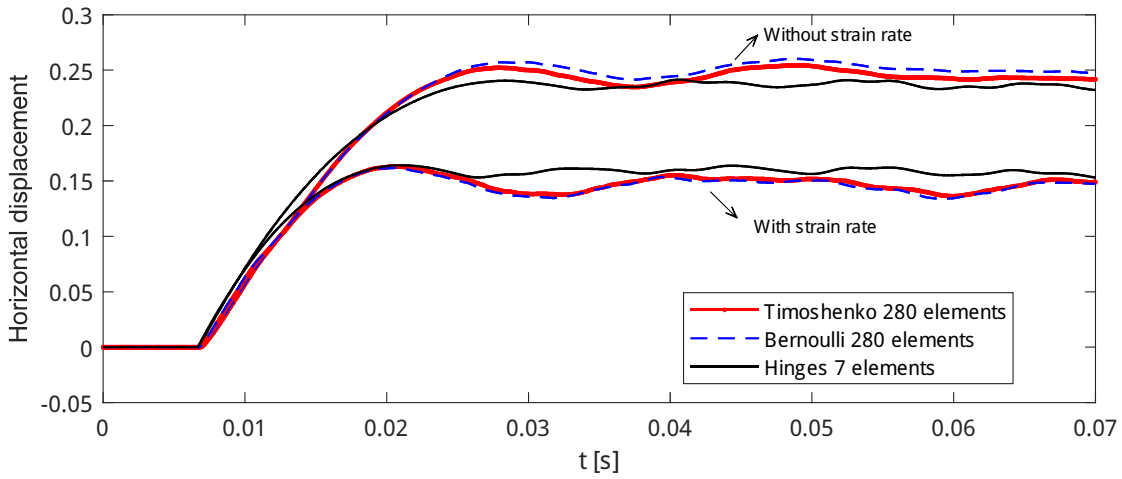

Figure 5.12: Evolution of the maximum horizontal displacements of the impacted column of frame c with $v_0 = 30$ m/s

using the Newton's impact law by a means of the coefficient of restitution ϵ to account for possible energy losses during the collisions. The dynamic equations of motion are solved by using the energy momentum conserving scheme developed by Chhang et al.[40, 41].

Example

Three steel frames are depicted in Fig. 5.11. The column of each structure is subjected to a mass m at the position A with the initial velocities v_0. The parameter of the member are: density of the material $\rho = 7850\text{kg/m}^3$, Young modulus $E = 210$ GPa, yield stress $\sigma_y = 355$ MPa and coefficient of poisson $\nu = 0.3$. The yield function of the hinges for elasto-(visco)-plastic model is $\Phi(N, M) = |M/M^p|^{1.05} + |N/N^p|^2 - 1$ for the square section. The time step for the analysis is $\Delta t = 10^{-5}$.

Regarding the element discretization, the size of the element is 0.1 m for the fiber model. For the hinges model, one element is taken for each member except for the impacted column where two elements have been considered. Figure 5.12 shows the evolution of the maximum displacements of the impacted column for the initial velocity of 30 m/s for frame *c*. For the elasto-perfectly plastic case, the result obtained with the generalized plastic-hinges are in good agreement comparing to the ones obtained with the two fiber models. Furthermore, the series of calculation on the maximum displacement of the impacted column are summarized in Table 5.3. The discrepancies between Timoshenko and Bernoulli fiber models are small and do not exceed 3%. Otherwise, the maximum difference between the generalized elasto-plastic hinges and the distributed plasticity models are about 11% which is acceptable considering the fact that the generalized hinges model used only a few number of elements.

Regarding to the study on the strain effect, $\zeta = 5$ and $D = 40.4$ s^{-1} are the material constants for the mild steel [130] which are employed for the fiber models whereas $\zeta = 5$ and $D^* = 2.025 \times 10^8$ s^{-1} are used for the generalized hinges model. Table 5.4 shows the maximum displacements of the impacted column. The discrepancies between the two fiber models are about 3% which indicates that the shear effect of the Timoshenko model does not influence the outcome of the displacements. Besides, with an appropriate value D^* (2.025×10^8 in this case), this model can reproduce the correct results (see Fig. 5.12) with an overall maximum difference of 11%.

Table 5.3: Elasto-perfectly Plasticity model: maximum displacement on the impacted column: Mass of vehicle 1500 kg, section 20 cm × 20 cm, $\epsilon = 0$

	Timoshenko	Bernoulli	Hinges
Frame *a* ($v_0 = 20$ m/s)	0.1085	0.1074	0.1030
Frame *a* ($v_0 = 30$ m/s)	0.1905	0.1909	0.1907
Frame *a* ($v_0 = 40$ m/s)	0.2718	0.2728	0.2739
Frame *b* ($v_0 = 20$ m/s)	0.1261	0.1232	0.1118
Frame *b* ($v_0 = 30$ m/s)	0.2454	0.2493	0.2351
Frame *b* ($v_0 = 40$ m/s)	0.3940	0.3994	0.3883
Frame *c* ($v_0 = 20$ m/s)	0.1200	0.1226	0.1125
Frame *c* ($v_0 = 30$ m/s)	0.2521	0.2579	0.2414
Frame *c* ($v_0 = 40$ m/s)	0.4136	0.4253	0.4086

Table 5.4: Elasto-visco-plasticity model: displacement maximum on the impacted column: Mass of vehicle 1500 kg, section 20 cm × 20 cm, $\epsilon = 0$

	Timoshenko	Bernoulli	Hinges
Frame *a* ($v_0 = 20$ m/s)	0.0804	0.0780	0.0763
Frame *a* ($v_0 = 30$ m/s)	0.1402	0.1367	0.1469
Frame *a* ($v_0 = 40$ m/s)	0.2011	0.1982	0.2228
Frame *b* ($v_0 = 20$ m/s)	0.0854	0.0856	0.0799
Frame *b* ($v_0 = 30$ m/s)	0.1645	0.1625	0.1625
Frame *b* ($v_0 = 40$ m/s)	0.2659	0.2638	0.2685
Frame *c* ($v_0 = 20$ m/s)	0.0853	0.0840	0.0806
Frame *c* ($v_0 = 30$ m/s)	0.1644	0.1635	0.1641
Frame *c* ($v_0 = 40$ m/s)	0.2718	0.2714	0.2743

Another serie of calculations (see Table 5.5) has been made for testing the value D^* with another mass (3000 kg) and a different coefficient of restitution (0.5). The results show that the maximum difference for the displacement does not exceed 10%. It can be concluded that these values can be used for this type of frame with square section.

Table 5.5: Elasto-visco-plasticity model: displacement maximum on the impacted column: Mass of vehicle 3000 kg, section 25 cm × 25 cm, $\epsilon = 0.5$

	Timoshenko	Bernoulli	Hinges
Frame a ($v_0 = 20$ m/s)	0.0842	0.0819	0.0761
Frame a ($v_0 = 30$ m/s)	0.1525	0.1495	0.1524
Frame a ($v_0 = 40$ m/s)	0.2240	0.2196	0.2389
Frame b ($v_0 = 20$ m/s)	0.0876	0.0869	0.0787
Frame b ($v_0 = 30$ m/s)	0.1697	0.1700	0.1630
Frame b ($v_0 = 40$ m/s)	0.2743	0.2746	0.2714
Frame c ($v_0 = 20$ m/s)	0.0860	0.0854	0.0793
Frame c ($v_0 = 30$ m/s)	0.1685	0.1700	0.1641
Frame c ($v_0 = 40$ m/s)	0.2775	0.2803	0.2765

5.4 Geometrically exact Euler-Bernoulli spatial curved beam (Paper IV)

In this paper, an alternative and direct approach to develop an Euler-Bernoulli-based three-dimensional beam theory is presented. The approach is based on the two following aspects. Based on the Euler-Bernoulli assumption, the only information available is that 1) the base vectors stay normal to each other after the deformation and 2) the central line is well defined by means of a displacement vector and the only vector which changes length is that tangent to the central line. Two approaches to define the position of the deformed base system in a way consistent with the overarching Euler-Bernoulli assumption is presented in chapter 4.

The general methodology for the systematic construction of energy-conserving schemes has been proposed by Sansour et al. [38, 39] and successfully applied to different shell and rod formulations in [82] and [35]. The methodology is based on the realisation that geometric and material non-linearities have to be treated differently. The complexities of the geometric non-linearities can be circumvented by resorting to strain velocities to provide, by means of integration, the expressions for the strain measures themselves.

The dynamic equation of motion is obtained from the application of the midpoint rule (Eq.5.2) to Equation (4.29):

$$\begin{aligned}
&\int_L \rho A \left(\frac{\partial \boldsymbol{u}}{\partial \boldsymbol{q}}\right)^{\mathrm{T}} \ddot{\boldsymbol{u}}_{n+\frac{1}{2}}\,\mathrm{d}s + \int_L \rho I_z \left(\frac{\partial \boldsymbol{n}}{\partial \boldsymbol{q}}\right)^{\mathrm{T}} \ddot{\boldsymbol{n}}_{n+\frac{1}{2}}\,\mathrm{d}s + \int_L \rho I_j \left(\frac{\partial \boldsymbol{m}}{\partial \boldsymbol{q}}\right)^{\mathrm{T}} \ddot{\boldsymbol{m}}_{n+\frac{1}{2}}\,\mathrm{d}s \\
&+ \int_L EA\, \varepsilon_{11\,n+\frac{1}{2}} \left(\frac{\partial \varepsilon_{11}}{\partial \boldsymbol{q}}\right)^{\mathrm{T}} \mathrm{d}s + \int_L EI_z\, \kappa_{1\,n+\frac{1}{2}} \left(\frac{\partial \kappa_1}{\partial \boldsymbol{q}}\right)^{\mathrm{T}} \mathrm{d}s + \int_L EI_j\, \kappa_{2\,n+\frac{1}{2}} \left(\frac{\partial \kappa_2}{\partial \boldsymbol{q}}\right)^{\mathrm{T}} \mathrm{d}s \\
&+ \int_L GJ\, \kappa_{12\,n+\frac{1}{2}} \left(\frac{\partial \kappa_{12}}{\partial \boldsymbol{q}}\right)^{\mathrm{T}} \mathrm{d}s - \int_L \left(\frac{\partial \boldsymbol{u}}{\partial \boldsymbol{q}}\right)^{\mathrm{T}} \boldsymbol{p}_{n+\frac{1}{2}}(s)\,\mathrm{d}s - \left(\frac{\partial \boldsymbol{u}}{\partial \boldsymbol{q}}\right)^{\mathrm{T}} \cdot \sum_{i=1}^{N} \boldsymbol{P}_{i\,n+\frac{1}{2}} = \boldsymbol{0} \quad (5.32)
\end{aligned}$$

The main idea is to employ kinematic and strain velocity fields to define the kinematic and strain fields $n + \frac{1}{2}$ instead the kinematic and strain fields defined from the global

displacements, velocities and accelerations directly. The kinematic and strain velocity fields are computed as:

$$
\begin{aligned}
\dot{\boldsymbol{n}}_{n+\frac{1}{2}} &= \frac{\partial \boldsymbol{n}}{\partial \boldsymbol{u}_{,s}}\, \dot{\boldsymbol{u}}_{,s\, n+\frac{1}{2}} + \frac{\partial \boldsymbol{n}}{\partial \gamma}\, \dot{\gamma}_{n+\frac{1}{2}} \\
\dot{\boldsymbol{m}}_{n+\frac{1}{2}} &= \frac{\partial \boldsymbol{m}}{\partial \boldsymbol{u}_{,s}}\, \dot{\boldsymbol{u}}_{,s\, n+\frac{1}{2}} + \frac{\partial \boldsymbol{m}}{\partial \gamma}\, \dot{\gamma}_{n+\frac{1}{2}} \\
\dot{\varepsilon}_{11\, n+\frac{1}{2}} &= \left(\boldsymbol{X}_{0,s} + \boldsymbol{u}_{,s\, n+\frac{1}{2}}\right) \cdot \dot{\boldsymbol{u}}_{,s\, n+\frac{1}{2}} \\
\dot{\kappa}_{1\, n+\frac{1}{2}} &= \dot{\boldsymbol{u}}_{,s\, n+\frac{1}{2}} \cdot \boldsymbol{n}_{,s\, n+\frac{1}{2}} + \left(\boldsymbol{X}_{0,s} + \boldsymbol{u}_{,s\, n+\frac{1}{2}}\right) \cdot \dot{\boldsymbol{n}}_{,s\, n+\frac{1}{2}} \\
\dot{\kappa}_{2\, n+\frac{1}{2}} &= \dot{\boldsymbol{u}}_{,s\, n+\frac{1}{2}} \cdot \boldsymbol{m}_{,s\, n+\frac{1}{2}} + \left(\boldsymbol{X}_{0,s} + \boldsymbol{u}_{,s\, n+\frac{1}{2}}\right) \dot{\boldsymbol{m}}_{,s\, n+\frac{1}{2}} \\
\dot{\kappa}_{12\, n+\frac{1}{2}} &= \dot{\boldsymbol{n}}_{n+\frac{1}{2}} \cdot \boldsymbol{m}_{,s\, n+\frac{1}{2}} + \boldsymbol{n}_{n+\frac{1}{2}} \cdot \dot{\boldsymbol{m}}_{,s\, n+\frac{1}{2}}
\end{aligned}
\tag{5.33}
$$

Given the strain and kinematic fields at time n and computing quantities of Eqs. (7.84) at step $n+\frac{1}{2}$, the same fields at step $n+\frac{1}{2}$ are then defined as follows:

$$
\begin{aligned}
\ddot{\boldsymbol{n}}_{n+\frac{1}{2}} &= \frac{2}{\Delta t}\dot{\boldsymbol{n}}_{n+\frac{1}{2}} - \frac{2}{\Delta t}\dot{\boldsymbol{n}}_{n} \\
\ddot{\boldsymbol{m}}_{n+\frac{1}{2}} &= \frac{2}{\Delta t}\dot{\boldsymbol{m}}_{n+\frac{1}{2}} - \frac{2}{\Delta t}\dot{\boldsymbol{m}}_{n} \\
\varepsilon_{11\, n+\frac{1}{2}} &= \varepsilon_{11\, n} + \frac{1}{2}\Delta t\, \dot{\varepsilon}_{11\, n+\frac{1}{2}} \\
\kappa_{1\, n+\frac{1}{2}} &= \kappa_{1\, n} + \frac{1}{2}\Delta t\, \dot{\kappa}_{1\, n+\frac{1}{2}} \\
\kappa_{2\, n+\frac{1}{2}} &= \kappa_{2\, n} + \frac{1}{2}\Delta t\, \dot{\kappa}_{2\, n+\frac{1}{2}} \\
\kappa_{12\, n+\frac{1}{2}} &= \kappa_{12\, n} + \frac{1}{2}\Delta t\, \dot{\kappa}_{12\, n+\frac{1}{2}}
\end{aligned}
\tag{5.34}
$$

By doing that, the proof of energy and linear momentum can be demonstrated theoretically as presented in Paper IV. Four numerical examples are considered in the numerical sections. These examples focus on the accuracy and the stability of the new algorithms.

Roorda-Koiter frame example [26] is presented in this section. In this problem, the connection between the column and the beam is not an easy task to solve because it requires nonlinear constraint equation. One possible solution for maintaining the continuity of this connection is to introduce a small radius R of 0.25 m, see Fig. 5.13(a). Lee's frame has a uniform rectangular cross-section and is subjected to two out-of-plane forces. Both applied forces follow the pattern of a hat function as shown in Fig. 5.13(b). The length L is 12 m, the width 0.3 m and the depth 0.2 m. The material characteristic are: Young modulus $E = 210\,\mathrm{GPa}$, Poisson's ratio $\nu = 0.3$ and density $\rho = 7850\,\mathrm{kg/m^3}$. The time step size is taken $\Delta t = 10^{-4}$ s.

The reference solution, obtained with 22 elements (11 elements per member), and the results obtained with the proposed formulation with 10 elements (4 straight beam elements and 1 curved beam per member) are shown in Figures 5.14(a), 5.14(b) and 5.15(a). It can be observed that with only 10 elements, the new total Lagrangian formulation gives results that are in good agreement with the reference solution. Additionally, Figure 5.15(b) shows the conservation of the energy for one million time steps after the external loads vanishes.

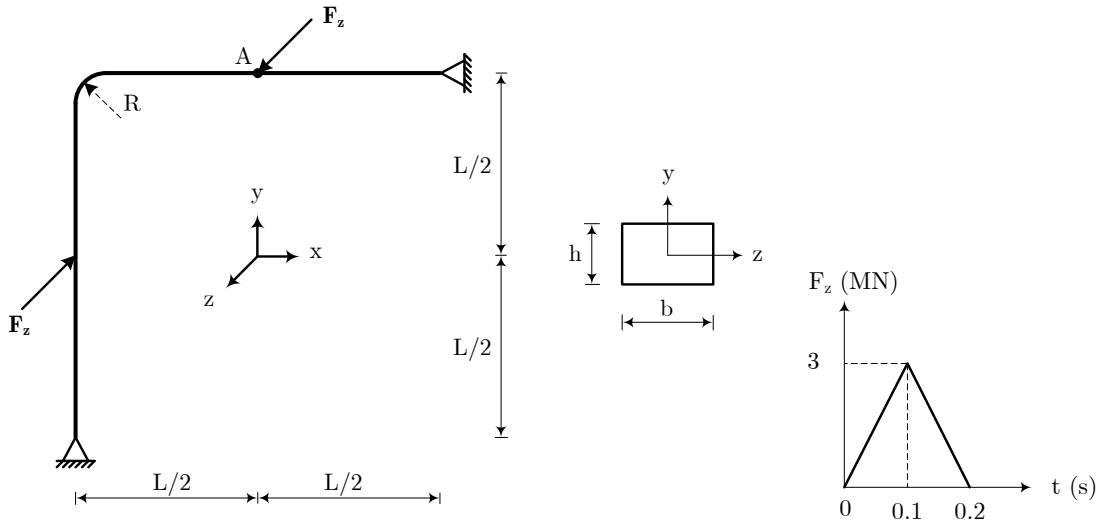

(a) (b)

Figure 5.13: (a). Geometrical data, (b). Loading history.

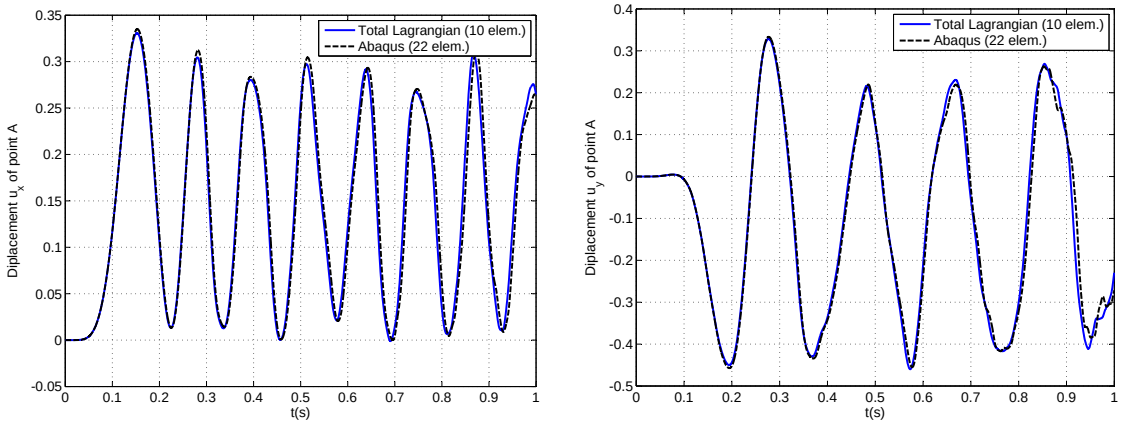

(a) (b)

Figure 5.14: (a). Displacement u_x of point A, (b). Displacement u_y of point A.

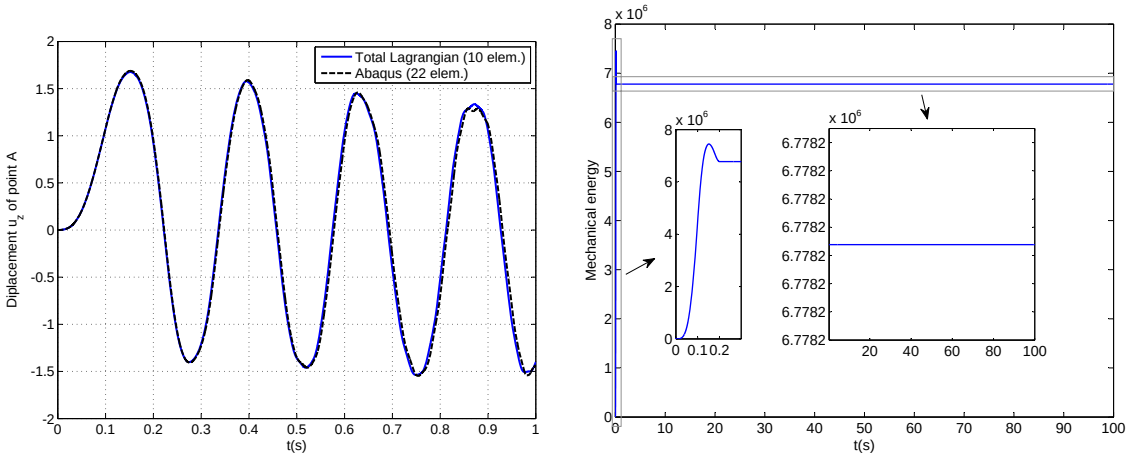

(a) (b)

Figure 5.15: (a). Displacement u_z of point A, (b). Time evolution of the energy.

Chapter 6

Conclusions and future research

6.1 Conclusions

Most effort in this thesis is devoted to the development of energy-momentum method for nonlinear finite beam elements. Several formulations with various purposes for corotational planar beam elements are presented in papers I, II and III. Paper IV focuses on the development of energy-conserving scheme for geometrically exact spatial curve beam in nonlinear dynamics.

2D co-rotational beam element models

2D Bernoulli beam element

The development of a stable momentum and energy conserving integration scheme for a co-rotational beam formulation has been achieved. The main idea is to use the classical midpoint rules for both the kinematic and strain quantities. The advantage of the proposed algorithm is that the conservation of the total energy of the system results in a very stable and accurate algorithm even for very large number of time steps. Besides, in the absence of applied external loads, the linear and angular momenta are constant. These characteristics have been proved theoretically and confirmed numerically by using four numerical examples.

2D shear flexible beam element

Three shear flexible co-rotational planar beam formulations have been developed and tested together with the energy-momentum method presented in paper I [40]. The three proposed shear flexible formulations share the same co-rotational framework and differ in the choice of the local strain definition and the local shape functions. If local linear strains and local linear shape functions are taken, the numerical results show that it is more efficient to adopt a local mixed approach instead of a pure displacement one: the CPU time is unchanged but the same accuracy is obtained with a less number of elements. The numerical results show also that it can be interesting to use a nonlinear local strain approach together with local cubic shape functions: the computational time is increased (due essentially to mathematically more complicated dynamic terms) but the same accuracy is obtained with a much less number of elements. For that approach, it has also been shown that a simplified dynamic tangent matrix should be taken and that the choice of an efficient predictor can be important.

A 2D elasto-(visco)-plastic fiber co-rotational beam element and a planar co-rotational beam element with generalized elasto-(visco)-plastic hinges

2D co-rotational beam element formulations for nonlinear dynamics of frame structures subjected to impact are developed. Based on the co-rotational framework, the inelastic behaviour of the frame structures is modelled by either distributed plasticity or generalized hinge approaches. Both Bernoulli and Timoshenko local beam formulations are employed for the distributed plasticity approaches whereas the Bernoulli formulation is associated with the generalized hinges element. For the latter, a condensation procedure is used to remove the internal degrees of freedom and to produce a two noded super-element that fits the standard co-rotational appraoch. For the proposed formulations, strain effects have been considered by replacing the plastic flow rule with its visco-plasticity counterpart.

The numerical examples show that the beam elements with distributed plasticity accurately predict the response of the structures and are then used as reference solutions by taking a large number of elements. The effects of the shear deformation in both elasto-plastic and visco-elasto-plastic models are not significant in the impact problem. Besides, the formulation with generalized hinges gives relatively accurate results with only few elements compared to the approach with distributed plasticity. The introduction of the strain rate in the constitutive law shows that the frame deformed less due to the hardening of the material.

3D geometrically exact beam element model

An energy-conserving scheme for geometrically exact Euler-Bernoulli spatial curved beam in nonlinear dynamic has been developed. Two approaches to define the position of the deformed base system in a way consistent with the overarching Euler-Bernoulli assumption are provided. The first approach makes use of the Gram-Schmidt orthogonalisation process coupled to a one-parametric rotation. The latter completes the description of the torsional cross sectional rotation and overcomes the non-uniqueness of the Gram-Schmidt procedure. In a second approach, the rotation tensor is defined by using the first and second derivatives of the displacement vector of the centre line, together along a one parametric rotation. The new formulation is able to produce accurate results with both straight and curved beams. Numerical comparisons with the co-rotational formulations [26] and Abaqus have been performed. Last but not least, the proposed energy-conserving algorithm can conserve the total energy of the system and remains stable even if a very large number of time steps are applied. In the absence of applied external loads, the linear and angular momenta remain constant.

6.2 Future research

The models developed in this thesis focus on the energy-momentum method for nonlinear beam elements. However, there is still room for more developments and enhancements. Some future research are suggested as the following:

Energy-momentum decaying scheme

Previous works, i.e. Kuhl and Ramm [75], Romero and Amero [76], Ibrahimbegović and Mamouri [77], Mamouri et al. [78], Gam et al. [79] to mention a few, have pointed out that it is very important to have a controllable numerical dissipation in the energy-momentum method in order to damp high frequencies especially for stiff beams. As discussed in [77, 79],

even though the energy is preserved in the global sense and the algorithm is unconditionally stable, the internal forces in the element level may exhibit spurious high frequencies. In this context, the numerical problem which may arise from the energy-momentum method or the refined mesh can disappear through numerical dissipation.

3D co-rotational energy-momentum method

The extension of the proposed energy-momentum method of co-rotational planar beams to co-rotational spatial beams is very challenging. The main difficulty is related to the large spatial rotations and the way these rotations affects the strain rates. The objectivity of the strain (see [56]) should be considered because it has been shown by Romero and Armero [57] that this strain could improve the accuracy and the stability of the algorithms.

Chapitre 7

Résumé en français

7.1 Introduction

Motivation

La dynamique non-linéaire des poutres flexibles reste un sujet de recherche très actif surtout dans le domaine de l'ingénerie. Les poutres flexibles sont utilisées dans de nombreuses applications pour l'instant des grandes structures déployées dans l'espace, les hélices d'avions, les pales d'éoliennes et des plateformes offshores. Ces structures peuvent subir de grands déplacements et de grandes rotations. Alors, la simulation de ces structures nécessite deux outils numériques efficaces : formulation des élément finis et méthode d'intégration temporelle.

Premièrement, il y a plusieurs méthodes pour le développement des formulations efficaces de la poutre : la formulation totale lagrangienne [1, 2, 3, 4, 5], la méthode flottante [6, 7, 8] et la méthode co-rotationnelle [9, 10, 11, 12, 13, 14, 15, 16, 17, 18, 19, 20]. Parmi de ces méthodes, la formulation totale lagrangienne est une approche naturelle pour la construction de théories de poutre géométriquement exacte. La méthode co-rotationnelle est une approche intéressante pour développer des éléments de poutre fortement non-linéaires car elle allie précision et efficacité numérique.

Deuxièmement, il est aujourd'hui reconnu que les méthodes de type Newmark, la méthode du point milieu classique ou la règle trapézoïdale posent des problèmes de stabilité en régime non-linéaire. Alors, la stabilité à long terme est considérée comme une caractéristique fondamentale pour la construction du schéma d'intégration temporelle. L'extension du schéma d'intégration temporelle traditionnelle (Newmark méthodes [21]) de la dynamique linéaire à celle de non-linéaire n'est pas banal et parfois cause l'instabilité. Greenspan [23, 24] avait démontré l'importance de la conservation de l'énergie totale, de la quantité de mouvement et du moment cinétique dans le développement du schéma d'intégration temporelle. Simo [22] découvrait comment modifier des algorithmes de la poutre spatiale pour la conservation de ces quantités qui améliorent la stabilité des algorithmes. Bien que son formulation n'applique qu'au matériau de Saint-Venant Kirchhoff, les schémas d'intégration conservatifs ont été enrichis même ou différemment manières dans des autres applications.

De nombreuses des travaux de recherche sur la formulation des éléments finis dans l'approche co-rotationnelle [12, 25, 26, 27, 28, 29, 31, 32, 33] et dans l'approche totale lagrangienne

[35, 36] ont été réalisés par le département de génie civil et architectural à KTH Royal Institute of Technology et la laboratoire LGCGM à l'INSA Rennes. Parmi de ces travaux, la formulation co-rotationnelle sur la poutre 2D proposée par Le et al. [12] est très efficace car les interpolations cubiques ont été utilisées pour dériver les termes d'inerties et les termes d'internes. Pourtant, la méthode d'intégration HHT-alpha [37] introduit la dissipation artificielle qui dissipe l'énergie dans le système. Sansour [35] a développé le schéma d'intégration temporelle qui conserve l'énergie totale, la quantité de mouvement et le moment cinétique pour la poutre Euler-Bernoulli 2D. Donc, c'est très intéressant de développer la poutre planaire co-rotationnelle et la poutre spatiale total lagrangienne avec ce schéma d'intégration conservatif.

Objective

Dans la première partie de la thèse, le schéma d'intégration conservatif est appliqué aux poutres co-rotationnelles 2D [40, 41]. Les cinématiques de Bernoulli et de Timoshenko sont abordées. Ces formulations produisent des expressions non-linéaires complexes pour l'énergie interne et l'énergie cinétique. L'idée centrale de l'algorithme consiste à définir, par intégration, le champ des déformations en fin de pas à partir du champ de vitesses de déformations et non à partir du champ des déplacements au travers de la relation déplacement-déformation [38, 82]. La même technique est appliquée aux termes d'inerties. Plusieurs exemples ont été considérés dans lesquels ils sont observés que l'énergie totale, la quantité de mouvement et le moment cinétique sont conservés pour les deux formulations. Ensuite, des poutres co-rotationnelles planes en considérant un comportement élasto-(visco)-plastique sont développées et sont comparées les uns aux autres pour les problèmes d'impact. Des exemples numériques montrent que les effets de la vitesse de déformation influencent sensiblement la réponse de la structure.

Dans la seconde partie de cette thèse, une théorie de poutre spatiale d'Euler-Bernoulli géométriquement exacte est développée. Le principal défi dans la construction d'une telle théorie réside dans le fait qu'il n'existe aucun moyen naturel de définir un trièdre orthonormé dans la configuration déformée. Une nouvelle méthodologie permettant de développer une théorie de poutre spatiale en incorporant l'hypothèse d'Euler-Bernoulli est fournie. Cette approche utilise le processus d'orthogonalisation de Gram-Schmidt couplé avec un paramètre rotation qui complète la description cinématique et qui décrit la rotation associée à la torsion. Il permet de surmonter le caractère non-unique de la procédure de Gram-Schmidt. La formulation est étendue au cas dynamique et un schéma intégration temporelle conservant l'énergie est également développé. Plusieurs exemples démontrent l'efficacité de cette formulation.

7.2 Poutres co-rotaionelles 2D (Article I, II et III)

La méthode co-rotationnelle est une approche intéressante pour dériver des éléments des poutres non-linéaires [9, 10, 11, 12, 13, 14, 15, 16, 17, 18, 19, 20, 25, 26, 27, 72, 73, 74]. L'idée principale est de décomposer le mouvement de l'élément en deux parties : un mouvement corps rigide et un mouvement en petites perturbations (déformation pures). Au cours du mouvement rigide, un système local déplace et tourne avec ce dernier. L'intérêt principal de cette approche est la possibilité d'utiliser des différentes formulations locales.

Dans cette section, la cinématique de la poutre, des déformations, le principe d'Hamilton sont présentés ainsi que les résumés des articles I, II et III.

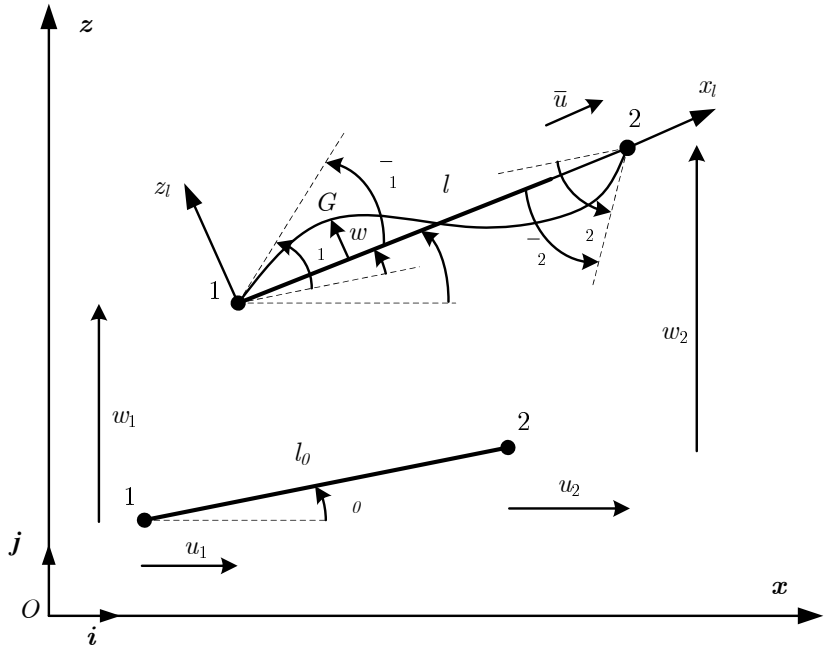

FIGURE 7.1: Cinétique de la poutre 2D.

7.2.1 Cinématique de la poutre

La cinématique d'un élément poutre co-rotationnelle à deux nœuds est représentée à la figure 7.1. Le nœud 1 est pris comme l'origine du système des coordonnées locales (x_l, z_l) qui continue à déplacer et tourner avec l'élément. L'axe x_l est coïncident avec la droite reliant les deux nœuds de l'élément. Par suite du choix du système local, le vecteur des déplacements globaux est défini par :

$$\boldsymbol{q} = \left[\begin{array}{cccccc} u_1 & w_1 & \theta_1 & u_2 & w_2 & \theta_2 \end{array} \right]^{\mathrm{T}}, \tag{7.1}$$

et le vecteur des déplacements locaux par :

$$\bar{\boldsymbol{q}} = \left[\begin{array}{ccc} \bar{u} & \bar{\theta}_1 & \bar{\theta}_2 \end{array} \right]^{\mathrm{T}} \tag{7.2}$$

7.2.2 Déformations

a) Formulations d'IIE/Bernoulli

Dans cette formulation locale, les fonctions d'interpolation de l'Interdependent Interpolation Element (IIE), proposées dans [97], ont été utilisées avec une théorie des poutres en arc à profondeur faible. Le développement de ces éléments est basé sur la solution exacte sous la forme homogène de l'équation d'équilibre d'une poutre Timoshenko. Par conséquent, l'IIE conserve non seulement la précision inhérente à l'interpolation cubique, mais comprend également la déformation de cisaillement. La fonction de forme de l'IIE est donnée par :

$$
\begin{aligned}
N_3 &= \mu\, x \left[6\,\Omega \left(1 - \frac{x}{l_0} \right) + \left(1 - \frac{x}{l_0} \right)^2 \right] \\
N_4 &= \mu\, x \left[6\,\Omega \left(\frac{x}{l_0} - 1 \right) - \frac{x}{l_0} + \frac{x^2}{l_0^2} \right] \\
N_5 &= \mu \left(1 + 12\,\Omega - \frac{12\,\Omega\, x}{l_0} - \frac{4\, x}{l_0} + \frac{3\, x^2}{l_0^2} \right) \\
N_6 &= \mu \left(\frac{12\,\Omega\, x}{l_0} - \frac{2\, x}{l_0} + \frac{3\, x^2}{l_0^2} \right)
\end{aligned}
\tag{7.3}
$$

Avec $\Omega = EI/(GA\, k_s\, l_0^2)$, $\mu = 1/(1 + 12\,\Omega)$ et k_s le coefficient de correction de cisaillement. En prenant Ω égale à 0, on retombe sur la poutre Bernoulli. Des études numériques effectuées par [12] ont montré que cette simplification ne modifie par les résultats numériques.

La déformation longitudinale en arc et la déformation de cisaillement sont définies par :

$$\varepsilon_{11} = \varepsilon - \kappa\, z \tag{7.4}$$

$$\gamma = \frac{\partial w}{\partial x} - \theta \tag{7.5}$$

dans lequel la déformation axiale ε et la courbure κ sont définies par

$$\varepsilon = \frac{1}{l_0} \int_{l_0} \left[\frac{\partial u}{\partial x} + \frac{1}{2} \left(\frac{\partial w}{\partial x} \right)^2 \right] \mathrm{d}x \tag{7.6}$$

$$\kappa = \frac{\partial^2 w}{\partial x^2} \tag{7.7}$$

Dans l'équation (7.7), la déformation axiale a été prise en moyen sur l'élément pour éviter le verrouillage de la membrane. Le but d'introduire la géométrie non-linéaire dans la formulation locale est d'augmenter la précision en comparant avec la déformation linéaire. Alors, l'efficacité de cette formulation reste précise avec peu nombre d'éléments.

b) Méthode d'intégration réduite (RIE)

La méthode d'intégration réduite est une approche classique de Timoshenko en basant sur l'interpolation linéaire. Un point d'intégration de Gauss est utilisé pour éviter le verrouillage de l'effort tranchant. La courbure κ, la déformation de cisaillement γ et la déformation axiale ϵ sont définies par :

$$\kappa = \frac{\partial \theta}{\partial x} = \frac{\bar{\theta}_2 - \bar{\theta}_1}{l_0} \tag{7.8}$$

$$\gamma = \frac{\partial w}{\partial x} - \theta = -N_1 \bar{\theta}_1 - N_2 \bar{\theta}_2 \tag{7.9}$$

$$\varepsilon_{11} = \varepsilon - \kappa\, z = \frac{\bar{u}}{l_0} - \frac{\bar{\theta}_2 - \bar{\theta}_1}{l_0} z \tag{7.10}$$

Alors, l'énergie interne pour l'IIE et la méthode d'intégration réduite est définie par :

$$\mathsf{U}_{int} = \frac{1}{2} \int_{l_0} EA\, \varepsilon^2 \mathrm{d}x + \frac{1}{2} \int_{l_0} EI\, \kappa^2 \mathrm{d}x + \frac{1}{2} \int_{l_0} k_s GA\, \gamma^2 \mathrm{d}x \tag{7.11}$$

avec E étant le module élastique et G le module de cisaillement, A l'aire de la section et I le moment inertie de la section.

c) Formulation de Hellinger-Reissner (MX)

Une formulation mixte à deux champs basée sur le principe variationnel de Hellinger-Reissner est considérée. Les déplacements et les forces internes le long de l'élément sont approximés par la fonction de forme linéaire indépendamment. Alors, l'énergie interne de Hellinger-Reissner s'écrit :

$$\mathsf{U}_{int} = \int_{l_0} \boldsymbol{S}^{\mathrm{T}} \left(\hat{\boldsymbol{e}} - \frac{1}{2} \boldsymbol{e} \right) \mathrm{d}x \tag{7.12}$$

Le résultant des contraintes généralisée est approximé par :

$$\boldsymbol{S} = \begin{bmatrix} N \\ M \\ Q \end{bmatrix} = \mathbf{N}_s \, \boldsymbol{f}_l = \begin{bmatrix} 1 & 0 & 0 \\ 0 & -N_1 & N_2 \\ 0 & -1/l_0 & -1/l_0 \end{bmatrix} \begin{bmatrix} N \\ M_1 \\ M_2 \end{bmatrix} \tag{7.13}$$

où $\mathbf{N}_s$ est la matrice des fonctions de forme satisfaisante à l'équilibre local. En utilisant les équations (7.8),(7.9) et (7.10), la déformation généralisée $\hat{\mathbf{e}}$ est définie par :

$$\hat{\boldsymbol{e}} = \begin{bmatrix} \varepsilon \\ \kappa \\ \gamma \end{bmatrix} = \mathbf{N}_{\hat{e}} \, \bar{\boldsymbol{q}} = \begin{bmatrix} 1/l_0 & 0 & 0 \\ 0 & -1/l_0 & 1/l_0 \\ 0 & -N_1 & -N_2 \end{bmatrix} \begin{bmatrix} \bar{u} \\ \bar{\theta}_1 \\ \bar{\theta}_2 \end{bmatrix} \tag{7.14}$$

Les déformations de la section transversale sont définies par :

$$\boldsymbol{e} = \mathbf{N}_{s1} \, \boldsymbol{f}_l = \begin{bmatrix} 1/(EA) & 0 & 0 \\ 0 & -N_1/(EI) & N_2/(EI) \\ 0 & -1/(k_s GA \, l_0) & -1/(k_s GA \, l_0) \end{bmatrix} \begin{bmatrix} N \\ M_1 \\ M_2 \end{bmatrix} \tag{7.15}$$

7.2.3 Principe d'Hamilton

Le principe d'Hamilton stipule que l'intégrale du lagrangien entre deux temps spécifiés t_1 et t_2 d'un système conservatif est stationnaire :

$$\delta \int_{t_n}^{t_{n+1}} \mathcal{L} \, \mathrm{d}t = \delta \int_{t_n}^{t_{n+1}} (\mathsf{K} - \mathsf{U}_{int} - \mathsf{U}_{ext}) \, \mathrm{d}t = 0 \tag{7.16}$$

où K est l'énergie cinétique et U_{ext} l'énergie externe. Les effets thermodynamiques ne sont pas inclus dans le système. L'énergie interne U_{int} est définie en fonction de chaque formulation (Voir Eqs. (7.11) et (7.12)). L'énergie cinétique est la somme des énergies cinétiques de translation et de rotation :

$$\mathsf{K} = \frac{1}{2} \int_{l_0} \rho A \, \dot{u}_G^2 \, \mathrm{d}x + \frac{1}{2} \int_{l_0} \rho A \, \dot{w}_G^2 \, \mathrm{d}x + \frac{1}{2} \int_{l_0} \rho I \, \dot{\theta}_G^2 \, \mathrm{d}x \tag{7.17}$$

et l'énergie externe est donnée par :

$$\mathsf{U}_{ext} = - \int_{l_0} p_u u_G \, \mathrm{d}x - \int_{l_0} p_w w_G \, \mathrm{d}x - \int_{l_0} p_\theta \theta_G \, \mathrm{d}x - \sum_{i=1}^{6} P_i q_i \tag{7.18}$$

avec ρ étant la masse volumique, p_u et p_w les charges distribuées horizontales et verticales, p_θ le moment distribué extérieur, P_i le composant i (forces et moments concentrés aux nœuds) du vecteur de la force externe $\mathbf{P}$.

Le système hamiltonien ci-dessus manifeste les propriétés de conservation suivantes. Si les charges externes sont conservatrices, l'énergie totale de l'élément de la poutre s'écrit :

$$\mathsf{K} + \mathsf{U}_{int} + \mathsf{U}_{ext} = \mathsf{constant} \tag{7.19}$$

La quantité de mouvement est définie par :

$$\mathbf{L} = \begin{bmatrix} \mathsf{L}_u \\ \mathsf{L}_w \end{bmatrix} = \int_{l_0} \rho A \begin{bmatrix} \dot{u}_G \\ \dot{w}_G \end{bmatrix} \mathrm{d}x \tag{7.20}$$

et le moment cinétique par :

$$\mathsf{J} = \int_{l_0} \rho A \begin{bmatrix} u_G \\ w_G \\ 0 \end{bmatrix} \times \begin{bmatrix} \dot{u}_G \\ \dot{w}_G \\ 0 \end{bmatrix} \mathrm{d}x + \int_{l_0} \rho I \begin{bmatrix} 0 \\ 0 \\ \dot{\theta}_G \end{bmatrix} \mathrm{d}x \tag{7.21}$$

La dérivée temporelle pour la quantité de mouvement et pour le moment cinétique est définie par :

$$\frac{\mathrm{d}}{\mathrm{d}t}\mathbf{L} = \begin{bmatrix} \int_{l_0} p_u \, \mathrm{d}x + P_1 + P_4 \\ \int_{l_0} p_w \, \mathrm{d}x + P_2 + P_5 \end{bmatrix} \tag{7.22}$$

$$\begin{aligned} \frac{\mathrm{d}}{\mathrm{d}t}\mathsf{J} = \int_{l_0} (u_G \, p_w - w_G \, p_u) \, \mathrm{d}x + (x_1 + u_1)P_2 - (z_1 + w_1)P_1 \\ + (x_2 + u_2)P_5 - (z_2 + w_2)P_4 + \int_{l_0} p_\theta \, \mathrm{d}x + P_3 + P_6 = M_{ext} \end{aligned} \tag{7.23}$$

La quantité de mouvement et le moment cinétique sont constants après la disparition des charges externes. L'expression "charge externe" désigne toutes les conditions de chargements possibles, y compris les réactions.

7.2.4 Article I

Dans cet article, le schéma d'intégration conservatif développé par Sansour [38, 39] est appliqué à la formulation poutre co-rotationnelle Bernoulli 2D. L'idée centrale de l'algorithme consiste à définir, par intégration, le champ des déformations en fin de pas à partir du champ de vitesses de déformations et non à partir du champ des déplacements au travers de la relation déplacement-déformation [38, 82]. La même technique est appliquée aux termes d'inertie. Le schéma d'intégration conservatif est basé sur la méthode du point milieu classique :

$$\int_{t_n}^{t_{n+1}} f(t) \, \mathrm{d}t = f(t_{n+\frac{1}{2}}) \, \Delta t = f_{n+\frac{1}{2}} \, \Delta t \tag{7.24}$$

Alors, l'équation des motions à $n + \frac{1}{2}$ est définie par :

$$\begin{aligned} &\int_{l_0} \rho A \, \ddot{u}_{G,n+\frac{1}{2}} \left(\frac{\partial u_{G,n+\frac{1}{2}}}{\partial \boldsymbol{q}_{n+\frac{1}{2}}} \right)^{\mathrm{T}} \mathrm{d}x + \int_{l_0} \rho A \, \ddot{w}_{G,n+\frac{1}{2}} \left(\frac{\partial w_{G,n+\frac{1}{2}}}{\partial \boldsymbol{q}_{n+\frac{1}{2}}} \right)^{\mathrm{T}} \mathrm{d}x \\ &+ \int_{l_0} \rho I \, \ddot{\theta}_{G,n+\frac{1}{2}} \left(\frac{\partial \theta_{G,n+\frac{1}{2}}}{\partial \boldsymbol{q}_{n+\frac{1}{2}}} \right)^{\mathrm{T}} \mathrm{d}x + \int_{l_0} EA \, \varepsilon_{n+\frac{1}{2}} \left(\frac{\partial \varepsilon_{n+\frac{1}{2}}}{\partial \boldsymbol{q}_{n+\frac{1}{2}}} \right)^{\mathrm{T}} \mathrm{d}x \\ &+ \int_{l_0} EI \, \kappa_{n+\frac{1}{2}} \left(\frac{\partial \kappa_{n+\frac{1}{2}}}{\partial \boldsymbol{q}_{n+\frac{1}{2}}} \right)^{\mathrm{T}} \mathrm{d}x - \int_{l_0} p_{u,n+\frac{1}{2}} \left(\frac{\partial u_{G,n+\frac{1}{2}}}{\partial \boldsymbol{q}_{n+\frac{1}{2}}} \right)^{\mathrm{T}} \mathrm{d}x \\ &- \int_{l_0} p_{w,n+\frac{1}{2}} \left(\frac{\partial w_{G,n+\frac{1}{2}}}{\partial \boldsymbol{q}_{n+\frac{1}{2}}} \right)^{\mathrm{T}} \mathrm{d}x - \int_{l_0} p_{\theta,n+\frac{1}{2}} \left(\frac{\partial \theta_{G,n+\frac{1}{2}}}{\partial \boldsymbol{q}_{n+\frac{1}{2}}} \right)^{\mathrm{T}} \mathrm{d}x - \boldsymbol{P}_{n+\frac{1}{2}} = 0 \end{aligned} \tag{7.25}$$

La dérivée du champ cinématique et du champ de déformations par rapport au déplacement global $\boldsymbol{q}$ (le côté droit de chaque composant) est calculée à partir des équations co-rotationnelles classiques. Les accélérations $\ddot{u}_{G,n+\frac{1}{2}}$, $\ddot{u}_{G,n+\frac{1}{2}}$, $\ddot{\theta}_{G,n+\frac{1}{2}}$ et les déformations locales ($\varepsilon_{n+\frac{1}{2}}$, $\kappa_{n+\frac{1}{2}}$) ne sont pas directement calculées à partir des déplacements nodaux, des vitesses nodales et des accélérations nodales. En fait, ces variables sont fortement non-linéaires, les comportements de couplages peuvent causer l'instabilité. Pour le voir clairement, on montre tout d'abord comment les déplacements nodaux et les accélérations nodales à $n + \frac{1}{2}$ sont calculés :

$$\boldsymbol{q}_{n+\frac{1}{2}} = \boldsymbol{q}_n + \frac{\Delta t}{2}\dot{\boldsymbol{q}}_{n+\frac{1}{2}} \tag{7.26}$$

$$\ddot{\boldsymbol{q}}_{n+\frac{1}{2}} = \frac{2}{\Delta t}\dot{\boldsymbol{q}}_{n+\frac{1}{2}} - \frac{2}{\Delta t}\dot{\boldsymbol{q}}_n \tag{7.27}$$

En observant les équations ci-dessus, les déplacements nodaux et les accélérations nodales dépendent principalement des vitesses nodales à $n + \frac{1}{2}$ et les variables précédentes à pas n. Pour éviter les couplages, chaque variable cinématique et déformation doit être appliquée la même procédure à l'aide des équations (7.26) et (7.27). Ces variables sont définies par :

$$\begin{aligned}
\ddot{u}_{G,n+\frac{1}{2}} &= \frac{2}{\Delta t}\,\dot{u}_{G,n+\frac{1}{2}} - \frac{2}{\Delta t}\,\dot{u}_{G,n} \\
\ddot{w}_{G,n+\frac{1}{2}} &= \frac{2}{\Delta t}\,\dot{w}_{G,n+\frac{1}{2}} - \frac{2}{\Delta t}\,\dot{w}_{G,n} \\
\ddot{\theta}_{G,n+\frac{1}{2}} &= \frac{2}{\Delta t}\dot{\theta}_{G,n+\frac{1}{2}} - \frac{2}{\Delta t}\dot{\theta}_{G,n}
\end{aligned} \tag{7.28}$$

$$\begin{aligned}
\varepsilon_{n+\frac{1}{2}} &= \varepsilon_n + \frac{\Delta t}{2}\,\dot{\varepsilon}_{n+\frac{1}{2}} \\
\kappa_{n+\frac{1}{2}} &= \dot{\kappa}_n + \frac{\Delta t}{2}\,\dot{\kappa}_{n+\frac{1}{2}}
\end{aligned} \tag{7.29}$$

L'algorithme proposé assure la conservation de l'énergie totale, de la quantité de mouvement et du moment cinétique. Ces propriétés sont prouvées théoriquement et sont présentées dans l'article I [40].

Exemple

Un seul exemple présenté ici est la poutre dans l'espace (cf. Fig. 7.2). La longueur est $L = 3$ m, l'aire de section $A = 0,002\,\mathrm{m}^2$ et le moment d'inertie $I = 6,667 \times 10^{-8}\,\mathrm{m}^4$. Les propriétés du matériau sont : module élastique $E = 210$ GPa et mass volumique $= 7850\,\mathrm{kg/m}^3$. Le nombre d'élément est 4 et le pas de temps est $\Delta t = 10^{-3}$ s.

Ce problème est convenu pour étudier la conservation de la quantité de mouvement et du moment cinétique. Puisque les charges verticales sont appliquées seulement au début, la quantité de mouvement dans la direction horizontale doit être nulle. La quantité de mouvement présentée à la figure 7.3(b) est presque nulle avec la valeur maximale de 3×10^{-7}. Les figures 7.3(a), 7.3(b) et 7.4(a) montrent que l'énergie, la quantité de mouvement de la direction verticale et le moment cinétique sont constants. Cet exemple a également été testé avec les méthodes d'accélération moyenne et de HHT-α ($\alpha = -0.01$). La figure 7.4(b) montre que le moment cinétique ne conserve pas avec ces deux méthodes.

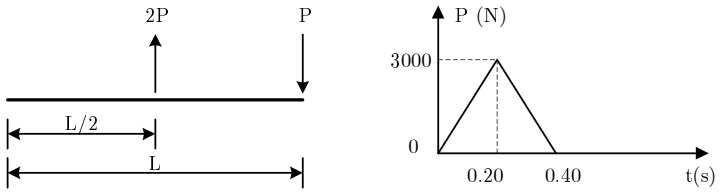

FIGURE 7.2: Géométrie et l'histoire de la charge

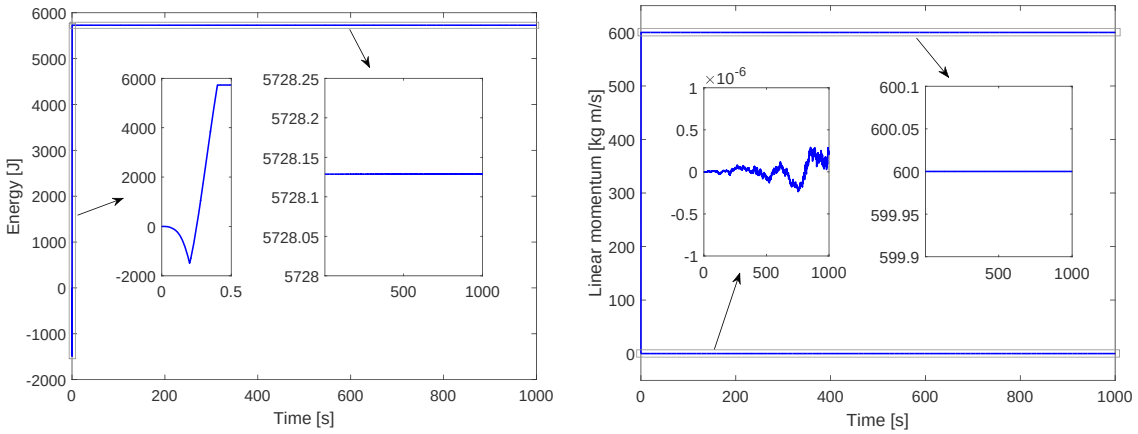

(a) (b)

FIGURE 7.3: (a). Energie totale de la poutre, (b). Quantité de mouvement.

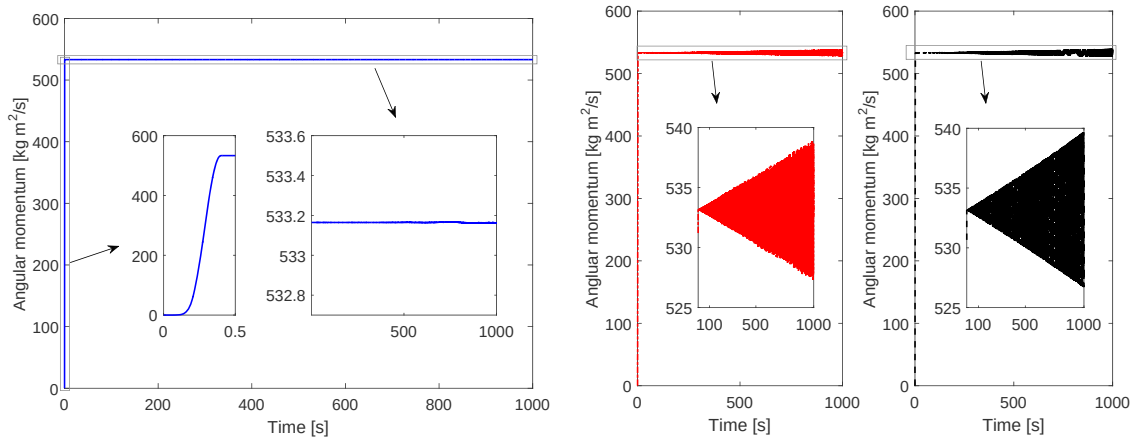

(a) (b)

FIGURE 7.4: (a). Moment cinétique du schéma d'intégration conservatif, (b). Moment cinétique de la méthode d'accélération moyenne (gauche) et de la méthode HHT-α $\alpha = -0.01$ (droite).

7.2.5 Article II

Dans ce travail, la même conception du schéma d'intégration conservatif de l'article I [40] est appliquée pour le développement de la formulation poutre co-rotationnelle plane Timoshenko. En basant sur la même description co-rotationnelle, trois formulations locales sont testées avec un grand nombre de pas de temps. Les fonctions de forme et les hypothèses de déformation pour chaque formulation locale sont présentées dans le tableau 7.1. Pour la

formulation d'IIE, l'expression du la matrice tangente dynamique est compliquée et une simplification est éventuellement étudiée. Pour les trois formulations, différents prédicteurs sont aussi testés en fonction de temps de calcul (CPU time).

TABLE 7.1: Formulations

Formulations	Interpolation	Terme statique
RIE	Linéaire	Déformation linéaire avec l'intégration reduite
MX	Linéaire	Déformation linéaire avec la formulation mixte
IIE	Cubique	Déformation de l'arc

Pour les formulations de RIE et MX, les interpolations linéaires sont utilisées dans les coordonnées co-rotationnelles locales : $u = N_2\,\bar{u}$, $w = 0$ et $\theta = N_1\,\bar{\theta}_1 + N_2\,\bar{\theta}_2$. Par conséquent, la matrice dynamique tangente s'écrit :

$$\mathbf{K}_k = \frac{2}{\Delta t^2}\,\mathbf{M} \tag{7.30}$$

où la masse matrice constante $\mathbf{M}$ est donnée par :

$$\mathbf{M} = \rho\, l_0 \begin{bmatrix} A/3 & 0 & 0 & A/6 & 0 & 0 \\ 0 & A/3 & 0 & 0 & A/6 & 0 \\ 0 & 0 & I/3 & 0 & 0 & I/6 \\ A/6 & 0 & 0 & A/3 & 0 & 0 \\ 0 & A/6 & 0 & 0 & A/3 & 0 \\ 0 & 0 & I/6 & 0 & 0 & I/3 \end{bmatrix} \tag{7.31}$$

Cependant, pour la formulation d'IIE, la matrice tangente dynamique pour les termes d'inertie est très compliquée et son expression s'exprime :

$$\begin{aligned} \mathbf{K}_k =& \frac{\partial \boldsymbol{f}_{k,n+\frac{1}{2}}}{\partial \boldsymbol{q}_{n+1}} \\ =& \frac{2}{\Delta t^2}\left[\mathbf{T}^{\mathrm{T}}\mathbf{M}_l\mathbf{T} + \frac{1}{2}\left(\mathbf{T}^{\mathrm{T}}\left(\boldsymbol{I}_1^{\mathrm{T}}\mathbf{M}_l + \mathbf{M}_l\boldsymbol{I}_1\right)\mathbf{T}\right)\left(\Delta\boldsymbol{q}\,\frac{\boldsymbol{z}^{\mathrm{T}}}{l_{n+\frac{1}{2}}}\right)\right. \\ &+ \frac{1}{2}\left(\mathbf{T}^{\mathrm{T}}\mathbf{M}_{l,l}\mathbf{T}\right)\left(\Delta\boldsymbol{q}\,\boldsymbol{r}^{\mathrm{T}}\right) + \left(\mathbf{T}^{\mathrm{T}}\mathbf{M}_{l,\bar{\theta}_1}\mathbf{T}\right)\left(\Delta\boldsymbol{q}\,\frac{\partial\bar{\theta}_{1,n+\frac{1}{2}}}{\partial\boldsymbol{q}_{n+1}}\right) \\ &\left.+ \left(\mathbf{T}^{\mathrm{T}}\mathbf{M}_{l,\bar{\theta}_2}\mathbf{T}\right)\left(\Delta\boldsymbol{q}\,\frac{\partial\bar{\theta}_{2,n+\frac{1}{2}}}{\partial\boldsymbol{q}_{n+1}}\right)\right] - \frac{2}{\Delta t}\,\frac{\partial\boldsymbol{f}_{uw\theta}}{\partial\boldsymbol{q}_{n+1}} \end{aligned} \tag{7.32}$$

La dernière expression est très longue et son opération nécessite beaucoup de temps de calcul. Afin de réduire ce temps de calcul, Geradin et Cardona [126, 101] ont suggéré de ne garder que la matrice de masse et négliger les matrices gyroscopiques et centrifuges. Pour la deuxième simplification, la matrice tangente dynamique est proposée :

$$\mathbf{K}_k = \frac{2}{\Delta t^2}\left(\mathbf{T}^{\mathrm{T}}\mathbf{M}_l\mathbf{T}\right) \tag{7.33}$$

avec $\mathbf{T}$ étant la matrice de rotation :

$$\mathbf{T} = \begin{bmatrix} c_{n+\frac{1}{2}} & s_{n+\frac{1}{2}} & 0 & 0 & 0 & 0 \\ -s_{n+\frac{1}{2}} & c_{n+\frac{1}{2}} & 0 & 0 & 0 & 0 \\ 0 & 0 & 1 & 0 & 0 & 0 \\ 0 & 0 & 0 & c_{n+\frac{1}{2}} & s_{n+\frac{1}{2}} & 0 \\ 0 & 0 & 0 & -s_{n+\frac{1}{2}} & c_{n+\frac{1}{2}} & 0 \\ 0 & 0 & 0 & 0 & 0 & 1 \end{bmatrix} \tag{7.34}$$

Par ailleurs, le choix du prédicteur est aussi important pour rendre le calcul plus efficace. Un prédicteur médiocre peut augmenter le nombre d'itérations, et dans certains cas la solution ne converge pas. Trois prédicteurs ont été proposés et testés :
• Le premier prédicteur (Pred.1), appelé "déplacements inchangés", est utilisé par Simo et Vu-Quoc [100]

$$\boldsymbol{q}_{n+1} = \boldsymbol{q}_n \tag{7.35}$$

• Le second prédicteur (Pred.2), appelé "accélérations nulles", est proposé par Cardona et Géradin [101], Mäkinen [127], Chung et Hulbert [128]. Les accélérations nulles sont utilisées pour la solution au temps $n+1$. Pour la méthode du point milieu, les accélérations nodales au temps $n+\frac{1}{2}$ sont nulles. Alors, les déplacements sont définis par :

$$\boldsymbol{q}_{n+1} = \boldsymbol{q}_n + \Delta t\, \dot{\boldsymbol{q}}_n \tag{7.36}$$

• L'idée du troisième prédicteur (Pred.3), proposée par de Borst [129], est de supposer que le système se comporte linéairement entre $n-\frac{1}{2}$ et $n+\frac{1}{2}$. Dans le cas présent, le Pred.3 s'écrit :

$$\left(\frac{2}{\Delta t^2}\,\mathbf{T}^{\mathrm{T}}\mathbf{M}_l\mathbf{T} + \mathbf{K}_g\right)_{n-\frac{1}{2}} \Delta\boldsymbol{q} = \frac{2}{\Delta t}\,\boldsymbol{f}_{uw\theta,n-\frac{1}{2}} - \boldsymbol{f}_{g,n-\frac{1}{2}} + \boldsymbol{f}_{ext,n+\frac{1}{2}} \tag{7.37}$$

Exemple

Un exemple de poutre en arc est présenté ici. Une poutre de portée $L = 10$ m avec les extrémités encastrés est présentée à la figure 7.5. Le rayon R est de 10 m et la hauteur H de 1.3997 m. La poutre est soumise à une charge concentrée $P = P_0 sin(\omega t)$ à mi-portée. L'amplitude de la charge P_0 est de 80 MN et sa fréquence est de 1000 rad/s. Les caractéristiques de la poutre sont : l'aire de section $A = 0,087\,\mathrm{m}^2$, le module élastique $E = 210$ GPa, le moment d'inertie $I = 3,562 \times 10^{-3}\,\mathrm{m}^4$, le coefficient de Poisson $\nu = 0,3$ et la masse volumique $\rho = 7850\,\mathrm{kg/m}^3$. La pas de temps est $\Delta t = 10^{-5}$ s.

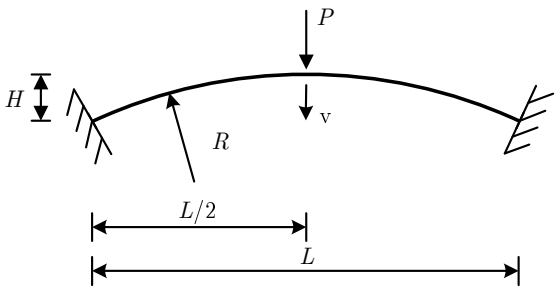

FIGURE 7.5: Géométrie et l'histoire de la charge.

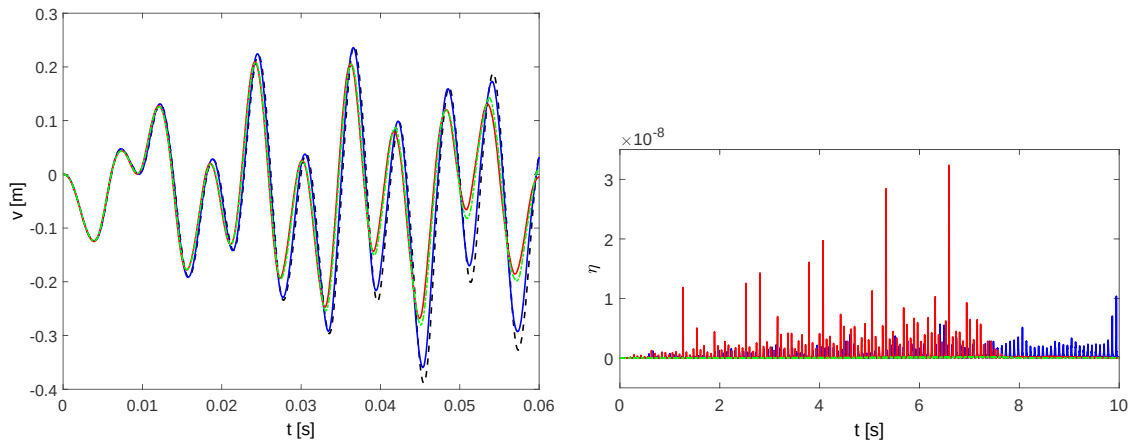

(a) (b)

FIGURE 7.6: (a). Déplacement vertical, (b). Erreur relative d'énergie.

Pour la présentation des résultats, les couleurs ci-dessous sont utilisées pour la figure 7.6.

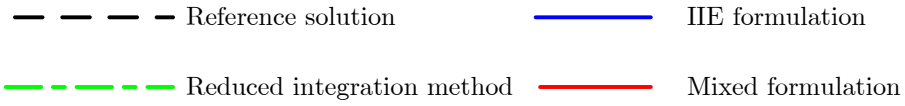

Le nombre d'éléments est : 8 pour la formulation IIE, 16 pour la formulation mixte, 24 pour la méthode d'intégration réduite et 100 pour la solution de référence. La figure 7.6(a) présente le déplacement vertical v à mi-portée pour les quatre analyses. Avec seulement 8 éléments, le résultat obtenu par la formulation d'IIE est légèrement différent en comparant avec la solution de référence. Cependant, des écarts importants sont observés entre les résultats obtenus par la formulation mixte (16 éléments) et par la méthode d'intégration réduite (24 éléments).

Pour les trois formulations, l'erreur relative d'énergie est présentée à la figure 7.6(b). La plus grande valeur est d'environ 3×10^{-8} pour une énergie externe maximale de $1,85 \times 10^{8}$ J. Ces résultats ont prouvé que la stabilité de l'alogrithme est assurée pour une durée longue même pour un grand nombre de pas (un million).

Les performances numériques des ces formulations sont détaillées dans l'article II [41]. Pour chaque formulation, les trois prédicteurs ci-dessus ont été testés. Pour l'approche IIE, la matrice tangente dynamique (Eq. 7.32) et la matrice simplifiée (Eq. 7.33) ont été testées. Pour chaque exemple, le même nombre d'éléments (correspondant au nombre des éléments de l'approche MX figurant dans le tableau 2 de l'article II) ont été utilisés dans toutes les analyses. Dans le tableau 7.2, le temps de calcul et le nombre total d'itérations (entre parenthèses) sont donnés pour chaque cas de 5000 pas.

TABLE 7.2: Peformances numériques pour la poutre en arc

	RIE	MX	IIE-exact	IIE-simp.
Pred.1	38 (14999)	38 (14999)	138 (18569)	110 (22902)
Pred.2	38 (14999)	38 (14999)	114 (15000)	97 (19951)
Pred.3	38 (14997)	38 (14997)	115 (14999)	99 (19996)

Les conclusions suivantes peuvent être conclues :
• Pour les approches RIE et MX, tous les prédicteurs donnent presque le même temps de calcul. Pour la formulation IIE, le Pred. 2 donne le temps de calcul le plus bas, mais la différence entre les prédicteurs 2 et 3 n'est pas significatif.
• Le temps de calcul et le nombre d'itérations pour les formulations RIE et MX sont quasiment identiques. Cela est juste puisque la seule différence entre ces approches réside dans différentes matrices de rigidité locales (constantes). Cependant, comme indiqué précédemment dans les exemples, l'approche RIE exige un plus grand nombre d'éléments afin d'obtenir une solution précise.
• Pour la formulation IIE, il est préférable d'utiliser la matrice de rigidité tangente simplifiée. Le nombre des itérations augmente mais le temps CPU diminue de 20% à 40% (Pred. 2).
• Avec le Pred. 2, la formulation IIE (avec matrice dynamique tangente simplifiée) nécessite environ 2,0 à 2,6 fois plus de temps processeur que la formulation MX. Par contre, les résultats ont montrés qu'avec deux fois plus d'éléments, la formulation MX donne moins des résultats précis que la formulation IIE. Il est donc difficile de conclure si une formulation est plus efficace que l'autre.

7.2.6 Article III

Dans cet article, une poutre co-rotationnelle plane avec rotules généralisées élasto-(visco)-plastiques aux extrémités est développée et comparée aux modèles fibres pour des problèmes d'impact. Pour le modèle avec des rotules généralisées, le comportement d'inélastique est simulé par des rotules généralisées placées aux deux extrémités d'un élément poutre Bernoulli élastique. Puisque ces éléments introduisent des degrés de liberté supplémentaires, la condensation statique est nécessaire au niveau de la formulation locale. Par conséquent, la poutre co-rotationelle classique à deux nœuds peut être utilisée. Les rotules généralisées prennent en compte l'interaction entre le moment de flexion M et la force normale N [132]. En plus, les coefficients de rigidité élastique de la poutre et des rotules sont déterminés de manière à ce que la rigidité élastique totale de l'élément soit conservée.

Modèle de plasiticté pour les poutres co-rotationnelles planes

Pour le modèle de poutre Bernoulli, l'élément est basé sur la théorie de poutre linéaire en utilisant une interpolation linéaire pour le déplacement axial local et une interpolation cubique pour le déplacement transversal local. Pour le modèle de poutre Timoshenko, une méthode d'intégration réduite est basée sur des fonctions de forme linéaire et un point d'intégration gaussien pour éviter le verrouillage par cisaillement.

Dans ces modèles, on suppose que la vitesse de déformation est la somme de la vitesse de déformation élastique et la vitesse de déformation plastique :

$$\dot{\boldsymbol{\Xi}} = \dot{\boldsymbol{\Xi}}^e + \dot{\boldsymbol{\Xi}}^p \tag{7.38}$$

La vitesse de déformation plastique est déterminée par la règle d'écoulement plastique :

$$\dot{\boldsymbol{\Xi}}^p = \dot{\lambda}\,\frac{\partial \Phi}{\partial \boldsymbol{\Sigma}} \tag{7.39}$$

où $\dot{\boldsymbol{\Xi}}^p$ est un multiplicateur plastique. $\boldsymbol{\Sigma}$ est le vecteur de champs des contraintes. La fonction de rendement Φ pour chaque formulation est définie par :

1/ Pour la poutre Bernoulli :

$$\Phi = |\sigma| - \sigma_y \tag{7.40}$$

avec $\mathbf{\Sigma} = \sigma$ et σ_y étant la limite élastique.
2/ Pour la poutre Timoshenko, la fonction de rendement de von Mises est utilisée :

$$\Phi = \left(\sigma^2 + 3\tau^2\right)^{1/2} - \sigma_y \tag{7.41}$$

avec $\mathbf{\Sigma} = [\sigma \quad \tau]$.

La règle d'écoulement vicso-plastique est introduite pour étudier les effets de taux de déformation. Ça s'écrit :

$$\begin{aligned} \dot{\lambda} &= D\left(\frac{\Phi}{\sigma_y}\right)^{\zeta} \quad \text{if} \quad \Phi \geq 0 \\ &= 0 \qquad\qquad\quad \text{if} \quad \Phi < 0 \end{aligned} \tag{7.42}$$

où Φ est donnée par une fonction de puissance de type Cowper-Symonds-Bonder [130, 131]. D and ζ sont des constantes matérielles ; pour l'acier doux, $\zeta = 5$ and $D = 40.4\ \mathrm{s}^{-1}$ selon Cowper et Symonds [130] et pour l'alliage d'aluminum, $\zeta = 4$ et $D = 6500\ \mathrm{s}^{-1}$ selon Bonder et Symonds [131].

Les détails de derivation de la matrice tangente sont présentés dans l'article III.

Rotules généralisés

Un élément poutre se compose de trois sous-éléments : un élément de poutre Bernoulli élastique et deux rotules elasto-(visco)-plastique généralisées modélisées par une combinaison de ressorts axiaux et rotatifs (cf. Fig. 7.7). L'allongement ou le raccourcissement des rotules se produit le long de l'axe de la poutre. Les rotules généralisées peuvent être considérées comme l'élément avec une longueur nulle en état initiale. En assemblant ces rotules avec l'élément de la poutre et en effectuant une condensation statique, un super élément à deux nœuds (cf. Fig. 7.7) est obtenu. Cet élément est ensuite incorporé dans la description co-rotationelle afin d'introduire des non-linéarités géométriques. Le déplacement axial local $\bar{u}_1$ est supposé à 0.

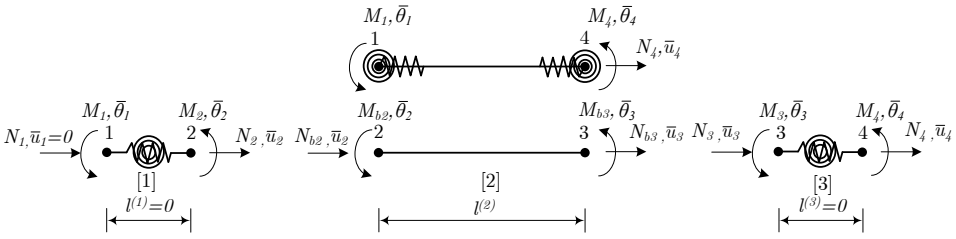

FIGURE 7.7: Local super-element.

La motion de l'élément poutre à deux nœuds est présenté à la figure 7.8. Les vecteurs des

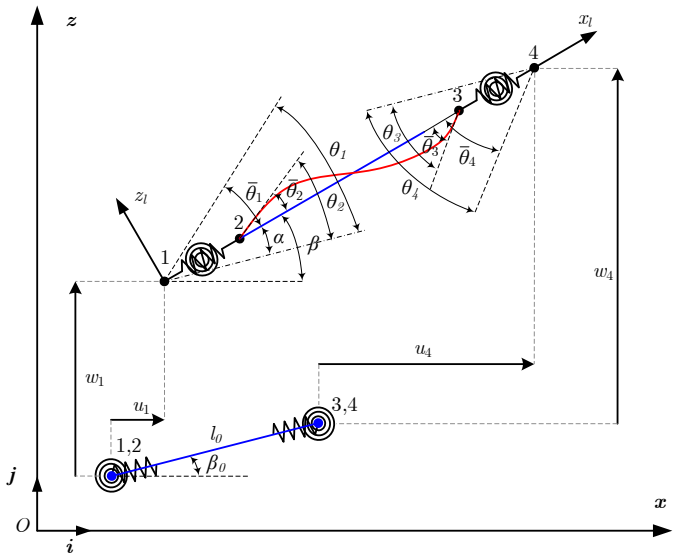

FIGURE 7.8: Beam kinematics.

déplacements globaux, locaux et des sous-éléments sont respectivement définis par :

$$\begin{aligned}
\boldsymbol{q} &= \begin{bmatrix} u_1 & w_1 & \theta_1 & u_4 & w_4 & \theta_4 \end{bmatrix}^{\mathrm{T}} \\
\bar{\boldsymbol{q}} &= \begin{bmatrix} \bar{u}_4 & \bar{\theta}_1 & \bar{\theta}_4 \end{bmatrix}^{\mathrm{T}} \\
\bar{\boldsymbol{q}}_{sub} &= \begin{bmatrix} \bar{u}_2 & \bar{\theta}_2 & \bar{u}_3 & \bar{\theta}_3 \end{bmatrix}^{\mathrm{T}}
\end{aligned} \tag{7.43}$$

Le modèle des rotules généralisées en elasto-plastique suppose que la plasticité est concentrée aux ressorts axial et rotatif situés à l'extrémité de l'élément de poutre flexible. Le comportement élastique des rotules généralisés est découplé tandis que l'interaction axiale-moment est considérée dans le domaine plastique. Nous adoptons la décomposition de la vitesse de déformation généralisée totale par des parties d'élastique et de plastique qui contiennnet la vitesse de déformation axiale et rotative. Pour une règle de flux associée, la direction de la vitesse de déformation plastique est donnée par le gradient à la fonction de rendement, avec son amplitude donnée par le taux de multiplicateur plastique. Le vecteur de contrainte généralisé contenant la force normale et la flexion est représenté par $\boldsymbol{\Sigma} = [N \quad M]^{\mathrm{T}}$. Le multiplicateur plastique $\dot{\lambda}$ est déterminé par les conditions complémentaires classiques :

$$\dot{\lambda} \geq 0, \quad \Phi(N, M) \leq 0, \quad \dot{\lambda}\,\Phi(M, N) = 0 \tag{7.44}$$

La règles de flux de visco-plasticité pour les rotules généralisées est définit par :

$$\begin{aligned}
\dot{\lambda} &= D^* \left(\Phi\right)^{\zeta} \quad \text{if} \quad \Phi \geq 0 \\
&= 0 \qquad\qquad\ \ \text{if} \quad \Phi < 0
\end{aligned} \tag{7.45}$$

où D^* and ζ sont des constants de matériaux. La valeur D^* sera sélectionnée de manière appropriée en fonciton de l'étude de cas.

On considère une famille des surfaces convexes et symétriques de formes super-elliptique généralisée :

$$\Phi(M, N) = \left(\left| \frac{M}{M^p} \right|^{\alpha} + \left| \frac{N}{N^p} \right|^{\beta} \right)^{\frac{1}{p}} \tag{7.46}$$

où α, β et p sont des paramètres pour la surface de rendement.

Matrice de rigidité locale pour les rotules généralisées

En supposant que le comportement élastique est linéaire, les contraintes généralisées sont données comme suit :

$$\boldsymbol{\Sigma} = \mathbf{C}_e \left(\boldsymbol{\Xi} - \boldsymbol{\Xi}^p \right) \tag{7.47}$$

et la matrice de rigidité élastique est donnée par :

$$\mathbf{C}_e = \begin{bmatrix} k_{\bar{u}} & 0 \\ 0 & k_{\bar{\theta}} \end{bmatrix} \tag{7.48}$$

Dans le cas de (visco)-plasticité, l'incrément de la contrainte résultante pour la première rotule (expression similaire pour la seconde rotule) est défini par :

$$\begin{bmatrix} \Delta N_2 \\ \Delta M_2 \end{bmatrix} = \begin{bmatrix} C_{11} & C_{12} \\ C_{21} & C_{22} \end{bmatrix} \begin{bmatrix} \Delta \bar{u}_2 - \Delta \bar{u}_1 \\ \Delta \bar{\theta}_2 - \Delta \bar{\theta}_1 \end{bmatrix} \tag{7.49}$$

Les détails sur les équations discrètes des rotules plastiques généralisées sont décrits dans [132, 133].

Pour la condensation statique, la force interne locale $\boldsymbol{f}_l$ et la matrice de rigidité locale $\mathbf{k}_l$ sont données par :

$$\begin{aligned} \Delta \boldsymbol{f}_l &= \mathbf{k}_l \, \Delta \bar{\boldsymbol{q}} \\ \mathbf{k}_l &= \mathbf{k}_{hh} - \mathbf{k}_{bh}^{\mathrm{T}} \, \mathbf{k}_{bb}^{-1} \, \mathbf{k}_{bh} \end{aligned} \tag{7.50}$$

En élasticité, la matrice de rigidité locale $\mathbf{k}_l$ devrait être la matrice rigidité locale de Bernoulli :

$$\begin{bmatrix} EA/l_0 & 0 & 0 \\ 0 & 4\,EI/l_0 & 2\,EI/l_0 \\ 0 & 2\,EI/l_0 & 4\,EI/l_0 \end{bmatrix} \tag{7.51}$$

Les paramètres de rigidité du sous-élément de la poutre élastique sont définis par :

$$\begin{aligned} k_{\bar{u}} &= \varrho_n \, EA/l_0 \\ k_{\bar{\theta}} &= \varrho_m \, EI/l_0 \end{aligned} \tag{7.52}$$

$$\begin{aligned} k_{11} &= \varpi_1 \, EA/l_0 \\ k_{22} &= k_{33} = \varpi_2 \, EI/l_0 \\ k_{23} &= k_{32} = \varpi_3 \, EI/l_0 \end{aligned} \tag{7.53}$$

En introduisant les équations (7.52) et (7.53) dans la deuxième expression des équations (7.50), les relations suivantes sont obtenues :

$$\begin{aligned} \varpi_1 &= \left(1 - 2\,\varrho_n^{-1} \right)^{-1} \\ \varpi_2 &= \frac{4\,\varrho_m(\varrho_m - 3)}{\varrho_m^2 - 8\,\varrho_m + 12} \\ \varpi_3 &= \frac{2\,\varrho_m^2}{\varrho_m^2 - 8\,\varrho_m + 12} \end{aligned} \tag{7.54}$$

L'idée de cette procédure est donc de choisir les coefficients des rotules ϱ_n, ϱ_m . Puis, on calcule des coefficients $\varpi_1, \varpi_2, \varpi_3$ en utilisant l'équation (7.54).

Concernant des analyses d'impact, le modèle de contact est développé dans un cadre rigoureux de la dynamique non-lisse. Les équations des motions sont dérivées en utilisant un ensemble de mesures différentielles et outils d'analyse convexe. Les sauts de vitesse aux instants d'impact sont considérés en utilisant les lois d'impact par un coefficient de restitution ϵ pour tenir compte d'éventuelles pertes d'énergie lors des collisions. Les équations dynamiques sont résolues en utilisant le schéma d'intégration conservatif [40, 41].

Exemple

Trois portiques métalliques sont présentés à la figure 7.9. Un poteau de chaque structure est soumi à une masse m de la position A avec la vitesse initale v_0. Les paramètres de l'élément de la poutre sont : le module élastique $E = 210$ GPa, la limite élastique $\sigma_y = 355$ MPa et le coefficient de poisson $\nu = 0.3$. La fonction de rendement de rotules est $\Phi(M, N) = |M/M^p|^{1.05} + |N/N^p|^2 - 1$ pour la section carrée. Le pas de temps est $\Delta t = 10^{-5}$.

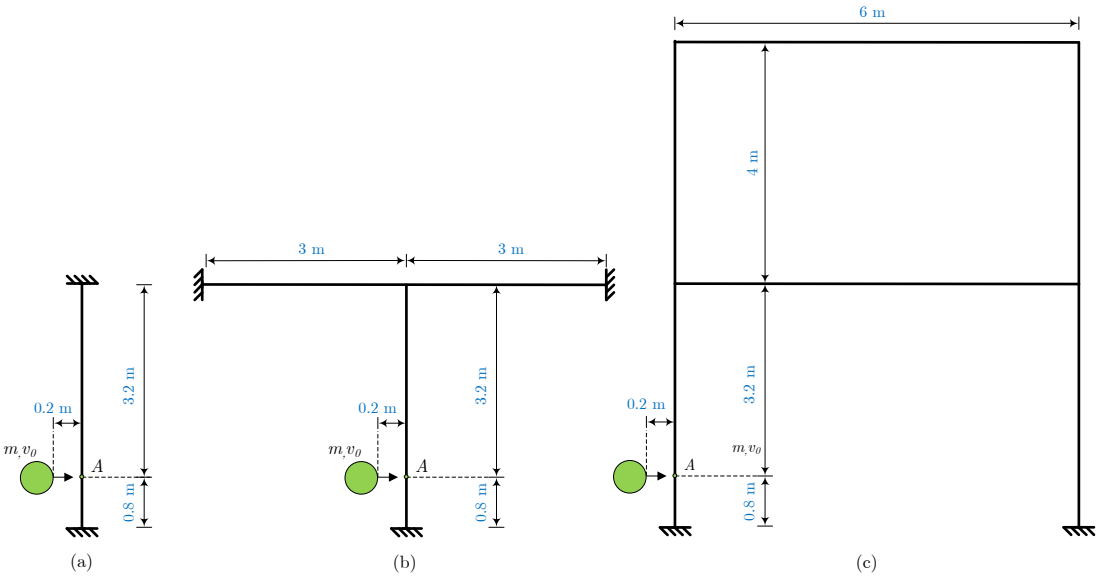

FIGURE 7.9: Géométrie avec l'impact

Concernant la discrétisation, le taille de chaque élément est de 0.1 m pour le modèle de fibre. Pour les rotules, un élément est pris pour chaque élément sauf deux éléments sont considérés pour le poteau sous l'impact. La figure 7.10 montre l'évolution des déplacements maximaux du poteau sous l'impact pour une vitesse initiale de 30 m/s (la structure c). Pour le cas plastique, le résultat obtenu par les rotules généralisées est en bon accord avec les deux modèles de fibre type Bernoulli et Timoshenko. En outre, la série de calcul sur le déplacement maximal du poteau sous l'impact est résumée dans le tableau 7.3. Les écarts entre les modèles de fibre Timoshenko et Bernoulli sont très faibles et ne dépassent pas de 3%. La différence maximale entre les rotules généralisées et les modèles de fibre avoisine 11%. Ce qui est acceptable compte tenu du fait que le modèle de rotule utilise peu nombre d'éléments.

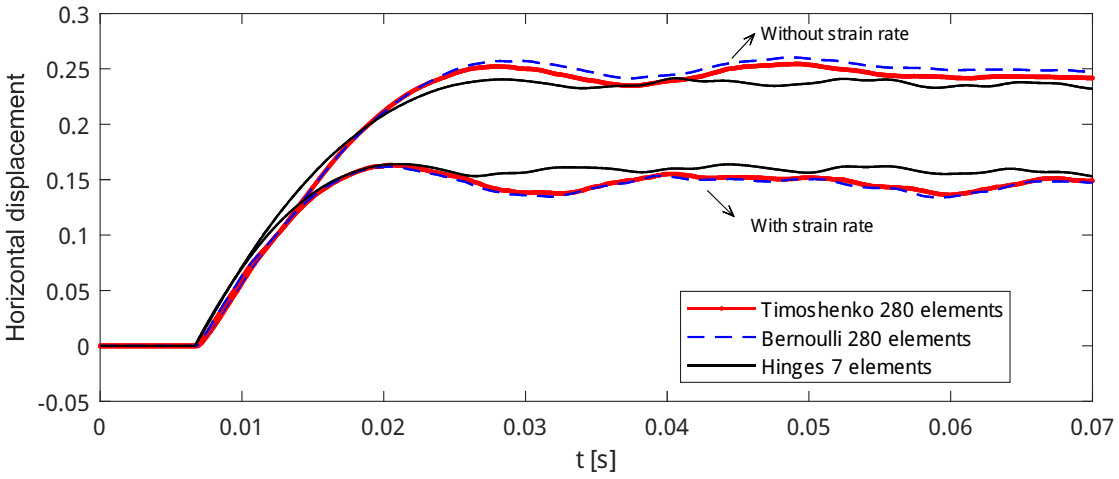

FIGURE 7.10: Évolution du déplacement maximal du poteau sous l'impact de la structure c avec $v_0 = 30$ m/s

TABLE 7.3: Modèle plastique : déplacement maximal du poteau sous l'impact : Mass de véhicule 1500 kg, section carrée 20 cm, $\epsilon = 0$

	Timoshenko	Bernoulli	Rotules
Structure a ($v_0 = 20$ m/s)	0.1085	0.1074	0.1030
Structure a ($v_0 = 30$ m/s)	0.1905	0.1909	0.1907
Structure a ($v_0 = 40$ m/s)	0.2718	0.2728	0.2739
Structure b ($v_0 = 20$ m/s)	0.1261	0.1232	0.1118
Structure b ($v_0 = 30$ m/s)	0.2454	0.2493	0.2351
Structure b ($v_0 = 40$ m/s)	0.3940	0.3994	0.3883
Structure c ($v_0 = 20$ m/s)	0.1200	0.1226	0.1125
Structure c ($v_0 = 30$ m/s)	0.2521	0.2579	0.2414
Structure c ($v_0 = 40$ m/s)	0.4136	0.4253	0.4086

Pour l'étude sur l'effet de déformation, $\zeta = 5$ et $D = 40.4$ s^{-1} sont employés pour le modèle de fibre tandis que $\zeta = 5$ et $D^* = 2.025 \times 10^8$ s^{-1} sont utilisé pour le modèle de rotules généralisées. Le tableau 7.4 montre le déplacement maximal du poteau sous l'impact. Les écarts entre les deux modèles de fibre ne sont que de 3% et cela indique que l'effet de cisaillement n'influence pas sur les déplacements globaux. Avec le choix de la valeur D^*, ce modèle peut reproduire les résultats corrects (voir l'évolution du déplacement à la figure 7.10). Sa différence maximale en comparant avec les modèles de fibre est 11%.

TABLE 7.4: Modèle visco-plastique : déplacement maximal du poteau sous l'impact : Mass de véhicule 1500 kg, section carré 20 cm, $\epsilon = 0$

	Timoshenko	Bernoulli	Rotules
Structure a ($v_0 = 20$ m/s)	0.0804	0.0780	0.0763
Structure a ($v_0 = 30$ m/s)	0.1402	0.1367	0.1469
Structure a ($v_0 = 40$ m/s)	0.2011	0.1982	0.2228
Structure b ($v_0 = 20$ m/s)	0.0854	0.0856	0.0799
Structure b ($v_0 = 30$ m/s)	0.1645	0.1625	0.1625
Structure b ($v_0 = 40$ m/s)	0.2659	0.2638	0.2685
Structure c ($v_0 = 20$ m/s)	0.0853	0.0840	0.0806
Structure c ($v_0 = 30$ m/s)	0.1644	0.1635	0.1641
Structure c ($v_0 = 40$ m/s)	0.2718	0.2714	0.2743

Une autre serie de calcul pour la masse de 3000 kg, la section carrée 25 cm et la valeur $\epsilon = 0.5$ est présentée dans le tableau 7.5. Avec la même valeur de $D^* = 2.025 \times 10^8$ s^{-1} , la différence du déplacement maximal entre le modèle de rotules généralisées et le modèle de fibre reste dans le même écart (10%).

TABLE 7.5: Modèle visco-plastique : déplacement maximal du poteau sous l'impact : Mass de véhicule 3000 kg, section carrée 25 cm, $\epsilon = 0.5$

	Timoshenko	Bernoulli	Rotules
Structure a ($v_0 = 20$ m/s)	0.0842	0.0819	0.0761
Structure a ($v_0 = 30$ m/s)	0.1525	0.1495	0.1524
Structure a ($v_0 = 40$ m/s)	0.2240	0.2196	0.2389
Structure b ($v_0 = 20$ m/s)	0.0876	0.0869	0.0787
Structure b ($v_0 = 30$ m/s)	0.1697	0.1700	0.1630
Structure b ($v_0 = 40$ m/s)	0.2743	0.2746	0.2714
Structure c ($v_0 = 20$ m/s)	0.0860	0.0854	0.0793
Structure c ($v_0 = 30$ m/s)	0.1685	0.1700	0.1641
Structure c ($v_0 = 40$ m/s)	0.2775	0.2803	0.2765

7.3 Poutre spatiale d'Euler-Bernoulli géométriquement exacte (Article IV)

Dans cet article, une théorie de poutre spatiale d'Euler-Bernoulli géométriquement exacte est développée. Le principal défi dans la construction d'une telle théorie réside dans le fait qu'il n'existe aucun moyen naturel de définir un trièdre orthonormé dans la configuration déformée. Une nouvelle méthodologie permettant de définir ce trièdre et par conséquent de développer une théorie de poutre spatiale en incorporant l'hypothèse d'Euler-Bernoulli est fournie. Cette approche utilise le processus d'orthogonalisation de Gram-Schmidt couplé avec un paramètre rotation qui complète la description cinématique et décrit la rotation associée à la torsion. Ce processus permet de surmonter le caractère non-unique de la procédure de Gram-Schmidt.

Dans ce chapitre, la cinématique de la poutre spatiale géométriquement exacte et ses déformations sont présentées. On présente le principe de travail virtuel pour dériver l'équation des motions. Ensuite, le schéma d'intégration conservatif est présenté et est appliqué à la nouvelle formulation ainsi qu'un exemple de grand déplacement.

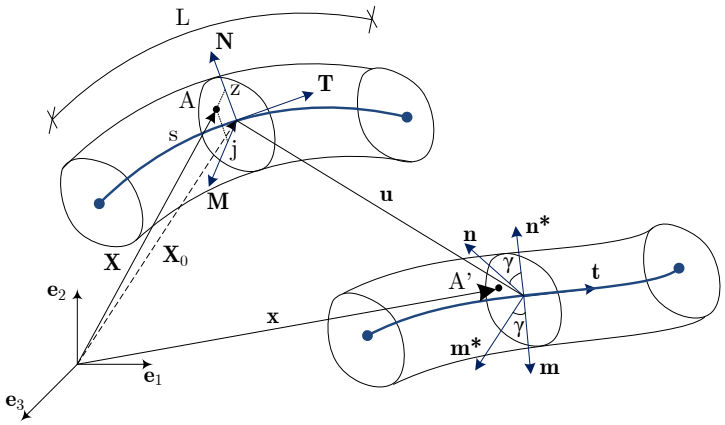

FIGURE 7.11: Cinématique de la poutre spatiale

7.3.1 Cinématique de la poutre

Soit $\mathcal{B} \subset \mathbb{R}^3$ oú $\mathcal{B}$ définit une configuration de référence d'un corps matériel. $\varphi(t) : \mathcal{B} \to \mathbb{R}^3$ est une incorporation dépendant d'un paramètre temporel $t \in \mathbb{R}$. Donc, $\varphi_0 = \varphi\,(t = t_0)$ définit une configuration de référence qui permet l'identification des points matériels. Alors, pour la position référentielle $\boldsymbol{X} \in \mathcal{B}$ et la position déformée $\boldsymbol{x} \in \mathcal{B}_t$, on a : $\boldsymbol{x}(t) = \varphi(\boldsymbol{X}, t)$ et $\boldsymbol{X}(t) = \varphi^{-1}(\boldsymbol{x}, t)$. Soit $\boldsymbol{e}_i$, $i = 1, 2, 3$ les vecteurs de base cartésiens. Dans la figure 7.11, tous les points centraux de la section transversale sont définis par une longueur de l'arc ($L \in \mathbb{R}$) au configuration de référence désignée par $s \in [0, L] \subset \mathbb{R}$. Par conséquent, un système de coordonnées curvilignes est décrit par le triple (s, z, j) pour tout point matériel de la section transversale.

Soit $\boldsymbol{X}_0$ la position de la ligne centre dans la configuration de référence et on a :

$$\boldsymbol{X}(s, z, j) = \boldsymbol{X}_0(s) + z\,\boldsymbol{N}(s) + j\,\boldsymbol{M}(s) \tag{7.55}$$

On définit le vecteur tangent d'unité $\boldsymbol{T} = \partial \boldsymbol{X}_0/\partial s|_{j=z=0}$. De même, on introduit les vecteurs : $\boldsymbol{T}_1 = \partial \boldsymbol{X}/\partial s$, $\boldsymbol{N} = \partial \boldsymbol{X}/\partial z$ et $\boldsymbol{M} = \partial \boldsymbol{X}/\partial j$. Ainsi, le triplet $(\boldsymbol{T}_1, \boldsymbol{N}, \boldsymbol{M})$ définit des bases locales curvilignes pour la configuration de référence. Les vecteurs correspondants à la base de contrevariantes sont ensuite donnés par $\left(\boldsymbol{T}^1, \boldsymbol{N}, \boldsymbol{M}\right)$ avec $\boldsymbol{T}^1 = \boldsymbol{T}_1/\left|\boldsymbol{T}_1\right|^2$ òu $|\bullet|$ dénote la norme d'un vecteur.

Les vecteurs tangents correspondants à la configuration déformée sont définis par $(\boldsymbol{g}, \boldsymbol{n}, \boldsymbol{m})$ avec $\boldsymbol{g} = \partial \boldsymbol{x}/\partial s$. $\boldsymbol{n}$ et $\boldsymbol{m}$ sont les vecteurs normaux de la section. À partir de la figure 7.11, la position $\boldsymbol{x}$ au point A' de la configuration déformée est définie par :

$$\boldsymbol{x}(s, z, j) = \boldsymbol{X}_0(s) + \boldsymbol{u}(s) + z\,\boldsymbol{n}(s) + j\,\boldsymbol{m}(s) \tag{7.56}$$

où $\boldsymbol{u}(s)$ est le vecteur de déplacement de la ligne centre. Le vecteur $\boldsymbol{g}$ est obtenu :

$$\boldsymbol{g} = \boldsymbol{x}_{,s} = \boldsymbol{X}_{0,s} + \boldsymbol{u}_{,s} + z\,\boldsymbol{n}_{,s} + j\,\boldsymbol{m}_{,s} \tag{7.57}$$

et le vecteur tangent unitaire $\boldsymbol{t}$ par

$$\boldsymbol{t} = \frac{\boldsymbol{X}_{0,s} + \boldsymbol{u}_{,s}}{|\boldsymbol{X}_{0,s} + \boldsymbol{u}_{,s}|} \tag{7.58}$$

où une virgule indique la dérivée.

Deux méthodes pour définir les vecteurs normaux de la section transversales dans la configuration déformée sont définies dans la section suivante :

Première methode

Par le processus de Gram-Schmidt, le vecteur $\boldsymbol{n}^*$ est construit par la base du vecteur tangent $\boldsymbol{t}$ et l'un des vecteurs normaux ($\boldsymbol{N}$ ou $\boldsymbol{M}$) dans la configuration de référence. Dans ce processus, l'orthogonalité de deux vecteurs ($\boldsymbol{n}^*$ et $\boldsymbol{t}$) est assuré. Par conséquent, le vecteur normal $\boldsymbol{n}^*$ est défini :

$$\boldsymbol{n}^* = \frac{\boldsymbol{N} - (\boldsymbol{N} \cdot \boldsymbol{t})\ \boldsymbol{t}}{|\boldsymbol{N} - (\boldsymbol{N} \cdot \boldsymbol{t})\ \boldsymbol{t}|} \quad Or \quad \boldsymbol{n}^* = \frac{\boldsymbol{M} - (\boldsymbol{M} \cdot \boldsymbol{t})\ \boldsymbol{t}}{|\boldsymbol{M} - (\boldsymbol{M} \cdot \boldsymbol{t})\ \boldsymbol{t}|} \tag{7.59}$$

où un point indique le produit scalaire de deux vecteurs.

Ce système de base est ensuite tourné vers le dernier déformé par un tenseur de rotation $\mathbf{R}_1$. Ce vecteur de la rotation est parallèle au vecteur tangent à la configuration déformée. Donc, cette rotation n'a qu'un seul paramètre γ. Ce paramètre définit un angle qui décrit le mouvement de torsion de la section transversale. Le tenseur de rotation $\mathbf{R}_1$ [124, 125] est défini par :

$$\mathbf{R}_1 = \mathbf{I} + \sin\gamma\, \underline{\boldsymbol{\Gamma}}_t + (1 - \cos\gamma)\, \underline{\boldsymbol{\Gamma}}_t\, \underline{\boldsymbol{\Gamma}}_t \tag{7.60}$$

où $\underline{\boldsymbol{\Gamma}}_t$ désigne la matrice asymétrique du vecteur $\boldsymbol{t}$:

$$\underline{\boldsymbol{\Gamma}}_t = \begin{bmatrix} 0 & -t(3) & t(2) \\ t(3) & 0 & -t(1) \\ -t(2) & t(1) & 0 \end{bmatrix} \tag{7.61}$$

Alors, le vecteur $\boldsymbol{n}$ dans la configuration déformée est obtenu :

$$\boldsymbol{n} = \mathbf{R}_1\, \boldsymbol{n}^* \tag{7.62}$$

Puisque l'hypothèse de la théorie Euler-Bernoulli est utilisée, le vecteur $\boldsymbol{m}$ reste normal avec les autres vecteurs ($\boldsymbol{n}$, $\boldsymbol{t}$) après la déformation et est donc défini par $\boldsymbol{m} = \boldsymbol{t} \times \boldsymbol{n}$ òu $\times$ désigne le produit croisé de deux vecteurs.

Deuxième methode

Dans une second approche, le tenseur de rotation est défini par la base des premières et secondes dérivées du vecteur de déplacement de la ligne centre associé avec un paramètre de rotation γ. La matrice de rotation totale est obtenue par une multiplication de deux matrices de rotation :

$$\mathbf{R} = \mathbf{R}_1\, (\gamma\, \boldsymbol{t})\, \mathbf{R}_2\, (\boldsymbol{w}) \tag{7.63}$$

où le tenseur de rotation $\mathbf{R}_1$ est defini dans la première méthode. $\boldsymbol{w}$ est le vecteur de rotation de $\mathbf{R}_2$ qui calcule à partir de l'expression suivante :

$$\boldsymbol{T} \cdot \boldsymbol{t} = |\boldsymbol{T}||\boldsymbol{t}| \cos\alpha = \cos\alpha \tag{7.64}$$

$$\boldsymbol{T} \times \boldsymbol{t} = |\boldsymbol{T}||\boldsymbol{t}| \sin\alpha \frac{\boldsymbol{w}}{|\boldsymbol{w}|} = \frac{\sin\alpha}{\alpha} \boldsymbol{w} \tag{7.65}$$

avec α étant l'angle de deux vecteurs $\boldsymbol{T}$ and $\boldsymbol{t}$. On a :

$$\boldsymbol{w} = \frac{\alpha}{\sin\alpha}\,(\boldsymbol{T} \times \boldsymbol{t}) \tag{7.66}$$

Le tenseur de rotation $\mathbf{R}_2$ est défini par :

$$\begin{aligned}\mathbf{R}_2 &= \mathbf{I} + \frac{\sin\alpha}{\alpha}\,\underline{\boldsymbol{\Gamma}}_w + \frac{1-\cos\alpha}{\alpha^2}\,\underline{\boldsymbol{\Gamma}}_w\,\underline{\boldsymbol{\Gamma}}_w \\ &= \mathbf{I} + \underline{\boldsymbol{\Gamma}}_v + \frac{1}{1+\boldsymbol{T}\cdot\boldsymbol{t}}\,\underline{\boldsymbol{\Gamma}}_v\,\underline{\boldsymbol{\Gamma}}_v\end{aligned} \tag{7.67}$$

où $\underline{\boldsymbol{\Gamma}}_w$ designe la matrice asymétrique du vecteur $\boldsymbol{w}$ et $\underline{\boldsymbol{\Gamma}}_v$ la matrice asymétrique du vecteur $\boldsymbol{v} = \boldsymbol{T} \times \boldsymbol{t}$.

Enfin, les vecteur normaux dans la configuration déformée sont définis par :

$$\boldsymbol{n} = \mathbf{R}\,\boldsymbol{N} \tag{7.68}$$

$$\boldsymbol{m} = \mathbf{R}\,\boldsymbol{M} \tag{7.69}$$

7.3.2 Déformations

Le gradient de déformation est défini par le système de bases curvilignes : $\mathbf{F} = \boldsymbol{g} \otimes \boldsymbol{T}^1 + \boldsymbol{n} \otimes \boldsymbol{N} + \boldsymbol{m} \otimes \boldsymbol{M}$. Le tenseur de déformation droite de Cauchy est défini comme $\mathbf{F}^{\mathrm{T}}\mathbf{F}$, ce qui donne sous la forme matricielle :

$$\mathbf{C} = \begin{bmatrix} \boldsymbol{g}\cdot\boldsymbol{g} & \boldsymbol{g}\cdot\boldsymbol{n} & \boldsymbol{g}\cdot\boldsymbol{m} \\ \boldsymbol{g}\cdot\boldsymbol{n} & 1 & 0 \\ \boldsymbol{g}\cdot\boldsymbol{m} & 0 & 1 \end{bmatrix} \tag{7.70}$$

Ensuite, on peut calculer le tenseur de déformation de Green par $\mathbf{E} = \frac{1}{2}\,(\mathbf{C} - \mathbf{I})$. Les composants non-triviaux du tenseur de Green s'écrivent :

$$E_{11} = \varepsilon_{11} + z\,\kappa_1 + j\,\kappa_2 \tag{7.71}$$

$$E_{12} = \frac{1}{2}\,j\,\kappa_{12} \tag{7.72}$$

$$E_{13} = \frac{1}{2}\,z\,\kappa_{13} \tag{7.73}$$

avec ε_{11} étant la déformation axiale, κ_1, κ_2 les courbures de la direction z et j, respectivement, κ_{12} et κ_{13} sont des torsions de la section transversale. Les déformations sont obtenues :

$$\varepsilon_{11} \approx \boldsymbol{X}_{0,s}\cdot\boldsymbol{u}_{,s} + \frac{1}{2}\boldsymbol{u}_{,s}\cdot\boldsymbol{u}_{,s} \tag{7.74}$$

$$\kappa_1 = (\boldsymbol{X}_{0,s} + \boldsymbol{u}_{,s})\cdot\boldsymbol{n}_{,s} - \boldsymbol{X}_{0,s}\cdot\boldsymbol{N}_{,s} \tag{7.75}$$

$$\kappa_2 = (\boldsymbol{X}_{0,s} + \boldsymbol{u}_{,s})\cdot\boldsymbol{m}_{,s} - \boldsymbol{X}_{0,s}\cdot\boldsymbol{M}_{,s} \tag{7.76}$$

$$\kappa_{12} = \boldsymbol{n}\cdot\boldsymbol{m}_{,s} - \boldsymbol{N}\cdot\boldsymbol{M}_{,s} \tag{7.77}$$

$$\kappa_{13} = \boldsymbol{n}_{,s}\cdot\boldsymbol{m} - \boldsymbol{N}_{,s}\cdot\boldsymbol{M} \tag{7.78}$$

La déformation axiale est simplifiée en négligeant des termes de second-ordre z^2 et j^2 puisque l'épaisseur de la poutre est faible par rapport à sa longueur. En plus, $\kappa_{12} = -\kappa_{13}$ sont égales en magnitude car la condition de normalité $(\boldsymbol{m}\cdot\boldsymbol{n} - \boldsymbol{M}\cdot\boldsymbol{N})_{,s} = 0$ est satisfaisante.

7.3.4 Principe du travail virtuel

Le principe du travail virtuel en dynamique est donné par :

$$\int_{t_1}^{t_2} \left(\int_V \rho\, \ddot{\boldsymbol{x}} \cdot \delta \boldsymbol{x}\, \mathrm{d}V + \int_V E\, E_{11}\, \delta E_{11}\, \mathrm{d}V + \int_V \frac{2E}{1+\nu}\, E_{12}\, \delta E_{12}\, \mathrm{d}V \right.$$
$$\left. + \int_V \frac{2E}{1+\nu}\, E_{13}\, \delta E_{13}\, \mathrm{d}V - \int_L \boldsymbol{p}(s) \cdot \delta \boldsymbol{u}\ \mathrm{d}s - \sum_{i=1}^{N} \boldsymbol{P}_i \cdot \delta \boldsymbol{u}_i \right) \mathrm{d}t = 0 \tag{7.79}$$

L'équation (7.79) réduit à

$$\int_{t_1}^{t_2} \left(\int_L \rho A\, \ddot{\boldsymbol{u}} \cdot \delta \boldsymbol{u}\, \mathrm{d}s + \int_L \rho I_z\, \ddot{\boldsymbol{n}} \cdot \delta \boldsymbol{n}\, \mathrm{d}s + \int_L \rho I_j\, \ddot{\boldsymbol{m}} \cdot \delta \boldsymbol{m}\, \mathrm{d}s \right.$$
$$+ \int_L EA\ \varepsilon_{11}\, \delta \varepsilon_{11}\, \mathrm{d}s + \int_L EI_z\, \kappa_1\, \delta \kappa_1\, \mathrm{d}s + \int_L EI_j\, \kappa_2\, \delta \kappa_2\, \mathrm{d}s$$
$$+ \int_L GI_j\, \kappa_{12}\, \delta \kappa_{12}\, \mathrm{d}s + \int_L GI_z\, \kappa_{13}\, \delta \kappa_{13}\, \mathrm{d}s$$
$$\left. - \int_L \boldsymbol{p}(s) \cdot \delta \boldsymbol{u}\ \mathrm{d}s - \sum_{i=1}^{N} \boldsymbol{P}_i \cdot \delta \boldsymbol{u}_i \right) \mathrm{d}t = 0 \tag{7.80}$$

où V est le volume et L la longueur de de la poutre, ρ le densité du matériau, A l'aire de la seciton transversale, I_z et I_j les moments d'inertie. E est le module élastique du matériau et G le module de cisaillement et le coefficient de Poisson ν. $\boldsymbol{P}_i$, $i = 1, 2, ..., N$ sont la force concentrée et $\boldsymbol{p}$ est la force externe distribuée.

Comme $\kappa_{12} = -\kappa_{13}$, les termes liés à la torsion peuvent être combinés en seul terme :

$$\int_L GI_j\, \kappa_{12}\, \delta \kappa_{12}\, \mathrm{d}s + \int_L GI_z\, \kappa_{13}\, \delta \kappa_{13}\, \mathrm{d}s = \int_L G\left(I_j + I_z\right)\, \kappa_{12}\, \delta \kappa_{12}\, \mathrm{d}s = \int_L GJ\, \kappa_{12}\, \delta \kappa_{12}\, \mathrm{d}s \tag{7.81}$$

En fait, la constante de torsion J égale à $I_j + I_z$ n'est que valable pour la section circulaire. Cependant, pour toute section transversale arbitraire, la constante de torsion réelle J est adoptée au lieu des termes $I_j + I_z$.

Alors, l'equation (7.82) s'écrit :

$$\int_{t_1}^{t_2} \left(\int_L \rho A\, \ddot{\boldsymbol{u}} \cdot \delta \boldsymbol{u}\, \mathrm{d}s + \int_L \rho I_z\, \ddot{\boldsymbol{n}} \cdot \delta \boldsymbol{n}\, \mathrm{d}s + \int_L \rho I_j\, \ddot{\boldsymbol{m}} \cdot \delta \boldsymbol{m}\, \mathrm{d}s \right.$$
$$+ \int_L EA\ \varepsilon_{11}\, \delta \varepsilon_{11}\, \mathrm{d}s + \int_L EI_z\, \kappa_1\, \delta \kappa_1\, \mathrm{d}s + \int_L EI_j\, \kappa_2\, \delta \kappa_2\, \mathrm{d}s$$
$$\left. + \int_L GJ\, \kappa_{12}\, \delta \kappa_{12}\, \mathrm{d}s - \int_L \boldsymbol{p}(s) \cdot \delta \boldsymbol{u}\ \mathrm{d}s - \sum_{i=1}^{N} \boldsymbol{P}_i \cdot \delta \boldsymbol{u}_i \right) \mathrm{d}t = 0 \tag{7.82}$$

7.3.5 Schéma d'intégration conservatif

La méthodologie générale pour la construction systématique de schéma d'intégration conservatif a été développée par Sansour [38, 39] et est appliquée avec succès aux différentes formulations de la coque et de la poutre. L'idée principale est que les non-linéarités géométriques et matérielles sont traités différemment. Les complexités de non-linéarités géométriques sont résolues en calculant la vitesse de déformation, par intégration, les expressions pour la mesures de déformation elles-mêmes. La même technique est appliquée aux termes d'inerties.

L'équation de motion est obtenue par l'application de l'équation (7.24) à l'équation (7.82) :

$$
\begin{aligned}
&\int_L \rho A \left(\frac{\partial \boldsymbol{u}}{\partial \boldsymbol{q}}\right)^{\mathrm{T}} \ddot{\boldsymbol{u}}_{n+\frac{1}{2}}\,\mathrm{d}s + \int_L \rho I_z \left(\frac{\partial \boldsymbol{n}}{\partial \boldsymbol{q}}\right)^{\mathrm{T}} \ddot{\boldsymbol{n}}_{n+\frac{1}{2}}\,\mathrm{d}s + \int_L \rho I_j \left(\frac{\partial \boldsymbol{m}}{\partial \boldsymbol{q}}\right)^{\mathrm{T}} \ddot{\boldsymbol{m}}_{n+\frac{1}{2}}\,\mathrm{d}s \\
&+ \int_L EA\, \varepsilon_{11\,n+\frac{1}{2}} \left(\frac{\partial \varepsilon_{11}}{\partial \boldsymbol{q}}\right)^{\mathrm{T}} \mathrm{d}s + \int_L EI_z\, \kappa_{1\,n+\frac{1}{2}} \left(\frac{\partial \kappa_1}{\partial \boldsymbol{q}}\right)^{\mathrm{T}} \mathrm{d}s \\
&+ \int_L EI_j\, \kappa_{2\,n+\frac{1}{2}} \left(\frac{\partial \kappa_2}{\partial \boldsymbol{q}}\right)^{\mathrm{T}} \mathrm{d}s + \int_L GJ\, \kappa_{12\,n+\frac{1}{2}} \left(\frac{\partial \kappa_{12}}{\partial \boldsymbol{q}}\right)^{\mathrm{T}} \mathrm{d}s \\
&- \int_L \left(\frac{\partial \boldsymbol{u}}{\partial \boldsymbol{q}}\right)^{\mathrm{T}} \boldsymbol{p}_{n+\frac{1}{2}}(s)\,\mathrm{d}s - \left(\frac{\partial \boldsymbol{u}}{\partial \boldsymbol{q}}\right)^{\mathrm{T}} \cdot \sum_{i=1}^{N} \boldsymbol{P}_{i\,n+\frac{1}{2}} = \boldsymbol{0}
\end{aligned}
\tag{7.83}
$$

L'idée principale est d'utiliser des champs de vitesses cinématiques et des champs de vitesses de déformations pour définir les champs cinématiques et des champs de déformations au lieu du calcul directement à partir des déplacement nodaux, des vitesses nodales et des accélérations nodales. Les champs de vitesses cinématiques et les champs des vitesses de déformations sont définis par :

$$
\begin{aligned}
\dot{\boldsymbol{n}}_{n+\frac{1}{2}} &= \frac{\partial \boldsymbol{n}}{\partial \boldsymbol{u}_{,s}}\, \dot{\boldsymbol{u}}_{,s\,n+\frac{1}{2}} + \frac{\partial \boldsymbol{n}}{\partial \gamma}\, \dot{\gamma}_{n+\frac{1}{2}} \\
\dot{\boldsymbol{m}}_{n+\frac{1}{2}} &= \frac{\partial \boldsymbol{m}}{\partial \boldsymbol{u}_{,s}}\, \dot{\boldsymbol{u}}_{,s\,n+\frac{1}{2}} + \frac{\partial \boldsymbol{m}}{\partial \gamma}\, \dot{\gamma}_{n+\frac{1}{2}} \\
\dot{\varepsilon}_{11\,n+\frac{1}{2}} &= \left(\boldsymbol{X}_{0,s} + \boldsymbol{u}_{,s\,n+\frac{1}{2}}\right) \cdot \dot{\boldsymbol{u}}_{,s\,n+\frac{1}{2}} \\
\dot{\kappa}_{1\,n+\frac{1}{2}} &= \dot{\boldsymbol{u}}_{,s\,n+\frac{1}{2}} \cdot \boldsymbol{n}_{,s\,n+\frac{1}{2}} + \left(\boldsymbol{X}_{0,s} + \boldsymbol{u}_{,s\,n+\frac{1}{2}}\right) \cdot \dot{\boldsymbol{n}}_{,s\,n+\frac{1}{2}} \\
\dot{\kappa}_{2\,n+\frac{1}{2}} &= \dot{\boldsymbol{u}}_{,s\,n+\frac{1}{2}} \cdot \boldsymbol{m}_{,s\,n+\frac{1}{2}} + \left(\boldsymbol{X}_{0,s} + \boldsymbol{u}_{,s\,n+\frac{1}{2}}\right) \dot{\boldsymbol{m}}_{,s\,n+\frac{1}{2}} \\
\dot{\kappa}_{12\,n+\frac{1}{2}} &= \dot{\boldsymbol{n}}_{n+\frac{1}{2}} \cdot \boldsymbol{m}_{,s\,n+\frac{1}{2}} + \boldsymbol{n}_{n+\frac{1}{2}} \cdot \dot{\boldsymbol{m}}_{,s\,n+\frac{1}{2}}
\end{aligned}
\tag{7.84}
$$

Alors, les champs de cinématiques et les champs des de déformations sont définis à pas $n+\frac{1}{2}$ par :

$$
\begin{aligned}
\ddot{\boldsymbol{n}}_{n+\frac{1}{2}} &= \frac{2}{\Delta t}\dot{\boldsymbol{n}}_{n+\frac{1}{2}} - \frac{2}{\Delta t}\dot{\boldsymbol{n}}_n \\
\ddot{\boldsymbol{m}}_{n+\frac{1}{2}} &= \frac{2}{\Delta t}\dot{\boldsymbol{m}}_{n+\frac{1}{2}} - \frac{2}{\Delta t}\dot{\boldsymbol{m}}_n \\
\varepsilon_{11\,n+\frac{1}{2}} &= \varepsilon_{11\,n} + \frac{1}{2}\Delta t\, \dot{\varepsilon}_{11\,n+\frac{1}{2}} \\
\kappa_{1\,n+\frac{1}{2}} &= \kappa_{1\,n} + \frac{1}{2}\Delta t\, \dot{\kappa}_{1\,n+\frac{1}{2}} \\
\kappa_{2\,n+\frac{1}{2}} &= \kappa_{2\,n} + \frac{1}{2}\Delta t\, \dot{\kappa}_{2\,n+\frac{1}{2}} \\
\kappa_{12\,n+\frac{1}{2}} &= \kappa_{12\,n} + \frac{1}{2}\Delta t\, \dot{\kappa}_{12\,n+\frac{1}{2}}
\end{aligned}
\tag{7.85}
$$

En faisant cette procédure, la conservation de l'énergie et de la quantité de mouvement ont été prouvées théoriquement et sont présentées dans l'article IV.

Exemple

Le portique de Roorda-Koiter [26] est présenté ici. Une seule différence est que la continuité de ce portique a été retenue par le petit rayon R égal à 0,25 m, voir la figure 7.12(a). Le portique a une section rectangulaire uniforme et est soumi à deux forces hors du plan. La forme de deux forces appliquées est présentée à la figure 7.12(b). La longueur L est de 12 m, la largeur de 0,3 m et la hauteur de 0.2 m. Le module élastique E du portique est 210 GPa et le coefficient de Poisson 0.3. La masse volumique est de 7850 kg/m^3. La pas de temps est $\Delta t = 10^{-4}$ s.

La discretization de l'élément de la poutre est : 22 éléments (11 éléments pour la poutre et 11 éléments pour le poteau) pour le référence et 10 éléments (4 éléments à poutre droite et 1 courbe) pour la formulation proposée. Les figures 7.13(a), 7.13(b) et 7.14(a) présentent des déplacements en point A. On observe qu'avec seuelement 10 éléments, la nouvelle formulation produit de bon résultat en comparant avec la solution de référence. Sur la figure 7.14(b), l'énergie est conservée pour un million de pas, ce qui montre la stabilité de l'algorithme.

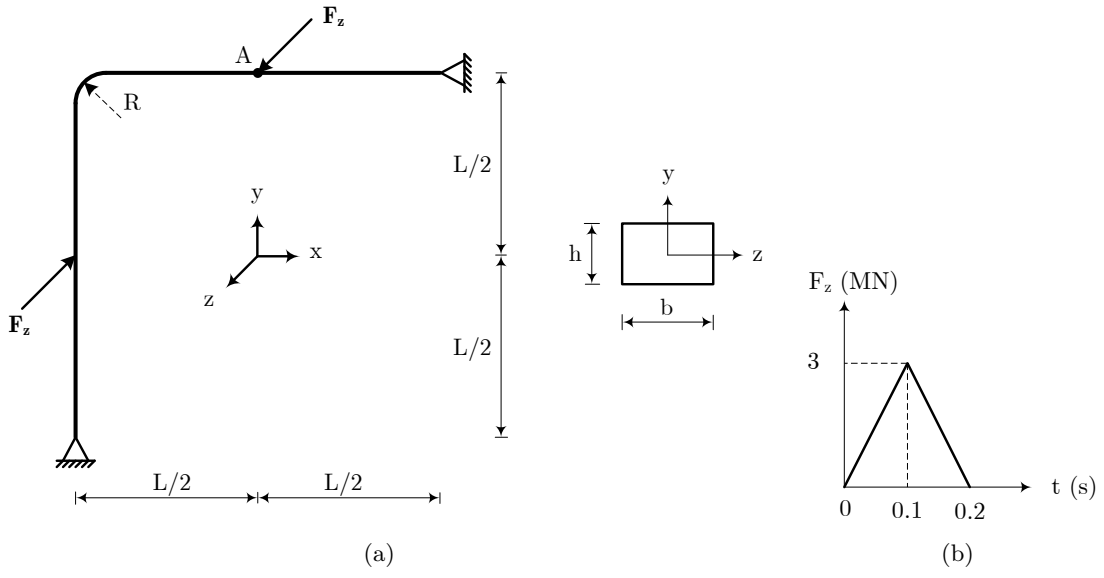

FIGURE 7.12: (a). Géométrie, (b). Histoire de la charge.

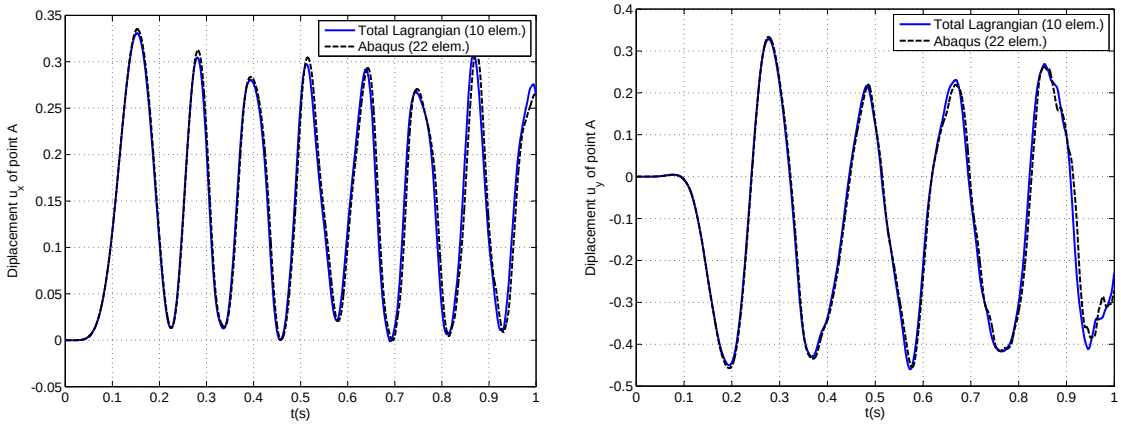

(a) (b)

FIGURE 7.13: (a). Déplacement u_x du point A, (b). Déplacement u_y du point A.

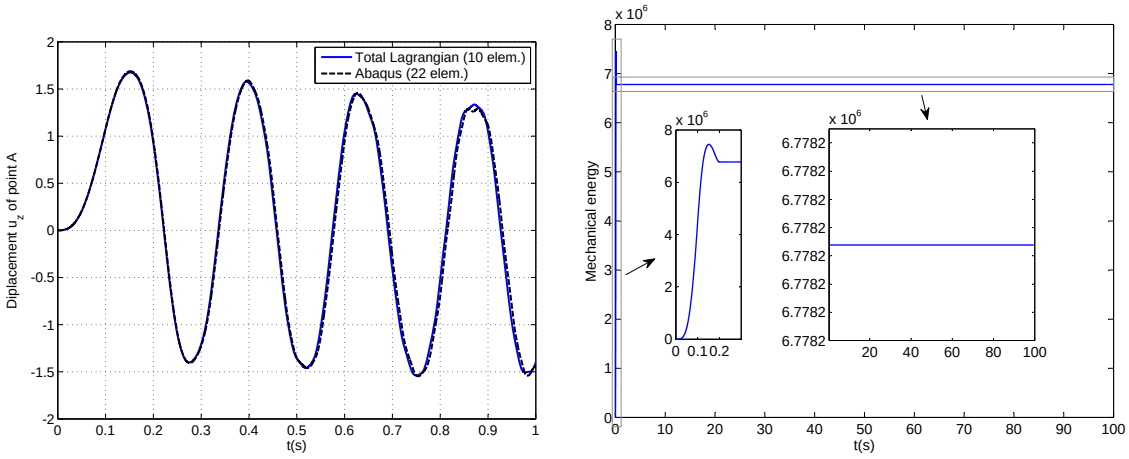

(a) (b)

FIGURE 7.14: (a). Déplacement u_z du point A, (b). Evolution de l'énergie.

7.4 Conclusion et perspective

7.4.1 Conclusion

Le plupart des efforts sont consacrés principalement au développement du schéma intégration conservatif qui conserve l'énergie totale, la quantité de mouvement et le moment cinétique pour la poutre planaire co-rotationnelle. Ces modèles sont développés avec divers buts et sont présentés dans les articles I, II et III. L'article IV est consacré au développement du schéma d'intégration conservatif de la nouvelle formulation de la poutre spatiale Euler-Bernoulli géométriquement exacte dans l'approche totale lagrangienne.

Poutre co-rotationnelle Bernoulli plane

Le schéma d'intégration conservatif pour la poutre planaire co-rotationnelle de type Bernoulli est développé. L'idée centrale de l'algorithme consiste à définir, par intégration, le champ des déformations en fin de pas à partir du champ de vitesses de déformations et non à partir du champ des déplacements au travers de la relation déplacement-déformation.

La même technique est appliquée aux termes d'inertie. L'avantage de cet algorithme est la conservation de l'énergie totale, de la quantité de mouvement et du moment cinétique. Ces caractéristiques ont été prouvées théoriquement et confirmées numériquement en utilisant quatre exemples numériques.

Poutre co-rotationnelle Timoshenko plane

Trois formulations de la poutre planaire co-rotationnelle Timosheko ont été présentées et testées en utilisant le schéma d'intégration conservatif. Les formulations proposées diffèrent dans le choix de la définition de la déformation locale et des interpolations locales. Si les déformations et les fonctions de forme linéaire locales sont prises, les résultats numériques montrent qu'il est plus efficace d'utiliser une approche mixte au lieu d'une méthode d'intégration réduite : le temps de calcul (CPU) est inchangé mais la même précision est obtenue avec peu nombre d'éléments. Les résultats numériques ont aussi montrés qu'il peut être intéressant d'utiliser une approche de déformation locale non-linéaire avec les interpolations cubiques. Tandis que le temps de calcul est augmenté car les termes dynamiques sont compliqués, mais la même précision est obtenue avec peu élément utilisé. Pour cette approche, une matrice tangente dynamique simplifiée devrait être prise et que le choix d'un prédicteur efficace peut être important.

Poutre co-rotationnelle plane en elasto-(visco)-plastique de l'élément fibre et des rotules généralisées élasto-(visco)-plastique

Une poutre co-rotationnelle plane avec rotules généralisées élasto-(visco)-plastiques aux extrémités est développée et comparée aux modèles fibres pour des problèmes d'impact. L'idée principale de rotules généralisées est de combiner un élément poutre élastique avec des rotules généralisées à ses extrémités. Pour incorporer l'élément obtenu dans le contexte de co-rotationnel, on effectue une condensation statique afin de supprimer les degrés de liberté supplémentaires. En outre, les équations de motion sont résolues en utilisant un schéma d'intégration conservatif qui conserve l'énergie totale en cas élastique.

Des résultats numériques montrent que les modèles de fibre sont très efficaces à prédire les déplacements de la structure et sont utilisées comme la solution de référence en prenant beaucoup d'éléments. En plus, les effets de la déformation par cisaillement pour les modèles de fibre n'influencent pas les résultats globales de déplacements. Par ailleurs, le modèle de l'élément poutre avec rotules généralisées en utilisant peu nombre d'éléments est capable de reproduire un bon résultat de déplacement maximal en comparant avec les modèles fibres de types Bernoulli et Timshenko. Enfin, les effets de la vitesse de déformation influencent sensiblement la réponse de la structure.

Poutre spatiale d'Euler-Bernoulli géométriquement exacte

Le schéma d'intégration conservatif pour la poutre spatiale géométriquement exacte a été développé. Le principal défi dans la construction d'une telle théorie réside dans le fait qu'il n'existe aucun moyen naturel de définir un trièdre orthonormé dans la configuration déformée. Une nouvelle méthodologie permettant de définir ce trièdre et par conséquent de développer une théorie de poutre spatiale en incorporant l'hypothèse d'Euler-Bernoulli est fournie. Cette approche utilise le processus d'orthogonalisation de Gram-Schmidt couplé avec un paramètre rotation qui complète la description cinématique et décrit la rotation associée à la torsion. Ce processus permet de surmonter le caractère non-unique

de la procédure de Gram-Schmidt. La formulation est étendue au cas dynamique et un schéma intégration temporelle conservant l'énergie est également développé. Cet algorithme proposé peut conserver l'énergie totale du système, la quantité de mouvement et le moment cinétique.

7.4.2 Perspective

Les modèles développés dans cette thèse se concentrent sur le schéma d'intégration conservatif pour les éléments poutres non-linéaires. Cependant, il y a autres modèles à développer et à perfectionner. Les recherches à l'avenir sont suggérées comme suit :

Schéma d'intégration conservatif avec la dissipation numérique

Les travaux précédents comme Kuhl et Ramm [75], Romero et Amero [76], Ibrahimbegović et Mamouri [77], Mamouri [78], Gams [79] ont été soulignés qu'il est très important d'avoir une dissipation numérique contrôlable dans le schéma d'intégration conservatif afin d'amortir des hautes fréquences, en particulier pour les problèmes raides. Comme discuté dans les articles [77, 79], même si l'énergie est préservée dans le sens global et est stable sans conditions, les forces internes au niveau de l'élément peuvent exposer de hautes fréquences parasites. Dans ce contexte, le problème numérique qui vient du schéma d'intégration conservatif ou du maillage raffiné peut être disparaitre par la dissipation numérique.

Schéma d'intégration conservatif de la poutre spatiale co-rotationnelle

L'extension du schéma d'intégration conservatif de la poutre co-rotationnelle plane à spatiale est très difficile et sera le but de travail de recherche à l'avenir. La principale difficulté est liée aux grandes rotations spatiales et comment ces rotations influencent les vitesses de déformation. L'objectivité de la déformation [56] devrait être considérée parce que Romero et Armero [57] ont montré que ça pourrait améliorer la précision et la stabilité du schéma d'intégration temporelle.

Bibliography

[1] M. Geradin, A. Cardona, Kinematics and dynamics of rigid and flexible mechanisms using finite elements and quaternion algebra, Computational Mechanics 4 (1989) 115–135.

[2] K.-J. Bathe, E. Ramm, E.L. Wilson, Finite element formulations for large deformation dynamic analysis, International Journal for Numerical Methods in Engineering 9 (1975) 353–386.

[3] M.R.M. Crespo Da Silva, Non-linear flexural-flexural-torsional-extensional dynamics of beams–I. Formulation, International Journal of Solids and Structures 24 (1988) 1225–1234.

[4] M. Iura, S.N. Atluri, Dynamic analysis of finitely stretched and rotated three-dimensional space-curved beams, Computers and Structures 29 (1988) 875–889.

[5] R. Rosen, K.G. Loewy, M.B. Mathew, Non-linear dynamics of slender rods, AIAA Journal 25 (1987) 611–619.

[6] J.O. Song, E.J. Haug, Dynamic analysis of planar flexible mechanisms, Computer Methods in Applied Mechanics and Engineering 24 (1980) 359–381.

[7] J.C. Simo, L. Vu-Quoc, On the dynamics of flexible beams under large overall motions–The plane case: Part I, Journal of Applied Mechanics 53 (1986) 849–854.

[8] J.C. Simo, L. Vu-Quoc, On the dynamics of flexible beams under large overall motions–The plane case: Part II, Journal of Applied Mechanics 53 (1986) 855–863.

[9] M.A. Crisfield, J. Shi, A co-rotational element/time-integration strategy for non-linear dynamics, International Journal for Numerical Methods in Engineering 37 (1994) 1897–1913.

[10] M.A. Crisfield, J. Shi, An energy conserving co-rotational procedure for non-linear dynamcis with finite elements, Nonlinear Dynamics 9 (1996) 37–52.

[11] U. Galvanetto, M.A. Crisfield, An energy-conserving co-rotational procedure for the dynamics of planar beam structures, International Journal for Numerical Methods in Engineering 39 (1996) 2265–2282.

[12] T.-N. Le, J.-M. Battini, M. Hjiaj, Efficient formulation for dynamics of corotational 2D beams, Computational Mechanics 48 (2011) 153–161.

[13] K.M. Hsiao, J. Jang, Dynamic analysis of planar flexible mechanisms by co-rotational formulation, Computer Methods in Applied Mechanics and Engineering 87 (1991) 1–14 .

[14] K.M. Hsiao, R.T. Yang, A co-rotational formulation for nonlinear dynamic analysis of curved Euler beam, Computers and Structures 54 (1995) 1091–1097.

[15] K. Behdinan, M.C. Stylianou, B. Tabarrok, Co-rotational dynamic analysis of flexible beams, Computer Methods in Applied Mechanics and Engineering 154 (1998) 151–161.

[16] H.A. Elkaranshawy, M.A. Dokainish, Corotational finite element analysis of planar flexible multibody systems, Computers and Structures 54 (1995) 881–890.

[17] M.A. Crisfield, U. Galvanetto, G. Jelenić, Dynamics of 3-D co-rotational beams, Computational Mechanics 20 (1997) 507–519.

[18] J. Salomon, A.A. Weiss, B.I. Wohlmuth, Energy-conserving algorithms for a corotational formulation, SIAM Journal on Numerical Analysis 46 (2008) 1842–1866.

[19] K.M. Hsiao, J.Y. Lin, W.Y. Lin, A consisten co-rotational finite element formulation for geometrically nonlinear dynamic analysis of 3-D beams, Computer Methods in Applied Mechanics and Engineering 169 (1999) 1–18. 3D dynamic corotational

[20] H.G. Zhong, M.A. Crisfield, An energy-conserving co-rotational procedure for the dynamics of shell structures, Engineering Computations 15 (1998) 552–576.

[21] N.M. Newmark, A Method of Computation for Structural Dynamics, Journal for American Society of Civil Engineers 1(1959) 67–94.

[22] J.C. Simo, N. Tarnow, The Discrete Energy-Momentum method. Conserving Algorithms for Nonlinear Elastodynamics, Journal of Applied Mathematics and Physics, 99(1992) 61–112.

[23] D. Greenspan, Discrete Models, Addison-Welsey, Reading, Mass (1973).

[24] R.A. LaBudde, D. Greenspan, Discrete Mechanics – A General Treatment, Journal of Computational Physics 15(1974) 134–167.

[25] T.-N. Le, J.-M. Battini, M. Hjiaj, Dynamics of 3D beam elements in a corotational context: A comparative study of established and new formulations, Finite Elements in Analysis and Design 61 (2012) 97–111.

[26] T.-N. Le, J.-M. Battini, M. Hjiaj, A consistent 3D corotational beam element for nonlinear dynamic analysis of flexible structures, Computer Methods in Applied Mechanics and Engineering 269 (2014) 538–565.

[27] T.-N. Le, J.-M. Battini, M. Hjiaj, Corotational formulation for nonlinear dynamics of beams with arbitrary thin-walled open cross-sections, Computers and Structures 134 (2014) 112–127.

[28] J.-M. Battini, C. Pacoste, Co-rotational beam elements with warping effects in instability problems, Computer Methods in Applied Mechanics and Engineering 191 (2002) 1755–1789.

[29] J.-M. Battini, C. Pacoste, Plastic instability of beam structures using co-rotational elements, Computer Methods in Applied Mechanics and Engineering 191 (2002) 5811–5831.

[30] R. Alsafadie, M. Hjiaj, J.-M. Battini, Corotational mixed finite element formulation for thin-walled beams with generic cross-section, Computer Methods in Applied Mechanics and Engineering 199 (2010) 3197–3212.

[31] R. Alsafadie, J.-M. Battini, H. Somja, M. Hjiaj, Local formulation for elasto-plastic corotational thin-walled beams based on higher-order curvature terms, Finite Elements in Analysis and Design 47 (2011) 119–128.

[32] R. Alsafadie, J.-M. Battini, M. Hjiaj, Efficient local formulation for elasto-plastic corotational thin-walled beams, International Journal for Numerical Methods in Biomedical Engineering 27 (2011) 498–509.

[33] R. Alsafadie, J.-M. Battini, M. Hjiaj, Three-dimensional formulation of a mixed corotational thin-walled beam element incorporating shear and warping deformation, Thin-Walled Structures 49 (2011) 523–533.

[34] R. Alsafadie, M. Hjiaj, H. Somja, J.-M. Battini, A comparative study of displacement and mixed-based corotational finite element formulations for elasto-plastic three-dimensional beam analysis, Engineering Computations 28 (2011) 939–982.

[35] C. Sansour, T.L. Nguyen, M. Hjiaj, An energy-momentum method for in-plane geometrically exact Euler-Bernoulli beam dynamics, International Journal for Numerical Methods in Engineering 102(2015) 99–134.

[36] T.L. Nguyen, C. Sansour, M. Hjiaj, Long-term stable time integration scheme for dynamic analysis of planar geometrically exact Timoshenko beams, Journal of Sound and Vibration 396(2017) 144–171.

[37] H.M. Hilber, T.J.R. Hugues and R.L. Talyor, Improved Numerical Dissipation for Time Integration Algorithms in Structural Dynamics, Earthquake Engineering and Structural Dynamics 5(1977) 283–292.

[38] C. Sansour, P. Wriggers, J. Sansour, Nonlinear Dynamics of Shells: Theory, Finite Element Formulation, and Integration Schemes, Nonlinear Dynamics, 13(1997) 279—305.

[39] C. Sansour, W. Wagner, P. Wriggers, J. Sansour, An energy–momentum integration scheme and enhanced strain finite elements for the non-linear dynamics of shells, International Journal of Non-Linear Mechanics 37(2002) 951–966.

[40] S. Chhang, C. Sansour , M. Hjiaj, J.-M. Battini, An energy-momentum co-rotational formulation for nonlinear dynamics of planar beams, Computers and Structures, 187(2017) 50–63.

[41] S. Chhang, J.-M. Battini, M. Hjiaj, Energy-momentum method for co-rotational plane beams: A comparative study of shear flexible formulations, Finite Elements in Analysis and Design 2017(134) 41–54.

[42] W.L. Wood, M. Bossak and O.C. Zienkiewicz, An Alpha Modification of Newmark's Method, International Journal for Numerical Methods in Engineering 15 (1980) 1562–1566.

[43] E.L Wilson, A Computer Program for Dynamic Stress Analysis of Underground Structures, University of California, Berkeley:Defense Technical Information Center (1968).

[44] K.C. Park, An improve Stiffly Stable Method for Direct Integration of Nonlinear Structural Dynamics Equations, Journal of Applied Mechanics, 42 (1975) 464–470.

[45] H.P. Shao, C.W. Cai, The Direct Integration Three-Parameters Optimal Schemes for Structural Dynamics (in English), in Proceeding of the International Conference: Machine Dynamics and Engineering Applications (1988).

[46] J. Chung, G. Hulbert, A Time Integration Method for Structural Dynamics with Improved Numerical Dissipation: The Generalize alpha-Method, Journal of Applied Mechanics 30 (1993) 371–375.

[47] K.K. Tamma, X. Zhou, D. Sha, A Thoery of Development and Design of Generalized Integration Operators for Computational Structural Dynamics, International Journal of Numerical Methods in Engineering 50(2001) 1619-1664.

[48] K.K. Tamma, X. Zhou, D. Sha, The Time Dimension: A Thoery Towards the Evaluation, Classification, Characterization and Design of Computational Algorithms for Transient/Dynamic Applications, Archive of Computational Methods in Engineering 7(2000) 67–290.

[49] X. Zhou, K.K. Tamma, A New Unified Theory Underlying Time Dependent Linear First-Order Systems: A Prelude to Algorithms by Design, International Journal for Numerical Methods in Engineering 66(2006) 1739–1790.

[50] X. Zhou, K.K. Tamma, Algorithms by design with illustrations to solid and structural mechanics/dynamics, International Journal for Numerical Methods in Engineering 66(2006) 1738–1790.

[51] T. Laursen and X. Meng, A New Solution Procedure for Application of Energy-Conserving Algorithms to General Constitutive Models in Nonlinear Elastodynamics, Computer Methods in Applied Mechanics and Engineering 190(2001) 6309–6322.

[52] T.A. Laursen, G.R. Love, Improved implicit integrators for transient impact problems—geometric admissibility within the conserving framework, International Journal for Numerical Methods in Engineering 53(2001) 245–274.

[53] J. Simo, O. Gonzalez, Recent Results on the Numerical Integration of Infinite-Dimensional Hamiltonian Systems,in Recent Developments in Finite Element Analysis, ICNME Spain (1994) 255–271.

[54] O. Gonzalez, Exact Energy and Momentum Conserving Algorithms for General Models in Nonlinear Elasticity, Computer Method in Applied Mechanics and Engineering, 190 (2000) 1763–1783.

[55] L. Noels, L. Stainier, J.P. Ponthot, An energy-momentum conserving algorithm for non-linear hypoelastic constitutive models, International Journal for Numerical Methods in Engineering 59 (2004) 83–114.

[56] M.A. Crisfield, An invariant energy-momentum conserving procedure for dynamics of 3D beams, in Computational Mechanics,CIMNE, Bacelona, Spain (1998).

[57] I. Romero, F. Armero, An objective finite element approximation of the kinematics of geometrically exact rods and its use in the formulation of an energy–momentum conserving scheme in dynamics, International Journal for Numerical Methods in Engineering 54(2002) 1683–1716.

[58] M. Gams, I. Planinc, M. Saje, Energy conserving time integration scheme for geometrically exact beam, Computer Methods in Applied Mechanics and Engineering 196(2007) 2117–2129.

[59] K.-J. Bathe, Conserving energy and momentum in nonlinear dynamics: A simple implicit time integration scheme, Computers and Structrures 85(2007) 437–445.

[60] S. Krenk, Global energy-momentum-based time integration in nonlinear dynamics, International Journal for Numerical Methods in Engineering 100(2014) 458–476.

[61] H. Lim, R.L. Taylor, An explicit–implicit method for flexible–rigid multibody systems, Finite Elements in Analysis and Design 37(2001) 881–900.

[62] P.M. Almonacid, Explicit symplectic momentum-conserving time-stepping scheme for the dynamics of geometrically exact rods, Finite Elements in Analysis and Design 96(2015) 11–22.

[63] L. Briseghella, C.E. Majorana, C. Pellegrino, Conservation of angular momentum and energy in the integration of nonlinear dynamic equations, Computer Methods in Applied Mechanics and Engineering, 179(1999) 247–263.

[64] P. Betsch, S. Uhlar, Energy-momentum conserving integration of multibody dynamics,Multibody System Dynamics 17(2007) 243-–289.

[65] M.A. Puso, An energy and momentum conserving method for rigid–flexible body dynamics, International Journal for Numerical Methods in Engineering 53(2002) 1393–1414.

[66] P. M. Pimenta, E.M.B. Campello, P. Wriggers, An exact conserving algorithm for nonlinear dynamics with rotational DOFS and general hyper elasticity: Part 1: Rods, Computational Mechanics 42(2008) 715-–732.

[67] A. Ibrahimbegović, S. Mamouri, Nonlinear dynamics of flexible beams in planar motion: formulation and time-stepping scheme for stiff problems, Computers and Structures 70(1999) 1–22.

[68] E.M.B. Campello, P.M. Pimenta, P. Wriggers, An exact conserving algorithm for nonlinear dynamics with rotational DOFS and general hyper elasticity: Part 2: shells, Computational Mechanics 48(2011) 195-–211.

[69] B. Brank, An energy conserving non-linear dynamic finite element formulation for flexible composite laminates, Computers and structures 80(2002) 677–689.

[70] C.S. Jog, P. Motamarri, An energy-momentum conserving algorithm for nonlinear transient analysis within the framework of hybrid elements, Journal of Mechanics of Materials and Structures 1(2009) 157–186.

[71] L.F.R. Espath, A.L. Braun, A.M. Awruch, Energy conserving and numerical stability in nonlinear dynamic using isogeometric analysis, in Mecánica Computacional, Mendoza, Argentina (2013).

[72] M. Iura, S.N. Atluri, Dynamic analysis of planar flexible beams with finite rotaions by using inertial and rotating frames, Computers and Structures 55 (1995) 453–462.

[73] F.S. Almeida, A.M. Awruch, Corotational nonlinear dynamic analysis of laminated composite shells, Finite Elements in Analysis and Design 47 (2011) 1131–1145.

[74] J. Yang, P. Xia, Corotational nonlinear dynamic analysis of thin-shell structures with finite rotations, AIAA Journal 53 (2015) 663–677.

[75] D. Kuhl, E. Ramm, Generalized energy-momentum method for nonlinear adaptive shell dynamics, International Journal for Numerical Methods in Engineering 178(1999)343-–366.

[76] F. Armero, I. Romero, On the formulation of high-frequency dissipative time-stepping algorithms for nonlinear dynamics, Part I: low-order methods for two model problems and nonlinear elastodynamics, Computer Methods in Applied Mechanics and Engineering 190(2001) 2603–2649.

[77] A. Ibrahimbegović, S. Mamouri, Energy conserving/decaying implicit time-stepping scheme for nonlinear dynamics of three-dimensional beams undergoing finite rotations, Computer Methods in Applied Mechanics and Engineering 191(2002) 4241–4258.

[78] S. Mamouri, R. Kouli, A. Benzegaou, A. Ibrahimbegović, Implicit controllable high-frequency dissipative scheme for nonlinear dynamics of 2D geometrically exact beam, Nonlinear Dynamics 84(2016) 1289—1302.

[79] M. Gams, I. Planinc, M. Saje, A heuristic viscosity-type dissipation for high frequency oscillation damping in time integration algorithms, Computational Mechanics 41(2017) 17—29.

[80] I. Stewart, Warning – handle with care, Nature 355(1992) 16—17.

[81] C.E. Yee, P.K. Sweby and D.F. Griffiths, Dynamical Approach Study of Spurious Steady-State Numerical Solutions of Nonlinear Differential Equations. I. The Dynamics of Time Integration and Its Implications for Algorithm Development in Computational Fluid Dynamics, Journal of Computational Physics, 97(1991) 249–310.

[82] C. Sansour, P. Wriggers, J. Sansour, On the design of energy-momentum integration schemes for arbitrary continuum formulations. Applications to classical and chaotic motion of shells, International Journal for Numerical Methods in Engineering 60 (2004) 2419–2440.

[83] Y. Urthaler Y, J.N. Reddy, A corotational finite element formulation for the analysis of planar beams, Communications in Numerical Methods in Engineering 21 (2005) 553–570.

[84] G. Garcea, A. Madeo, R. Casciaro, The implicit corotational method and its use in the derivation of nonlinear structural models for beams and plates, Journal of Mechanics of Materials and Structures 7 (2012) 509–538.

[85] C. Pacoste, A. Eriksson, Beam elements in instability problems, Computer Methods in Applied Mechanics and Engineering 144 (1997) 163–197.

[86] G. Prathap, G.R. Bhashyam, Reduced integration and the shear-flexible beam element, International Journal for Numerical Methods in Engineering 18(1982) 195–210.

[87] J.N. Reddy, An Introduction to the Finite Element Method, 2nd edtion, McGraw-Hill, New York, 1993.

[88] A. Ibrahimbegović, F. Frey, Finite element analysis of linear and non-linear planar deformations of elastic initially curved beams, International Journal for Numerical Methods in Engineering, 36(1993) 3239–3258.

[89] M.L. Day, T.Y. Yang, A mixed variational principle for finite element analysis, International Journal for Numerical Methods in Engineering 18(1982) 1213–1230.

[90] R.L. Taylor and F.C. Filippou, A. Saritas and F. Auricchio, A mixed finite element method for beam and frame problems, Computational Mechanics 31(2003) 192–203.

[91] B.N. Almedar, D.W. White, Displacement, flexibility, and mixed beam-column finite element formuations for distributed plasticity analysis, Journal of Structural Engineering 131(2005) 1811–1819.

[92] P.K.V.V. Nukal, D.W. White, Variationally consistent state determination algorithms for nonlinear mixed beam finite elements, Computer Methods in Applied Mechanics and Engineering 193(2004) 3647–3666.

[93] P.Wriggers, J.Korelc, On enhanced strain methods for small and finite deformations of solids, Computational Mechanics 18(1996) 413–428.

[94] E.P. Kasper, R.L. Taylor, A mixed-enhanced strain method. Part I: Geometrically linear problems, Computers and structures 75(2000) 237–250.

[95] J. Korelc, P. Wriggers, Consistent gradient formulation for a stable enhanced strain method for large deformations, Engineering Computations, 13(1984) 103–123.

[96] J.C. Simo, F. Armero, Geometrically non-linear enhanced strain mixed methods and the method of incompatible modes, International Journal for Numerical Methods in Engineering, 33(1192) 1413–1449.

[97] J.N. Reddy, On locking-free shear deformable beam finite elements, Computer Methods in Applied Mechanics and Engineering 149(1997) 113–132.

[98] J.H. Argyris, H. Balmer, J.St. Doltsinis, P.C. Dunne, M. Hasse, M. Kleiber, G.A. Malejannakis, H.-P. Meljnek, M. Müller, and D.W. Scharpf, Finite element method-the natural approach, Computer Methods in Applied Mechanics and Engineering 17-18(Part I) (1979) 1–106.

[99] K.-J. Bathe, S. Bolourchi, Large displacement analysis of three-dimensional beam structures. International Journal for Numerical Methods in Engineering 14 (1979) 961–986.

[100] J.C. Simo, L. Vu-Quoc, On the dynamics in space of rods undergoing large motions - a geometrically exact approach, Computer Methods in Applied Mechanics and Engineering 66 (1988) 125–161.

[101] A. Cardona, M. Géradin, A beam finite element non-linear theory with finite rotations, International Journal for Numerical Methods in Engineering 26 (1988) 2403–2438.

[102] P.M. Pimento, T. Yojo, Geometrically exact analysis of spatial frames, Applied Mechanics Reviews 46 (1993) 118–128.

[103] O.A. Bauchau, G. Damilano, N.J. Theron, Numerical integration of non-linear elastic multi-body systems. International Journal for Numerical Methods in Engineering 38 (1995) 2727–2751.

[104] A. Ibrahmibegović, On finite element implementation of geometrically nonlinear Reissner's beam theory: Three-dimensional curved beam element, Computer Methods in Applied Mechanics and Engineering 122 (1995) 11–26.

[105] A. Ibrahmibegović, On the choice of finite rotation parameters, Computer Methods in Applied Mechanics and Engineering 149 (1997) 49–71.

[106] F. Gruttmannm, R. Sauer, W. Wagner, Theory and numerics of three-dimensional beams with elastoplastic material behaviour, International Journal for Numerical Methods in Engineering 48 (2000) 1675–1702.

[107] D. Zupan, M. Saje, Finite-element formulation of geometrically exact three-dimensional beam theories based on interpolation of strain mesures, Computer Methods in Applied Mechanics and Engineering 192 (2003) 5209–5248.

[108] C. Sansour, W. Wagner, Mutliplicative update of the rotation tensor in the finite element analysis of rods and shells - a path independent appraoch, Computational Mechanics 31 (2003) 153-162.

[109] R. Kapania, J. Li, A formulation and implementation of geometrically exact curved beam elements incorporating finite strains and finite rotations. Computational Mechanics 30 (2003) 444-459.

[110] I. Romero, The interpolation of rotations and its application to finite element models of geometrically exact rods. Computational Mechanics 34 (2004) 121–133.

[111] P. Mata, S. Oller, A.H. Barbat, Static analysis of beam structures under nonlinear geometric and constitutive behavior, Computer Methods in Applied Mechanics and Engineering 196 (2007) 4458-4478.

[112] E. Zupan, M. Saje, D. Zupan, Quaternion-based dynamics of geometrically nonlinear spatial beams using the Runge-Kutta method, Finite Elements in Analysis and Design 54 (2012) 48–60.

[113] H. Zhong, R. Zhang, N. Xiao, A quaternion-based weak form quadrature element formulation for spatial geometrically exact beams, Archive of Applied Mechanics 84 (2014) 1825–1840.

[114] W. Li, H. Ma, W. Gao, Geoemtrically exact curved beam element using interal force field defined in deformed configuration. International Journal of Non-Linear Mechanics 89 (2017) 116-126.

[115] P. Nanakorn, L.N.Vu, A 2D field-consistent beam element for large displacement analysis using the total Lagrangian formulation, Finite Elements in Analysis and Design 134 (2017) 41–54.

[116] F. Armero, J. Valverde, Invariant Hermitian finite elements for thin Kirchhoff rods. I: The linear plane case, Computer Methods in Applied Mechanics and Engineering 213-216:427–457, 2012.

[117] F.P. Pai, Geometrically exact beam theory without Euler angles, Internation Journal of Solids and Structures 48 (2011) 3075–3090.

[118] Z. Zhao, G. Ren, A quaternion-based formulation of Euler–Bernoulli beam without singularity, Nonlinear Dynamics 67 (2012) :1825-–1835

[119] L. Greco, M. Cuomo, B-Spline interpolation of Kirchhoff-Love space rods, Computer Methods in Applied Mechanics and Engineering 256 (2013) 251-–269.

[120] A.M. Bauer, M. Breitenberger, B. Philipp, R. Wüchner, K.-U. Bletzinger, Nonlinear isogeometric spatial Bernoulli beam, Computer Methods in Applied Mechanics and Engineering 303 (2016) 101-–127.

[121] C. Meier, A. Popp, W.A. Wall, Geometrically exact finite element formulations for slender beams: Kirchhoff–love theory versus Simo-Reissner theory. Archives of Computational Methods Engineering (2017) 1–81.

[122] A.A. Shabana, H.A. Hussien, J.L.Escalona, Application of the absolute nodal coordinate formulation of large rotation and large deformation problems. Journal of Mechanical Design 120 (1998) 188–195.

[123] A.A. Shabana, R.Y. Yakoub, Three dimensional absolute nodal coordinate formulation for beam theory: Theory. Journal of Mechanical Design 123 (2000) 606–613.

[124] Y. Choquet-Bruhat, C. DeWitt-Morette, M. Dillard-Bleick. Analysis, Manifolds and Physics Part I. North-Holland, Amsterdam.

[125] B.A. Dubrovin, A.T. Fomenko, S.P. Novikov. Modern Geometry-Methods and Applications I. Springer-Verlag, New York.

[126] M. Geradin, A. Cardona, Flexible Multibody Dynamics, A Finite Element Approach, John Wiley and Sons 2001.

[127] J. Mäkinen, Critical study of Newmark-scheme on manifold of finite rotations, Computer Methods in Applied Mechanics and Engineering 191(2001) 817–828.

[128] J. Chung, G.M. Hulbert, A predictor-corrector algorithm of the generalized-α Method for analysis of structural dynamics, Korean Society for Noise and Vibration Engineering 5(1995) 207–213.

[129] R.de. Borst and M.A. Crisfield, J.J.C. Remmers, C.V. Verhoosel, Non-linear finite element analysis of solids and structures, 2nd edition, John Wiley and Sons (2002).

[130] G. Cowper, P. Symonds. Strain hardening and strain rate effects in the impact loading of cantilever Beams, Technical Report No. 28, Brown Universitym Providence, R.I. (1957).

[131] S. Bonder, P. Symonds. Experimental and theoretical investigation of the plastic deformation of cantilever beams subjected to impulsive loadings. Journal of Applied Mechanics 29 (1962) 719-728.

[132] P. Heng, M. Hjiaj, J.-M. Battini, A. Limam. A simplified model for nonlinear dynamic analysis of steel column subjected to impact, International Journal of Non-Linear Mechanics 86(2016) 37–54.

[133] A. Alhasawi, P. Heng, M. Hjiaj, S. Guezouli, J.-M. Battini. Co-rotational planar beam element with generalized elasto-plastic hinges. Engineering Structures 154 (2017)188–205.

Paper I:

An energy-momentum co-rotational formulation for nonlinear dynamics of planar beams

Computers and Structures, Volume 187, pages 50-63, 2017.
DOI: 10.1016/j.compstruc.2017.03.021

Computers and Structures, Volume 187, pages 50-63, 2017.

An Energy-Momentum Co-Rotational Formulation for Nonlinear Dynamics of Planar Beams

Sophy Chhang[a,b], Carlo Sansour[a], Mohammed Hjiaj[a], Jean-Marc Battini[b,*]

[a] *INSA Rennes, LGCGM, Univeristé Bretagne Loire, Rennes, France*
[b] *Department of Civil and Architectural Enginneering, Royal Insititute of Technology KTH, Stockholm, Sweden*

Abstract

This article presents an energy-momentum integration scheme for the nonlinear dynamic analysis of planar Euler-Bernoulli beams. The co-rotational approach is adopted to describe the kinematics of the beam and Hermitian functions are used to interpolate the local transverse displacements. In this paper, the same kinematic description is used to derive both the elastic and the inertia terms. The classical midpoint rule is used to integrate the dynamic equations. The central idea, to ensure energy and momenta conservation, is to apply the classical midpoint rule to both the kinematic and the strain quantities. This idea, developed by one of the authors in previous work, is applied here in the context of the co-rotational formulation to the first time. By doing so, we circumvent the nonlinear geometric equations relating the displacement to the strain which is the origin of many numerical difficulties. It is rigorously shown that the proposed method conserves the total energy of the system and, in absence of external loads, the linear and angular momenta remain constant. The accuracy and stability of the proposed algorithm, especially in long term dynamics with a very large number of time steps, is assessed through four numerical examples.

Keywords: Co-rotational formulation; energy-momentum method; conserving energy; nonlinear dynamic; 2D Beam.

1. Introduction

Dynamics of slender beams is still a very active research field especially when it comes to large deformations and displacements. Flexible beams are used in many applications, for instance large deployable space structures, aircrafts and wind turbines propellers, offshore platforms. These structures undergo large displacements and rotations and in some cases moderate-to-large strains. Several approaches are available to model the dynamics of geometrically flexible nonlinear beams. In addition to the Total

*Corresponding author
Email addresses: sophy.chhang@insa-rennes.fr (Sophy Chhang), carlo.sansour@nottingham.ac.uk (Carlo Sansour), mohammed.hjiaj@insa-rennes.fr (Mohammed Hjiaj), jean-marc.battini@byv.kth.se (Jean-Marc Battini)

Lagrangian approach [1, 2, 3, 4, 5], floating approach [6, 7, 8] and co-rotational ones [9, 10, 11, 12, 13, 14, 15, 16, 17, 18, 19, 20, 21, 22, 23, 24, 25, 26] have been considered for the development of efficient formulations. Whilst the total Lagrangian approach can be considered as the natural setting for geometrically exact dynamics, the co-rotational method is still an attractive approach to derive highly nonlinear beam elements because it combines accuracy with numerical efficiency. Especially for very large structures with a high number of beam elements, efficiency is still of great importance for successful simulation.

Response of large structures to earthquake, to impact or to extreme loading conditions are some examples where dynamics is essential with efficiency being a key ingredient that decides about the choice of the finite element. Here, long term stability is a fundamental feature of a time integration method to capture extended responses over sufficiently long time intervals. Implicit time stepping methods are often used together with nonlinear finite elements to investigate complex dynamic problems. It is well known that Newmark's method [37] and alike are conditionally stable for nonlinear dynamics. To avoid these instabilities, Geradin and Cardona [38] introduced numerical dissipations (Alpha method [39]) in order to damp the high frequencies with the consequence that the system energy is not conserved [41, 40]. Since the early work of Simo and Tarnow [41], it is accepted that energy conservation, respectively control, is key for stability. In their work, they presented a methodology to construct time integration algorithms that inherit, by design, the conservation of momenta and energy for geometrically nonlinear problem involving quadratic Green-Lagrange strains. Generally, the design of energy-momentum conserving algorithms comes with conservation of linear and angular momentum as well, hence the term energy-momentum methods. The core idea of these methods is to use a discrete directional derivative to construct scheme that preserve the Hamiltonian along with other integrals. This concept can be traced back to Gotusso [42] and was first applied to elastodynamics by Gonzalez [43]. Since then much effort was devoted to develop energy-momentum methods for various types of formulations and structural elements. For nonlinear rod dynamics we refer to [48, 49, 50, 52, 51] and contributions to nonlinear shell dynamics have been made in [53, 54, 55, 56, 57], among others. In all cases, some form of shearable structures were considered, that is, either the Reissner-Mindlin kinematic for shells or the equivalent Timoshenko one for the rod. Nonlinear dynamics of hypoelastic continuum has been addressed by [44, 43, 45]. Further energy-momentum-related work is that of Betsch and Steinmann [46]. A simple parameter free collocation-type composite time integration scheme has been proposed by Bathe [47] with the objective to conserve energy. Of special interest, also with regard to this work, is the formulation by Sansour et al. [54, 55], which is designed to secure energy conservation independently of the nonlinear complexities involved in the strain-displacement relations. It has been applied to arbitrary continuum formulations [61] and to geometrically exact Bernoulli beam model [49]. Gams et al. [50] developed a time integration algorithm in the spirit of the method described in [61] for the geometrically exact planar Reissner beam. Besides, they considered the dissipation of high frequency oscillations associated to energy-momentum methods [62].

With regard to the co-rotational formulation for rods, we employ here the one originally proposed by Rankin and Nour-Omid [58, 59] , and further developed by Battini and Pacoste [30, 31] and many other authors. The fundamental idea of a

co-rotational formulation is to decompose the large motion of the element into rigid body and pure deformation parts through the use of a local system which continuously rotates and translates with the element. The deformation is captured at the level of the local reference frame, whereas the geometric nonlinearity induced by the large rigid-body motion, is incorporated in the transformation matrices relating local and global quantities. The main interest is that the pure deformation part can be assumed as small and can be represented by a linear or a low order nonlinear theory. Avoiding the nonlinear relationship between the strain tensor and the displacement gradient is what makes the co-rotational approach very attractive and efficient for nonlinear static analysis. For a general account, we refer also to [27, 29, 28, 30, 31, 32, 33, 34, 35, 36].

As one may expect, there have been many efforts to develop energy-momentum methods for co-rotational formulations as well. These efforts have been only partially successful. Examples of previous attempts are that of Crisfield and Shi [9] who developed a mid-point energy-conserving time integrator for co-rotating planar trusses. In their formulation, the time-integration strategy is closely linked to the co-rotational procedure which is "external" to the element. A similar approach was applied to the dynamic of co-rotational shell [24] and laminated composite shells [25]. Yang and Xia [26] proposed the energy-decaying and momentum-conserving algorithm in the context of thin-shell structures. Galvanetto and Crisfield [11] applied the previously developed energy-conserving time-integration procedure to implicit nonlinear dynamic analysis of planar beam structures. Various end- and mid-point time integration schemes for the nonlinear dynamic analysis of 3D co-rotational beams are discussed in [18]. They concluded that the proposed mid-point scheme is an "approximately energy conserving algorithm". Le et al. [12] adopted Interpolation Interdependent Element formulation [60], hence cubic interpolation functions, to derive both the inertia and elastic terms in conjunction with a Newmark-type time integration algorithm and considering simplifications in the expression of the mass matrix. Le et al. [12] showed that this formulation is more efficient than using constant mass matrices as it requires less elements. The formulation was extended to 3D Bernoulli beam elements without [19, 20] and with warping [21]. Salomon et al. [22] showed the conservation of energy and momentum in the 2D analysis. But, they did not get exact angular momentum conservation in the 3D analysis.

It was soon recognized that the decomposition of the beam motion into a rigid and deformation-related parts with the help of a local frame that moves with the beam produces complex kinetic energy terms as a result of the movement of the local frame regardless of order of the interpolating functions. To circumvent these difficulties, Iura et al. [13] proposed to use an inertial frame to derive kinetic energy function in terms the global displacement components. Similar approach has been followed by Crisfield et al.[10, 18] who suggested to derive the mass matrix by interpolating global quantities with linear shape functions (Timoshenko model). The use an inertial frame to derive kinetic energy function in terms the global displacement components was also recommended in Crisfield et al. [18] as a remedy to complicated expressions of kinetic energy-related terms.

In all the above examples energy conservation is either approximately achieved or enforced by means of constraint equations. Indeed, so far no method exists which inherently fulfills the conservation properties of energy and momenta in the context of co-rotational formulation. It is with this goal in mind that we approach the present

research. At the heart of the approach is to apply the fundamental ideas of Sansour et al. [54, 55] in the context of the present co-rotational formulation. The complexities induced by the decomposition of the beam movement have hampered the development of a consistent energy-momentum conserving co-rotational formulation. While the fundamental idea of Sansour et al. [54, 55] can be summarized as using the strain-displacement relations to deduce strain rate quantities with the help of which then a strain filed is integrated using the same schemes as for the displacement fields, the task as such is not as straightforward as it may seem. The choice of the correct strain rates is crucial since multiple nonlinear relations exist between the displacements and further quantities which constitute the strain field. Questions arise as to which of the nonlinear quantities are to be integrated first. Also and beyond the possible formulation, the applicability of the same in long-term dynamics is to be tested as well.

The outline of the paper is as follows. In Section 2, the kinematics and strain measures of the 2D beam element are shortly presented. Section 3 is devoted to the Hamilton's principle and the conserving properties. In Section 4, the energy momentum scheme is developed, the element (i.e. the elastic and inertia terms) is fully derived. Proofs of the conservation of energy, linear and angular momenta are given in section 5. In Section 6, four numerical applications are presented in order to assess the performances of the proposed method. The paper concludes in Section 7.

2. Beam Kinematics and strain definition

2.1. Co-rotational beam kinematics

The kinematics of the beam and all the notations used in this section are shown in Figure 1. The motion of the element is decomposed in two parts. In a first step, a rigid body motion is defined by the global translation (u_1,w_1) of the node 1 as well as the rigid rotation α. This rigid motion defines a local coordinate system (x_l, z_l) which continuously translates and rotates with the element. In a second step, the element deformation is defined in the local coordinate system. Assuming that the length of the element is properly selected, the deformational part of the motion is always small relative to the local co-ordinate systems. Consequently, the local deformations can be expressed in a simplified manner. The vectors of global and local displacements are now defined by

$$\boldsymbol{q} = \left[\begin{array}{cccccc} u_1 & w_1 & \theta_1 & u_2 & w_2 & \theta_2 \end{array} \right]^{\mathrm{T}}, \tag{1}$$

and

$$\bar{\boldsymbol{q}} = \left[\begin{array}{ccc} \bar{u} & \bar{\theta}_1 & \bar{\theta}_2 \end{array} \right]^{\mathrm{T}} \tag{2}$$

Explicitly, the components of $\bar{\boldsymbol{q}}$ are given by

$$\begin{aligned} \bar{u} &= l - l_0 \\ \bar{\theta}_1 &= \theta_1 - \alpha \\ \bar{\theta}_2 &= \theta_2 - \alpha \end{aligned} \tag{3}$$

where l_0 and l denote the initial and current lengths of the element, respectively:

$$\begin{aligned} l_0 &= \sqrt{(x_2 - x_1)^2 + (z_2 - z_1)^2} \\ l &= \sqrt{(x_2 + u_2 - x_1 - u_1)^2 + (z_2 + w_2 - z_1 - w_1)^2} \end{aligned} \tag{4}$$

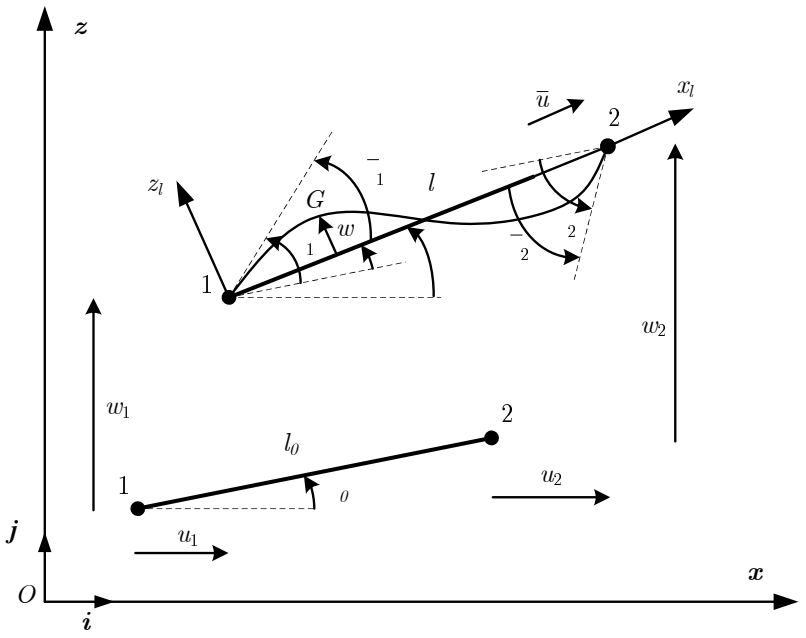

Figure 1: Beam kinematics 1

The rigid rotation α can be related to the node co-ordinates and the corresponding displacements as follows:

$$\begin{aligned} \sin\alpha &= c_0\, s - s_0\, c \\ \cos\alpha &= c_0\, c + s_0\, s \end{aligned} \tag{5}$$

with

$$\begin{aligned} c_0 = \cos\beta_0 &= \frac{1}{l_0}(x_2 - x_1) \\ s_0 = \sin\beta_0 &= \frac{1}{l_0}(z_2 - z_1) \end{aligned} \tag{6}$$

and

$$\begin{aligned} c = \cos\beta &= \frac{1}{l}(x_2 + u_2 - x_1 - u_1) \\ s = \sin\beta &= \frac{1}{l}(z_2 + w_2 - z_1 - w_1) \end{aligned} \tag{7}$$

The current global co-ordinate of the cross-section centroid G is given by

$$\boldsymbol{OG} = (x_1 + u_1)\,\mathbf{i} + (z_1 + w_1)\,\mathbf{j} + \frac{l}{l_0} x\,\boldsymbol{a} + w\,\boldsymbol{b} \tag{8}$$

with

$$\begin{aligned} \boldsymbol{a} &= \cos\beta\,\mathbf{i} + \sin\beta\,\mathbf{j} \\ \boldsymbol{b} &= -\sin\beta\,\mathbf{i} + \cos\beta\,\mathbf{j} \end{aligned} \tag{9}$$

and w as the local transversal displacement of G. By using Eqs.(7), the components of the global displacement of G are obtained as

$$u_G = N_1(x_1 + u_1) + N_2(x_2 + u_2) - w\sin\beta \tag{10}$$

$$w_G = N_1(z_1 + w_1) + N_2(z_2 + w_2) + w\cos\beta \tag{11}$$

with

$$\begin{aligned} N_1 &= 1 - \frac{x}{l_0} \\ N_2 &= \frac{x}{l_0} \end{aligned} \tag{12}$$

Finally, the global rotation of the cross-section is related to the local cross section rotation ϑ via

$$\theta_G = \vartheta + \alpha \tag{13}$$

2.2. Strain measures

The Bernoulli assumption is adopted for the local formulation. Hence, linear interpolation is considered for the axial displacement u and a cubic function for the transversal displacement w. With the interpolation functions

$$\begin{aligned} N_3 &= x\left(1 - \frac{x}{l_0}\right)^2 \\ N_4 &= x\left(-\frac{x}{l_0} + \frac{x^2}{l_0^2}\right) \\ N_5 &= 1 - \frac{4x}{l_0} + \frac{3x^2}{l_0^2} \\ N_6 &= -\frac{2x}{l_0} + \frac{3x^2}{l_0^2} \end{aligned} \tag{14}$$

the above choice results in the following local displacement distribution

$$\begin{aligned} u &= \frac{x}{l_0}\bar{u} \\ w &= N_3\,\bar{\theta}_1 + N_4\,\bar{\theta}_2 \\ \vartheta &= N_5\,\bar{\theta}_1 + N_6\,\bar{\theta}_2 \end{aligned} \tag{15}$$

The local normal strain follows directly from the Bernoulli hypothesis:

$$\varepsilon_{11} = \varepsilon - \kappa\, z \tag{16}$$

in which the axial strain ε and the curvature κ are defined by

$$\varepsilon = \frac{1}{l_0}\int_{l_0}\left[\frac{\partial u}{\partial x} + \frac{1}{2}\left(\frac{\partial w}{\partial x}\right)^2\right]\mathrm{d}x \tag{17}$$

$$\kappa = \frac{\partial^2 w}{\partial x^2} \tag{18}$$

In Eq.(17), a shallow arch strain definition has been considered. To avoid membrane locking, the axial strain is averaged over the element. The purpose of introducing a mild geometrical nonlinearity in the local formulation is to increase the accuracy of the formulation as compared to a purely linear strain definition, while still retaining the efficiency.

3. Hamilton's principle and conserving properties

Hamilton's principle states that the integral of the Lagrangian between two specified time instants t_1 and t_2 of a conservative mechanical system is stationary

$$\delta \int_{t_1}^{t_2} \mathcal{L}\, \mathrm{d}t = 0 \tag{19}$$

The Lagrangian $\mathcal{L}$ is given by

$$\mathcal{L} = \mathsf{K} - \mathsf{U}_{int} - \mathsf{U}_{ext} \tag{20}$$

with K as the kinetic energy, U_{int} and U_{ext} are the internal and the external potentials, respectively. The body is a non-conducting linear elastic solid and thermodynamic effects are not included in the system. The kinetic energy is the sum of the translational and rotational kinetic energies:

$$\mathsf{K} = \frac{1}{2}\int_{l_0} \rho A\, \dot{u}_G^2\, \mathrm{d}x + \frac{1}{2}\int_{l_0} \rho A\, \dot{w}_G^2\, \mathrm{d}x + \frac{1}{2}\int_{l_0} \rho I\, \dot{\theta}_G^2\, \mathrm{d}x \tag{21}$$

The elastic potential is defined as

$$\mathsf{U}_{int} = \frac{1}{2}\int_{l_0} EA\, \varepsilon^2 \mathrm{d}x + \frac{1}{2}\int_{l_0} EI\, \kappa^2 \mathrm{d}x \tag{22}$$

while the external potential is given as

$$\mathsf{U}_{ext} = -\int_{l_0} p_u u_G\, \mathrm{d}x - \int_{l_0} p_w w_G\, \mathrm{d}x - \int_{l_0} p_\theta \theta_G\, \mathrm{d}x - \sum_{i=1}^{6} P_i q_i \tag{23}$$

E is Young's modulus of the material, A is the area of the cross-section, I is the second moment of area of the cross-section, p_u and p_w are the distributed horizontal and vertical loads, p_θ is the distributed external moment, P_i is the i component (concentrated forces and moments at the nodes) of external force vector $\boldsymbol{P}$.

Standard variational arguments and integration by parts provide the following expression :

$$\begin{aligned}
&\int_{l_0} \rho A\, \ddot{u}_G \delta u_G\, \mathrm{d}x + \int_{l_0} \rho A\, \ddot{w}_G \delta w_G\, \mathrm{d}x + \int_{l_0} \rho I\, \ddot{\theta}_G \delta\theta_G\, \mathrm{d}x \\
&+ \int_{l_0} EA\, \varepsilon \delta\varepsilon\, \mathrm{d}x + \int_{l_0} EI\, \kappa \delta\kappa\, \mathrm{d}x - \int_{l_0} p_u \delta u_G\, \mathrm{d}x - \int_{l_0} p_w \delta w_G\, \mathrm{d}x \\
&- \int_{l_0} p_\theta \delta\theta_G\, \mathrm{d}x - \sum_{i=1}^{6} P_i \delta q_i = 0
\end{aligned} \tag{24}$$

The above equation is the starting point for further developments. Further, the above Hamiltonian system exhibits the following conservation properties. If the external loads are conservative, the total energy of the beam element can be written as

$$\mathsf{K} + \mathsf{U}_{int} + \mathsf{U}_{ext} = \mathsf{constant} \tag{25}$$

The linear momentum is defined by

$$\mathsf{L} = \begin{bmatrix} \mathsf{L}_u \\ \mathsf{L}_w \end{bmatrix} = \int_{l_0} \rho A \begin{bmatrix} \dot{u}_G \\ \dot{w}_G \end{bmatrix} \mathrm{d}x \tag{26}$$

and the angular momentum by

$$\mathsf{J} = \int_{l_0} \rho A \begin{bmatrix} u_G \\ w_G \\ 0 \end{bmatrix} \times \begin{bmatrix} \dot{u}_G \\ \dot{w}_G \\ 0 \end{bmatrix} \mathrm{d}x + \int_{l_0} \rho I \begin{bmatrix} 0 \\ 0 \\ \dot{\theta}_G \end{bmatrix} \mathrm{d}x \tag{27}$$

The time derivative of the two momenta define the equations of motion:

$$\frac{\mathrm{d}}{\mathrm{d}t}\mathsf{L} = \begin{bmatrix} \int_{l_0} p_u \,\mathrm{d}x + P_1 + P_4 \\ \int_{l_0} p_w \,\mathrm{d}x + P_2 + P_5 \end{bmatrix} \tag{28}$$

and

$$\begin{aligned} \frac{\mathrm{d}}{\mathrm{d}t}\mathsf{J} = \int_{l_0} (u_G\, p_w - w_G\, p_u)\,\mathrm{d}x + (x_1 + u_1)P_2 - (z_1 + w_1)P_1 \\ + (x_2 + u_2)P_5 - (z_2 + w_2)P_4 + \int_{l_0} p_\theta \,\mathrm{d}x + P_3 + P_6 = M_{ext} \end{aligned} \tag{29}$$

from which it can be seen that, with vanishing external load, the linear momentum is a constant and, with vanishing external moments, the angular momentum is a constant. It should be noted that the expression "external load" refers to all possible loading conditions including reactions forces.

4. Energy-momentum conserving time integration scheme

Implicit time stepping methods are often used together with nonlinear finite elements to study dynamic problems. The midpoint rule or Newmark's method [37] have applied successfully in the linear dynamic problems. However, these methods present instabilities [41, 40] in nonlinear dynamic problems, especially in long-term analysis. Since the early work of Simo and Tarnow [41], it is known that the energy-momentum method enhances considerably the stability of time-stepping algorithms. The main idea is to ensure the conservation of the linear and angular momenta, and the total energy. Therefore, we aim to develop the energy-momentum method to a co-rotational beam formulation where the central idea of this method starts from the classical midpoint rule.

4.1. Classical midpoint rule

The classical midpoint time integration scheme is defined by the following equations:

$$\begin{aligned} \boldsymbol{q}_{n+\frac{1}{2}} &= \frac{\boldsymbol{q}_{n+1} + \boldsymbol{q}_n}{2} = \boldsymbol{q}_n + \frac{1}{2}\Delta\boldsymbol{q} \\ \dot{\boldsymbol{q}}_{n+\frac{1}{2}} &= \frac{\dot{\boldsymbol{q}}_{n+1} + \dot{\boldsymbol{q}}_n}{2} = \frac{\boldsymbol{q}_{n+1} - \boldsymbol{q}_n}{\Delta t} = \frac{\Delta\boldsymbol{q}}{\Delta t} \\ \ddot{\boldsymbol{q}}_{n+\frac{1}{2}} &= \frac{\ddot{\boldsymbol{q}}_{n+1} + \ddot{\boldsymbol{q}}_n}{2} = \frac{\dot{\boldsymbol{q}}_{n+1} - \dot{\boldsymbol{q}}_n}{\Delta t} = \frac{2}{\Delta t^2}\Delta\boldsymbol{q} - \frac{2}{\Delta t}\dot{\boldsymbol{q}}_n \end{aligned} \tag{30}$$

from which follows

$$\begin{aligned}
\boldsymbol{q}_{n+1} &= \boldsymbol{q}_n + \Delta\boldsymbol{q} \\
\dot{\boldsymbol{q}}_{n+1} &= \frac{2}{\Delta t}\Delta\boldsymbol{q} - \dot{\boldsymbol{q}}_n \\
\ddot{\boldsymbol{q}}_{n+1} &= \frac{4}{\Delta t^2}\Delta\boldsymbol{q} - \frac{4}{\Delta t}\dot{\boldsymbol{q}}_n - \ddot{\boldsymbol{q}}_n
\end{aligned} \tag{31}$$

4.2. Time integration scheme

The previously developed time integration scheme [55, 54] is here adapted in the present context of the co-rotational formulation. While the core idea to develop the strain fields from expressions related to the strain velocity still applies, the specific realisation is not straightforward and is to be developed, in what follows, for the first time. The midpoint velocities are applied to both the kinematic variables and strains as well. Formally it takes the following generic form:

$$\begin{aligned}
&\int_{t_n}^{t_{n+1}} f(t)\,\mathrm{d}t = f(t_{n+\frac{1}{2}})\,\Delta t = f_{n+\frac{1}{2}}\,\Delta t \\
&f_{n+\frac{1}{2}} = f_n + \frac{\Delta t}{2}\,\dot{f}_{n+\frac{1}{2}}
\end{aligned} \tag{32}$$

where the function f can represent either a kinematic variable or deformational quantity.

The application of the midpoint rule (32) to Hamilton's principle (24) gives

$$\begin{aligned}
&\Delta t \left(\int_{l_0} \rho A\, \ddot{u}_{G,n+\frac{1}{2}} \delta u_{G,n+\frac{1}{2}}\,\mathrm{d}x + \int_{l_0} \rho A\, \ddot{w}_{G,n+\frac{1}{2}} \delta w_{G,n+\frac{1}{2}}\,\mathrm{d}x \right. \\
&+ \int_{l_0} \rho I\, \ddot{\theta}_{G,n+\frac{1}{2}} \delta\theta_{G,n+\frac{1}{2}}\,\mathrm{d}x + \int_{l_0} EA\, \varepsilon_{n+\frac{1}{2}} \delta\varepsilon_{n+\frac{1}{2}}\,\mathrm{d}x + \int_{l_0} EI\, \kappa_{n+\frac{1}{2}} \delta\kappa_{n+\frac{1}{2}}\,\mathrm{d}x \\
&- \int_{l_0} p_{u,n+\frac{1}{2}} \delta u_{G,n+\frac{1}{2}}\,\mathrm{d}x - \int_{l_0} p_{w,n+\frac{1}{2}} \delta w_{G,n+\frac{1}{2}}\,\mathrm{d}x - \int_{l_0} p_{\theta,n+\frac{1}{2}} \delta\theta_{G,n+\frac{1}{2}}\,\mathrm{d}x \\
&\left. - \sum_{i=1}^{6} P_{i,n+\frac{1}{2}} \delta q_{i,n+\frac{1}{2}} \right) = 0
\end{aligned} \tag{33}$$

After eliminating Δt, Eq.(33) can be simplified to

$$\begin{aligned}
\delta\boldsymbol{q}^{\mathrm{T}} \Bigg[&\int_{l_0} \rho A\, \ddot{u}_{G,n+\frac{1}{2}} \left(\frac{\partial u_{G,n+\frac{1}{2}}}{\partial \boldsymbol{q}_{n+\frac{1}{2}}} \right)^{\mathrm{T}} \mathrm{d}x + \int_{l_0} \rho A\, \ddot{w}_{G,n+\frac{1}{2}} \left(\frac{\partial w_{G,n+\frac{1}{2}}}{\partial \boldsymbol{q}_{n+\frac{1}{2}}} \right)^{\mathrm{T}} \mathrm{d}x \\
&+ \int_{l_0} \rho I\, \ddot{\theta}_{G,n+\frac{1}{2}} \left(\frac{\partial \theta_{G,n+\frac{1}{2}}}{\partial \boldsymbol{q}_{n+\frac{1}{2}}} \right)^{\mathrm{T}} \mathrm{d}x + \int_{l_0} EA\, \varepsilon_{n+\frac{1}{2}} \left(\frac{\partial \varepsilon_{n+\frac{1}{2}}}{\partial \boldsymbol{q}_{n+\frac{1}{2}}} \right)^{\mathrm{T}} \mathrm{d}x \\
&+ \int_{l_0} EI\, \kappa_{n+\frac{1}{2}} \left(\frac{\partial \kappa_{n+\frac{1}{2}}}{\partial \boldsymbol{q}_{n+\frac{1}{2}}} \right)^{\mathrm{T}} \mathrm{d}x - \int_{l_0} p_{u,n+\frac{1}{2}} \left(\frac{\partial u_{G,n+\frac{1}{2}}}{\partial \boldsymbol{q}_{n+\frac{1}{2}}} \right)^{\mathrm{T}} \mathrm{d}x \\
&- \int_{l_0} p_{w,n+\frac{1}{2}} \left(\frac{\partial w_{G,n+\frac{1}{2}}}{\partial \boldsymbol{q}_{n+\frac{1}{2}}} \right)^{\mathrm{T}} \mathrm{d}x - \int_{l_0} p_{\theta,n+\frac{1}{2}} \left(\frac{\partial \theta_{G,n+\frac{1}{2}}}{\partial \boldsymbol{q}_{n+\frac{1}{2}}} \right)^{\mathrm{T}} \mathrm{d}x - \boldsymbol{P}_{n+\frac{1}{2}} \Bigg] = 0
\end{aligned} \tag{34}$$

As the variation $\delta\boldsymbol{q}$ is arbitrary, the dynamic equilibrium at time $n+\frac{1}{2}$ is governed by the relation

$$\begin{aligned}
&\int_{l_0} \rho A\, \ddot{u}_{G,n+\frac{1}{2}} \left(\frac{\partial u_{G,n+\frac{1}{2}}}{\partial \boldsymbol{q}_{n+\frac{1}{2}}}\right)^{\mathrm{T}} \mathrm{d}x + \int_{l_0} \rho A\, \ddot{w}_{G,n+\frac{1}{2}} \left(\frac{\partial w_{G,n+\frac{1}{2}}}{\partial \boldsymbol{q}_{n+\frac{1}{2}}}\right)^{\mathrm{T}} \mathrm{d}x \\
&+ \int_{l_0} \rho I\, \ddot{\theta}_{G,n+\frac{1}{2}} \left(\frac{\partial \theta_{G,n+\frac{1}{2}}}{\partial \boldsymbol{q}_{n+\frac{1}{2}}}\right)^{\mathrm{T}} \mathrm{d}x + \int_{l_0} EA\, \varepsilon_{n+\frac{1}{2}} \left(\frac{\partial \varepsilon_{n+\frac{1}{2}}}{\partial \boldsymbol{q}_{n+\frac{1}{2}}}\right)^{\mathrm{T}} \mathrm{d}x \\
&+ \int_{l_0} EI\, \kappa_{n+\frac{1}{2}} \left(\frac{\partial \kappa_{n+\frac{1}{2}}}{\partial \boldsymbol{q}_{n+\frac{1}{2}}}\right)^{\mathrm{T}} \mathrm{d}x - \int_{l_0} p_{u,n+\frac{1}{2}} \left(\frac{\partial u_{G,n+\frac{1}{2}}}{\partial \boldsymbol{q}_{n+\frac{1}{2}}}\right)^{\mathrm{T}} \mathrm{d}x \\
&- \int_{l_0} p_{w,n+\frac{1}{2}} \left(\frac{\partial w_{G,n+\frac{1}{2}}}{\partial \boldsymbol{q}_{n+\frac{1}{2}}}\right)^{\mathrm{T}} \mathrm{d}x - \int_{l_0} p_{\theta,n+\frac{1}{2}} \left(\frac{\partial \theta_{G,n+\frac{1}{2}}}{\partial \boldsymbol{q}_{n+\frac{1}{2}}}\right)^{\mathrm{T}} \mathrm{d}x - \boldsymbol{P}_{n+\frac{1}{2}} = 0
\end{aligned} \tag{35}$$

The midpoint rule is applied to the kinematic variables defined in Eqs. (10), (11) and (13):

$$\dot{u}_{G,n+\frac{1}{2}} = \frac{\Delta u_G}{\Delta t} = \boldsymbol{f}_1^{\mathrm{T}} \frac{\Delta \boldsymbol{q}}{\Delta t} \tag{36}$$

$$\dot{w}_{G,n+\frac{1}{2}} = \frac{\Delta w_G}{\Delta t} = \boldsymbol{f}_2^{\mathrm{T}} \frac{\Delta \boldsymbol{q}}{\Delta t} \tag{37}$$

$$\dot{\theta}_{G,n+\frac{1}{2}} = \frac{\Delta \theta_G}{\Delta t} = \boldsymbol{f}_3^{T} \frac{\Delta \boldsymbol{q}}{\Delta t} \tag{38}$$

in which the vectors $\boldsymbol{f}_1$, $\boldsymbol{f}_2$ and $\boldsymbol{f}_3$ are defined at time $n+\frac{1}{2}$ as

$$\begin{aligned}
\boldsymbol{f}_1^{\mathrm{T}} &= \boldsymbol{b}_1^{\mathrm{T}} - s_{n+\frac{1}{2}} \left(N_3\, \boldsymbol{b}_3^{\mathrm{T}} + N_4\, \boldsymbol{b}_4^{\mathrm{T}}\right) - c_{n+\frac{1}{2}} \left(N_3\, \bar{\theta}_{1,n+\frac{1}{2}} + N_4\, \bar{\theta}_{2,n+\frac{1}{2}}\right) \frac{\boldsymbol{z}^{\mathrm{T}}}{l_{n+\frac{1}{2}}} \\
\boldsymbol{f}_2^{\mathrm{T}} &= \boldsymbol{b}_2^{\mathrm{T}} + c_{n+\frac{1}{2}} \left(N_3\, \boldsymbol{b}_3^{\mathrm{T}} + N_4\, \boldsymbol{b}_4^{\mathrm{T}}\right) - s_{n+\frac{1}{2}} \left(N_3\, \bar{\theta}_{1,n+\frac{1}{2}} + N_4\, \bar{\theta}_{2,n+\frac{1}{2}}\right) \frac{\boldsymbol{z}^{\mathrm{T}}}{l_{n+\frac{1}{2}}} \\
\boldsymbol{f}_3^{\mathrm{T}} &= N_5\, \boldsymbol{b}_3^{\mathrm{T}} + N_6\, \boldsymbol{b}_4^{\mathrm{T}} + \frac{\boldsymbol{z}^{\mathrm{T}}}{l_{n+\frac{1}{2}}}
\end{aligned} \tag{39}$$

with the following notations

$$\begin{aligned}
\boldsymbol{z} &= \begin{bmatrix} s_{n+\frac{1}{2}} & -c_{n+\frac{1}{2}} & 0 & -s_{n+\frac{1}{2}} & c_{n+\frac{1}{2}} & 0 \end{bmatrix}^{\mathrm{T}} \\
\boldsymbol{b}_1 &= \begin{bmatrix} N_1 & 0 & 0 & N_2 & 0 & 0 \end{bmatrix}^{\mathrm{T}} \\
\boldsymbol{b}_2 &= \begin{bmatrix} 0 & N_1 & 0 & 0 & N_2 & 0 \end{bmatrix}^{\mathrm{T}} \\
\boldsymbol{b}_3 &= \begin{bmatrix} 0 & 0 & 1 & 0 & 0 & 0 \end{bmatrix}^{\mathrm{T}} - \frac{\boldsymbol{z}}{l_{n+\frac{1}{2}}} \\
\boldsymbol{b}_4 &= \begin{bmatrix} 0 & 0 & 0 & 0 & 0 & 1 \end{bmatrix}^{\mathrm{T}} - \frac{\boldsymbol{z}}{l_{n+\frac{1}{2}}}
\end{aligned} \tag{40}$$

With the help of the third relation in Eqs.(30), the accelerations at the midpoint are

obtained as

$$\ddot{u}_{G,n+\frac{1}{2}} = \frac{2}{\Delta t^2}\,\Delta u_G - \frac{2}{\Delta t}\,\dot{u}_{G,n} = \frac{2}{\Delta t^2}\,\boldsymbol{f}_1^{\mathrm{T}}\,\Delta \boldsymbol{q} - \frac{2}{\Delta t}\,\dot{u}_{G,n} \tag{41}$$

$$\ddot{w}_{G,n+\frac{1}{2}} = \frac{2}{\Delta t^2}\,\Delta w_G - \frac{2}{\Delta t}\,\dot{w}_{G,n} = \frac{2}{\Delta t^2}\,\boldsymbol{f}_2^{\mathrm{T}}\,\Delta \boldsymbol{q} - \frac{2}{\Delta t}\,\dot{w}_{G,n} \tag{42}$$

$$\ddot{\theta}_{G,n+\frac{1}{2}} = \frac{2}{\Delta t^2}\Delta\theta_G - \frac{2}{\Delta t}\dot{\theta}_{G,n} = \frac{2}{\Delta t^2}\boldsymbol{f}_3^{\mathrm{T}}\,\Delta \boldsymbol{q} - \frac{2}{\Delta t}\dot{\theta}_{G,n} \tag{43}$$

Further, from Eq.(32), the strain fields at time $n+\frac{1}{2}$ are obtained as

$$\varepsilon_{n+\frac{1}{2}} = \varepsilon_n + \frac{\Delta t}{2}\,\dot{\varepsilon}_{n+\frac{1}{2}} \tag{44}$$

$$\kappa_{n+\frac{1}{2}} = \kappa_n + \frac{\Delta t}{2}\,\dot{\kappa}_{n+\frac{1}{2}} \tag{45}$$

in which the strain velocity fields can be calculated using Eqs.(17),(18) and (30) as

$$\dot{\varepsilon}_{n+\frac{1}{2}} = \frac{\Delta\varepsilon}{\Delta t} = \boldsymbol{f}_4^{\mathrm{T}}\,\frac{\Delta \boldsymbol{q}}{\Delta t} \tag{46}$$

$$\dot{\kappa}_{n+\frac{1}{2}} = \frac{\Delta\kappa}{\Delta t} = \boldsymbol{f}_5^{\mathrm{T}}\,\frac{\Delta \boldsymbol{q}}{\Delta t} \tag{47}$$

with

$$\boldsymbol{f}_4^{\mathrm{T}} = \frac{\boldsymbol{r}^{\mathrm{T}}}{l_0} + \left(\frac{2}{15}\boldsymbol{b}_3^{\mathrm{T}} - \frac{1}{30}\boldsymbol{b}_4^{\mathrm{T}}\right)\bar{\theta}_{1,n+\frac{1}{2}} + \left(\frac{2}{15}\boldsymbol{b}_4^{\mathrm{T}} - \frac{1}{30}\boldsymbol{b}_3^{\mathrm{T}}\right)\bar{\theta}_{2,n+\frac{1}{2}} \tag{48}$$

$$\boldsymbol{f}_5^{\mathrm{T}} = N_{3,xx}\,\boldsymbol{b}_3^{\mathrm{T}} + N_{4,xx}\,\boldsymbol{b}_4^{\mathrm{T}} \tag{49}$$

and

$$\boldsymbol{r} = \begin{bmatrix} -c_{n+\frac{1}{2}} & -s_{n+\frac{1}{2}} & 0 & c_{n+\frac{1}{2}} & s_{n+\frac{1}{2}} & 0 \end{bmatrix}^{\mathrm{T}} \tag{50}$$

It can be observed that updating the strains by integrated the strain velocity using Eqs. (44) and (45) produces strains at $n+1$ that are not equal to the strains determined from the total displacements and rotations at $n+1$. However, the displacement field itself is approximated using the mid-point rule and so the suggested strain field updates based on strain velocities follows the same line of the displacement update and is accordingly consistent with the second order accuracy know for single step method.

4.3. Residual force vector and tangent stiffness matrix

The residual force vector at $t = n+\frac{1}{2}$ is defined from Eq.(35) as

$$\boldsymbol{f}_{R,n+\frac{1}{2}} = \boldsymbol{f}_{k,n+\frac{1}{2}} + \boldsymbol{f}_{g,n+\frac{1}{2}} - \boldsymbol{f}_{ext,n+\frac{1}{2}} = 0 \tag{51}$$

in which $\boldsymbol{f}_{k,n+\frac{1}{2}}$ is the inertia force vector, $\boldsymbol{f}_{g,n+\frac{1}{2}}$ the elastic force vector and $\boldsymbol{f}_{ext,n+\frac{1}{2}}$ the external load vector. By inserting Eqs. (41), (42) and (43) into (35), the following expression for the inertia force vector is obtained

$$\begin{aligned}\boldsymbol{f}_{k,n+\frac{1}{2}} = {} & \frac{2}{\Delta t^2}\int_{l_0}\left[\rho A\,\left(\boldsymbol{f}_1\boldsymbol{f}_1^{\mathrm{T}} + \boldsymbol{f}_2\boldsymbol{f}_2^{\mathrm{T}}\right) + \rho I\,\boldsymbol{f}_3\boldsymbol{f}_3^{\mathrm{T}}\right]\Delta \boldsymbol{q}\,\mathrm{d}x \\ & - \frac{2}{\Delta t}\int_{l_0}\left[\rho A\,\left(\dot{u}_{G,n}\,\boldsymbol{f}_1 + \dot{w}_{G,n}\,\boldsymbol{f}_2\right) + \rho I\,\dot{\theta}_{G,n}\,\boldsymbol{f}_3\right]\mathrm{d}x\end{aligned} \tag{52}$$

in which the velocities at time n are evaluated, using Eqs. (10), (11) and (13);

$$\begin{aligned}
\dot{u}_{G,n} &= N_1\, v_{u1,n} + N_2\, v_{u2,n} + N_3\, v_{u3,n} + N_4\, v_{u4,n} \\
\dot{w}_{G,n} &= N_1\, v_{w1,n} + N_2\, v_{w2,n} + N_3\, v_{w3,n} + N_4\, v_{w4,n} \\
\dot{\theta}_{G,n} &= N_5\, v_{\theta 1,n} + N_6\, v_{\theta 2,n} + v_{\theta 3,n}
\end{aligned} \tag{53}$$

The quantities v_{ui}, v_{wi} $(i = 1:4)$ and $v_{\theta j}$ $(j = 1:3)$ are updated at the end of each step by according to

$$\begin{aligned}
v_{u1,n+1} &= \frac{2}{\Delta t}\left[\begin{array}{cccccc} 1 & 0 & 0 & 0 & 0 & 0 \end{array}\right]\Delta \boldsymbol{q} - v_{u1,n} \\
v_{u2,n+1} &= \frac{2}{\Delta t}\left[\begin{array}{cccccc} 0 & 0 & 0 & 1 & 0 & 0 \end{array}\right]\Delta \boldsymbol{q} - v_{u2,n} \\
v_{u3,n+1} &= \frac{2}{\Delta t}\left(-s_{n+\frac{1}{2}}\,\boldsymbol{b}_3^{\mathrm{T}} - c_{n+\frac{1}{2}}\,\bar{\theta}_{1,n+\frac{1}{2}}\frac{\boldsymbol{z}^{\mathrm{T}}}{l_{n+\frac{1}{2}}}\right)\Delta \boldsymbol{q} - v_{u3,n} \\
v_{u4,n+1} &= \frac{2}{\Delta t}\left(-s_{n+\frac{1}{2}}\,\boldsymbol{b}_4^{\mathrm{T}} - c_{n+\frac{1}{2}}\,\bar{\theta}_{2,n+\frac{1}{2}}\frac{\boldsymbol{z}^{\mathrm{T}}}{l_{n+\frac{1}{2}}}\right)\Delta \boldsymbol{q} - v_{u4,n}
\end{aligned} \tag{54}$$

$$\begin{aligned}
v_{w1,n+1} &= \frac{2}{\Delta t}\left[\begin{array}{cccccc} 0 & 1 & 0 & 0 & 0 & 0 \end{array}\right]\Delta \boldsymbol{q} - v_{w1,n} \\
v_{w2,n+1} &= \frac{2}{\Delta t}\left[\begin{array}{cccccc} 0 & 0 & 0 & 0 & 1 & 0 \end{array}\right]\Delta \boldsymbol{q} - v_{w2,n} \\
v_{w3,n+1} &= \frac{2}{\Delta t}\left(c_{n+\frac{1}{2}}\,\boldsymbol{b}_3^{\mathrm{T}} - s_{n+\frac{1}{2}}\,\bar{\theta}_{1,n+\frac{1}{2}}\frac{\boldsymbol{z}^{\mathrm{T}}}{l_{n+\frac{1}{2}}}\right)\Delta \boldsymbol{q} - v_{w3,n} \\
v_{w4,n+1} &= \frac{2}{\Delta t}\left(c_{n+\frac{1}{2}}\,\boldsymbol{b}_4^{\mathrm{T}} - s_{n+\frac{1}{2}}\,\bar{\theta}_{2,n+\frac{1}{2}}\frac{\boldsymbol{z}^{\mathrm{T}}}{l_{n+\frac{1}{2}}}\right)\Delta \boldsymbol{q} - v_{w4,n}
\end{aligned} \tag{55}$$

$$\begin{aligned}
v_{\theta 1,n+1} &= \frac{2}{\Delta t}\boldsymbol{b}_3^{\mathrm{T}}\,\Delta \boldsymbol{q} - v_{\theta 1,n} \\
v_{\theta 2,n+1} &= \frac{2}{\Delta t}\boldsymbol{b}_4^{\mathrm{T}}\,\Delta \boldsymbol{q} - v_{\theta 2,n} \\
v_{\theta 3,n+1} &= \frac{2}{\Delta t}\left(\frac{\boldsymbol{z}^{\mathrm{T}}}{l_{n+\frac{1}{2}}}\right)\Delta \boldsymbol{q} - v_{\theta 3,n}
\end{aligned} \tag{56}$$

The inertia tangent stiffness matrix is computed by considering the derivative of the corresponding force vector with respect to the kinematic variables:

$$\mathbf{K}_k = \frac{\partial \boldsymbol{f}_{k,n+\frac{1}{2}}}{\partial \boldsymbol{q}_{n+1}} \tag{57}$$

Inserting Eqs.(44) and (45) into Eq.(35), the elastic force vector takes the form

$$\begin{aligned}
\boldsymbol{f}_{g,n+\frac{1}{2}} = \frac{1}{2}\int_{l_0} &\left(EA\,\boldsymbol{f}_4\boldsymbol{f}_4^{\mathrm{T}} + EI\,\boldsymbol{f}_5\boldsymbol{f}_5^{\mathrm{T}}\right)\Delta \boldsymbol{q}\,\mathrm{d}x \\
&+ \int_{l_0}\left(EA\,\varepsilon_n\,\boldsymbol{f}_4 + EI\,\kappa_n\,\boldsymbol{f}_5\right)\mathrm{d}x
\end{aligned} \tag{58}$$

The axial strain and the curvature are updated at the end of each step by using

$$\varepsilon_{n+1} = \varepsilon_n + \Delta t\, \dot{\varepsilon}_{n+\frac{1}{2}} = \varepsilon_n + \boldsymbol{f}_4^{\mathrm{T}} \Delta \boldsymbol{q} \tag{59}$$

$$\kappa_{n+1} = \kappa_n + \Delta t\, \dot{\kappa}_{n+\frac{1}{2}} = \kappa_n + \boldsymbol{f}_5^{\mathrm{T}} \Delta \boldsymbol{q} \tag{60}$$

The curvature κ_n is calculated as follows

$$\kappa_n = N_{3,xx}\, \bar{\theta}_{1,n} + N_{4,xx}\, \bar{\theta}_{2,n} \tag{61}$$

and the local nodal rotations are updated at the end of each step according to

$$\begin{aligned} \bar{\theta}_{1,n+1} &= \bar{\theta}_{1,n} + \boldsymbol{b}_3^{\mathrm{T}}\, \Delta \boldsymbol{q} \\ \bar{\theta}_{2,n+1} &= \bar{\theta}_{2,n} + \boldsymbol{b}_4^{\mathrm{T}}\, \Delta \boldsymbol{q} \end{aligned} \tag{62}$$

The elastic tangent stiffness matrix follows as

$$\mathbf{K}_g = \frac{\partial \boldsymbol{f}_{g,n+\frac{1}{2}}}{\partial \boldsymbol{q}_{n+1}} \tag{63}$$

The external force vector is defined as

$$\boldsymbol{f}_{ext,n+\frac{1}{2}} = \int_{l_0} p_{u,n+\frac{1}{2}} \boldsymbol{f}_1 \,\mathrm{d}x + \int_{l_0} p_{w,n+\frac{1}{2}} \boldsymbol{f}_2 \,\mathrm{d}x + \int_{l_0} p_{\theta,n+\frac{1}{2}} \boldsymbol{f}_3 \,\mathrm{d}x + \boldsymbol{P}_{n+\frac{1}{2}} \tag{64}$$

from which the external tangent stiffness matrix follows as

$$\mathbf{K}_{ext} = \frac{\partial \boldsymbol{f}_{ext,n+\frac{1}{2}}}{\partial \boldsymbol{q}_{n+1}} \tag{65}$$

Hence, the total tangent matrix is

$$\mathbf{K}_{\mathrm{T}} = \mathbf{K}_k + \mathbf{K}_g - \mathbf{K}_{ext} \tag{66}$$

The details of the calculations of the force vectors $\boldsymbol{f}_{k,n+\frac{1}{2}}$, $\boldsymbol{f}_{g,n+\frac{1}{2}}$, $\boldsymbol{f}_{ext,n+\frac{1}{2}}$ and the tangent matrices $\mathbf{K}_k$, $\mathbf{K}_g$, $\mathbf{K}_{ext}$ are presented in the appendix. It can be noted that all these quantities are computed exactly by performing exact integrations over the element length. Both the tangent stiffness ($\mathbf{K}_g$) and tangent dynamic ($\mathbf{K}_k$) matrices are not symmetric. Symmetrizing these matrices is an option but in some cases, it will require a larger number of iterations at each step.

Algorithm 1 : Energy conserving scheme

1. Variables at time t_n
Nodal displacement, velocity and acceleration : $\boldsymbol{q}_n, \dot{\boldsymbol{q}}_n, \ddot{\boldsymbol{q}}_n$
Kinematic quantities : $v_{ui,n}, v_{wi,n}, v_{\theta j,n}$ for $i = 1:4, j = 1:3$
Axial strain and curvature-related quantities : $\varepsilon_n, \bar{\theta}_{1,n}, \bar{\theta}_{2,n}$
2. Initialization: $\boldsymbol{q}_{n+1}^j = \boldsymbol{q}_n^j$ and $\Delta \boldsymbol{q} = \boldsymbol{0}$
3. Loop over the iteration step j
Compute the residual force $\boldsymbol{f}_{R,n+\frac{1}{2}}(\boldsymbol{q}_{n+1}^j)$ (51)
Compute the tangent stiffness matrix $\mathbf{K}_{\mathrm{T}}(\boldsymbol{q}_{n+1}^j)$ (66)
Compute the incremental displacement $\Delta \boldsymbol{q}^j = -\mathbf{K}_{\mathrm{T}}^{-1} \boldsymbol{f}_{R,n+\frac{1}{2}}$
Check the convergence
if $\| \boldsymbol{f}_{R,n+\frac{1}{2}} \| > tol_1$ and $\| \Delta \boldsymbol{q}^j \| > tol_2$
$\boldsymbol{q}_{n+1}^{j+1} = \boldsymbol{q}_{n+1}^j + \Delta \boldsymbol{q}^j$
$j+1 \rightarrow j$ and go to (**3**)
else
Update the variables at time $n+1$: $\dot{\boldsymbol{q}}_{n+1}, \ddot{\boldsymbol{q}}_{n+1}$ (31)
$v_{ui,n+1}$ (54) , $v_{wi,n+1}$ (55) , $v_{\theta j,n+1}$ (56) for $i = 1:4, j = 1:3$
ε_{n+1} (59), $\bar{\theta}_{1,n+1}, \bar{\theta}_{2,n+1}$ (62), $n+1 \rightarrow n$ and go to (**1**)
end if

5. Conservation properties of the scheme

In this section we rigorously prove that the proposed method conserves the total energy of the system and, in absence of external loads, the linear and angular momenta remain constant.

5.1. Proof of the conservation of energy

The purpose of this section is to prove that the proposed energy-momentum algorithm conserves the total energy of the system while the external load is assumed conservative. To this end Eq.(35) is multiplied with the midpoint velocity $\dot{\boldsymbol{q}}_{n+\frac{1}{2}}$ to yield

$$\begin{aligned}
&\int_{l_0} \rho A\, \ddot{u}_{G,n+\frac{1}{2}} \dot{u}_{G,n+\frac{1}{2}}\, \mathrm{d}x + \int_{l_0} \rho A\, \ddot{w}_{G,n+\frac{1}{2}} \dot{w}_{G,n+\frac{1}{2}}\, \mathrm{d}x + \int_{l_0} \rho I\, \ddot{\theta}_{G,n+\frac{1}{2}} \dot{\theta}_{G,n+\frac{1}{2}}\, \mathrm{d}x \\
&+ \int_{l_0} EA\, \varepsilon_{n+\frac{1}{2}} \dot{\varepsilon}_{n+\frac{1}{2}}\, \mathrm{d}x + \int_{l_0} EI\, \kappa_{n+\frac{1}{2}} \dot{\kappa}_{n+\frac{1}{2}}\, \mathrm{d}x - \int_{l_0} p_u\, \dot{u}_{G,n+\frac{1}{2}}\, \mathrm{d}x \\
&- \int_{l_0} p_w\, \dot{w}_{G,n+\frac{1}{2}}\, \mathrm{d}x - \int_{l_0} p_\theta\, \dot{\theta}_{G,n+\frac{1}{2}}\, \mathrm{d}x - \sum_{i=1}^{6} P_i\, \dot{q}_{i,n+\frac{1}{2}} = 0
\end{aligned} \tag{67}$$

which, with the help of the midpoint rule, gives

$$\begin{aligned}
&\int_{l_0} \rho A\, \frac{\dot{u}_{G,n+1} - \dot{u}_{G,n}}{\Delta t}\, \frac{\dot{u}_{G,n+1} + \dot{u}_{G,n}}{2}\, \mathrm{d}x + \int_{l_0} \rho A\, \frac{\dot{w}_{G,n+1} - \dot{w}_{G,n}}{\Delta t}\, \frac{\dot{w}_{G,n+1} + \dot{w}_{G,n}}{2}\, \mathrm{d}x \\
&+ \int_{l_0} \rho I\, \frac{\dot{\theta}_{G,n+1} - \dot{\theta}_{G,n}}{\Delta t}\, \frac{\dot{\theta}_{G,n+1} + \dot{\theta}_{G,n}}{2}\, \mathrm{d}x + \int_{l_0} EA\, \frac{\varepsilon_{n+1} + \varepsilon_n}{2}\, \frac{\varepsilon_{n+1} - \varepsilon_n}{\Delta t}\, \mathrm{d}x \\
&+ \int_{l_0} EI\, \frac{\kappa_{n+1} + \kappa_n}{2}\, \frac{\kappa_{n+1} - \kappa_n}{\Delta t}\, \mathrm{d}x - \int_{l_0} p_u\, \frac{u_{G,n+1} - u_{G,n}}{\Delta t}\, \mathrm{d}x \\
&- \int_{l_0} p_w\, \frac{w_{G,n+1} - w_{G,n}}{\Delta t}\, \mathrm{d}x - \int_{l_0} p_\theta\, \frac{\theta_{G,n+1} - \theta_{G,n}}{\Delta t}\, \mathrm{d}x - \sum_{i=1}^{6} P_i\, \frac{q_{i,n+1} - q_{i,n}}{\Delta t} = 0
\end{aligned} \tag{68}$$

This equation can be rewritten as

$$\begin{aligned}
&\frac{1}{2}\int_{l_0} \rho A\, \left(\dot{u}_{G,n+1}\, \dot{u}_{G,n+1} - \dot{u}_{G,n}\, \dot{u}_{G,n}\right) \mathrm{d}x + \frac{1}{2}\int_{l_0} \rho A\, \left(\dot{w}_{G,n+1}\, \dot{w}_{G,n+1} - \dot{w}_{G,n}\, \dot{w}_{G,n}\right) \mathrm{d}x \\
&+\frac{1}{2}\int_{l_0} \rho I\, \left(\dot{\theta}_{G,n+1}\, \dot{\theta}_{G,n+1} - \dot{\theta}_{G,n}\, \dot{\theta}_{G,n}\right) \mathrm{d}x + \frac{1}{2}\int_{l_0} EA\, \left(\varepsilon_{n+1}\, \varepsilon_{n+1} - \varepsilon_n\, \varepsilon_n\right) \mathrm{d}x \\
&+\frac{1}{2}\int_{l_0} EI\, \left(\kappa_{n+1}\, \kappa_{n+1} - \kappa_n\, \kappa_n\right) \mathrm{d}x - \int_{l_0} p_u\, \left(u_{G,n+1} - u_{G,n}\right)\, \mathrm{d}x \\
&- \int_{l_0} p_w\, \left(w_{G,n+1} - w_{G,n}\right)\, \mathrm{d}x - \int_{l_0} p_\theta\, \left(\theta_{G,n+1} - \theta_{G,n}\right) - \sum_{i=1}^{6} P_i\, \left(q_{i,n+1} - q_{i,n}\right) = 0
\end{aligned} \tag{69}$$

Finally, from the Eqs. (21), (22) and (23), Equation (69) is equivalent to

$$\left[\mathsf{K} + \mathsf{U}_{int} + \mathsf{U}_{ext}\right]_{n+1} = \left[\mathsf{K} + \mathsf{U}_{int} + \mathsf{U}_{ext}\right]_n \tag{70}$$

which shows that the proposed midpoint algorithm conserves the total energy of the system.

5.2. Proof of the conservation of linear momentum

In this subsection we prove that, for vanishing external loading, the proposed energy-momentum algorithm conserves the linear momentum. The equation of motion (35) can be written as

$$\begin{aligned}\boldsymbol{f}_{R,n+\frac{1}{2}} = &\int_{l_0} \rho A\, \ddot{u}_{G,n+\frac{1}{2}}\, \boldsymbol{f}_1\, \mathrm{d}x + \int_{l_0} \rho A\, \ddot{w}_{G,n+\frac{1}{2}}\, \boldsymbol{f}_2\, \mathrm{d}x + \int_{l_0} \rho I\, \ddot{\theta}_{G,n+\frac{1}{2}}\, \boldsymbol{f}_3\, \mathrm{d}x \\ &+ \int_{l_0} EA\, \varepsilon_{n+\frac{1}{2}}\, \boldsymbol{f}_4 \mathrm{d}x + \int_{l_0} EI\, \kappa_{n+\frac{1}{2}}\, \boldsymbol{f}_5\, \mathrm{d}x - \int_{l_0} p_{u,n+\frac{1}{2}}\, \boldsymbol{f}_1\, \mathrm{d}x \\ &- \int_{l_0} p_{w,n+\frac{1}{2}}\, \boldsymbol{f}_2\, \mathrm{d}x - \int_{l_0} p_{\theta,n+\frac{1}{2}}\, \boldsymbol{f}_3 \mathrm{d}x - \boldsymbol{P}_{n+\frac{1}{2}} = 0 \end{aligned} \tag{71}$$

The components $f_{Ri,n+\frac{1}{2}}$ of the residual vector are shown in Figure 2. Since each component is equal to zero, the following expressions, corresponding to the sums of the residual forces in horizontal and vertical directions, can be considered:

$$\begin{bmatrix} f_{R1,n+\frac{1}{2}} + f_{R4,n+\frac{1}{2}} \\ f_{R2,n+\frac{1}{2}} + f_{R5,n+\frac{1}{2}} \end{bmatrix} = \begin{bmatrix} 0 \\ 0 \end{bmatrix} \tag{72}$$

Besides, from Eqs.(39), (48) and (49) the following expressions can be derived

$$\begin{aligned} \begin{bmatrix} f_{11} + f_{14} \\ f_{12} + f_{15} \end{bmatrix} &= \begin{bmatrix} 1 \\ 0 \end{bmatrix} \\ \begin{bmatrix} f_{21} + f_{24} \\ f_{22} + f_{25} \end{bmatrix} &= \begin{bmatrix} 0 \\ 1 \end{bmatrix} \\ \begin{bmatrix} f_{31} + f_{34} \\ f_{32} + f_{35} \end{bmatrix} &= \begin{bmatrix} 0 \\ 0 \end{bmatrix} \end{aligned} \tag{73}$$

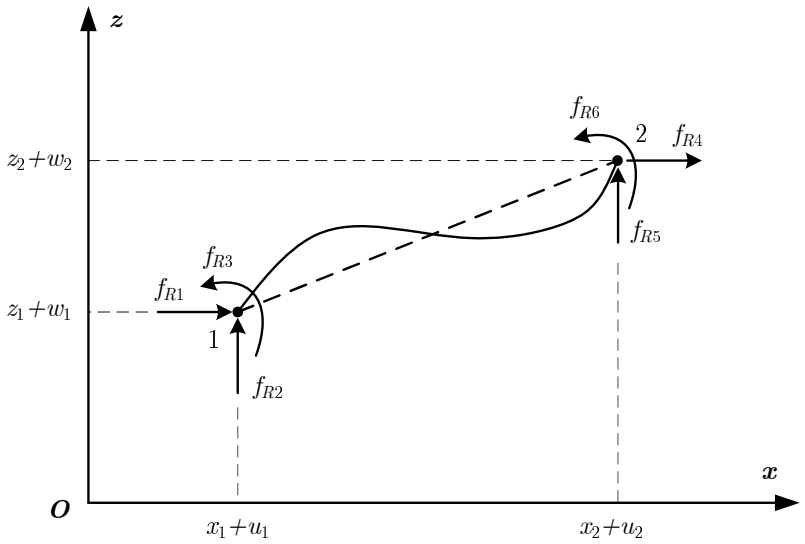

Figure 2: Components of the residual force vector

and

$$\begin{aligned}\left[\begin{array}{c} f_{41}+f_{44} \\ f_{42}+f_{45} \end{array}\right] &= \left[\begin{array}{c} 0 \\ 0 \end{array}\right] \\ \left[\begin{array}{c} f_{51}+f_{54} \\ f_{52}+f_{55} \end{array}\right] &= \left[\begin{array}{c} 0 \\ 0 \end{array}\right]\end{aligned} \tag{74}$$

where f_{ij} is the j^{th} component of vector $\boldsymbol{f}_i$. By combining Eqs.(73) and (74), Eq.(72) can be rewritten as

$$\begin{aligned}&\int_{l_0} \rho A\, \ddot{u}_{G,n+\frac{1}{2}} \left[\begin{array}{c} 1 \\ 0 \end{array}\right] \mathrm{d}x + \int_{l_0} \rho A\, \ddot{w}_{G,n+\frac{1}{2}} \left[\begin{array}{c} 0 \\ 1 \end{array}\right] \mathrm{d}x + \int_{l_0} \rho I\, \ddot{\theta}_{G,n+\frac{1}{2}} \left[\begin{array}{c} 0 \\ 0 \end{array}\right] \mathrm{d}x \\ &+ \int_{l_0} EA\, \varepsilon_{n+\frac{1}{2}} \left[\begin{array}{c} 0 \\ 0 \end{array}\right] \mathrm{d}x + \int_{l_0} EI\, \kappa_{n+\frac{1}{2}} \left[\begin{array}{c} 0 \\ 0 \end{array}\right] \mathrm{d}x - \int_{l_0} p_{u,n+\frac{1}{2}} \left[\begin{array}{c} 1 \\ 0 \end{array}\right] \mathrm{d}x \\ &- \int_{l_0} p_{w,n+\frac{1}{2}} \left[\begin{array}{c} 0 \\ 1 \end{array}\right] \mathrm{d}x - \int_{l_0} p_{\theta,n+\frac{1}{2}} \left[\begin{array}{c} 0 \\ 0 \end{array}\right] \mathrm{d}x - \left[\begin{array}{c} P_{1,n+\frac{1}{2}} + P_{4,n+\frac{1}{2}} \\ P_{2,n+\frac{1}{2}} + P_{5,n+\frac{1}{2}} \end{array}\right] = 0\end{aligned} \tag{75}$$

which simplifies to

$$\int_{l_0} \rho A \left[\begin{array}{c} \ddot{u}_{G,n+\frac{1}{2}} \\ \ddot{w}_{G,n+\frac{1}{2}} \end{array}\right] \mathrm{d}x = \left[\begin{array}{c} \int_{l_0} p_{u,n+\frac{1}{2}}\, \mathrm{d}x + P_{1,n+\frac{1}{2}} + P_{4,n+\frac{1}{2}} \\ \int_{l_0} p_{w,n+\frac{1}{2}}\, \mathrm{d}x + P_{2,n+\frac{1}{2}} + P_{5,n+\frac{1}{2}} \end{array}\right] \tag{76}$$

For vanishing external loading, together with the midpoint rule, the last equation becomes

$$\int_{l_0} \rho A \left[\begin{array}{c} \dot{u}_{G,n+1} \\ \dot{w}_{G,n+1} \end{array}\right] \mathrm{d}x = \int_{l_0} \rho A \left[\begin{array}{c} \dot{u}_{G,n} \\ \dot{w}_{G,n} \end{array}\right] \mathrm{d}x \tag{77}$$

which means that the linear momentum is conserved:

$$\mathbf{L}_{n+1} = \mathbf{L}_n$$

5.3. Proof of the conservation of angular momentum

The purpose of this section is formally prove that for vanishing external moments, the proposed energy-momentum algorithm conserves the angular momentum. As for the linear momentum, the residual vector, see Eq.(71) and Figure 2 is used. Since each component of $f_{Ri,n+\frac{1}{2}}$ is equal to zero, the following expression, corresponding to the sum of the moments about the origin **O** can be considered:

$$\begin{aligned}\mu(\boldsymbol{f}_{R,n+\frac{1}{2}}) = &(x_1 + u_{1,n+\frac{1}{2}}) f_{R2,n+\frac{1}{2}} - (z_1 + w_{1,n+\frac{1}{2}}) f_{R1,n+\frac{1}{2}} \\ &+ (x_2 + u_{2,n+\frac{1}{2}}) f_{R5,n+\frac{1}{2}} - (z_2 + w_{2,n+\frac{1}{2}}) f_{R4,n+\frac{1}{2}} \\ &+ f_{R3,n+\frac{1}{2}} + f_{R6,n+\frac{1}{2}} = 0\end{aligned} \tag{78}$$

Moreover, the following expressions can easily be obtained:

$$\begin{aligned}\mu\left(\frac{\boldsymbol{z}}{l_{n+\frac{1}{2}}}\right) = &\frac{1}{l_{n+\frac{1}{2}}} \Big[c_{n+\frac{1}{2}} \left(x_2 + u_{2,n+\frac{1}{2}} - x_1 - u_{1,n+\frac{1}{2}} \right) \\ &+ s_{n+\frac{1}{2}} \left(z_2 + w_{2,n+\frac{1}{2}} - z_1 - w_{1,n+\frac{1}{2}} \right) \Big] = c_{n+\frac{1}{2}}^2 + s_{n+\frac{1}{2}}^2 = 1\end{aligned} \tag{79}$$

$$\begin{aligned}\mu\left(\boldsymbol{r}\right) = &s_{n+\frac{1}{2}} \left(x_2 + u_{2,n+\frac{1}{2}} - x_1 - u_{1,n+\frac{1}{2}} \right) \\ &- c_{n+\frac{1}{2}} \left(z_2 + w_{2,n+\frac{1}{2}} - z_1 - w_{1,n+\frac{1}{2}} \right) = 0\end{aligned} \tag{80}$$

$$
\begin{aligned}
\mu(\boldsymbol{f}_1) &= -N_1\left(z_1 + w_{1,n+\frac{1}{2}}\right) - N_2\left(z_2 + w_{2,n+\frac{1}{2}}\right) \\
&\quad + \left[s_{n+\frac{1}{2}}\,(N_3+N_4) - c_{n+\frac{1}{2}}\,w_{n+\frac{1}{2}}\right]\mu\left(\frac{\boldsymbol{z}}{l_{n+\frac{1}{2}}}\right) - s_{n+\frac{1}{2}}(N_3+N_4) \\
&= -N_1\left(z_1 + w_{1,n+\frac{1}{2}}\right) - N_2\left(z_2 + w_{2,n+\frac{1}{2}}\right) - c_{n+\frac{1}{2}}\,w_{n+\frac{1}{2}} \\
&= -w_{G,n+\frac{1}{2}} \qquad (81) \\
\mu(\boldsymbol{f}_2) &= N_1\left(x_1 + u_{1,n+\frac{1}{2}}\right) + N_2\left(x_2 + u_{2,n+\frac{1}{2}}\right) \\
&\quad + \left[-c_{n+\frac{1}{2}}(N_3+N_4) - s_{n+\frac{1}{2}}\,w_{n+\frac{1}{2}}\right]\mu\left(\frac{\boldsymbol{z}}{l_{n+\frac{1}{2}}}\right) + c_{n+\frac{1}{2}}\,(N_3+N_4) \\
&= N_1\left(x_1 + u_{1,n+\frac{1}{2}}\right) + N_2\left(x_2 + u_{2,n+\frac{1}{2}}\right) - s_{n+\frac{1}{2}}\,w_{n+\frac{1}{2}} \\
&= u_{G,n+\frac{1}{2}} \qquad (82) \\
\mu(\boldsymbol{f}_3) &= (1 - N_5 - N_6)\,\mu\left(\frac{\boldsymbol{z}}{l_{n+\frac{1}{2}}}\right) + N_5 + N_6 = 1 \qquad (83)
\end{aligned}
$$

$$
\begin{aligned}
\mu(\boldsymbol{f}_4) &= \frac{1}{l_0}\mu(\boldsymbol{r}) - \frac{1}{10}\left(\bar{\theta}_{1,n+\frac{1}{2}} + \bar{\theta}_{2,n+\frac{1}{2}}\right)\mu\left(\frac{\boldsymbol{z}}{l_{n+\frac{1}{2}}}\right) \\
&\quad + \frac{1}{10}\left(\bar{\theta}_{1,n+\frac{1}{2}} + \bar{\theta}_{2,n+\frac{1}{2}}\right) = 0 \qquad (84) \\
\mu(\boldsymbol{f}_5) &= -\left(N_{3,xx} + N_{4,xx}\right)\,\mu\left(\frac{\boldsymbol{z}}{l_{n+\frac{1}{2}}}\right) + N_{3,xx} + N_{4,xx} = 0 \qquad (85)
\end{aligned}
$$

With the help of Eqs.(81) to (85), Eq. (78) can be rewritten as

$$
\begin{aligned}
&\int_{l_0} \rho A\left(u_{G,n+\frac{1}{2}}\ddot{w}_{G,n+\frac{1}{2}} - w_{G,n+\frac{1}{2}}\ddot{u}_{G,n+\frac{1}{2}}\right)\mathrm{d}x + \int_{l_0}\rho I\,\ddot{\theta}_{G,n+\frac{1}{2}}\mathrm{d}x \\
&= \int_{l_0}\left(u_{G,n+\frac{1}{2}}p_{w,n+\frac{1}{2}} - w_{G,n+\frac{1}{2}}p_{u,n+\frac{1}{2}}\right)\mathrm{d}x + (x_1 + u_{1,n+\frac{1}{2}})P_{2,n+\frac{1}{2}} \\
&-(z_1 + w_{1,n+\frac{1}{2}})P_{1,n+\frac{1}{2}} + (x_2 + u_{2,n+\frac{1}{2}})P_{5,n+\frac{1}{2}} - (z_2 + w_{2,n+\frac{1}{2}})P_{4,n+\frac{1}{2}} \\
&+ \int_{l_0} p_{\theta,n+\frac{1}{2}}\,\mathrm{d}x + P_{3,n+\frac{1}{2}} + P_{6,n+\frac{1}{2}} \qquad (86)
\end{aligned}
$$

Applying the midpoint rule to the previous equation gives

$$
\begin{aligned}
&\int_{l_0}\rho A\begin{bmatrix} u_{G,n+1} \\ w_{G,n+1} \\ 0 \end{bmatrix} \times \begin{bmatrix} \dot{u}_{G,n+1} \\ \dot{w}_{G,n+1} \\ 0 \end{bmatrix}\mathrm{d}x + \int_{l_0}\rho I\begin{bmatrix} 0 \\ 0 \\ \dot{\theta}_{G,n+1} \end{bmatrix}\mathrm{d}x \\
&= \int_{l_0}\rho A\begin{bmatrix} u_{G,n} \\ w_{G,n} \\ 0 \end{bmatrix} \times \begin{bmatrix} \dot{u}_{G,n} \\ \dot{w}_{G,n} \\ 0 \end{bmatrix}\mathrm{d}x + \int_{l_0}\rho I\begin{bmatrix} 0 \\ 0 \\ \dot{\theta}_{G,n} \end{bmatrix}\mathrm{d}x + \Delta t\,M_{ext,n+\frac{1}{2}} \qquad (87)
\end{aligned}
$$

where M_{ext} is defined in (29). In the case of vanishing external moments, the result is immediate

$$
\mathsf{J}_{n+1} = \mathsf{J}_n \qquad (88)
$$

which shows the conservation of the angular momentum.

6. Numerical examples

Four numerical applications are presented in this section. The first purpose of these examples is to verify numerically that the proposed energy-momentum algorithm conserves the total energy of the system and remains stable even if a very large number of time steps are considered. The second purpose is to show that in the absence of applied external loads, the proposed algorithm conserves the linear and angular momenta. For all the examples, the number of iterations at each step was between 3 and 5.

6.1. Cantilever beam

The first example, see Figure 3, is a cantilever beam loaded by a concentrated force at its free end. The load history is as depicted in the same figure. The parameters of the problem are:

$$L = 3 \text{ m}, A = 0.1 \text{ m}^2, I = 8.33 \times 10^{-5} \text{ m}^4$$
$$E = 200 \text{ GPa}, \rho = 48831 \text{ kg/m}^3$$
$$\Delta t = 10^{-3} \text{ s, Number of elements} = 4$$

The results obtained with the present energy-momentum formulation are compared against the ones obtained with the co-rotational formulation proposed by Le et al. [12]. In this previous formulation, the alpha method was used to solve the equations of motion. Three cases are considered here, $\alpha = 0$, which corresponds to the classical average acceleration method, $\alpha = -0.01$ and $\alpha = -0.001$ which gives a small numerical damping that limits the influence of higher modes on the response.

The results presented in Figure 4 show that in the early stage of the motion all three approaches give exactly the same results. Figures 5 and 6 show clearly that with the average acceleration method, the total energy of the system does blow up after some $24s$, causing the solution to diverge. With the alpha method, the solution does not diverge, but as expected, there is a loss of the total energy due to numerical damping. With $\alpha = -0.001$ the loss of energy is small. However, with the present energy-momentum approach, the total energy is constant and the solution remains stable even if a very large number of steps (one million) is applied.

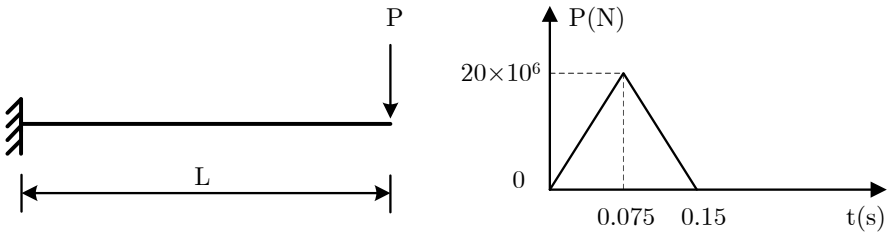

Figure 3: Geometry and load history of cantilever beam

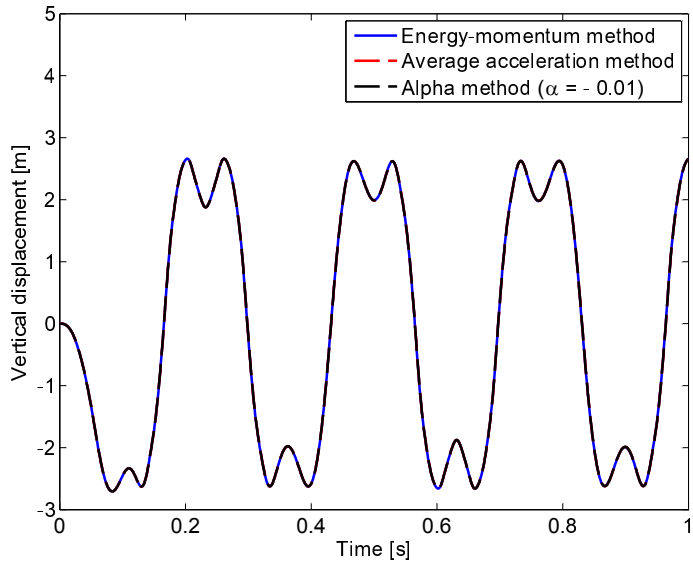

Figure 4: Comparison the displacements at the end of the tip

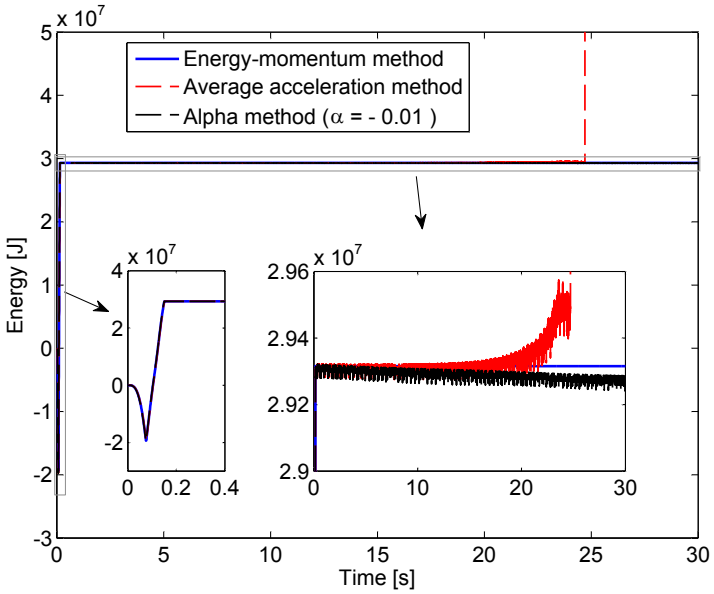

Figure 5: Comparison of energy from 0s to 30s

6.2. Lee's frame

The second example, see Figure 7, is the Lee's frame [63] subjected to an applied constant load after the time $t = 2.5 \times 10^{-4} s$. The parameters of the problem are

$$L = 2.4 \text{ m}, A = 0.06 \text{ m}^2, I = 2 \times 10^{-4} \text{ m}^4$$
$$E = 210 \text{ GPa}, \rho = 7850 \text{ kg/m}^3$$
$$\Delta t = 2.5 \times 10^{-4} \text{ s}, \text{ Number of elements} = 10$$

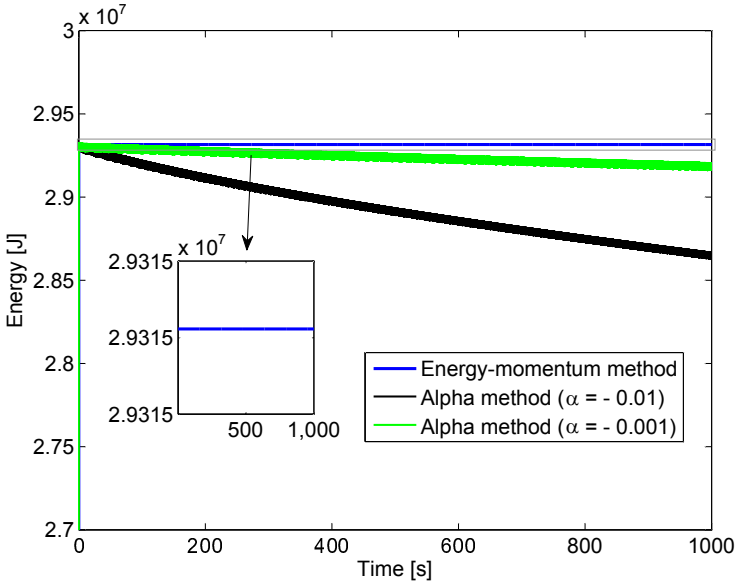

Figure 6: Comparison of energy from 0s to 1000s

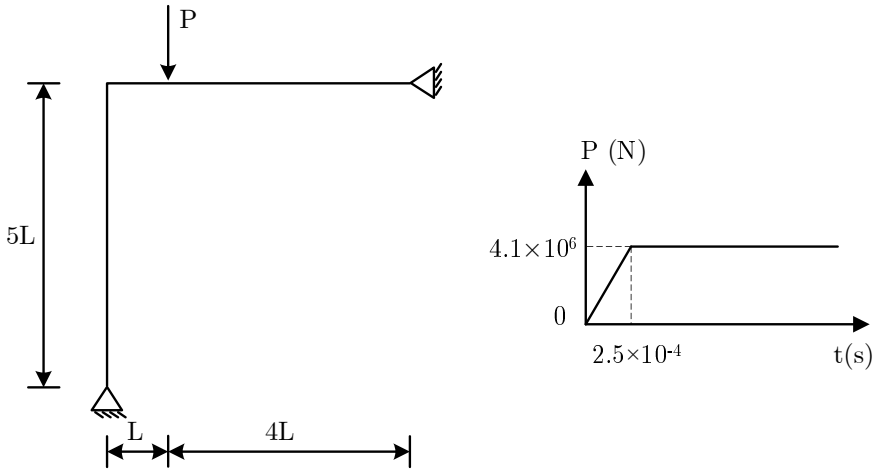

Figure 7: Geometry and load history of Lee's frame

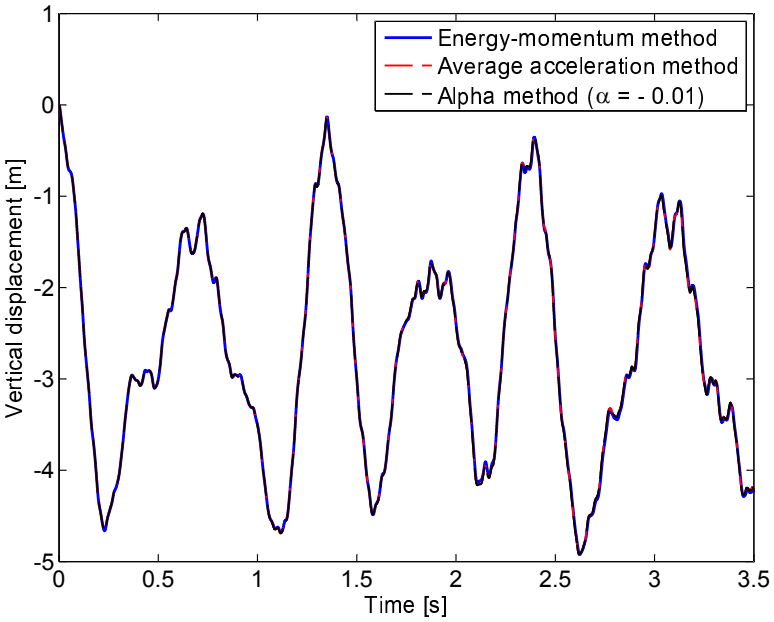

Figure 8: Comparison the vertical displacements at the point load

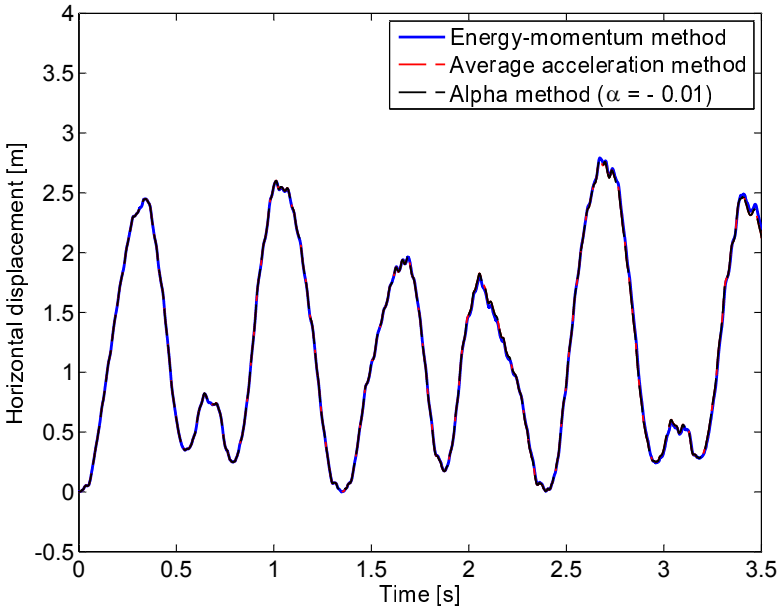

Figure 9: Comparison horizontal displacements at the point load

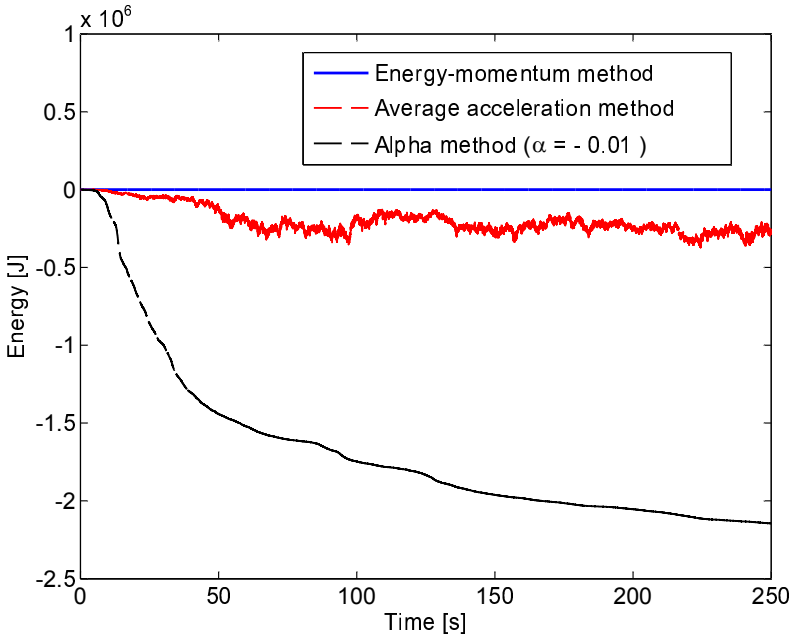

Figure 10: Comparison of energy of Lee's frame

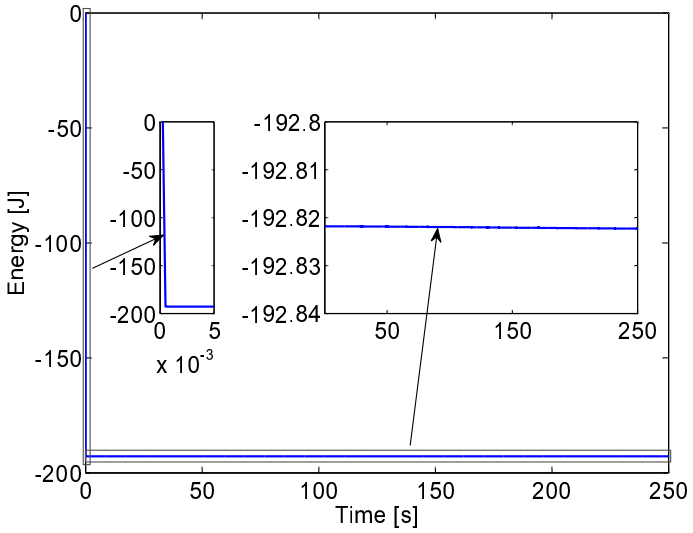

Figure 11: Energy of Lee's frame (by Energy-momentum method)

This example has been also studied with the average acceleration and alpha methods. The vertical and horizontal displacements at the loading point are depicted in Figures 8 and 9. It can be observed that exactly the same results are obtained with the three methods. Besides, Figure 10 shows that the average acceleration and alpha methods does not conserve the energy of the system when the load is constant. However, with the energy-momentum method, the energy remains constant (detail in Figure 11) even if one million time steps are performed. It can be noted that the absolute maximum external potential is about $2 \times 10^7 J$.

6.3. Shallow arch beam

The third example is the shallow arch depicted in Figure 12. The structure is subjected to a time-dependent concentrated force $P = Fsin(\omega\, t)$ at its mid span. The amplitude of the load is $F = 160$ MN and its frequency $\omega = 1000\, rad/s$. The parameters of the problem are:

$$L = 10 \text{ m}, H = 1.3397 \text{ m}, R = 30 \text{ m}, A = 0.087 \text{ m}^2, I = 3,562 \times 10^{-3} \text{ m}^4,$$
$$E = 210 \text{ GPa}, \rho = 7850 \text{ kg/m}^3$$
$$\Delta t = 10^{-5}\text{s}, \text{ Number of elements} = 10$$

In this example, the external load is not constant and consequently Equation (70), in which the external load is assumed to be constant, cannot be used to show the conservation of energy. However, it can be shown that the difference between the kinetic and elastic energies between the time instants t_n and t_{n+1} is equal to the external work performed by the applied force P between the time instants t_n and t_{n+1}:

$$[\mathsf{K} + \mathsf{U}_{int}]_{n+1} - [\mathsf{K} + \mathsf{U}_{int}]_n = \mathsf{W}_{ext}|_n^{n+1} \tag{89}$$

Applying the midpoint rule provides

$$\mathsf{W}_{ext}|_n^{n+1} = \int_n^{n+1} P dq = P_{n+\frac{1}{2}} \left(q_{n+1} - q_n\right) \tag{90}$$

Moreover, since at the beginning there is no energy in the system, the above equation gives

$$[\mathsf{K} + \mathsf{U}_{int} - \mathsf{W}_{ext}]_n = 0, \qquad \mathsf{W}_{ext,n} = \int_0^n P dq \tag{91}$$

At each step, the relative error is defined as

$$\eta = \frac{|\mathsf{K} + \mathsf{U}_{int} - \mathsf{W}_{ext}|}{|\mathsf{W}_{ext}|} \tag{92}$$

This quantity has been calculated for one million time steps. The maximum obtained value is 9.35×10^{-9} whereas the maximum external energy is about 14.7×10^7J. Furthermore, the beam undergoes large displacements with high oscillations as shown in Figure 13. These results proved a good stability of the proposed algorithm for a long period analysis.

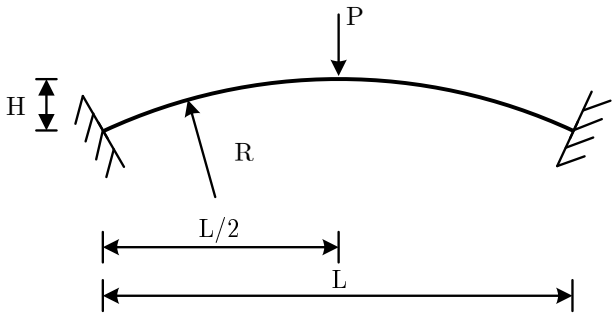

Figure 12: Geometry and load history of shallow arch beam

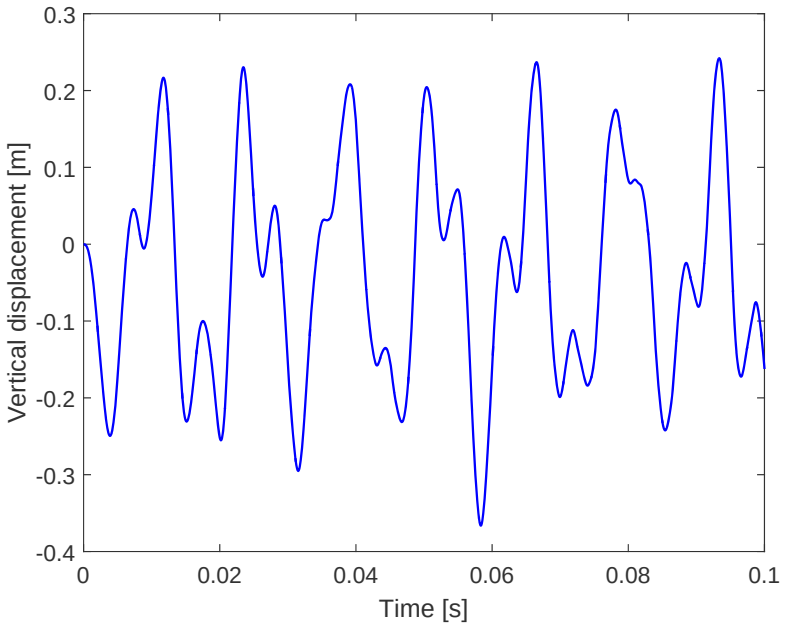

Figure 13: Vertical displacements at mid-span from 0s to 0.1s

6.4. Free flying beam

The last example is a free flying beam, see Figure 14. The parameters of the problems are

$$L = 3 \text{ m}, A = 0.002 \text{ m}^2, I = 6.667 \times 10^{-8} \text{ m}^4$$
$$E = 210 \text{ GPa}, \rho = 7850 \text{ kg/m}^3$$
$$\Delta t = 10^{-4} \text{ s}, \text{ Number of elements} = 4$$

The interest of this problem is that after 0.4s, no forces and moments are applied to the beam. Consequently, this problem is suitable to study the conservation of the linear and angular momenta. Since only vertical loads are applied at the beginning, the linear momentum in the horizontal direction should be zero. As shown in Figure 16, this linear momentum is almost zero with the maximum value of 3×10^{-7}. Figures 15, 16 and 17 show that the energy, the linear momentum in the vertical direction and the angular momentum are constant. This example has also been studied with the average acceleration and alpha ($\alpha = -0.01$) methods. As shown in Figure 18, the angular momentum does not remain with these two methods. Finally, the snap shots of the motion are shown in Figure 19. The points A and B are the two ends of the beam.

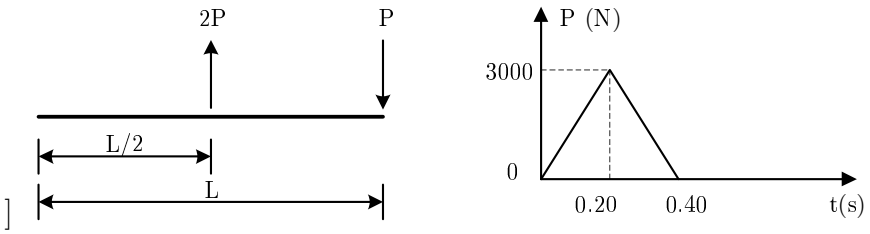

Figure 14: Geometry and load history of free flying beam

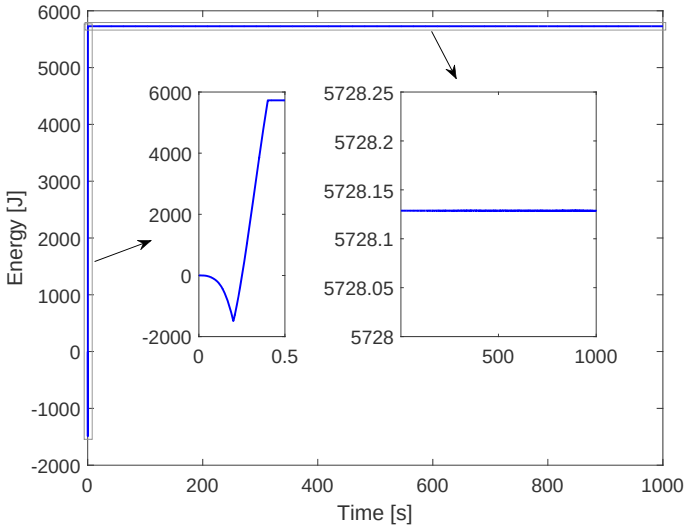

Figure 15: Energy of free flying beam

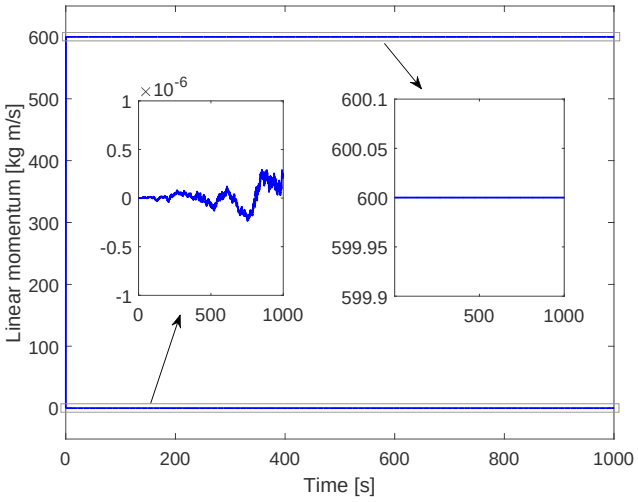

Figure 16: Linear momentum

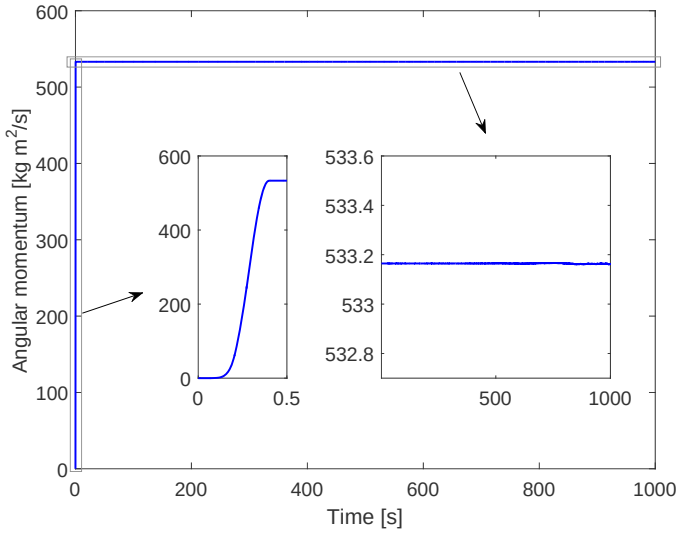

Figure 17: Angular momentum of Energy-Momentum method

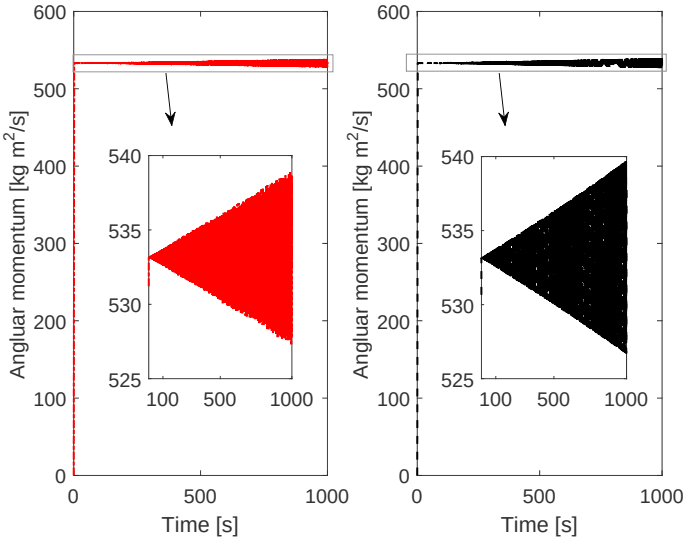

Figure 18: Angular momentum of Average acceleration method (left) and Alpha method $\alpha = -0.01$ (right)

7. Conclusion

In this paper the development of a stable momentum and energy conserving integration scheme for a co-rotational beam formulation has been achieved. The main idea is to use the classical midpoint rules for both the kinematic and strain quantities. Although the idea as such was developed in previous work, its realization is problem-specific and had to be developed here in the context of the co-rotational 2D beam element formulation. In that context the developments here are novel. The advantage of the proposed algorithm lies in the fact that conservation of the total energy of the system results in a very stable and accurate algorithm even for very large number of time steps. Besides, in the absence of applied external loads, the linear and angular momenta are constant. These characteristics have been proved theoretically and confirmed numerically by using four numerical examples.

The extension of the proposed method to co-rotational 3D beams is very challenging and will be the purpose of future research work. In that context, the main difficult is related to the large spatial rotations and the way these rotations affect the strain rates.

Acknowledgements

The first and the third authors gratefully acknowledge financial support by the European Commission (Research Fund for Coal and Steel) through the project RobustImpact under grant agreement RFSR-CT-2012-00029 and the financial support of the region of Brittany (France) through the ARED funding scheme.

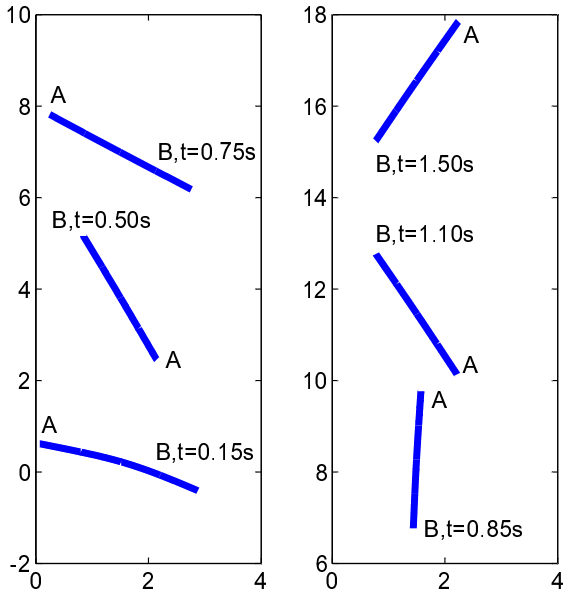

Figure 19: Snap shot

Appendix A Residual force and stiffness matrix

The residual vector force is defined as

$$\begin{aligned}\boldsymbol{f}_{R,n+\frac{1}{2}} =& \boldsymbol{f}_{k,n+\frac{1}{2}} + \boldsymbol{f}_{g,n+\frac{1}{2}} - \boldsymbol{f}_{ext,n+\frac{1}{2}} \\ =& \frac{2}{\Delta t^2}\int_{l_0}\left[\rho A\,\left(\boldsymbol{f}_1\boldsymbol{f}_1^{\mathrm{T}} + \boldsymbol{f}_2\boldsymbol{f}_2^{\mathrm{T}}\right) + \rho I\boldsymbol{f}_3\boldsymbol{f}_3^{\mathrm{T}}\right]\Delta\boldsymbol{q}\,dx \\ &-\frac{2}{\Delta t}\int_{l_0}\left[\rho A\,\left(\dot{u}_{G,n}\boldsymbol{f}_1 + \dot{w}_{G,n}\boldsymbol{f}_2\right) + \rho I\,\dot{\theta}_{G,n}\boldsymbol{f}_3\right]dx \\ &+\frac{1}{2}\int_{l_0}\left(EA\,\boldsymbol{f}_4\boldsymbol{f}_4^{\mathrm{T}} + EI\,\boldsymbol{f}_5\boldsymbol{f}_5^{\mathrm{T}}\right)\Delta\boldsymbol{q}\,dx \\ &+\int_{l_0}\left(EA\,\varepsilon_n\boldsymbol{f}_4 + EI\,\kappa_n\boldsymbol{f}_5\right)dx - \int_{l_0} p_{u,n+\frac{1}{2}}\boldsymbol{f}_1\,dx \\ &-\int_{l_0} p_{w,n+\frac{1}{2}}\boldsymbol{f}_2\,dx - \int_{l_0} p_{\theta,n+\frac{1}{2}}\boldsymbol{f}_3\,dx - P_{i,n+\frac{1}{2}}\end{aligned} \tag{A.93}$$

The following matrices are introduced:

$$\begin{aligned}&\int_{l_0}\left[\rho A\,\left(\boldsymbol{f}_1\boldsymbol{f}_1^{\mathrm{T}} + \boldsymbol{f}_2\boldsymbol{f}_2^{\mathrm{T}}\right)\right]\,dx = \mathbf{T}^{\mathrm{T}}\mathbf{M}_{l1}\mathbf{T} \\ &\int_{l_0}\rho I\boldsymbol{f}_3\boldsymbol{f}_3^{\mathrm{T}}\,dx = \mathbf{T}^{\mathrm{T}}\mathbf{M}_{l2}\mathbf{T} \\ &\int_{l_0} EA\,\boldsymbol{f}_4\boldsymbol{f}_4^{\mathrm{T}}\,dx = \mathbf{T}^{\mathrm{T}}\mathbf{K}_{\varepsilon}\mathbf{T} \\ &\int_{l_0} EI\,\boldsymbol{f}_5\boldsymbol{f}_5^{\mathrm{T}}\,dx = \boldsymbol{T}^{\mathrm{T}}\mathbf{K}_{\kappa}\mathbf{T}\end{aligned} \tag{A.94}$$

where $\mathbf{T}$ is the rotation matrix

$$\mathbf{T} = \begin{bmatrix} c_{n+\frac{1}{2}} & s_{n+\frac{1}{2}} & 0 & 0 & 0 & 0 \\ -s_{n+\frac{1}{2}} & c_{n+\frac{1}{2}} & 0 & 0 & 0 & 0 \\ 0 & 0 & 1 & 0 & 0 & 0 \\ 0 & 0 & 0 & c_{n+\frac{1}{2}} & s_{n+\frac{1}{2}} & 0 \\ 0 & 0 & 0 & -s_{n+\frac{1}{2}} & c_{n+\frac{1}{2}} & 0 \\ 0 & 0 & 0 & 0 & 0 & 1 \end{bmatrix} \tag{A.95}$$

$\mathbf{M}_{l1}$ is the mass matrix due to the local axial and transversal displacements, $\mathbf{M}_{l2}$ is the mass matrix due to the rotation, $\mathbf{K}_{\varepsilon}$ is the stiffness matrix due to the axial strain and $\mathbf{K}_{\kappa}$ is the stiffness matrix due to the curvature. Then, the matrices $\mathbf{M}_l = \mathbf{M}_{l1} + \mathbf{M}_{l2}$ and $\mathbf{K}_{\varepsilon\kappa} = \mathbf{K}_{\varepsilon} + \mathbf{K}_{\kappa}$ are introduced. All these matrices are calculated exactly by using MATLAB symbolic. The following vectors are introduced:

$$\begin{aligned}&\int_{l_0}\dot{u}_{G,n}\,\boldsymbol{f}_1\,dx = \boldsymbol{f}_u \\ &\int_{l_0}\dot{w}_{G,n}\,\boldsymbol{f}_2\,dx = \boldsymbol{f}_w \\ &\int_{l_0}\dot{\theta}_{G,n}\,\boldsymbol{f}_3\,dx = \boldsymbol{f}_\theta \\ &\int_{l_0}\kappa_n\boldsymbol{f}_5 dx = \boldsymbol{f}_\kappa\end{aligned} \tag{A.96}$$

and

$$\begin{aligned}\int_{l_0} \boldsymbol{f}_1\, dx &= \boldsymbol{f}_{p1}\\ \int_{l_0} \boldsymbol{f}_2\, dx &= \boldsymbol{f}_{p2}\\ \int_{l_0} \boldsymbol{f}_3\, dx &= \boldsymbol{f}_{p3}\end{aligned} \tag{A.97}$$

All these vectors are calculated exactly by using MATLAB Symbolic. The residual vector force can be reformulated as

$$\begin{aligned}\boldsymbol{f}_{R,n+\frac{1}{2}}(\boldsymbol{q}_{n+1}) =& \frac{2}{\Delta t^2}\left(\mathbf{T}^{\mathrm{T}}\mathbf{M}_l\mathbf{T}\right)\Delta\boldsymbol{q} - \frac{2}{\Delta t}\left[\rho A\,\left(\boldsymbol{f}_u+\boldsymbol{f}_w\right)+\rho I\,\boldsymbol{f}_\theta\right]\\ &+\frac{1}{2}\left(\mathbf{T}^{\mathrm{T}}\mathbf{K}_{\varepsilon\kappa}\mathbf{T}\right)\Delta\boldsymbol{q} + EA\,l_0\,\varepsilon_n\boldsymbol{f}_4 + EI\boldsymbol{f}_\kappa\\ &-p_{u,n+\frac{1}{2}}\boldsymbol{f}_{p1} - p_{w,n+\frac{1}{2}}\boldsymbol{f}_{p2} - p_{\theta,n+\frac{1}{2}}\boldsymbol{f}_{p3} - P_{i,n+\frac{1}{2}}\end{aligned} \tag{A.98}$$

The local rotations $\bar{\theta}_{1,n+\frac{1}{2}}$ and $\bar{\theta}_{2,n+\frac{1}{2}}$ are calculated by

$$\begin{aligned}\bar{\theta}_{1,n+\frac{1}{2}} &= \bar{\theta}_{1,n} + \frac{\Delta t}{2}\dot{\bar{\theta}}_{1,n+\frac{1}{2}} = \bar{\theta}_{1,n} + \frac{1}{2}\boldsymbol{b}_3^{\mathrm{T}}\Delta\boldsymbol{q}\\ \bar{\theta}_{2,n+\frac{1}{2}} &= \bar{\theta}_{2,n} + \frac{\Delta t}{2}\dot{\bar{\theta}}_{2,n+\frac{1}{2}} = \bar{\theta}_{2,n} + \frac{1}{2}\boldsymbol{b}_4^{\mathrm{T}}\Delta\boldsymbol{q}\end{aligned} \tag{A.99}$$

The tangent matrix is given by

$$\begin{aligned}\mathbf{K}_T =& \frac{\partial \boldsymbol{f}_{R,n+\frac{1}{2}}}{\partial \boldsymbol{q}_{n+1}}\\ =& \frac{2}{\Delta t^2}\left[\mathbf{T}^{\mathrm{T}}\mathbf{M}_l\mathbf{T} + \frac{1}{2}\left(\mathbf{T}^{\mathrm{T}}\left(\boldsymbol{I}_1^{\mathrm{T}}\mathbf{M}_l + \mathbf{M}_l\boldsymbol{I}_1\right)\mathbf{T}\right)\left(\Delta\boldsymbol{q}\,\frac{\boldsymbol{z}^{\mathrm{T}}}{l_{n+\frac{1}{2}}}\right)\right.\\ &+\frac{1}{2}\left(\mathbf{T}^{\mathrm{T}}\mathbf{M}_{l,l}\mathbf{T}\right)\left(\Delta\boldsymbol{q}\,\boldsymbol{r}^{\mathrm{T}}\right) + \left(\mathbf{T}^{\mathrm{T}}\mathbf{M}_{l,\bar{\theta}_1}\mathbf{T}\right)\left(\Delta\boldsymbol{q}\,\frac{\partial\bar{\theta}_{1,n+\frac{1}{2}}}{\partial\boldsymbol{q}_{n+1}}\right)\\ &\left.+\left(\mathbf{T}^{\mathrm{T}}\mathbf{M}_{l,\bar{\theta}_2}\mathbf{T}\right)\left(\Delta\boldsymbol{q}\,\frac{\partial\bar{\theta}_{2,n+\frac{1}{2}}}{\partial\boldsymbol{q}_{n+1}}\right)\right] - \frac{2}{\Delta t}\left[\rho A\,\left(\frac{\partial\boldsymbol{f}_u}{\partial\boldsymbol{q}_{n+1}}+\frac{\partial\boldsymbol{f}_w}{\partial\boldsymbol{q}_{n+1}}\right)+\rho I\,\frac{\partial\boldsymbol{f}_\theta}{\partial\boldsymbol{q}_{n+1}}\right]\\ &+\frac{1}{2}\left[\mathbf{T}^{\mathrm{T}}\mathbf{K}_{\varepsilon\kappa}\mathbf{T} + \frac{1}{2}\left(\mathbf{T}^{\mathrm{T}}\left(\boldsymbol{I}_1^{\mathrm{T}}\mathbf{K}_{\varepsilon\kappa} + \mathbf{K}_{\varepsilon\kappa}\boldsymbol{I}_1\right)\mathbf{T}\right)\left(\Delta\boldsymbol{q}\,\frac{\boldsymbol{z}^{\mathrm{T}}}{l_{n+\frac{1}{2}}}\right)\right.\\ &+\frac{1}{2}\left(\mathbf{T}^{\mathrm{T}}\mathbf{K}_{\varepsilon\kappa,l}\mathbf{T}\right)\left(\Delta\boldsymbol{q}\,\boldsymbol{r}^{\mathrm{T}}\right) + \left(\mathbf{T}^{\mathrm{T}}\mathbf{K}_{\varepsilon\kappa,\bar{\theta}_1}\mathbf{T}\right)\left(\Delta\boldsymbol{q}\,\frac{\partial\bar{\theta}_{1,n+\frac{1}{2}}}{\partial\boldsymbol{q}_{n+1}}\right)\\ &\left.+\left(\mathbf{T}^{\mathrm{T}}\mathbf{K}_{\varepsilon\kappa,\bar{\theta}_2}\mathbf{T}\right)\left(\Delta\boldsymbol{q}\,\frac{\partial\bar{\theta}_{2,n+\frac{1}{2}}}{\partial\boldsymbol{q}_{n+1}}\right)\right] + EA\,l_0\,\varepsilon_n\frac{\partial\boldsymbol{f}_4}{\partial\boldsymbol{q}_{n+1}} + EI\frac{\partial\boldsymbol{f}_\kappa}{\partial\boldsymbol{q}_{n+1}}\\ &-p_{u,n+\frac{1}{2}}\frac{\partial\boldsymbol{f}_{p1}}{\partial\boldsymbol{q}_{n+1}} - p_{w,n+\frac{1}{2}}\frac{\partial\boldsymbol{f}_{p2}}{\partial\boldsymbol{q}_{n+1}} - p_{\theta,n+\frac{1}{2}}\frac{\partial\boldsymbol{f}_{p3}}{\partial\boldsymbol{q}_{n+1}}\end{aligned} \tag{A.100}$$

where

$$\mathbf{I} = \frac{\partial \mathbf{T}}{\partial \beta} = \begin{bmatrix} 0 & 1 & 0 & 0 & 0 & 0 \\ -1 & 0 & 0 & 0 & 0 & 0 \\ 0 & 0 & 0 & 0 & 0 & 0 \\ 0 & 0 & 0 & 0 & 1 & 0 \\ 0 & 0 & 0 & -1 & 0 & 0 \\ 0 & 0 & 0 & 0 & 0 & 0 \end{bmatrix} \tag{A.101}$$

$$\begin{aligned} \mathbf{M}_{l,l} &= \frac{\partial \mathbf{M}_l}{\partial l_{n+\frac{1}{2}}} \\ \mathbf{M}_{l,\bar{\theta}_1} &= \frac{\partial \mathbf{M}_l}{\partial \bar{\theta}_{1,n+\frac{1}{2}}} \\ \mathbf{M}_{l,\bar{\theta}_2} &= \frac{\partial \mathbf{M}_l}{\partial \bar{\theta}_{2,n+\frac{1}{2}}} \\ \mathbf{K}_{\varepsilon\kappa,l} &= \frac{\partial \mathbf{K}_{\varepsilon\kappa}}{\partial l_{n+\frac{1}{2}}} \\ \mathbf{K}_{\varepsilon\kappa,\bar{\theta}_1} &= \frac{\partial \mathbf{K}_{\varepsilon\kappa}}{\partial \bar{\theta}_{1,n+\frac{1}{2}}} \\ \mathbf{K}_{\varepsilon\kappa,\bar{\theta}_2} &= \frac{\partial \mathbf{K}_{\varepsilon\kappa}}{\partial \bar{\theta}_{2,n+\frac{1}{2}}} \end{aligned} \tag{A.102}$$

and

$$\begin{aligned} \frac{\partial \bar{\theta}_{1,n+\frac{1}{2}}}{\partial \boldsymbol{q}_{n+1}} &= \frac{1}{2}\boldsymbol{b}_3^{\mathrm{T}} + \frac{1}{4}\Delta \boldsymbol{q}^{\mathrm{T}} \frac{\boldsymbol{r}\boldsymbol{z}^{\mathrm{T}} + \boldsymbol{z}\boldsymbol{r}^{\mathrm{T}}}{l_{n+\frac{1}{2}}^2} \\ \frac{\partial \bar{\theta}_{2,n+\frac{1}{2}}}{\partial \boldsymbol{q}_{n+1}} &= \frac{1}{2}\boldsymbol{b}_4^{\mathrm{T}} + \frac{1}{4}\Delta \boldsymbol{q}^{\mathrm{T}} \frac{\boldsymbol{r}\boldsymbol{z}^{\mathrm{T}} + \boldsymbol{z}\boldsymbol{r}^{\mathrm{T}}}{l_{n+\frac{1}{2}}^2} \end{aligned} \tag{A.103}$$

The derivation and calculation of the tangent matrix have been performed using MATLAB symbolic.

References

[1] M. Geradin, A. Cardona, Kinematics and dynamics of rigid and flexible mechanisms using finite elements and quaternion algebra, Computational Mechanics 4 (1989) 115–135.

[2] K.-J. Bathe, E. Ramm, E.L. Wilson, Finite element formulations for large deformation dynamic analysis, International Journal for Numerical Methods in Engineering 9 (1975) 353–386.

[3] M.R.M. Crespo Da Silva, Non-linear flexural-flexural-torsional-extensional dynamics of beams–I. Formulation, International Journal of Solids and Structures 24 (1988) 1225–1234.

[4] M. Iura, S.N. Atluri, Dynamic analysis of finitely stretched and rotated three-dimensional space-curved beams, Computers and Structures 29 (1988) 875–889.

[5] R. Rosen, K.G. Loewy, M.B. Mathew, Non-linear dynamics of slender rods, AIAA Journal 25 (1987) 611–619.

[6] J.O. Song, E.J. Haug, Dynamic analysis of planar flexible mechanisms, Computer Methods in Applied Mechanics and Engineering 24 (1980) 359–381.

[7] J.C. Simo, L. Vu-Quoc, On the dynamics of flexible beams under large overall motions–The plane case: Part I, Journal of Applied Mechanics 53 (1986) 849–854.

[8] J.C. Simo, L. Vu-Quoc, On the dynamics of flexible beams under large overall motions–The plane case: Part II, Journal of Applied Mechanics 53 (1986) 855–863.

[9] M.A. Crisfield, J. Shi, A co-rotational element/time-integration strategy for non-linear dynamics, International Journal for Numerical Methods in Engineering 37 (1994) 1897–1913.

[10] M.A. Crisfield, J. Shi, An energy conserving co-rotational procedure for non-linear dynamcis with finite elements, Nonlinear Dynamics 9 (1996) 37–52.

[11] U. Galvanetto, M.A. Crisfield, An energy-conserving co-rotational procedure for the dynamics of planar beam structures, International Journal for Numerical Methods in Engineering 39 (1996) 2265–2282.

[12] T.-N. Le, J.-M. Battini, M. Hjiaj, Efficient formulation for dynamics of corotational 2D beams, Computational Mechanics 48 (2011) 153–161.

[13] M. Iura, S.N. Atluri, Dynamic analysis of planar flexible beams with finite rotaions by using inertial and rotating frames, Computers and Structures 55 (1995) 453–462.

[14] K.M. Hsiao, J. Jang, Dynamic analysis of planar flexible mechanisms by co-rotational formulation, Computer Methods in Applied Mechanics and Engineering 87 (1991) 1–14 .

[15] K.M. Hsiao, R.T. Yang, A co-rotational formulation for nonlinear dynamic analysis of curved Euler beam, Computers and Structures 54 (1995) 1091–1097.

[16] K. Behdinan, M.C. Stylianou, B. Tabarrok, Co-rotational dynamic analysis of flexible beams, Computer Methods in Applied Mechanics and Engineering 154 (1998) 151–161.

[17] H.A. Elkaranshawy, M.A. Dokainish, Corotational finite element analysis of planar flexible multibody systems, Computers and Structures 54 (1995) 881–890.

[18] M.A. Crisfield, U. Galvanetto, G. Jelenić, Dynamics of 3-D co-rotational beams, Computational Mechanics 20 (1997) 507–519.

[19] T.-N. Le, J.-M. Battini, M. Hjiaj, Dynamics of 3D beam elements in a corotational context: A comparative study of established and new formulations, Finite Elements in Analysis and Design 61 (2012) 97–111.

[20] T.-N. Le, J.-M. Battini, M. Hjiaj, A consistent 3D corotational beam element for nonlinear dynamic analysis of flexible structures, Computer Methods in Applied Mechanics and Engineering 269 (2014) 538–565.

[21] T.-N. Le, J.-M. Battini, M. Hjiaj, Corotational formulation for nonlinear dynamics of beams with arbitrary thin-walled open cross-sections, Computers and Structures 134 (2014) 112–127.

[22] J. Salomon, A.A Weiss, B.I. Wohlmuth, Energy-conserving algorithms for a corotational formulation, SIAM Journal on Numerical Analysis 46 (2008) 1842–1866.

[23] K.M. Hsiao, J.Y. Lin, W.Y. Lin, A consisten co-rotational finite element formulation for geometrically nonlinear dynamic analysis of 3-D beams, Computer Methods in Applied Mechanics and Engineering 169 (1999) 1–18.

[24] H.G. Zhong, M.A. Crisfield, An energy-conserving co-rotational procedure for the dynamics of shell structures, Engineering Computations 15 (1998) 552–576.

[25] F.S. Almeida, A.M. Awruch, Corotational nonlinear dynamic analysis of laminated composite shells, Finite Elements in Analysis and Design 47 (2011) 1131–1145.

[26] J. Yang, P. Xia, Corotational nonlinear dynamic analysis of thin-shell structures with finite rotations, AIAA Journal 53 (2015) 663–677.

[27] Y. Urthaler Y, J.N. Reddy, A corotational finite element formulation for the analysis of planar beams, Communications in Numerical Methods in Engineering 21 (2005) 553–570.

[28] G. Garcea, A. Madeo, R. Casciaro, The implicit corotational method and its use in the derivation of nonlinear structural models for beams and plates, Journal of Mechanics of Materials and Structures 7 (2012) 509–538.

[29] C. Pacoste, A. Eriksson, Beam elements in instability problems, Computer Methods in Applied Mechanics and Engineering 144 (1997) 163–197.

[30] J.-M. Battini, C. Pacoste, Co-rotational beam elements with warping effects in instability problems, Computer Methods in Applied Mechanics and Engineering 191 (2002) 1755–1789.

[31] J.-M. Battini, C. Pacoste, Plastic instability of beam structures using co-rotational elements, Computer Methods in Applied Mechanics and Engineering 191 (2002) 5811–5831.

[32] R. Alsafadie, M. Hjiaj, J.-M. Battini, Corotational mixed finite element formulation for thin-walled beams with generic cross-section, Computer Methods in Applied Mechanics and Engineering 199 (2010) 3197–3212.

[33] R. Alsafadie, J.-M. Battini, H. Somja, M. Hjiaj, Local formulation for elasto-plastic corotational thin-walled beams based on higher-order curvature terms, Finite Elements in Analysis and Design 47 (2011) 119–128.

[34] R. Alsafadie, J.-M. Battini, M. Hjiaj, Efficient local formulation for elasto-plastic corotational thin-walled beams, International Journal for Numerical Methods in Biomedical Engineering 27 (2011) 498–509.

[35] R. Alsafadie, J.-M. Battini, M. Hjiaj, Three-dimensional formulation of a mixed corotational thin-walled beam element incorporating shear and warping deformation, Thin-Walled Structures 49 (2011) 523–533.

[36] R. Alsafadie, M. Hjiaj, H. Somja, J.-M. Battini, A comparative study of displacement and mixed-based corotational finite element formulations for elasto-plastic three-dimensional beam analysis, Engineering Computations 28 (2011) 939–982.

[37] N.M. Newmark, A method of computation for structural dynamics, Journal of the Enginneering Mechanics division ASCE 85 (1959) 67–94.

[38] M. Geradin, A. Cardona, Time integration of the equations of motion in mechanism analysis, Computers and Structures 33 (1989) 801–820.

[39] H.M. Hilber, T.J.R Hughes, R.L. Taylor, Improved numerical dissipation for time integration algorithms in structural dynamics, Earthquake Engineering Strucuture Dynamic 5 (1977) 282–292.

[40] M. Geradin, A. Cardona, Flexible Multibody Dynamics, A Finite Element Approach, John Wiley and Sons 2001.

[41] J.C. Simo, N. Tarnow, The discrete energy-momentum method. Conserving algorithms for nonlinear elastodynamics, Journal of Applied Mathematics and Physics 43 (1992) 757–792.

[42] L. Gotusso, On the Energy Theorem for the Lagrange Equations in the Discrete Case, Applied Mathematics and Computation 17 (1985) 129–136.

[43] O. Gonzalez, Exact energy and momentum conserving algorithms for general models in nonlinear elasticity, Computer Methods in Applied Mechanics and Engineering, 190 (2000) 1763–1783.

[44] L. Noels, L. Stainier, J.P. Ponthot, An energy-momentum conserving algorithm for non-linear hypoelastic constitutive models, International Journal for Numerical Methods in Engineering 59 (2004) 83–114.

[45] I. Romero, An analysis of the stress formula for energy-momentum methods in nonlinear elastodynamics, Computational Mechanics 50 (2012) 603–610.

[46] P. Betsch, P. Steinmann, Conservation properties of a time FE method—part II: Time-stepping schemes for non-linear elastodynamics, International Journal for Numerical Methods in Engineering 50 (2001) 1931–1955.

[47] K.-J. Bathe, Conserving energy and momentum in nonlinear dynamics: A simple implicit time integration scheme, Computers and Structures 85 (2007) 437–445.

[48] J.C. Simo, N. Tarnow, M. Doblare, Non-linear dynamics of three-dimensional rods: exact energy and momentum conserving algorithms, International Journal for Numerical Methods in Engineering 38 (1995) 1431–1473.

[49] C. Sansour, T.L. Nguyen, M. Hjiaj, An energy-momentum method for in-plane geometrically exact Euler-Bernoulli beam dynamcis, International Journal for Numerical Methods in Engineering 102 (2015) 99–134.

[50] M. Gams, I. Planinc, M. Saje, Energy conserving time integration scheme for geometrically exact beam, Computer Methods in Applied Mechanics and Engineering 196 (2007) 2117–2129.

[51] D. Kuhl, M.A. Crisfield, Energy-conserving and decaying algorithms in non-linear structural dynamics, International Journal for Numerical Methods in Engineering 45 (1999) 569–599.

[52] I. Romero, F. Armero, An objective finite element approximation of the kinematics of geometrically exact rods and its use in the formulation of an energy-momentum conserving scheme in dynamics, International Journal for Numerical Methods in Engineering 54 (2002) 1683–1716.

[53] J.C. Simo, N. Tarnow, A new energy and momentum conserving algorithms for the non-linear dynamics of shells, International Journal for Numerical Methods in Engineering 37 (1994) 2527–2549.

[54] C. Sansour, W. Wagner, P. Wriggers, J. Sansour, An energy-momentum integration scheme and enhanced strain finite elements for the non-linear dynamics of shells, International Journal of Non-linear Mechanics 37 (2002) 951–966.

[55] C. Sansour, P. Wriggers, J. Sansour, Nonlinear dynamics of shells: theory, finite element formulation, and integration schemes, Nonlinear Dynamics 13 (1997) 279–305.

[56] B. Brank, L. Briseghella, N. Tonello, F.B Damjanic, On non-linear dynamics of shells: implementation of energy-momentum conserving algorithm for a finite rotation shell model, International Journal for Numerical Methods in Engineering 42 (1998) 409–442.

[57] D. Kuhl, E. Ramm, Generalized energy-momentum method for non-linear adaptive shell dynamics, Computer Methods in Applied Mechanics and Engineering 178 (1999) 343–366.

[58] C.C. Rankin, B. Nour-Omid, The use of projectors to improve finite element performance, Computers and Structures 30 (1988) 257–267.

[59] B. Nour-Omid, C.C. Rankin, Finite rotation analysis and consistent linearization using projectors, Computer Methods in Applied Mechanics and Engineering 93 (1991) 353–384.

[60] J.N. Reddy, On locking-free shear deformable beam finite elements, Computer Methods in Applied Mechanics and Engineering 149 (1997) 113–132.

[61] C. Sansour, P. Wriggers, J. Sansour, On the design of energy-momentum integration schemes for arbitrary continuum formulations. Applications to classical and chaotic motion of shells, International Journal for Numerical Methods in Engineering 60 (2004) 2419–2440.

[62] M. Gams, I. Planinc, M. Saje, A heuristic viscosity-type dissipation for high frequency oscillication damping in time integration algorithms, Computational Mechanics 41 (2007) 17–29.

[63] S. Lee, F.S. Manuel, E.C. Rossow, Large deflections and stability of elastic frames, Journal of the Engineering Mechanics Division 94 (1968) 521–547.

Paper II:

Energy-momentum method for co-rotational plane beams: A comparative study of shear flexible formulations

Finite Elements in Analysis and Design, Volume 134, pages 41-54, 2017.
DOI: 10.1016/j.finel.2017.04.001

Finite Elements in Analysis and Design, Volume 134, pages 41-54, 2017.
http://dx.doi.org/10.1016/j.finel.2017.04.001

Energy-momentum method for co-rotational plane beams: A comparative study of shear flexible formulations

Sophy Chhang[a,b], Jean-Marc Battini[b,*], Mohammed Hjiaj[a]

[a]*INSA Rennes, LGCGM, Univeristé Bretagne Loire, Rennes, France*
[b]*Department of Civil and Architectural Enginneering, Royal Insititute of Technology KTH, Stockholm, Sweden*

Abstract

This paper presents an energy-momentum method for three dynamic co-rotational formulations of shear flexible 2D beams. The classical midpoint rule is applied for both kinematic and strain quantities. Although the idea as such was developed in previous work, its realization and testing in the context of co-rotational Timoshenko 2D beam elements is done here for the first time. The main interest of the method is that the total energy and momenta are conserved. The three proposed formulations are based on the same co-rotational framework but they differ in the assumptions done to derive the local formulations. Four numerical applications are used to assess the accuracy and efficiency of each formulation. In particularly, the conservation of energy with a very large number of steps and the possibility to simplify the tangent dynamic matrix are investigated.

Keywords: Co-rotational formulation; Energy-momentum method; nonlinear dynamics; 2D beams; Shear.

1. Introduction

Flexible beams are used in many applications, for instance large deployable space structures, aircrafts, wind turbines propellers and offshore platforms. These structures undergo large displacements and rotations, but still with small deformations. The simulation of their nonlinear dynamic behaviour is usually performed using beam finite elements. The co-rotational method is a very attractive approach to derive highly nonlinear beam elements [1, 2, 3, 4, 5, 6, 7, 8, 9, 10, 11, 12, 13, 14, 15, 16, 17, 18]. The fundamental idea is to decompose the motion of the element into rigid body and pure deformational parts through the use of a local system which continuously rotates and translates with the element. The deformational response is captured at the level of the

*Corresponding author
Email addresses: sophy.chhang@insa-rennes.fr (Sophy Chhang), jean.marc.battini@byv.kth.se (Jean-Marc Battini), mohammed.hjiaj@insa-rennes.fr (Mohammed Hjiaj)

local reference frame, whereas the geometric non-linearity induced by the large rigid-body motion, is incorporated in the transformation matrices relating local and global quantities. The main interest is that the pure deformational parts can be assumed small and can be represented by a linear or a low order nonlinear theory [19, 20, 21, 22, 23, 24, 25, 26, 27, 28].

One important issue in the co-rotational method is the choice of the local formulation. Whereas the Euler-Bernoulli beam theory is completely sufficient for the applications of slender beams, the Timoshenko beam theory takes into account shear deformation, making it suitable for describing the behaviour of short beams, composite beams, or beams subject to high-frequency excitation. The classical and simplest Timoshenko local element is obtained by using linear shape functions, a linear strain-displacement relation and a reduced integration [29, 30, 31]. However, such a formulation requires a large number of elements in order to obtain accurate results. Several alternatives for the local part are possible in order to obtain a more efficient element: a mixed approach in which the displacements and the stress are interpolated independently [32, 33, 34, 35], an enhanced strain formulation [36, 37, 38, 39] or the Interdependent Interpolation element (IIE) [40].

Regarding the inertia terms in the co-rotational context, Crisfield et al. [2, 10] used linear local interpolations although they took local cubic interpolations to derive the elastic terms. Then, the inertia terms are easily derived and the classical constant Timoshenko mass matrix is obtained. However, Le at al. [4] adopted the IIE formulation [40], and hence cubic shape functions, to derive both the inertia and elastic terms. This leads to a formulation that requires a less number of elements but also to more complicated expressions for the inertia force vector and tangent dynamic matrix. The formulation was then extended to 3D beams without [11, 12] and with [13] warping.

Another important issue in the context of non-linear dynamics is the choice of the time stepping method. In commercial finite element programs, the Alpha method [41] is usually used. However, this approach introduces numerical dissipations and consequently, the energy in the system is not conserved [42, 43]. In the last decades, it has been recognized that energy conservation is a key for the stability of time-stepping algorithms in dynamics of solids and structures. Simo and Tarnow [42] were the first authors to design energy-momentum algorithms that inherit the conservation of momenta and energy for geometrically nonlinear problem involving quadratic Green-Lagrange strains. Since then, much effort was devoted to develop energy-momentum methods for various types of formulations such as nonlinear rod dynamics [44, 45, 46, 47, 48], nonlinear shell dynamics [49, 50, 51, 52, 53, 54], hypoelastic continuum [55, 56] and elastodynamics [56, 57, 58]. With the same objective of conserving energy and momenta, Bathe [59] proposed a simple composite time stepping scheme when large deformations and long-time durations are considered.

In the co-rotational context, there have been some efforts to develop energy-momentum methods as well. Crisfield and Shi [1] proposed a mid-point energy-conserving time algorithm for two-dimensional truss elements. This concept was further developed by Galvanetto and Crisfield [3] for planar beam structures. Various end- and mid-point time integration schemes for the nonlinear dynamic analysis of 3D co-rotational beams are discussed in [10]. The authors concluded that the proposed mid-point scheme can be considered as an "approximately energy conserving algorithm". A similar approach was applied to the dynamic of co-rotational shells [16], laminated composite shells [17]

and thin-shell structures [18]. Salomon et al. [14] showed the conservation of energy and momenta in the 2D and 3D analyses for the simulation of elastodynamic problems. They mentioned that, for some cases, the angular momentum is asymptotically preserved and an *a priori* estimate is obtained. However, despite of all these works, the design of an effective time integration scheme for co-rotational elements that inherently fulfils the conservation properties of energy and momenta is still an open question.

In this paper, a new energy-momentum method in the context of co-rotational shear flexible 2D beam elements is proposed. Based on the previous works of Sansour et al. [50, 52], the main idea is to apply the midpoint rule not only to nodal displacements, velocities and accelerations but also to the strain fields. It means that the strains are updated by using the strain velocities instead of using directly the strain-displacement relation. The conservation of energy, linear and angular momentum is proved theoretically and also observed in the numerical applications.

Based on the same co-rotational framework, three different local formulations are implemented and tested for a large number of time steps. The respective shape functions and strain assumptions for each local formulation are presented in Table 1. The reduced integration method (RIE) is the classical Timoshenko approach based on linear interpolations and one Gauss point integration for the static terms. The mixed formulation (MX) is also based on linear interpolations but a mixed approach is used to derive the static terms. For IIE formulation, the IIE cubic shape functions [40] are used and a nonlinear shallow arch strain definition is adopted. For this last element, the expression of the tangent dynamic matrix is complicated and a possible simplification is carefully studied. For the three formulations, different predictors are tested.

Table 1: Formulations

Formulations	Shape function	Static term
RIE	Linear	Linear strain with reduced integration
MX	Linear	Linear strain with mixed formulation
IIE	Cubic	Shallow arch strain

The paper is organized as follows: the beam kinematics is presented in Section 2. In Section 3, Hamilton's principle and conserving properties are presented. In Section 4, the energy-momentum method is developed. The inertia and elastic terms are derived respectively in Sections 5 and 6. In Section 7, the equation of motion for all formulations is presented along with the choice of predictors and the algorithm. The proofs of the conservation of energy, linear and angular momenta are given in Section 8. In Section 9, four numerical applications are presented in order to assess the numerical performances of the proposed formulations. Finally, conclusions are presented in Section 10.

2. Beam kinematics

The kinematics of the beam and all the notations used in this section are shown in Fig. 1. The motion of the element is decomposed in two parts. In a first step, a rigid body motion is defined by the global translation (u_1,w_1) of the node 1 as well as the rigid rotation α. This rigid motion defines a local coordinate system (x_l, z_l) which continuously translates and rotates with the element. In a second step, the element deformation is defined in the local coordinate system. Assuming that the length of the element is properly selected, the deformational part of the motion is always small

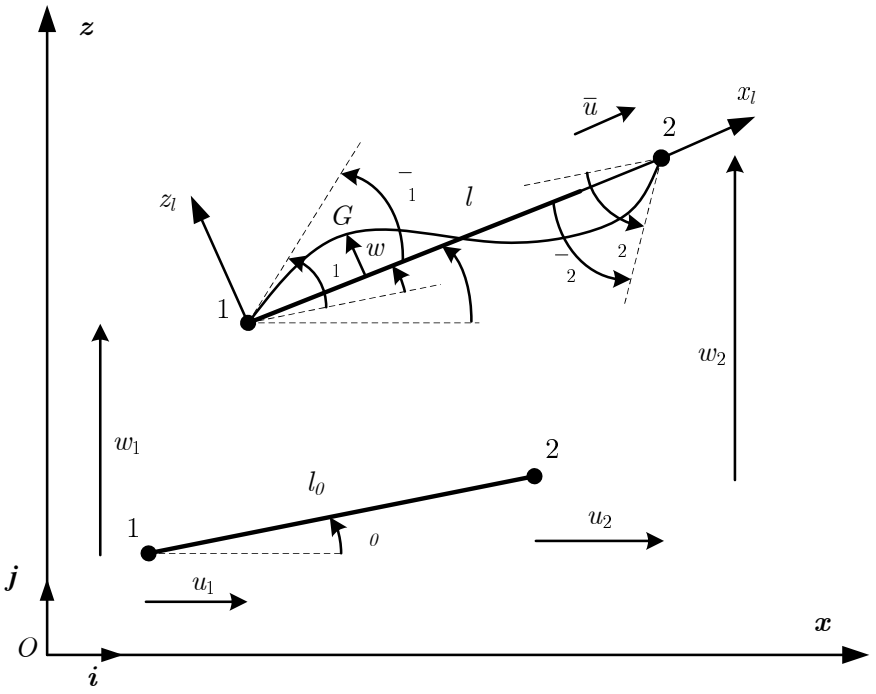

Figure 1: Beam kinematics

relative to the local co-ordinate systems. Consequently, the local deformations can be expressed in a simplified manner.

The vectors of global and local displacements are defined by

$$\boldsymbol{q} = \left[\begin{array}{cccccc} u_1 & w_1 & \theta_1 & u_2 & w_2 & \theta_2 \end{array} \right]^{\mathrm{T}} \tag{1}$$

and

$$\bar{\boldsymbol{q}} = \left[\begin{array}{ccc} \bar{u} & \bar{\theta}_1 & \bar{\theta}_2 \end{array} \right]^{\mathrm{T}} \tag{2}$$

Explicitly, the components of $\bar{\boldsymbol{q}}$ are given by

$$\begin{aligned} \bar{u} &= l - l_0 \\ \bar{\theta}_1 &= \theta_1 - \alpha = \theta_1 - \beta + \beta_0 \\ \bar{\theta}_2 &= \theta_2 - \alpha = \theta_2 - \beta + \beta_0 \end{aligned} \tag{3}$$

where l_0 and l denote the initial and current lengths of the element, respectively:

$$\begin{aligned} l_0 &= \sqrt{(x_2 - x_1)^2 + (z_2 - z_1)^2} \\ l &= \sqrt{(x_2 + u_2 - x_1 - u_1)^2 + (z_2 + w_2 - z_1 - w_1)^2} \end{aligned} \tag{4}$$

The current angle of the local system with respect to the global system is denoted as β and is given by

$$\begin{aligned} c = cos\beta &= \frac{1}{l}\left(x_2 + u_2 - x_1 - u_1\right) \\ s = sin\beta &= \frac{1}{l}\left(z_2 + w_2 - z_1 - w_1\right) \end{aligned} \tag{5}$$

The differentiation of the expressions (3) gives

$$\delta\bar{\boldsymbol{q}} = \mathbf{B}\,\delta\boldsymbol{q} \tag{6}$$

with

$$\mathbf{B} = \begin{bmatrix} -c & -s & 0 & c & s & 0 \\ -s/l & c/l & 1 & s/l & -c/l & 0 \\ -s/l & c/l & 0 & s/l & -c/l & 1 \end{bmatrix} \tag{7}$$

3. Hamilton's principle

Hamilton's principle states that the integral of the Lagrangian between two specified time instants t_1 and t_2 of a conservative mechanical system is stationary

$$\delta \int_{t_1}^{t_2} \mathcal{L}\,\mathrm{d}t = 0 \tag{8}$$

The Lagrangian $\mathcal{L}$ is given by

$$\mathcal{L} = \mathsf{K} - \mathsf{U}_{int} - \mathsf{U}_{ext} \tag{9}$$

with K as the kinetic energy. U_{int} and U_{ext} are the internal and the external potentials, respectively. The body is non-conducting linear elastic solid and thermodynamic effects are not included in the system. The kinetic energy and the internal potential for each formulation will be defined in the following sections. The external potential is defined as

$$\mathsf{U}_{ext} = -\sum_{i=1}^{6} P_i\, q_i \tag{10}$$

where P_i is the i component (concentrated forces and moments at the nodes) of the external force vector $\boldsymbol{P}$.
If the external loads are conservative, the total energy of the beam element can be written as

$$\mathsf{K} + \mathsf{U}_{int} + \mathsf{U}_{ext} = \mathsf{constant} \tag{11}$$

The linear momentum is defined by

$$\mathsf{L} = \begin{bmatrix} \mathsf{L}_u \\ \mathsf{L}_w \end{bmatrix} = \int_{l_0} \rho A \begin{bmatrix} \dot{u}_G \\ \dot{w}_G \end{bmatrix} \mathrm{d}x \tag{12}$$

and the angular momentum by

$$\mathsf{J} = \int_{l_0} \rho A \begin{bmatrix} u_G \\ w_G \\ 0 \end{bmatrix} \times \begin{bmatrix} \dot{u}_G \\ \dot{w}_G \\ 0 \end{bmatrix} \mathrm{d}x + \int_{l_0} \rho I \begin{bmatrix} 0 \\ 0 \\ \dot{\theta}_G \end{bmatrix} \mathrm{d}x \tag{13}$$

In the above equations, $\dot{u}_G$, $\dot{w}_G$ and $\dot{\theta}_G$ are the global velocities of the centroid G of the cross-section.
The time derivative of the two momenta define the equations of motion:

$$\frac{\mathrm{d}}{\mathrm{d}t}\mathsf{L} = \begin{bmatrix} P_1 + P_4 \\ P_2 + P_5 \end{bmatrix} \tag{14}$$

and

$$\frac{\mathrm{d}}{\mathrm{d}t}\mathsf{J} = (x_1 + u_1)\, P_2 - (z_1 + w_1)\, P_1 + (x_2 + u_2)\, P_5 \\ - (z_2 + w_2) P_4 + P_3 + P_6 = M_{ext} \tag{15}$$

from which it can be seen that, with vanishing external load, the linear momentum is a constant and, with vanishing external moments, the angular momentum is a constant.

4. Energy-momentum method

The Newmark family's method [60], which is the most widely used in the implicit time stepping method, is said to be unconditionally stable in linear analyses but it suffers severe shortcomings [42, 43] in nonlinear dynamics. Since the achievement of Simo and Tarnow [42], it is accepted that the energy-momentum method is the key for stability which ensure the conservation of the linear and angular momenta, and the total energy. Therefore, we aim to develop the energy-momentum method for co-rotational shear flexible formulations where the central idea starts from the classical midpoint rule.
The classical midpoint time integration scheme is defined by the following equations:

$$\begin{aligned} \boldsymbol{q}_{n+\frac{1}{2}} &= \frac{\boldsymbol{q}_{n+1} + \boldsymbol{q}_n}{2} = \boldsymbol{q}_n + \frac{1}{2}\Delta\boldsymbol{q} \\ \dot{\boldsymbol{q}}_{n+\frac{1}{2}} &= \frac{\dot{\boldsymbol{q}}_{n+1} + \dot{\boldsymbol{q}}_n}{2} = \frac{\boldsymbol{q}_{n+1} - \boldsymbol{q}_n}{\Delta t} = \frac{\Delta\boldsymbol{q}}{\Delta t} \\ \ddot{\boldsymbol{q}}_{n+\frac{1}{2}} &= \frac{\ddot{\boldsymbol{q}}_{n+1} + \ddot{\boldsymbol{q}}_n}{2} = \frac{\dot{\boldsymbol{q}}_{n+1} - \dot{\boldsymbol{q}}_n}{\Delta t} = \frac{2}{\Delta t^2}\Delta\boldsymbol{q} - \frac{2}{\Delta t}\dot{\boldsymbol{q}}_n \end{aligned} \tag{16}$$

from which follows

$$\begin{aligned} \boldsymbol{q}_{n+1} &= \boldsymbol{q}_n + \Delta\boldsymbol{q} \\ \dot{\boldsymbol{q}}_{n+1} &= \frac{2}{\Delta t}\Delta\boldsymbol{q} - \dot{\boldsymbol{q}}_n \\ \ddot{\boldsymbol{q}}_{n+1} &= \frac{4}{\Delta t^2}\Delta\boldsymbol{q} - \frac{4}{\Delta t}\dot{\boldsymbol{q}}_n - \ddot{\boldsymbol{q}}_n \end{aligned} \tag{17}$$

To develop the energy-momentum method, we follow the ideas developed in Sansour et al. [52, 50]. While the main idea is to applied midpoint rule to the strain field, the task is not as straightforward and is to be developed for the first time. The midpoint midpoint rule is applied to both the kinematic variables and strains as well. Formally, it takes the following generic form:

$$\begin{aligned} &\int_{t_n}^{t_{n+1}} f(t)\,\mathrm{d}t = f(t_{n+\frac{1}{2}})\,\Delta t = f_{n+\frac{1}{2}}\,\Delta t \\ &f_{n+\frac{1}{2}} = f_n + \frac{\Delta t}{2}\,\dot{f}_{n+\frac{1}{2}} \\ &f_{n+1} = f_n + \Delta t\,\dot{f}_{n+\frac{1}{2}} \end{aligned} \tag{18}$$

where the function f can represent either a kinematic variable or deformational quantity.

5. Inertia force vector and tangent dynamic matrix

The purpose of this section is to derive the dynamic terms (i.e. the inertia force vector and tangent dynamic matrix) for the three formulations.

5.1. IIE formulation

The Interdependent Interpolation Element (IIE), proposed in [40], is adopted for the local beam kinematic description. The development of this beam element is based on the exact solution of the homogeneous form of the equilibrium equations for a Timoshenko beam. Consequently, the IIE element retains not only the accuracy inherent to the cubic interpolation, but also includes the bending shear deformation. The shape functions of the IIE element are given by

$$\begin{aligned} N_3 &= \mu\, x \left[6\,\Omega \left(1 - \frac{x}{l_0} \right) + \left(1 - \frac{x}{l_0} \right)^2 \right] \\ N_4 &= \mu\, x \left[6\,\Omega \left(\frac{x}{l_0} - 1 \right) - \frac{x}{l_0} + \frac{x^2}{l_0^2} \right] \\ N_5 &= \mu \left(1 + 12\,\Omega - \frac{12\,\Omega\, x}{l_0} - \frac{4\, x}{l_0} + \frac{3\, x^2}{l_0^2} \right) \\ N_6 &= \mu \left(\frac{12\,\Omega\, x}{l_0} - \frac{2\, x}{l_0} + \frac{3\, x^2}{l_0^2} \right) \end{aligned} \tag{19}$$

where $\Omega = EI/(GA\, k_s\, l_0^2)$, $\mu = 1/(1 + 12\,\Omega)$ and k_s is the shear correction coefficient. For a rectangular cross-section, k_s is equal to 5/6. For the dynamic terms, Ω is taken to 0 because this simplification does not affect the numerical results. In addition, with $\Omega = 0$ the Hermitian shape functions of the classical Bernoulli element are recovered.

The local axial displacement u, the local transversal displacement w and the local rotation θ are calculated by

$$\begin{aligned} u &= N_2\, \bar{u} \\ w &= N_3\, \bar{\theta}_1 + N_4\, \bar{\theta}_2 \\ \theta &= N_5\, \bar{\theta}_1 + N_6\, \bar{\theta}_2 \end{aligned} \tag{20}$$

From Fig. 1, the components u_G, w_G of the global displacements of the centroid G and the global rotation θ_G of the cross section are obtained as

$$\begin{aligned} u_G &= N_1\,(x_1 + u_1) + N_2\,(x_2 + u_2) - w \sin\beta \\ w_G &= N_1\,(z_1 + w_1) + N_2\,(z_2 + w_2) + w \cos\beta \\ \theta_G &= \theta + \alpha \end{aligned} \tag{21}$$

where the linear interpolations N_1, N_2 are

$$\begin{aligned} N_1 &= 1 - \frac{x}{l_0} \\ N_2 &= \frac{x}{l_0} \end{aligned} \tag{22}$$

The kinetic energy is defined by the sum of the translational and rotational kinetic energies

$$\mathsf{K} = \frac{1}{2} \int_{l_0} \rho A\, \dot{u}_G^2 \,\mathrm{d}x + \frac{1}{2} \int_{l_0} \rho A\, \dot{w}_G^2 \,\mathrm{d}x + \frac{1}{2} \int_{l_0} \rho I\, \dot{\theta}_G^2 \,\mathrm{d}x \tag{23}$$

where ρ is the density, A the cross-section area and I the moment of inertia of the cross-section.

The variation of Eq.(23) gives

$$\delta \int_{t_1}^{t_2} \mathsf{K}\,\mathrm{d}t = \int_{t_1}^{t_2} \left(\int_{l_0} \rho A\, \dot{u}_G\, \delta \dot{u}_G\, \mathrm{d}x + \int_{l_0} \rho A\, \dot{w}_G\, \delta \dot{w}_G\, \mathrm{d}x + \int_{l_0} \rho I\, \dot{\theta}_G\, \delta \dot{\theta}_G\, \mathrm{d}x \right) \mathrm{d}t \quad (24)$$

By using integration by parts and since the virtual displacement of the two end points vanishes, Eq.(24) can be reformulated as

$$\delta \int_{t_1}^{t_2} \mathsf{K}\,\mathrm{d}t = -\int_{t_1}^{t_2} \left(\int_{l_0} \rho A\, \ddot{u}_G\, \delta u_G\, \mathrm{d}x + \int_{l_0} \rho A\, \ddot{w}_G\, \delta w_G\, \mathrm{d}x + \int_{l_0} \rho I\, \ddot{\theta}_G\, \delta \theta_G\, \mathrm{d}x \right) \mathrm{d}t \quad (25)$$

The application of the midpoint rule (18) to Eq.(25) gives

$$\begin{aligned} \delta \int_{t_1}^{t_2} \mathsf{K}\,\mathrm{d}t = -\Delta t\, \delta \boldsymbol{q}_{n+\frac{1}{2}}^{\mathrm{T}} \Bigg(& \int_{l_0} \rho A\, \ddot{u}_{G,n+\frac{1}{2}} \frac{\partial u_{G,n+\frac{1}{2}}}{\partial \boldsymbol{q}_{n+\frac{1}{2}}}\,\mathrm{d}x + \int_{l_0} \rho A\, \ddot{w}_{G,n+\frac{1}{2}} \frac{\partial w_{G,n+\frac{1}{2}}}{\partial \boldsymbol{q}_{n+\frac{1}{2}}}\,\mathrm{d}x \\ & + \int_{l_0} \rho I\, \ddot{\theta}_{G,n+\frac{1}{2}} \frac{\partial \theta_{G,n+\frac{1}{2}}}{\partial \boldsymbol{q}_{n+\frac{1}{2}}}\,\mathrm{d}x \Bigg)^{\mathrm{T}} \end{aligned} \quad (26)$$

Since the variation $\delta \boldsymbol{q}_{n+\frac{1}{2}}^{\mathrm{T}}$ is arbitrary, the inertia force vector is defined as

$$\begin{aligned} \boldsymbol{f}_{k,n+\frac{1}{2}} = & \int_{l_0} \rho A\, \ddot{u}_{G,n+\frac{1}{2}} \left(\frac{\partial u_{G,n+\frac{1}{2}}}{\partial \boldsymbol{q}_{n+\frac{1}{2}}} \right)^{\mathrm{T}} \mathrm{d}x + \int_{l_0} \rho A\, \ddot{w}_{G,n+\frac{1}{2}} \left(\frac{\partial w_{G,n+\frac{1}{2}}}{\partial \boldsymbol{q}_{n+\frac{1}{2}}} \right)^{\mathrm{T}} \mathrm{d}x \\ & + \int_{l_0} \rho I\, \ddot{\theta}_{G,n+\frac{1}{2}} \left(\frac{\partial \theta_{G,n+\frac{1}{2}}}{\partial \boldsymbol{q}_{n+\frac{1}{2}}} \right)^{\mathrm{T}} \mathrm{d}x \end{aligned} \quad (27)$$

With the help of the third relationship of Eqs.(16), the accelerations at midpoint are obtained as

$$\begin{aligned} \ddot{u}_{G,n+\frac{1}{2}} &= \frac{2}{\Delta t^2}\,\Delta u_G - \frac{2}{\Delta t}\,\dot{u}_{G,n} = \frac{2}{\Delta t^2}\,\boldsymbol{f}_1^{\mathrm{T}}\,\Delta \boldsymbol{q} - \frac{2}{\Delta t}\,\dot{u}_{G,n} \\ \ddot{w}_{G,n+\frac{1}{2}} &= \frac{2}{\Delta t^2}\,\Delta w_G - \frac{2}{\Delta t}\,\dot{w}_{G,n} = \frac{2}{\Delta t^2}\,\boldsymbol{f}_2^{\mathrm{T}}\,\Delta \boldsymbol{q} - \frac{2}{\Delta t}\,\dot{w}_{G,n} \\ \ddot{\theta}_{G,n+\frac{1}{2}} &= \frac{2}{\Delta t^2}\,\Delta \theta_G - \frac{2}{\Delta t}\,\dot{\theta}_{G,n} = \frac{2}{\Delta t^2}\,\boldsymbol{f}_3^{\mathrm{T}}\,\Delta \boldsymbol{q} - \frac{2}{\Delta t}\,\dot{\theta}_{G,n} \end{aligned} \quad (28)$$

in which the vectors $\boldsymbol{f}_1$, $\boldsymbol{f}_2$ and $\boldsymbol{f}_3$ at time $n+\frac{1}{2}$ are obtained by differentiation of Eqs.(21):

$$\begin{aligned} \boldsymbol{f}_1 &= \left(\frac{\partial u_{G,n+\frac{1}{2}}}{\partial \boldsymbol{q}_{n+\frac{1}{2}}} \right)^{\mathrm{T}} = \boldsymbol{b}_1 - s_{n+\frac{1}{2}}\,(N_3\,\boldsymbol{b}_3 + N_4\,\boldsymbol{b}_4) - c_{n+\frac{1}{2}}\,w_{n+\frac{1}{2}}\,\frac{\boldsymbol{z}}{l_{n+\frac{1}{2}}} \\ \boldsymbol{f}_2 &= \left(\frac{\partial w_{G,n+\frac{1}{2}}}{\partial \boldsymbol{q}_{n+\frac{1}{2}}} \right)^{\mathrm{T}} = \boldsymbol{b}_2 + c_{n+\frac{1}{2}}\,(N_3\,\boldsymbol{b}_3 + N_4\,\boldsymbol{b}_4) - s_{n+\frac{1}{2}}\,w_{n+\frac{1}{2}}\,\frac{\boldsymbol{z}}{l_{n+\frac{1}{2}}} \\ \boldsymbol{f}_3 &= \left(\frac{\partial \theta_{G,n+\frac{1}{2}}}{\partial \boldsymbol{q}_{n+\frac{1}{2}}} \right)^{\mathrm{T}} = N_5\,\boldsymbol{b}_3 + N_6\,\boldsymbol{b}_4 + \frac{\boldsymbol{z}}{l_{n+\frac{1}{2}}} \end{aligned} \quad (29)$$

with the following notations

$$
\begin{aligned}
\boldsymbol{z} &= \left[\begin{array}{cccccc} s_{n+\frac{1}{2}} & -c_{n+\frac{1}{2}} & 0 & -s_{n+\frac{1}{2}} & c_{n+\frac{1}{2}} & 0 \end{array}\right]^{\mathrm{T}} \\
\boldsymbol{b}_1 &= \left[\begin{array}{cccccc} N_1 & 0 & 0 & N_2 & 0 & 0 \end{array}\right]^{\mathrm{T}} \\
\boldsymbol{b}_2 &= \left[\begin{array}{cccccc} 0 & N_1 & 0 & 0 & N_2 & 0 \end{array}\right]^{\mathrm{T}} \\
\boldsymbol{b}_3 &= \left[\begin{array}{cccccc} 0 & 0 & 1 & 0 & 0 & 0 \end{array}\right]^{\mathrm{T}} - \frac{\boldsymbol{z}}{l_{n+\frac{1}{2}}} \\
\boldsymbol{b}_4 &= \left[\begin{array}{cccccc} 0 & 0 & 0 & 0 & 0 & 1 \end{array}\right]^{\mathrm{T}} - \frac{\boldsymbol{z}}{l_{n+\frac{1}{2}}}
\end{aligned}
\tag{30}
$$

The velocities at time n are evaluated by using Eqs. (21):

$$
\begin{aligned}
\dot{u}_{G,n} &= N_1\,\dot{u}_{1,n} + N_2\,\dot{u}_{2,n} + N_3\,v_{u3,n} + N_4\,v_{u4,n} \\
\dot{w}_{G,n} &= N_1\,\dot{w}_{1,n} + N_2\,\dot{w}_{2,n} + N_3\,v_{w3,n} + N_4\,v_{w4,n} \\
\dot{\theta}_{G,n} &= N_5\,\dot{\theta}_{1,n} + N_6\,\dot{\theta}_{2,n} + (1 - N_5 - N_6)\,v_{\theta,n}
\end{aligned}
\tag{31}
$$

where $\dot{u}_{1,n}, \dot{u}_{2,n}, \dot{w}_{1,n}, \dot{w}_{2,n}, \dot{\theta}_{1,n}$ and $\dot{\theta}_{2,n}$ are the global nodal velocities at time n and the quantities $v_{u3}, v_{u4}, v_{w3}, v_{w4}$ and v_θ are updated at the end of each step according to

$$
\begin{aligned}
v_{u3,n+1} &= \frac{2}{\Delta t}\left(-s_{n+\frac{1}{2}}\,\boldsymbol{b}_3^{\mathrm{T}} - c_{n+\frac{1}{2}}\,\bar{\theta}_{1,n+\frac{1}{2}}\,\frac{\boldsymbol{z}^{\mathrm{T}}}{l_{n+\frac{1}{2}}}\right)\Delta\boldsymbol{q} - v_{u3,n} \\
v_{u4,n+1} &= \frac{2}{\Delta t}\left(-s_{n+\frac{1}{2}}\,\boldsymbol{b}_4^{\mathrm{T}} - c_{n+\frac{1}{2}}\,\bar{\theta}_{2,n+\frac{1}{2}}\,\frac{\boldsymbol{z}^{\mathrm{T}}}{l_{n+\frac{1}{2}}}\right)\Delta\boldsymbol{q} - v_{u4,n}
\end{aligned}
\tag{32}
$$

$$
\begin{aligned}
v_{w3,n+1} &= \frac{2}{\Delta t}\left(c_{n+\frac{1}{2}}\,\boldsymbol{b}_3^{\mathrm{T}} - s_{n+\frac{1}{2}}\,\bar{\theta}_{1,n+\frac{1}{2}}\,\frac{\boldsymbol{z}^{\mathrm{T}}}{l_{n+\frac{1}{2}}}\right)\Delta\boldsymbol{q} - v_{w3,n} \\
v_{w4,n+1} &= \frac{2}{\Delta t}\left(c_{n+\frac{1}{2}}\,\boldsymbol{b}_4^{\mathrm{T}} - s_{n+\frac{1}{2}}\,\bar{\theta}_{2,n+\frac{1}{2}}\,\frac{\boldsymbol{z}^{\mathrm{T}}}{l_{n+\frac{1}{2}}}\right)\Delta\boldsymbol{q} - v_{w4,n}
\end{aligned}
\tag{33}
$$

$$
v_{\theta,n+1} = \frac{2}{\Delta t}\left(\frac{\boldsymbol{z}^{\mathrm{T}}}{l_{n+\frac{1}{2}}}\right)\Delta\boldsymbol{q} - v_{\theta,n} \tag{34}
$$

and the local rotations are calculated by using the second relationship of Eqs.(18):

$$
\bar{\theta}_{1,n+\frac{1}{2}} = \bar{\theta}_{1,n} + \frac{\Delta t}{2}\,\dot{\bar{\theta}}_{1,n+\frac{1}{2}} = \bar{\theta}_{1,n} + \frac{1}{2}\,\boldsymbol{b}_3^{\mathrm{T}}\,\Delta\boldsymbol{q} \tag{35}
$$

$$
\bar{\theta}_{2,n+\frac{1}{2}} = \bar{\theta}_{2,n} + \frac{\Delta t}{2}\,\dot{\bar{\theta}}_{2,n+\frac{1}{2}} = \bar{\theta}_{2,n} + \frac{1}{2}\,\boldsymbol{b}_4^{\mathrm{T}}\,\Delta\boldsymbol{q} \tag{36}
$$

Inserting Eqs.(28) and (29) into Eq.(27), the inertia force vector is obtained as

$$
\begin{aligned}
\boldsymbol{f}_{k,n+\frac{1}{2}} = {} & \frac{2}{\Delta t^2}\int_{l_0}\left[\rho A\,\left(\boldsymbol{f}_1\,\boldsymbol{f}_1^{\mathrm{T}} + \boldsymbol{f}_2\,\boldsymbol{f}_2^{\mathrm{T}}\right) + \rho I\,\boldsymbol{f}_3\,\boldsymbol{f}_3^{\mathrm{T}}\right]\Delta\boldsymbol{q}\,dx \\
& - \frac{2}{\Delta t}\int_{l_0}\left[\rho A\,\left(\dot{u}_{G,n}\,\boldsymbol{f}_1 + \dot{w}_{G,n}\,\boldsymbol{f}_2\right) + \rho I\,\dot{\theta}_{G,n}\,\boldsymbol{f}_3\right]dx
\end{aligned}
\tag{37}
$$

All these vectors are calculated exactly by using MATLAB Symbolic. Hence, the following expressions are introduced:

$$\begin{aligned}
&\int_{l_0} \left[\rho A \left(\boldsymbol{f}_1 \boldsymbol{f}_1^{\mathrm{T}} + \boldsymbol{f}_2 \boldsymbol{f}_2^{\mathrm{T}}\right) + \rho I \, \boldsymbol{f}_3 \boldsymbol{f}_3^{\mathrm{T}}\right] \mathrm{d}x = \mathbf{T}^{\mathrm{T}} \mathbf{M}_l \mathbf{T} \\
&\int_{l_0} \left[\rho A \left(\dot{u}_{G,n} \boldsymbol{f}_1 + \dot{w}_{G,n} \boldsymbol{f}_2\right) + \rho I \, \dot{\theta}_{G,n} \boldsymbol{f}_3\right] \mathrm{d}x = \boldsymbol{f}_{uw\theta}
\end{aligned} \tag{38}$$

with $\mathbf{M}_l$ is the nonlinear mass matrix and $\mathbf{T}$ is the rotation matrix:

$$\mathbf{T} = \begin{bmatrix}
c_{n+\frac{1}{2}} & s_{n+\frac{1}{2}} & 0 & 0 & 0 & 0 \\
-s_{n+\frac{1}{2}} & c_{n+\frac{1}{2}} & 0 & 0 & 0 & 0 \\
0 & 0 & 1 & 0 & 0 & 0 \\
0 & 0 & 0 & c_{n+\frac{1}{2}} & s_{n+\frac{1}{2}} & 0 \\
0 & 0 & 0 & -s_{n+\frac{1}{2}} & c_{n+\frac{1}{2}} & 0 \\
0 & 0 & 0 & 0 & 0 & 1
\end{bmatrix} \tag{39}$$

Inserting Eqs.(38) into Eq. (37), the inertia force vector takes the form

$$\boldsymbol{f}_{k,n+\frac{1}{2}} = \frac{2}{\Delta t^2} \left(\mathbf{T}^{\mathrm{T}} \mathbf{M}_l \mathbf{T}\right) \Delta \boldsymbol{q} - \frac{2}{\Delta t} \boldsymbol{f}_{uw\theta} \tag{40}$$

The exact tangent dynamic matrix is given by

$$\begin{aligned}
\mathbf{K}_k =& \frac{\partial \boldsymbol{f}_{k,n+\frac{1}{2}}}{\partial \boldsymbol{q}_{n+1}} \\
=& \frac{2}{\Delta t^2} \left[\mathbf{T}^{\mathrm{T}} \mathbf{M}_l \mathbf{T} + \frac{1}{2} \left(\mathbf{T}^{\mathrm{T}} \left(\boldsymbol{I}_1^{\mathrm{T}} \mathbf{M}_l + \mathbf{M}_l \boldsymbol{I}_1\right) \mathbf{T}\right) \left(\Delta \boldsymbol{q} \, \frac{\boldsymbol{z}^{\mathrm{T}}}{l_{n+\frac{1}{2}}}\right)\right. \\
&+ \frac{1}{2} \left(\mathbf{T}^{\mathrm{T}} \mathbf{M}_{l,l} \mathbf{T}\right) \left(\Delta \boldsymbol{q} \, \boldsymbol{r}^{\mathrm{T}}\right) + \left(\mathbf{T}^{\mathrm{T}} \mathbf{M}_{l,\bar{\theta}_1} \mathbf{T}\right) \left(\Delta \boldsymbol{q} \, \frac{\partial \bar{\theta}_{1,n+\frac{1}{2}}}{\partial \boldsymbol{q}_{n+1}}\right) \\
&\left. + \left(\mathbf{T}^{\mathrm{T}} \mathbf{M}_{l,\bar{\theta}_2} \mathbf{T}\right) \left(\Delta \boldsymbol{q} \, \frac{\partial \bar{\theta}_{2,n+\frac{1}{2}}}{\partial \boldsymbol{q}_{n+1}}\right)\right] - \frac{2}{\Delta t} \frac{\partial \boldsymbol{f}_{uw\theta}}{\partial \boldsymbol{q}_{n+1}}
\end{aligned} \tag{41}$$

with

$$\begin{aligned}
\mathbf{M}_{l,l} &= \frac{\partial \mathbf{M}_l}{\partial l_{n+\frac{1}{2}}} \\
\mathbf{M}_{l,\bar{\theta}_1} &= \frac{\partial \mathbf{M}_l}{\partial \bar{\theta}_{1,n+\frac{1}{2}}} \\
\mathbf{M}_{l,\bar{\theta}_2} &= \frac{\partial \mathbf{M}_l}{\partial \bar{\theta}_{2,n+\frac{1}{2}}} \\
\boldsymbol{r} &= \begin{bmatrix} -c_{n+\frac{1}{2}} & -s_{n+\frac{1}{2}} & 0 & c_{n+\frac{1}{2}} & s_{n+\frac{1}{2}} & 0 \end{bmatrix}^{\mathrm{T}}
\end{aligned} \tag{42}$$

and

$$\mathbf{I} = \frac{\partial \mathbf{T}}{\partial \beta} = \begin{bmatrix} 0 & 1 & 0 & 0 & 0 & 0 \\ -1 & 0 & 0 & 0 & 0 & 0 \\ 0 & 0 & 0 & 0 & 0 & 0 \\ 0 & 0 & 0 & 0 & 1 & 0 \\ 0 & 0 & 0 & -1 & 0 & 0 \\ 0 & 0 & 0 & 0 & 0 & 0 \end{bmatrix} \tag{43}$$

The expression of the tangent dynamic matrix is very long and its computation requires a lot of computational time. In order to reduce the computational time, Geradin and Cardona [61, 43] suggested to keep only the mass matrix and to neglect the gyroscopic and centrifugal matrices. Hence, a simplified tangent dynamic matrix is proposed:

$$\mathbf{K}_k = \frac{2}{\Delta t^2} \left(\mathbf{T}^{\mathrm{T}} \mathbf{M}_l \mathbf{T} \right) \tag{44}$$

5.2. Reduced integration and Hellinger-Reissner formulations

For both formulations, linear interpolations for u, w and θ are used in the local corotational coordinates system. This gives

$$\begin{aligned} u &= N_2 \, \bar{u} \\ w &= 0 \\ \theta &= N_1 \, \bar{\theta}_1 + N_2 \, \bar{\theta}_2 \end{aligned} \tag{45}$$

Therefore, the kinetic energy (23) can be written as

$$\mathsf{K} = \frac{1}{2} \, \dot{\boldsymbol{q}}_{n+\frac{1}{2}}^{\mathrm{T}} \mathbf{M} \, \dot{\boldsymbol{q}}_{n+\frac{1}{2}} \tag{46}$$

and the inertia term (27) as

$$\boldsymbol{f}_{k,n+\frac{1}{2}} = \mathbf{M} \, \ddot{\boldsymbol{q}}_{n+\frac{1}{2}} \tag{47}$$

where the constant mass matrix $\mathbf{M}$ is given by

$$\mathbf{M} = \rho \, l_0 \begin{bmatrix} A/3 & 0 & 0 & A/6 & 0 & 0 \\ 0 & A/3 & 0 & 0 & A/6 & 0 \\ 0 & 0 & I/3 & 0 & 0 & I/6 \\ A/6 & 0 & 0 & A/3 & 0 & 0 \\ 0 & A/6 & 0 & 0 & A/3 & 0 \\ 0 & 0 & I/6 & 0 & 0 & I/3 \end{bmatrix} \tag{48}$$

Hence, the tangent dynamic matrix is obtained as

$$\mathbf{K}_k = \frac{2}{\Delta t^2} \, \mathbf{M} \tag{49}$$

6. Elastic force vector and tangent stiffness matrix

The purpose of this section is to derive the elastic force vector and tangent stiffness matrix for the three formulations.

6.1. Reduced integration method

The reduced integration formulation (RIE) is the classical Timoshenko approach based on linear interpolations and one Gauss point integration in order to avoid shear locking. The curvature κ, shear deformation γ and strain ε are defined by

$$\kappa = \frac{\partial \theta}{\partial x} = \frac{\bar{\theta}_2 - \bar{\theta}_1}{l_0} \tag{50}$$

$$\gamma = \frac{\partial w}{\partial x} - \theta = -N_1 \bar{\theta}_1 - N_2 \bar{\theta}_2 \tag{51}$$

$$\varepsilon_{11} = \varepsilon - \kappa\, z = \frac{\bar{u}}{l_0} - \frac{\bar{\theta}_2 - \bar{\theta}_1}{l_0} z \tag{52}$$

The elastic potential energy is defined by

$$\mathsf{U}_{int} = \frac{1}{2} \int_{l_0} EA\, \varepsilon^2 \mathrm{d}x + \frac{1}{2} \int_{l_0} EI\, \kappa^2 \mathrm{d}x + \frac{1}{2} \int_{l_0} k_s GA\, \gamma^2 \mathrm{d}x \tag{53}$$

where E is the elastic modulus and G the shear modulus of the material.

The application of the midpoint rule (18) to Eq.(53) gives

$$\begin{aligned} \delta \int_{t_1}^{t_2} \mathsf{U}_{int}\, \mathrm{d}t = \Delta t\, \delta \bar{\boldsymbol{q}}_{n+\frac{1}{2}}^{\mathrm{T}} \Bigg(& \int_{l_0} EA\, \varepsilon_{n+\frac{1}{2}} \frac{\partial \varepsilon_{n+\frac{1}{2}}}{\partial \bar{\boldsymbol{q}}_{n+\frac{1}{2}}} \mathrm{d}x \\ & + \int_{l_0} EI\, \kappa_{n+\frac{1}{2}} \frac{\partial \kappa_{n+\frac{1}{2}}}{\partial \bar{\boldsymbol{q}}_{n+\frac{1}{2}}} \mathrm{d}x + \int_{l_0} k_s GA\, \gamma_{n+\frac{1}{2}} \frac{\partial \gamma_{n+\frac{1}{2}}}{\partial \bar{\boldsymbol{q}}_{n+\frac{1}{2}}} \mathrm{d}x \Bigg)^{\mathrm{T}} \end{aligned} \tag{54}$$

By using the relation (6), the previous equation leads to

$$\begin{aligned} \delta \int_{t_1}^{t_2} \mathsf{U}_{int}\, \mathrm{d}t = \Delta t\, \delta \boldsymbol{q}_{n+\frac{1}{2}}^{\mathrm{T}}\, \mathbf{B}^{\mathrm{T}} \Bigg(& \int_{l_0} EA\, \varepsilon_{n+\frac{1}{2}} \frac{\partial \varepsilon_{n+\frac{1}{2}}}{\partial \bar{\boldsymbol{q}}_{n+\frac{1}{2}}} \mathrm{d}x \\ & + \int_{l_0} EI\, \kappa_{n+\frac{1}{2}} \frac{\partial \kappa_{n+\frac{1}{2}}}{\partial \bar{\boldsymbol{q}}_{n+\frac{1}{2}}} \mathrm{d}x + \int_{l_0} k_s GA\, \gamma_{n+\frac{1}{2}} \frac{\partial \gamma_{n+\frac{1}{2}}}{\partial \bar{\boldsymbol{q}}_{n+\frac{1}{2}}} \mathrm{d}x \Bigg)^{\mathrm{T}} \end{aligned} \tag{55}$$

where the components of matrix $\mathbf{B}$ are computed at time $n+\frac{1}{2}$. As the variation $\delta \boldsymbol{q}_{n+\frac{1}{2}}^{\mathrm{T}}$ is arbitrary, the global elastic force vector is given as

$$\boldsymbol{f}_{g,n+\frac{1}{2}} = \mathbf{B}^{\mathrm{T}}\, \boldsymbol{f}_{l,n+\frac{1}{2}} \tag{56}$$

in which the local elastic force vector $\boldsymbol{f}_{l,n+\frac{1}{2}}$ is defined as

$$\begin{aligned} \boldsymbol{f}_{l,n+\frac{1}{2}} = & \int_{l_0} EA\, \varepsilon_{n+\frac{1}{2}} \left(\frac{\partial \varepsilon_{n+\frac{1}{2}}}{\partial \bar{\boldsymbol{q}}_{n+\frac{1}{2}}} \right)^{\mathrm{T}} \mathrm{d}x + \int_{l_0} EI\, \kappa_{n+\frac{1}{2}} \left(\frac{\partial \kappa_{n+\frac{1}{2}}}{\partial \bar{\boldsymbol{q}}_{n+\frac{1}{2}}} \right)^{\mathrm{T}} \mathrm{d}x \\ & + \int_{l_0} k_s GA\, \gamma_{n+\frac{1}{2}} \left(\frac{\partial \gamma_{n+\frac{1}{2}}}{\partial \bar{\boldsymbol{q}}_{n+\frac{1}{2}}} \right)^{\mathrm{T}} \mathrm{d}x \end{aligned} \tag{57}$$

By using the local strains (Eqs.(50),(51),(52)), the local elastic force is obtained as

$$\boldsymbol{f}_{l,n+\frac{1}{2}} = \left[\begin{array}{ccc} N & M_1 & M_2 \end{array} \right]^{\mathrm{T}} = \mathbf{K}_l \, \bar{\boldsymbol{q}}_{n+\frac{1}{2}} \tag{58}$$

in which the local stiffness matrix is

$$\mathbf{K}_l = \left[\begin{array}{ccc} EA/l_0 & 0 & 0 \\ 0 & k_s GA\, l_0/4 + EI/l_0 & k_s GA\, l_0/4 - EI/l_0 \\ 0 & k_s GA\, l_0/4 - EI/l_0 & k_s GA\, l_0/4 + EI/l_0 \end{array} \right] \tag{59}$$

The local rotations $\bar{\theta}_{1,n+\frac{1}{2}}$ and $\bar{\theta}_{2,n+\frac{1}{2}}$ are defined respectively in Eqs.(35),(36) and the axial local displacement is defined by

$$\bar{u}_{n+\frac{1}{2}} = \bar{u}_n + \frac{\Delta t}{2}\, \dot{\bar{u}}_{n+\frac{1}{2}} = \bar{u}_n + \frac{1}{2}\, \boldsymbol{r}^{\mathrm{T}} \Delta \boldsymbol{q} \tag{60}$$

By taking the derivative of Eq.(56) with respect to the global displacements at time $n+1$ and by using the local displacements (Eqs.(35),(36),(60)), the global tangent stiffness matrix is obtained as

$$\begin{aligned} \mathbf{K}_g &= \frac{\partial \boldsymbol{f}_{g,n+\frac{1}{2}}}{\partial \boldsymbol{q}_{n+1}} = \mathbf{B}^{\mathrm{T}} \frac{\partial \boldsymbol{f}_{l,n+\frac{1}{2}}}{\partial \boldsymbol{q}_{n+1}} + \left. \frac{\partial \left(\mathbf{B}^{\mathrm{T}} \boldsymbol{f}_{l,n+\frac{1}{2}} \right)}{\partial \boldsymbol{q}_{n+1}} \right|_{\boldsymbol{f}_{l,n+\frac{1}{2}}} \\ &= \frac{1}{2}\, \mathbf{B}^{\mathrm{T}} \mathbf{K}_l \left(\mathbf{B} + \frac{1}{2}\, \mathbf{B}_0 \right) + \frac{\boldsymbol{z}\boldsymbol{z}^{\mathrm{T}}}{2\, l_{n+\frac{1}{2}}} N + \frac{\boldsymbol{r}\boldsymbol{z}^{\mathrm{T}} + \boldsymbol{z}\boldsymbol{r}^{\mathrm{T}}}{2\, l^2_{n+\frac{1}{2}}} \left(M_1 + M_2 \right) \end{aligned} \tag{61}$$

with

$$\mathbf{B}_0 = \left[\begin{array}{c} \Delta \boldsymbol{q}^{\mathrm{T}} \left(\boldsymbol{z}\boldsymbol{z}^{\mathrm{T}} \right) / l_{n+\frac{1}{2}} \\ \Delta \boldsymbol{q}^{\mathrm{T}} \left(\boldsymbol{r}\boldsymbol{z}^{\mathrm{T}} + \boldsymbol{z}\boldsymbol{r}^{\mathrm{T}} \right) / l^2_{n+\frac{1}{2}} \\ \Delta \boldsymbol{q}^{\mathrm{T}} \left(\boldsymbol{r}\boldsymbol{z}^{\mathrm{T}} + \boldsymbol{z}\boldsymbol{r}^{\mathrm{T}} \right) / l^2_{n+\frac{1}{2}} \end{array} \right] \tag{62}$$

6.2. Hellinger-Reissner formulation

A two-field mixed formulation in this work based on the Hellinger–Reissner variational principle is considered. Both displacements and internal forces along the element are approximated by independent linear interpolation functions. The elastic potential of the Hellinger-Reissner mixed formulation is written as

$$\mathsf{U}_{int} = \int_{l_0} \boldsymbol{S}^{\mathrm{T}} \left(\hat{\boldsymbol{e}} - \frac{1}{2} \boldsymbol{e} \right) \mathrm{d}x \tag{63}$$

The generalized stress resultant vector $\boldsymbol{S}$ is approximate by

$$\boldsymbol{S} = \left[\begin{array}{c} N \\ M \\ Q \end{array} \right] = \mathbf{N}_s \, \boldsymbol{f}_l = \left[\begin{array}{ccc} 1 & 0 & 0 \\ 0 & -N_1 & N_2 \\ 0 & -1/l_0 & -1/l_0 \end{array} \right] \left[\begin{array}{c} N \\ M_1 \\ M_2 \end{array} \right] \tag{64}$$

where $\mathbf{N}_s$ is the matrix of shape functions satisfying local equilibrium.

From Eqs.(50),(51) and (52), the generalized strain vector $\hat{\mathbf{e}}$ is written as

$$\hat{\boldsymbol{e}} = \begin{bmatrix} \varepsilon \\ \kappa \\ \gamma \end{bmatrix} = \mathbf{N}_{\hat{e}}\, \bar{\boldsymbol{q}} = \begin{bmatrix} 1/l_0 & 0 & 0 \\ 0 & -1/l_0 & 1/l_0 \\ 0 & -N_1 & -N_2 \end{bmatrix} \begin{bmatrix} \bar{u} \\ \bar{\theta}_1 \\ \bar{\theta}_2 \end{bmatrix} \tag{65}$$

The cross-section deformation vector $\boldsymbol{e}$ is defined by

$$\boldsymbol{e} = \mathbf{N}_{s1}\, \boldsymbol{f}_l = \begin{bmatrix} 1/(EA) & 0 & 0 \\ 0 & -N_1/(EI) & N_2/(EI) \\ 0 & -1/(k_s GA\, l_0) & -1/(k_s GA\, l_0) \end{bmatrix} \begin{bmatrix} N \\ M_1 \\ M_2 \end{bmatrix} \tag{66}$$

The variation of Eq.(63) gives

$$\delta \mathsf{U}_{int} = \delta \bar{\boldsymbol{q}}^{\mathrm{T}}_{n+\frac{1}{2}} \left(\frac{\partial \mathsf{U}_{int}}{\partial \bar{\boldsymbol{q}}_{n+\frac{1}{2}}} \right)^{\mathrm{T}} + \delta \boldsymbol{f}^{\mathrm{T}}_{l,n+\frac{1}{2}} \left(\frac{\partial \mathsf{U}_{int}}{\partial \boldsymbol{f}_{l,n+\frac{1}{2}}} \right)^{\mathrm{T}} \tag{67}$$

where

$$\left(\frac{\partial \mathsf{U}_{int}}{\partial \bar{\boldsymbol{q}}_{n+\frac{1}{2}}} \right)^{\mathrm{T}} = \mathbf{G}\, \boldsymbol{f}_{l,n+\frac{1}{2}} \tag{68}$$

$$\left(\frac{\partial \mathsf{U}_{int}}{\partial \boldsymbol{f}_{l,n+\frac{1}{2}}} \right)^{\mathrm{T}} = \mathbf{G}^{\mathrm{T}} \bar{\boldsymbol{q}}_{n+\frac{1}{2}} - \mathbf{H}\, \boldsymbol{f}_{l,n+\frac{1}{2}} \tag{69}$$

with

$$\mathbf{G} = \int_{l_0} \mathbf{N}^{\mathrm{T}}_{\hat{e}} \mathbf{N}_s \mathrm{d}x = \begin{bmatrix} 1 & 0 & 0 \\ 0 & 1 & 0 \\ 0 & 0 & 1 \end{bmatrix} \tag{70}$$

$$\mathbf{H} = \int_{l_0} \mathbf{N}^{\mathrm{T}}_{s} \mathbf{N}_{s1} \mathrm{d}x = \begin{bmatrix} \frac{l_0}{EA} & 0 & 0 \\ 0 & \frac{l_0}{3EI} + \frac{1}{k_s GA\, l_0} & -\frac{l_0}{6EI} + \frac{1}{k_s GA\, l_0} \\ 0 & -\frac{l_0}{6EI} + \frac{1}{k_s GA\, l_0} & \frac{l_0}{3EI} + \frac{1}{k_s GA\, l_0} \end{bmatrix} \tag{71}$$

As the variation $\delta \boldsymbol{f}_{l,n+\frac{1}{2}}$ is arbitrary, the expression (69) is equal to zero. Therefore, $\boldsymbol{f}_{l,n+\frac{1}{2}}$ is obtained as

$$\boldsymbol{f}_{l,n+\frac{1}{2}} = \mathbf{K}_l\, \bar{\boldsymbol{q}}_{n+\frac{1}{2}} \tag{72}$$

in which the local stiffness matrix is

$$\mathbf{K}_l = \mathbf{H}^{-1} \tag{73}$$

The expression of the local internal force vector (Eq.(72)) is similar to the one of the Mixed formulation (Eq.(58)) but with a different local constant stiffness matrix. Hence, the global quantities $\boldsymbol{f}_{g,n+\frac{1}{2}}$ and $\mathbf{K}_g$ are obtained in the same way by using Eqs.(56) and (61) respectively .

6.3. IIE formulation

The shape functions of the IIE are used together with a shallow arch beam theory. The shallow arch longitudinal and shear strains are given by

$$\varepsilon_{11} = \varepsilon - \kappa\, z \tag{74}$$

$$\gamma = \frac{\partial w}{\partial x} - \theta \tag{75}$$

in which the axial strain ε and the curvature κ are defined by

$$\varepsilon = \frac{1}{l_0}\int_{l_0}\left[\frac{\partial u}{\partial x} + \frac{1}{2}\left(\frac{\partial w}{\partial x}\right)^2\right]\mathrm{d}x \tag{76}$$

$$\kappa = \frac{\partial^2 w}{\partial x^2} \tag{77}$$

In Eq.(77), the axial strain is averaged over the element in order to avoid membrane locking. The purpose of introducing a mild geometrical non-linearity in the local formulation is to increase the accuracy of the formulation as compared to a purely linear strain definition, while still retaining the efficiency.

By using Eqs.(53–57) and introducing the strain definitions (Eqs.(75–77)) together with the local quantities (Eqs.(20)) and shape functions (Eqs.(19)), the local elastic force vector $\boldsymbol{f}_{l,n+\frac{1}{2}}$ is obtained after some basic manipulations:

$$\boldsymbol{f}_{l,n+\frac{1}{2}} = \mathbf{K}_{l1}\,\bar{\boldsymbol{q}}_{n+\frac{1}{2}} + \boldsymbol{f}_{\varepsilon} \tag{78}$$

in which

$$\mathbf{K}_{l1} = \frac{EI}{l_0}\begin{bmatrix} 0 & 0 & 0 \\ 0 & 3\mu^2+1 & 3\mu^2-1 \\ 0 & 3\mu^2-1 & 3\mu^2+1 \end{bmatrix} + k_s GA\, l_0\,(6\Omega\mu)^2 \begin{bmatrix} 0 & 0 & 0 \\ 0 & 1 & 1 \\ 0 & 1 & 1 \end{bmatrix} \tag{79}$$

$$\boldsymbol{f}_{\varepsilon} = EA\, l_0\, \varepsilon_{n+\frac{1}{2}}\, \boldsymbol{b}_5 \tag{80}$$

$$\boldsymbol{b}_5 = \begin{bmatrix} (1/l_0) & \left(ct_1\,\bar{\theta}_{1,n+\frac{1}{2}} + ct_2\,\bar{\theta}_{2,n+\frac{1}{2}}\right) & \left(ct_2\,\bar{\theta}_{1,n+\frac{1}{2}} + ct_1\,\bar{\theta}_{2,n+\frac{1}{2}}\right) \end{bmatrix}^{\mathrm{T}} \tag{81}$$

with

$$\begin{aligned} ct_1 &= \frac{\mu^2}{20} + \frac{1}{12} \\ ct_2 &= \frac{\mu^2}{20} - \frac{1}{12} \end{aligned} \tag{82}$$

The axial strain is updated as

$$\varepsilon_{n+\frac{1}{2}} = \varepsilon_n + \frac{\Delta t}{2}\,\dot{\varepsilon}_{n+\frac{1}{2}} = \varepsilon_n + \frac{1}{2}\,\boldsymbol{f}_4^{\mathrm{T}}\,\Delta\boldsymbol{q} \tag{83}$$

in which the vector $\boldsymbol{f}_4$ at time $n+\frac{1}{2}$ is obtained from Eq.(76):

$$\boldsymbol{f}_4 = \left(\frac{\partial \varepsilon_{n+\frac{1}{2}}}{\partial \boldsymbol{q}_{n+\frac{1}{2}}} \right)^{\mathrm{T}} = \frac{\boldsymbol{r}}{l_0} + \bar{\theta}_{1,n+\frac{1}{2}} \left(ct_1\, \boldsymbol{b}_3 + ct_2\, \boldsymbol{b}_4 \right) + \bar{\theta}_{2,n+\frac{1}{2}} \left(ct_2\, \boldsymbol{b}_3 + ct_1\, \boldsymbol{b}_4 \right) \tag{84}$$

The global elastic force vector $\boldsymbol{f}_{g,n+\frac{1}{2}}$ is obtained by using Eq.(56). Besides, since the local elastic force vector is not a linear function of $\bar{\boldsymbol{q}}_{n+\frac{1}{2}}$, the expression of the global stiffness matrix is different from Eq.(61) and is obtained as

$$\begin{aligned} \mathbf{K}_g = {} & \frac{1}{2}\, \mathbf{B}^{\mathrm{T}} \left(\mathbf{K}_{l1} + \mathbf{K}_{l2} \right) \left(\mathbf{B} + \frac{1}{2}\, \mathbf{B}_0 \right) + \frac{\boldsymbol{z}\boldsymbol{z}^{\mathrm{T}}}{2\, l_{n+\frac{1}{2}}} N + \frac{\boldsymbol{r}\boldsymbol{z}^{\mathrm{T}} + \boldsymbol{z}\boldsymbol{r}^{\mathrm{T}}}{2\, l^2_{n+\frac{1}{2}}} \left(M_1 + M_2 \right) \\ & + \frac{1}{2}\, EA\, l_0\, \boldsymbol{f}_4 \left(\boldsymbol{f}_4^{\mathrm{T}} + \Delta \boldsymbol{q}^{\mathrm{T}} \frac{\partial \boldsymbol{f}_4}{\partial \boldsymbol{q}_{n+1}} \right) \end{aligned} \tag{85}$$

with

$$\mathbf{K}_{l2} = EA\, l_0\, \varepsilon_{n+\frac{1}{2}} \begin{bmatrix} 0 & 0 & 0 \\ 0 & ct_1 & ct_2 \\ 0 & ct_2 & ct_1 \end{bmatrix} \tag{86}$$

and

$$\begin{aligned} \frac{\partial \boldsymbol{f}_4}{\partial \boldsymbol{q}_{n+1}} = {} & \frac{\boldsymbol{z}\boldsymbol{z}^{\mathrm{T}}}{2\, l_0\, l_{n+\frac{1}{2}}} + \frac{1}{24} \left(\boldsymbol{b}_3 - \boldsymbol{b}_4 \right) \left(\boldsymbol{b}_3 - \boldsymbol{b}_4 \right)^{\mathrm{T}} + \frac{\mu^2}{20} \left(\bar{\theta}_{1,n+\frac{1}{2}} + \bar{\theta}_{2,n+\frac{1}{2}} \right) \frac{\boldsymbol{r}\boldsymbol{z}^{\mathrm{T}} + \boldsymbol{z}\boldsymbol{r}^{\mathrm{T}}}{l^2_{n+\frac{1}{2}}} \\ & + \frac{\mu^2}{40} \left(\boldsymbol{b}_3 + \boldsymbol{b}_4 \right) \left[\left(\boldsymbol{b}_3 + \boldsymbol{b}_4 \right)^{\mathrm{T}} + \Delta \boldsymbol{q}^{\mathrm{T}} \frac{\boldsymbol{r}\boldsymbol{z}^{\mathrm{T}} + \boldsymbol{z}\boldsymbol{r}^{\mathrm{T}}}{l^2_{n+\frac{1}{2}}} \right] \end{aligned} \tag{87}$$

7. Solution of the equation of motion: choice of the predictor

In the previous sections, the inertia and elastic force vectors have been defined for each formulation. By applying Hamilton's principle (8), the equation of motion is given as

$$\boldsymbol{f}_{R,n+\frac{1}{2}} = \boldsymbol{f}_{k,n+\frac{1}{2}} + \boldsymbol{f}_{g,n+\frac{1}{2}} - \boldsymbol{f}_{ext,n+\frac{1}{2}} = \mathbf{0} \tag{88}$$

in which the external force vector is defined as

$$\boldsymbol{f}_{ext,n+\frac{1}{2}} = \boldsymbol{P}_{n+\frac{1}{2}} \tag{89}$$

The total tangent matrix is defined by

$$\mathbf{K}_{\mathrm{T}} = \mathbf{K}_k + \mathbf{K}_g \tag{90}$$

The predictor provides the initial value for the solution at time $n+1$. A poor predictor can increase the number of iterations and in some cases makes the procedure fail to converge. In this work, three predictors have been implemented and tested:

• The first predictor (Pred.1), referred to as "Unchanged displacements", is used by Simo and Vu-Quoc [62].

$$\boldsymbol{q}_{n+1} = \boldsymbol{q}_n \tag{91}$$

• The second predictor (Pred.2), called as "Null accelerations", is proposed by Cardona and Geradin [61], Mäkinen [63], Chung and Hulbert [64]. Zero accelerations are taken as predictor for the solution at time $n+1$. In the case of midpoint rule the nodal accelerations at time $n+\frac{1}{2}$ are taken to zero, hence the new prediction for displacements is obtained as

$$\boldsymbol{q}_{n+1} = \boldsymbol{q}_n + \Delta t\, \dot{\boldsymbol{q}}_n \tag{92}$$

• The idea of the third predictor (Pred.3), proposed by de Borst et al. [65], is to assume that the system behaves linearly between steps $n-\frac{1}{2}$ and $n+\frac{1}{2}$. In that case, the elastic force vector can be written as

$$\boldsymbol{f}_{g,n+\frac{1}{2}} = \boldsymbol{f}_{g,n-\frac{1}{2}} + \mathbf{K}_{g,n-\frac{1}{2}}\, \Delta \boldsymbol{q} \tag{93}$$

If the inertia term is linear, it can be written as

$$\boldsymbol{f}_{k,n+\frac{1}{2}} = \mathbf{M}\, \ddot{\boldsymbol{q}}_{n+\frac{1}{2}} = \mathbf{M} \left(\frac{2}{\Delta t^2}\, \Delta \boldsymbol{q} - \frac{2}{\Delta t}\, \dot{\boldsymbol{q}}_n \right) \tag{94}$$

Inserting Eqs.(93) and (94) into the Eq.(88), it is obtained:

$$\left(\frac{2}{\Delta t^2}\, \mathbf{M} + \mathbf{K}_{g,n-\frac{1}{2}} \right) \Delta \boldsymbol{q} = \frac{2}{\Delta t}\, \mathbf{M}\, \dot{\boldsymbol{q}}_n - \boldsymbol{f}_{g,n-\frac{1}{2}} + \boldsymbol{f}_{ext,n+\frac{1}{2}} \tag{95}$$

If the inertia term is nonlinear and by considering the similarity between Eqs.(40) and (94), one idea is to take:

$$\boldsymbol{f}_{k,n+\frac{1}{2}} = \frac{2}{\Delta t^2} \left(\mathbf{T}^{\mathrm{T}} \mathbf{M}_l \mathbf{T} \right)_{n-\frac{1}{2}} \Delta \boldsymbol{q} - \frac{2}{\Delta t}\, \boldsymbol{f}_{uw\theta,n-\frac{1}{2}} \tag{96}$$

Introducing Eqs.(93) and (96) into the Eq.(88) leads to

$$\left(\frac{2}{\Delta t^2}\, \mathbf{T}^{\mathrm{T}} \mathbf{M}_l \mathbf{T} + \mathbf{K}_g \right)_{n-\frac{1}{2}} \Delta \boldsymbol{q} = \frac{2}{\Delta t}\, \boldsymbol{f}_{uw\theta,n-\frac{1}{2}} - \boldsymbol{f}_{g,n-\frac{1}{2}} + \boldsymbol{f}_{ext,n+\frac{1}{2}} \tag{97}$$

The present algorithm can be summarised as follows:

Algorithm : Energy conserving scheme

1. Parameters at time n

Nodal displacement, velocity and acceleration : $\boldsymbol{q}_n, \dot{\boldsymbol{q}}_n, \ddot{\boldsymbol{q}}_n$

IIE: $v_{u3,n}$, $v_{u4,n}$, $v_{w3,n}$, $v_{w4,n}$, $v_{\theta,n}$, $\varepsilon_n, \bar{\theta}_{1,n}, \bar{\theta}_{2,n}$

RIE and MX: $\bar{u}_n, \bar{\theta}_{1,n}, \bar{\theta}_{2,n}$

2. Initialization: $\boldsymbol{q}^j_{n+1}$ (see the predictors)

3. Loop over the iteration step j

Compute $\boldsymbol{f}_{R,n+\frac{1}{2}}(\boldsymbol{q}^j_{n+1})$ (88) and $\mathbf{K}_{\mathrm{T}}(\boldsymbol{q}^j_{n+1})$ (90)

Compute the displacement increment $\Delta\boldsymbol{q}^j = -\mathbf{K}_{\mathrm{T}}^{-1}\boldsymbol{f}_{R,n+\frac{1}{2}}$

Check the convergence

if $\| \boldsymbol{f}_R \| > tol_1$ or $\| \Delta\boldsymbol{q}^j \| > tol_2$

$\boldsymbol{q}^{j+1}_{n+1} = \boldsymbol{q}^j_{n+1} + \Delta\boldsymbol{q}^j, \quad j+1 \to j$ and go to (**3**)

else

Update the parameters at time $n+1$: $\dot{\boldsymbol{q}}_{n+1}, \ddot{\boldsymbol{q}}_{n+1}$ (17)

IIE: $v_{u3,n+1}$, $v_{u4,n+1}$ (32),$v_{w3,n+1}$, $v_{w4,n+1}$ (33), $v_{\theta,n+1}$ (34)
ε_{n+1} (83), $\bar{\theta}_{1,n+1}$ (35), $\bar{\theta}_{2,n+1}$ (36)

RIE and MX: $\bar{u}_{n+1}$ (60), $\bar{\theta}_{1,n+1}$ (35), $\bar{\theta}_{2,n+1}$ (36)

$n+1 \to n$ and go to (**1**)

end

8. Conservation properties of the scheme

In this section, we rigorously prove that the proposed method conserves the total energy of the system and, in absence of external loads, that the linear and angular momenta remain constant.

8.1. Proof of the conservation of linear momentum

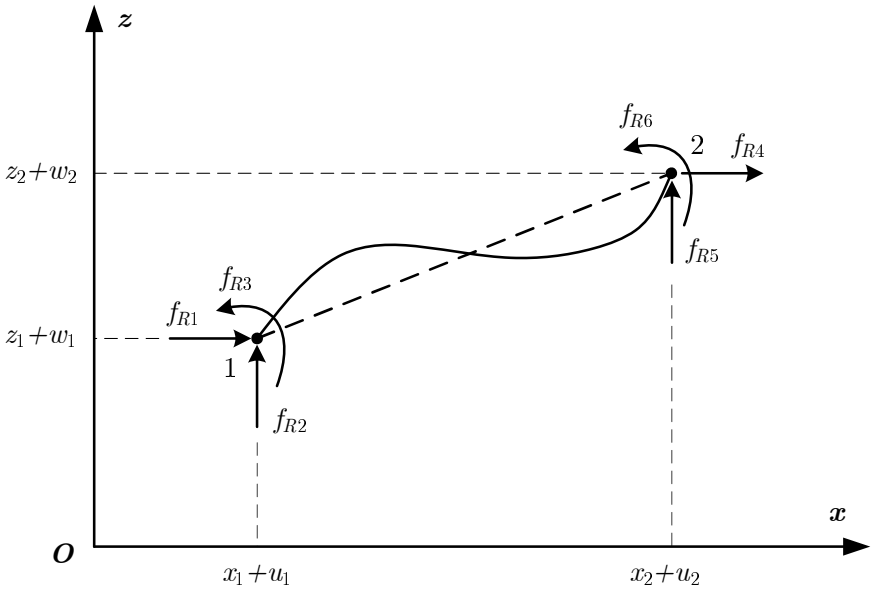

Figure 2: Components of the residual force vector

The purpose of this section is to prove that without external loads, the proposed energy-momentum method gives a constant linear momentum (see Eq.(12)).

The components $f_{Ri,n+\frac{1}{2}}$ (Eq.(88)) of the residual vector are shown in Figure 2. Since each component is equal to zero, the following expressions, corresponding to the sums of the residual forces in horizontal and vertical directions, can be considered:

$$\left[\begin{array}{c} f_{R1,n+\frac{1}{2}} + f_{R4,n+\frac{1}{2}} \\ f_{R2,n+\frac{1}{2}} + f_{R5,n+\frac{1}{2}} \end{array} \right] = \left[\begin{array}{c} 0 \\ 0 \end{array} \right] \tag{98}$$

For the three formulations, the sum of inertia forces (Eqs.(27),(47)) and elastic forces (Eqs.(56)) in horizontal and vertical directions give after some algebraic manipulations:

$$\begin{array}{l} \left[\begin{array}{c} f_{k1,n+\frac{1}{2}} + f_{k4,n+\frac{1}{2}} \\ f_{k2,n+\frac{1}{2}} + f_{k5,n+\frac{1}{2}} \end{array} \right] = \displaystyle\int_{l_0} \rho A \left[\begin{array}{c} \ddot{u}_{G,n+\frac{1}{2}} \\ \ddot{w}_{G,n+\frac{1}{2}} \end{array} \right] \mathrm{d}x \\ \left[\begin{array}{c} f_{g1,n+\frac{1}{2}} + f_{g4,n+\frac{1}{2}} \\ f_{g2,n+\frac{1}{2}} + f_{g5,n+\frac{1}{2}} \end{array} \right] = \left[\begin{array}{c} 0 \\ 0 \end{array} \right] \end{array} \tag{99}$$

where $f_{kj,n+\frac{1}{2}}$ and $f_{gj,n+\frac{1}{2}}$ are respectively the j component of vectors $\boldsymbol{f}_{k,n+\frac{1}{2}}$ and $\boldsymbol{f}_{g,n+\frac{1}{2}}$. By using Eqs.(99), Eq.(98) can be rewritten as

$$\int_{l_0} \rho A \left[\begin{array}{c} \ddot{u}_{G,n+\frac{1}{2}} \\ \ddot{w}_{G,n+\frac{1}{2}} \end{array} \right] \mathrm{d}x = \left[\begin{array}{c} P_{1,n+\frac{1}{2}} + P_{4,n+\frac{1}{2}} \\ P_{2,n+\frac{1}{2}} + P_{5,n+\frac{1}{2}} \end{array} \right] \tag{100}$$

Without external forces and by introducing the midpoint rule (the third relationship of Eqs.(16)), the last equation gives $\mathbf{L}_{n+1} = \mathbf{L}_n$ which shows the conservation of the linear momentum.

8.2. Proof of the conservation of angular momentum

The purpose of this section is to prove that without external moments, the proposed energy-momentum algorithm gives a constant angular momentum (see Eq.(13)).

As for the linear momentum, the residual vector, see Eq.(88) and Figure 2 is used. Since each component of $f_{Ri,n+\frac{1}{2}}$ is equal to zero, the following expression, corresponding to the sum of the moments about the origin O can be considered:

$$\begin{array}{r} \xi(\boldsymbol{f}_{R,n+\frac{1}{2}}) = (x_1 + u_1)\, f_{R2,n+\frac{1}{2}} - (z_1 + w_1)\, f_{R1,n+\frac{1}{2}} + (x_2 + u_2)\, f_{R5,n+\frac{1}{2}} \\ - (z_2 + w_2)\, f_{R4,n+\frac{1}{2}} + f_{R3,n+\frac{1}{2}} + f_{R6,n+\frac{1}{2}} = 0 \end{array} \tag{101}$$

For the three formulations, the application of (101) to the elastic force vector $\boldsymbol{f}_{g,n+\frac{1}{2}}$ (see Eq.(56)) gives zero. Therefore, the previous equation gives after some algebraic manipulations

$$\begin{array}{l} \displaystyle\int_{l_0} \rho A \left(u_{G,n+\frac{1}{2}}\, \ddot{w}_{G,n+\frac{1}{2}} - w_{G,n+\frac{1}{2}}\, \ddot{u}_{G,n+\frac{1}{2}} \right) \mathrm{d}x + \int_{l_0} \rho I\, \ddot{\theta}_{G,n+\frac{1}{2}}\, \mathrm{d}x \\ = (x_1 + u_{1,n+\frac{1}{2}})\, P_{2,n+\frac{1}{2}} - (z_1 + w_{1,n+\frac{1}{2}})\, P_{1,n+\frac{1}{2}} + (x_2 + u_{2,n+\frac{1}{2}})\, P_{5,n+\frac{1}{2}} \\ - (z_2 + w_{2,n+\frac{1}{2}})\, P_{4,n+\frac{1}{2}} + P_{3,n+\frac{1}{2}} + P_{6,n+\frac{1}{2}} \end{array} \tag{102}$$

Then, by introducing the midpoint rule (16), the previous equation leads to

$$\int_{l_0} \rho A \begin{bmatrix} u_{G,n+1} \\ w_{G,n+1} \\ 0 \end{bmatrix} \times \begin{bmatrix} \dot{u}_{G,n+1} \\ \dot{w}_{G,n+1} \\ 0 \end{bmatrix} \mathrm{d}x + \int_{l_0} \rho I \begin{bmatrix} 0 \\ 0 \\ \dot{\theta}_{G,n+1} \end{bmatrix} \mathrm{d}x$$
$$= \int_{l_0} \rho A \begin{bmatrix} u_{G,n} \\ w_{G,n} \\ 0 \end{bmatrix} \times \begin{bmatrix} \dot{u}_{G,n} \\ \dot{w}_{G,n} \\ 0 \end{bmatrix} \mathrm{d}x + \int_{l_0} \rho I \begin{bmatrix} 0 \\ 0 \\ \dot{\theta}_{G,n} \end{bmatrix} \mathrm{d}x + \Delta t\, M_{ext} \tag{103}$$

where M_{ext} is defined in (15). In case of vanishing external moments, it found that $\mathsf{J}_{n+1} = \mathsf{J}_n$ which shows the conservation of the angular momentum.

8.3. Proof of the conservation of energy

The purpose of this section is to prove that the proposed energy-momentum algorithm conserves the total energy (see Eq.(11)) of the system when the external load is assumed conservative.

8.3.1. Reduced integration and IIE formulation

Eq.(88) (see also Eqs.(27),(56)) is multiplied the midpoint velocity $\dot{\boldsymbol{q}}^{\mathrm{T}}_{n+\frac{1}{2}}$ to yield

$$\int_{l_0} \rho A\, \ddot{u}_{G,n+\frac{1}{2}}\, \dot{u}_{G,n+\frac{1}{2}}\, \mathrm{d}x + \int_{l_0} \rho A\, \ddot{w}_{G,n+\frac{1}{2}}\, \dot{w}_{G,n+\frac{1}{2}}\, \mathrm{d}x + \int_{l_0} \rho I\, \ddot{\theta}_{G,n+\frac{1}{2}}\, \dot{\theta}_{G,n+\frac{1}{2}}\, \mathrm{d}x$$
$$+ \int_{l_0} EA\, \varepsilon_{n+\frac{1}{2}}\, \dot{\varepsilon}_{n+\frac{1}{2}}\, \mathrm{d}x + \int_{l_0} EI\, \kappa_{n+\frac{1}{2}}\, \dot{\kappa}_{n+\frac{1}{2}}\, \mathrm{d}x + \int_{l_0} k_s GA\, \gamma_{n+\frac{1}{2}}\, \dot{\gamma}_{n+\frac{1}{2}}\, \mathrm{d}x$$
$$- \sum_{i=1}^{6} P_{i,n+\frac{1}{2}}\, \dot{q}_{i,n+\frac{1}{2}} = 0 \tag{104}$$

which, by using the midpoint rule (16), gives

$$\int_{l_0} \rho A\, \frac{\dot{u}_{G,n+1} - \dot{u}_{G,n}}{\Delta t}\, \frac{\dot{u}_{G,n+1} + \dot{u}_{G,n}}{2}\, \mathrm{d}x + \int_{l_0} \rho A\, \frac{\dot{w}_{G,n+1} - \dot{w}_{G,n}}{\Delta t}\, \frac{\dot{w}_{G,n+1} + \dot{w}_{G,n}}{2}\, \mathrm{d}x$$
$$+ \int_{l_0} \rho I\, \frac{\dot{\theta}_{G,n+1} - \dot{\theta}_{G,n}}{\Delta t}\, \frac{\dot{\theta}_{G,n+1} + \dot{\theta}_{G,n}}{2}\, \mathrm{d}x + \int_{l_0} EA\, \frac{\varepsilon_{n+1} + \varepsilon_n}{2}\, \frac{\varepsilon_{n+1} - \varepsilon_n}{\Delta t}\, \mathrm{d}x$$
$$+ \int_{l_0} EI\, \frac{\kappa_{n+1} + \kappa_n}{2}\, \frac{\kappa_{n+1} - \kappa_n}{\Delta t}\, \mathrm{d}x + \int_{l_0} k_s GA\, \frac{\gamma_{n+1} + \gamma_n}{2}\, \frac{\gamma_{n+1} - \gamma_n}{\Delta t}\, \mathrm{d}x$$
$$- \sum_{i=1}^{6} P_{i,n+\frac{1}{2}}\, \frac{q_{i,n+1} - q_{i,n}}{\Delta t} = 0 \tag{105}$$

The last equation can be rewritten as

$$\frac{1}{2} \int_{l_0} \rho A\, (\dot{u}_{G,n+1}\, \dot{u}_{G,n+1} - \dot{u}_{G,n}\, \dot{u}_{G,n})\, \mathrm{d}x + \frac{1}{2} \int_{l_0} \rho A\, (\dot{w}_{G,n+1}\, \dot{w}_{G,n+1} - \dot{w}_{G,n}\, \dot{w}_{G,n})\, \mathrm{d}x$$
$$+ \frac{1}{2} \int_{l_0} \rho I \left(\dot{\theta}_{G,n+1}\, \dot{\theta}_{G,n+1} - \dot{\theta}_{G,n}\, \dot{\theta}_{G,n} \right) \mathrm{d}x + \frac{1}{2} \int_{l_0} EA\, (\varepsilon_{n+1}\, \varepsilon_{n+1} - \varepsilon_n\, \varepsilon_n)\, \mathrm{d}x$$
$$+ \frac{1}{2} \int_{l_0} EI\, (\kappa_{n+1}\, \kappa_{n+1} - \kappa_n\, \kappa_n)\, \mathrm{d}x + \frac{1}{2} \int_{l_0} k_s GA\, (\gamma_{n+1}\, \gamma_{n+1} - \gamma_n\, \gamma_n)\, \mathrm{d}x$$
$$- \sum_{i=1}^{6} P_{i,n+\frac{1}{2}}\, (q_{i,n+1} - q_{i,n}) = 0 \tag{106}$$

By using Eqs. (23), (53) and (10), Eq.(106) is equivalent to

$$[\mathsf{K} + \mathsf{U}_{int} + \mathsf{U}_{ext}]_{n+1} = [\mathsf{K} + \mathsf{U}_{int} + \mathsf{U}_{ext}]_n \tag{107}$$

which shows that the proposed midpoint algorithm conserves the total energy of the system.

8.3.2. Hellinger-Reissner formulation

The Eqs.(88) and (69) are rewritten as:

$$\boldsymbol{f}_{R,n+\frac{1}{2}} = \mathbf{M}\,\ddot{\boldsymbol{q}}_{n+\frac{1}{2}} + \mathbf{B}^{\mathrm{T}}\boldsymbol{f}_{l,n+\frac{1}{2}} - \boldsymbol{f}_{ext,n+\frac{1}{2}} = \mathbf{0} \tag{108}$$

$$\left(\frac{\partial \mathcal{U}_{int}}{\partial \boldsymbol{f}_{l,n+\frac{1}{2}}}\right)^{\mathrm{T}} = \bar{\boldsymbol{q}}_{n+\frac{1}{2}} - \mathbf{H}\,\boldsymbol{f}_{l,n+\frac{1}{2}} = \mathbf{0} \tag{109}$$

By multiplying Eq.(108) by $\dot{\boldsymbol{q}}^{\mathrm{T}}_{n+\frac{1}{2}}$ and Eq.(109) by $\dot{\boldsymbol{f}}^{\mathrm{T}}_{l,n+\frac{1}{2}}$, and adding outcomes it is found, after some algebraic manipulations, that

$$\begin{aligned}&\dot{\boldsymbol{q}}^{\mathrm{T}}_{n+\frac{1}{2}}\,\mathbf{M}\,\ddot{\boldsymbol{q}}_{n+\frac{1}{2}} + \int_{l_0} \boldsymbol{S}^{\mathrm{T}}_{n+\frac{1}{2}}\,\dot{\hat{\boldsymbol{e}}}_{n+\frac{1}{2}}\mathrm{d}x - \sum_{i=1}^{6} P_{i,n+\frac{1}{2}}\,\dot{q}_{i,n+\frac{1}{2}} \\ &+ \int_{l_0} \dot{\boldsymbol{S}}^{\mathrm{T}}_{n+\frac{1}{2}} \left(\hat{\boldsymbol{e}} - \frac{1}{2}\boldsymbol{e}\right)_{n+\frac{1}{2}} \mathrm{d}x - \frac{1}{2}\int_{l_0} \boldsymbol{S}^{\mathrm{T}}_{n+\frac{1}{2}}\,\dot{\boldsymbol{e}}_{n+\frac{1}{2}}\mathrm{d}x = 0\end{aligned} \tag{110}$$

By using the midpoint rule (16), the above equation gives

$$\begin{aligned}&\frac{\dot{\boldsymbol{q}}^{\mathrm{T}}_{n+1} + \dot{\boldsymbol{q}}^{\mathrm{T}}_{n}}{2}\,\mathbf{M}\,\frac{\dot{\boldsymbol{q}}_{n+1} - \dot{\boldsymbol{q}}_{n}}{\Delta t} + \int_{l_0} \frac{\boldsymbol{S}^{\mathrm{T}}_{n+1} + \boldsymbol{S}^{\mathrm{T}}_{n}}{2}\,\frac{\left(\hat{\boldsymbol{e}} - \frac{1}{2}\boldsymbol{e}\right)_{n+1} - \left(\hat{\boldsymbol{e}} - \frac{1}{2}\boldsymbol{e}\right)_{n}}{\Delta t}\,\mathrm{d}x \\ &+ \int_{l_0} \frac{\boldsymbol{S}^{\mathrm{T}}_{n+1} - \boldsymbol{S}^{\mathrm{T}}_{n}}{\Delta t}\,\frac{\left(\hat{\boldsymbol{e}} - \frac{1}{2}\boldsymbol{e}\right)_{n+1} + \left(\hat{\boldsymbol{e}} - \frac{1}{2}\boldsymbol{e}\right)_{n}}{2}\,\mathrm{d}x - \sum_{i=1}^{6} P_{i,n+\frac{1}{2}}\,\frac{q_{i,n+1} - q_{i,n}}{\Delta t} = 0\end{aligned} \tag{111}$$

The last equation can be rewritten as

$$\begin{aligned}&\frac{1}{2}\left(\dot{\boldsymbol{q}}^{\mathrm{T}}\,\mathbf{M}\,\dot{\boldsymbol{q}}\right)_{n+1} - \frac{1}{2}\left(\dot{\boldsymbol{q}}^{\mathrm{T}}\,\mathbf{M}\,\dot{\boldsymbol{q}}\right)_{n} + \int_{l_0} \boldsymbol{S}^{\mathrm{T}}_{n+1}\left(\hat{\boldsymbol{e}} - \frac{1}{2}\boldsymbol{e}\right)_{n+1}\mathrm{d}x \\ &- \int_{l_0} \boldsymbol{S}^{\mathrm{T}}_{n}\left(\hat{\boldsymbol{e}} - \frac{1}{2}\boldsymbol{e}\right)_{n}\mathrm{d}x - \sum_{i=1}^{6} P_{i,n+\frac{1}{2}}\,(q_{i,n+1} - q_{i,n}) = 0\end{aligned} \tag{112}$$

Finally, from Eqs. (46) and (63), Eq. (112) is equivalent to

$$[\mathsf{K} + \mathsf{U}_{int} + \mathsf{U}_{ext}]_{n+1} = [\mathsf{K} + \mathsf{U}_{int} + \mathsf{U}_{ext}]_n \tag{113}$$

This proves the conservation of the total energy of the system.

9. Numerical examples

Four numerical examples are presented in this section. The first purpose is to verify that the proposed algorithm conserves the total energy of the system and remain

stable even if a very large number of time steps are applied. The second purpose is to show that the proposed algorithm conserves the linear and angular momenta in the absence of applied external loads. The third purpose is to assess the efficiency of the three proposed formulations, both regarding the required number of elements and the computational time. For that, a reference solution is calculated. This reference solution is obtained by taking a large number of elements and is identical for the three formulations. Regarding the computational time, the possibility of using a simplified tangent dynamic matrix for the IIE formulation and the choice of the predictor are carefully studied. The number of elements for each example is given in Table 2.

Table 2: Number of elements

Examples	IIE	MX	RIE	Reference
Lee's frame	10	20	30	100
Simple beam	8	16	24	100
Shallow arch beam	8	16	24	100
Free fly beam	4	8	12	50

For the presentation of the results, the following colors are used in all figures:

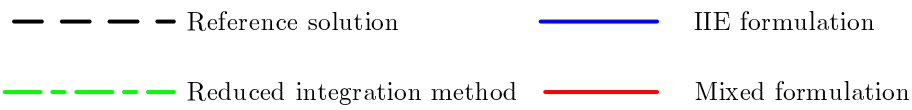

9.1. Lee's frame

Consider a Lee's frame (as shown in Fig. 3) subjected to a concentrated load P. The length is $L = 2.4$ m. The cross-section width and depth are $b = 0.3$ m and $h = 0.2$ m. The mechanical properties are: elastic modulus $E = 210$ GPa, Poisson's ratio $\nu = 0.3$, density $\rho = 7850$ kg/m^3. The time step is $\Delta t = 5 \times 10^{-4}$ s.

Figs. 4 and 5 show the vertical and horizontal displacements at the applied load P respectively for the four analyses. The results obtained with the IIE formulation (only 10 elements) are in very good agreement with the reference solution. However, even with a large number of elements (20 for the mixed formulation and 30 for the reduced integration method), large discrepancies are obtained between these two formulations and the reference solution. Finally, the results show in Fig. 6 that the total energy for all formulations is conserved when the load is constant even if one million time steps are applied.

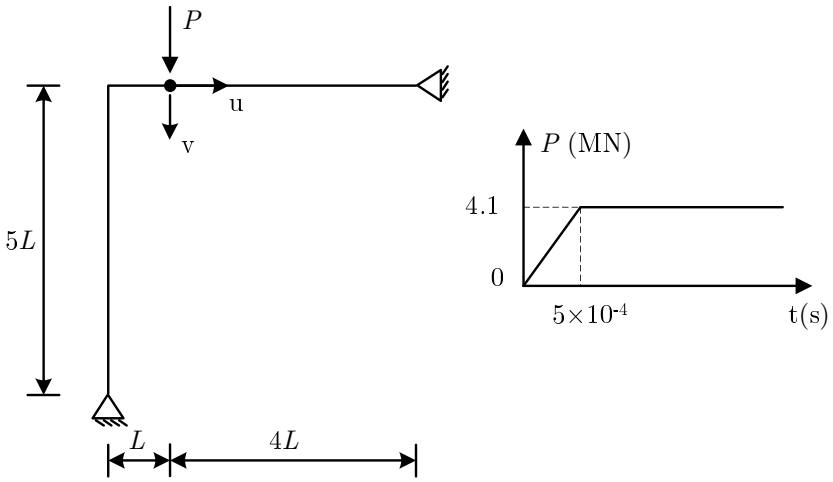

Figure 3: Lee's frame: geometry and loading history.

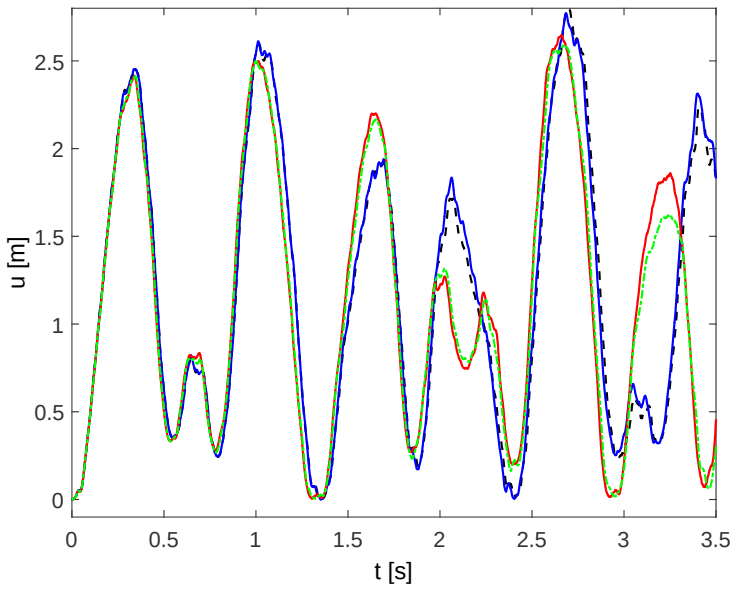

Figure 4: Lee's frame: horizontal displacement u.

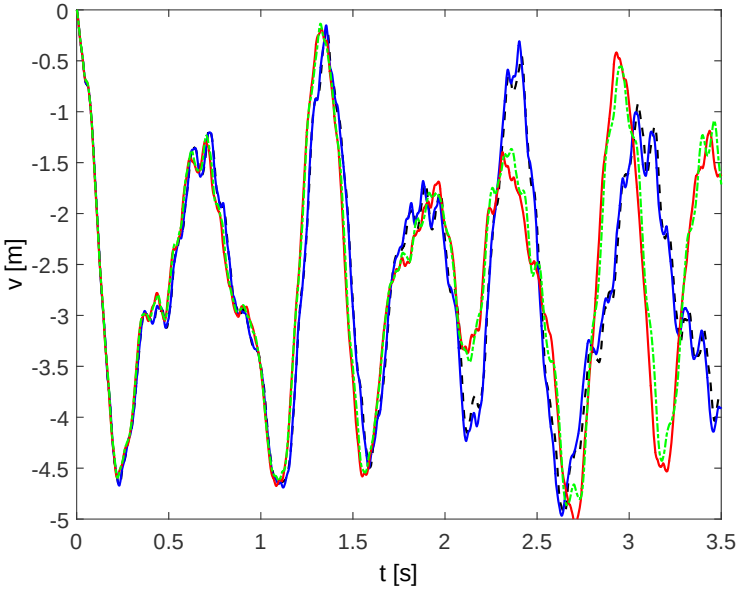

Figure 5: Lee's frame: vertical displacement v.

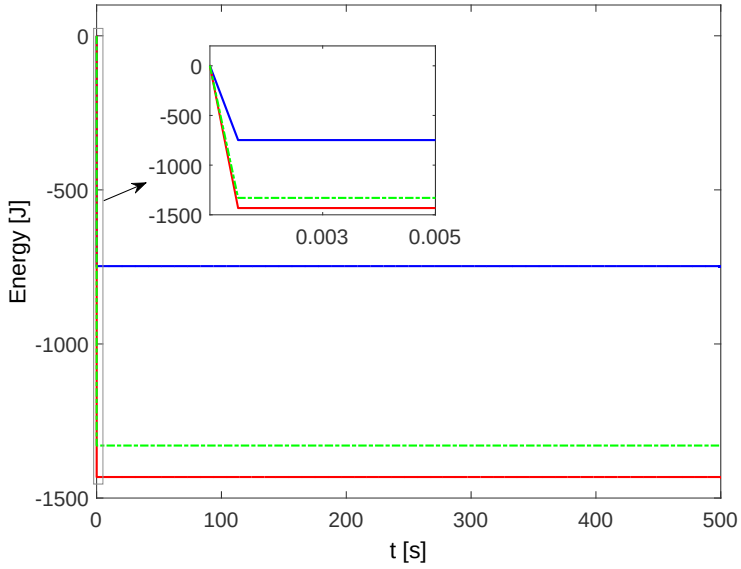

Figure 6: Lee's frame: energy.

9.2. Simple beam

A simply-supported beam depicted in Fig. 7 is subjected to a vertical concentrated load $P = 4.1$ MN at mid-span. The length of the beam is $L = 1$ m. The cross-section width and depth are $b = 0.20$ m and $h = 0.15$ m. The material parameters are: elastic modulus $E = 1$ GPa, Poisson's ratio $\nu = 0.3$, density $\rho = 7850$ kg/m^3. The time step size is $\Delta t = 10^{-4}$ s. The interest of this example is that for this short beam the shear effect is important.

The horizontal displacement at the right end and the vertical displacement at mid-span for the four analyses are depicted in Figs. 8 and 9. The number of elements for each formulation is: 8 for IIE formulation, 16 for mixed formulation, 24 for reduced integration method and 100 for the reference solution. The results show that the displacements of all formulations are nearly identical to the reference solution. In Fig. 10, it is shown that the three proposed formulations conserve the total energy of the system and that the solutions remain stable for one million time steps.

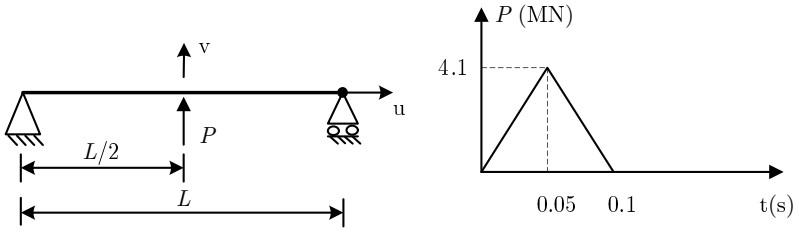

Figure 7: Simple beam: geometry and loading history.

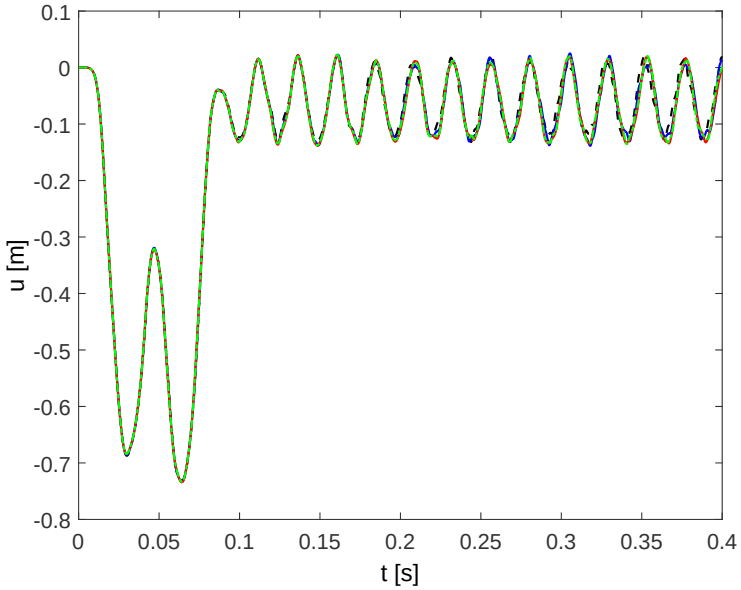

Figure 8: Simple beam: horizontal displacement u.

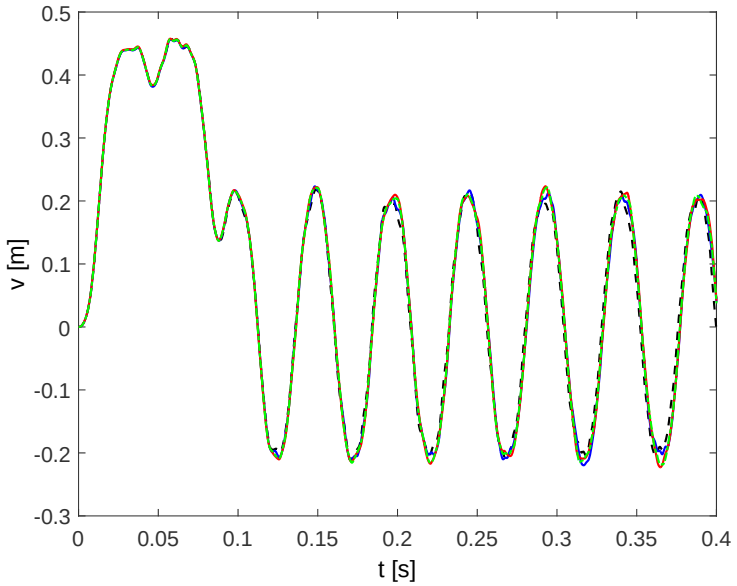

Figure 9: Simple beam: vertical displacement v.

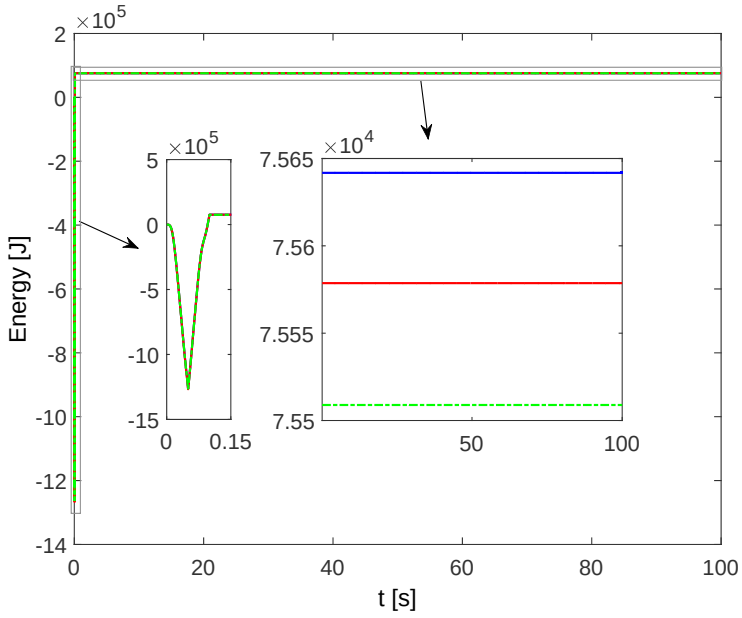

Figure 10: Simple beam: energy.

9.3. Shallow arch beam

A shallow arch beam of span $L = 10$ m with clamped ends is depicted in Fig. 11. The radius R of the arch is 10 m and the height H is 1.3997 m. The shallow arch is subjected to a time-dependent concentrated load $P = P_0\, sin(\omega t)$ at mid-span. The amplitude of the load P_0 is 80 MN and its frequency ω is 1000 rad/s. The characteristics of the arch are: cross-sectional area $A = 0.087$ m^2, elastic modulus $E = 210$ GPa, moment of inertia $I = 3.562 \times 10^{-3}$ m^4, Poisson's ratio $\nu = 0.3$ and density $\rho = 7850$ kg/m^3. The size of time step is $\Delta t = 10^{-5}$ s.

In Fig. 12, the vertical displacement v at mid-span is depicted for the four analyses. With only 8 elements, the result obtained with IIE formulation is slightly different from the reference solution. However, large discrepancies can be observed between the results obtained with the mixed formulation (16 elements)and with the reduced integration method (24 elements) compared to the reference solution.

In this example, the external force is not constant and consequently Eq.(11) cannot be directly used. However, it can be easily shown from Eq.(11) that the difference of the kinetic and elastic energies between the times n and $n+1$ is equal to the external work performed by the applied force P between the times n and $n+1$:

$$[\mathsf{K} + \mathsf{U}_{int}]_{n+1} - [\mathsf{K} + \mathsf{U}_{int}]_n = \mathsf{W}_{ext}|_n^{n+1} \tag{114}$$

Applying the midpoint rule provides

$$\mathsf{W}_{ext}|_n^{n+1} = \int_n^{n+1} P\, \mathrm{d}q = P_{n+\frac{1}{2}}\, (q_{n+1} - q_n) \tag{115}$$

Since, there is no energy in the system at the beginning, the above equations give

$$[\mathsf{K} + \mathsf{U}_{int} - \mathsf{W}_{ext}]_n = 0, \qquad \mathsf{W}_{ext,n} = \int_0^n P\, \mathrm{d}q \tag{116}$$

At each step, the relative error is defined as

$$\eta = \frac{|\mathsf{K} + \mathsf{U}_{int} - \mathsf{W}_{ext}|}{|\mathsf{W}_{ext}|} \tag{117}$$

For the three formulations, the relative energy error is depicted in Fig. 13. The largest value is about 3×10^{-8} for a maximum external energy of 1.85×10^8 J. These results proved the good stability of the proposed algorithm even for a large number of steps (one million).

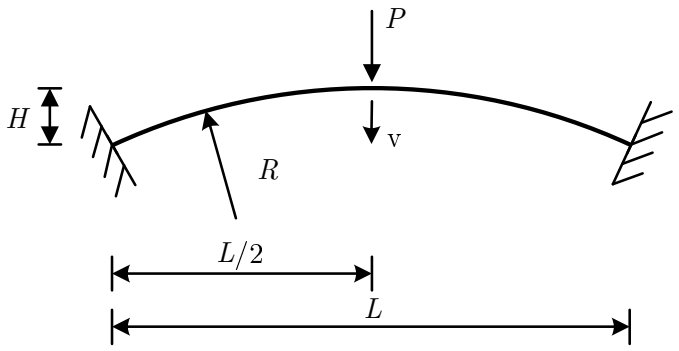

Figure 11: Shallow arch beam: geometry and loading history.

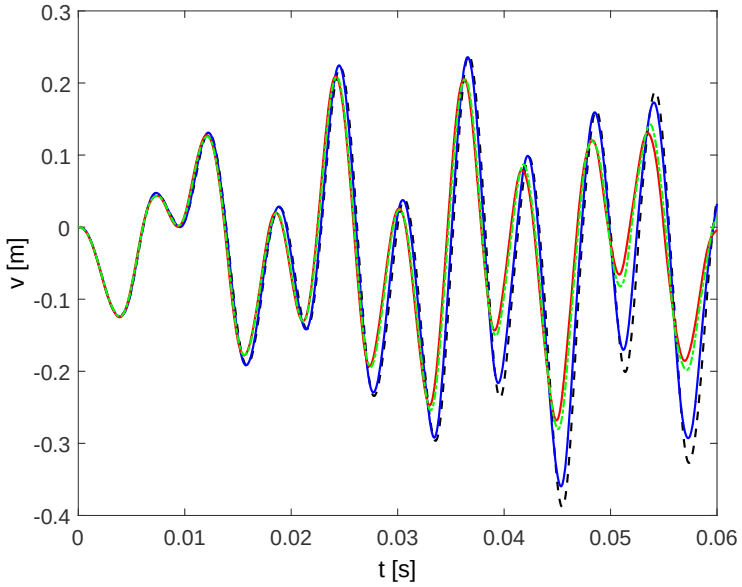

Figure 12: Shallow arch beam: vertical displacement v.

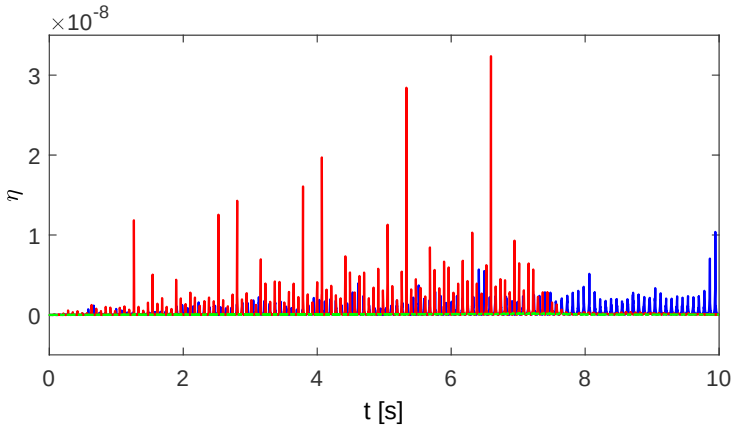

Figure 13: Shallow arch beam: relative energy error.

9.4. Free fly beam

Consider a free fly beam without support subjected to a concentrate load P as shown in Fig. 14. The length of the beam is $L = 3$ m, the cross-sectional area is $A = 200$ cm^2 and the moment of inertia $I = 66.67$ cm^4. The material properties are: elastic modulus $E = 200$ GPa, Poisson's ratio $\nu = 0.3$, density $\rho = 48831$ kg/m^3. The time step size is $\Delta t = 10^{-4}$ s.

In Fig. 15, the horizontal displacement at mid-span is depicted for the four analyses. The solution with the IIE formulation (4 elements) is nearly identical to the reference solution. But, with a larger number of elements (8 for the mixed formulation and 12 for the reduced integration method), some discrepancies are observed between the reference solution and these two formulations. In Fig. 16, the results show the conservation of the total energy for all formulations even if one million time steps are applied.

The interest of this problem is to study the conservation of the linear and angular momenta after the time 0.4 s because no forces and moments are then applied to the

beam. Since only vertical loads are applied at the beginning, the linear momentum Lu for the horizontal direction should be zero. As shown in Fig. 17, the linear momentum Lu is conserved with the maximum value 2×10^{-5}. Moreover, Figs. 17 and 18 show the conservation of linear momentum Lw for the vertical direction and the angular momentum for one million time steps.

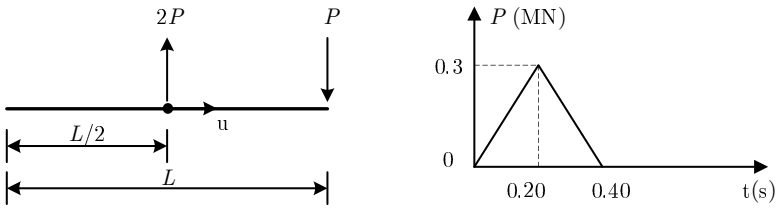

Figure 14: Free fly beam: geometry and loading history.

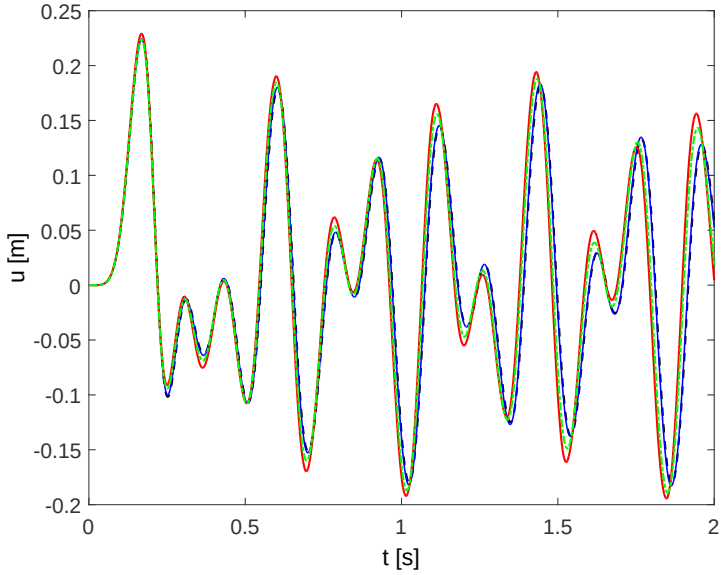

Figure 15: Free fly beam: horizontal displacement u.

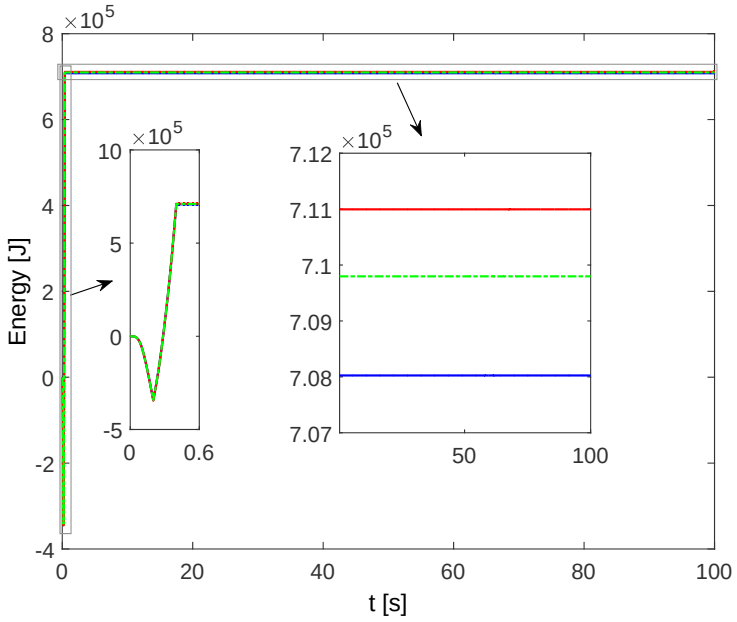

Figure 16: Free fly beam: energy.

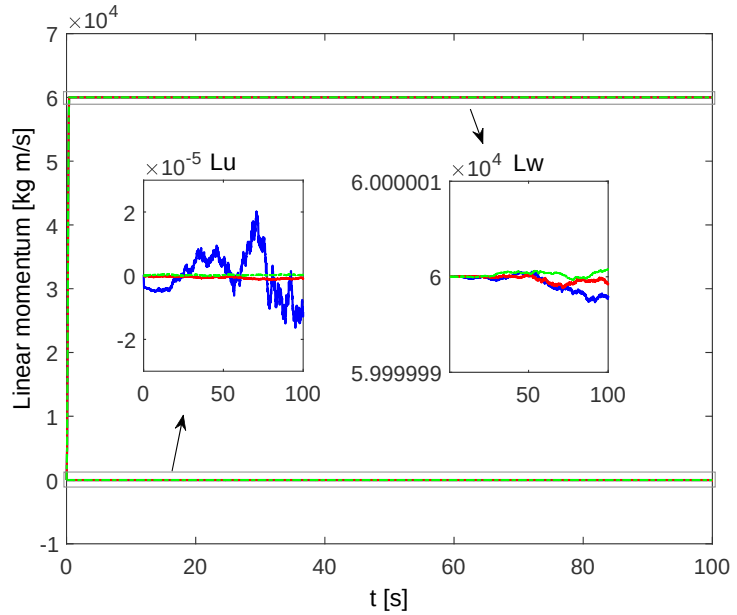

Figure 17: Free fly beam: linear momentum.

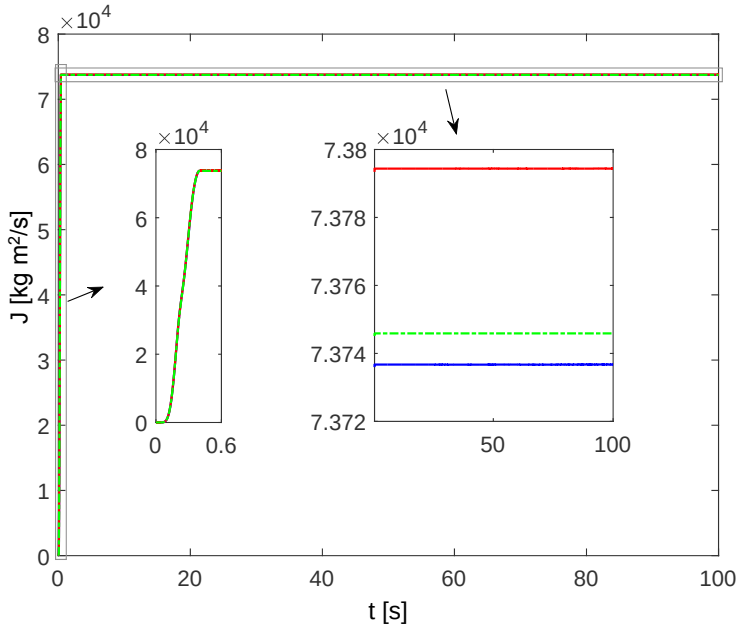

Figure 18: Free fly beam: angular momentum.

9.5. Choice of the predictor and numerical performance

The numerical performances of the three proposed formulations are presented in Tables 3 to 6. For each formulation, the three predictors described in Section 7 have been tested. For the IIE approach, both the exact tangent dynamic matrix (Eq.(41)) and the simplified one (Eq. (44)) have been tested. For each example, the same number elements (corresponding to the number of elements for the MX approach in Table 2) have been used in all analyses. In Tables 3 to 6, the computational time and the total number of iterations (in parenthesis) are given for each case considering 5000 steps. The following conclusions can be drawn:

• For the RIE and MX approaches, all the predictors give almost the same computational time. For the IIE formulation, Predictor 2 gives the lowest computational time, but the difference between Predictors 2 and 3 is not significant.

• The CPU time and number of iterations for the RIE and MX formulations are almost the same. This was expected since the only difference between these approaches resides in different constant local stiffness matrices. However, as shown previously in the examples, the RIE approach requires a larger number of elements in order to get an accurate solution.

• For the IIE formulation, it is better to use the simplified tangent stiffness matrix. The number of iterations increases but the CPU time decreases by 20% to 40% (Predictor 2).

• With Predictor 2, the IIE formulation (with simplified tangent dynamic matrix) requires about 2.0-2.6 times more CPU time than the MX formulation. On the other hand, the numerical examples have shown that with twice the number of elements, the MX formulation gives less accurate results that the IIE one. It is therefore difficult to conclude if one formulation is more efficient than the other one.

Table 3: Numerical performances for Lee's frame

Examples	RIE	MX	IIE-exact	IIE-simp.
Pred.1	38 (15000)	38 (15007)	145 (19526)	112 (23539)
Pred.2	38 (15000)	38 (15000)	115 (15000)	99 (20482)
Pred.3	38 (14999)	38 (14999)	116 (15043)	104 (21370)

Table 4: Numerical performances for simple beam

Examples	RIE	MX	IIE-exact	IIE-simp.
Pred.1	60 (19980)	60 (19998)	185 (19999)	139 (23873)
Pred.2	47 (15000)	47 (15000)	141 (15011)	120 (19996)
Pred.3	47 (15007)	49 (15567)	151 (15874)	122 (20002)

Table 5: Numerical performances for shallow arch beam

Examples	RIE	MX	IIE-exact	IIE-simp.
Pred.1	38 (14999)	38 (14999)	138 (18569)	110 (22902)
Pred.2	38 (14999)	38 (14999)	114 (15000)	97 (19951)
Pred.3	38 (14997)	38 (14997)	115 (14999)	99 (19996)

Table 6: Numerical performances for free fly beam

Examples	RIE	MX	IIE-exact	IIE-simp.
Pred.1	21 (14994)	21 (14994)	76 (19467)	51 (20025)
Pred.2	21 (14774)	21 (14801)	60 (14799)	42 (15862)
Pred.3	21 (14953)	21 (14981)	61 (14985)	45 (16623)

10. Conclusion

In this paper, three dynamic co-rotational shear flexible 2D beam formulations have been presented and tested together with an energy-momentum method. The main idea of this method is to use the classical midpoint rule for both kinematic and strain quantities. Although the idea as such was developed in previous work, its realization to these specific elements had not been done. The advantage of the proposed algorithm is that it conserves the total energy of the system and the solution remains stable even if a very large number of steps are applied. Moreover, in the absence of applied external loads, the linear and angular momenta are constant. These characteristics have been proved theoretically and also confirmed numerically by using four numerical applications.

The three proposed shear flexible formulations share the same co-rotational framework and differ in the choice of the local strain definition and the local shape functions. If local linear strains and local linear shape functions are taken, the numerical results show that it is more efficient to adopt a local mixed approach instead of a pure displacement one: the CPU time is unchanged but the same accuracy is obtained with a less number of elements. The numerical results also show that it can be interesting to use a nonlinear local strain approach together with local cubic shape functions: the computational time is increased (due essentially to mathematically more complicated dynamic terms) but the same accuracy is obtained with a much less number of elements. For that approach, it has also been shown that a simplified dynamic tangent matrix should be taken and that the choice of an efficient predictor can be important.

Acknowledgements

The first and the third authors gratefully acknowledge financial support by the European Commission (Research Fund for Coal and Steel) through the project RobustImpact under grant agreement RFSR-CT-2012-00029 and the financial support of the region of Brittany (France) through the ARED funding scheme.

References

[1] M. A. Crisfield, J. Shi, A co-rotational element/time-integration strategy for non-linear dynamics, International Journal for Numerical Methods in Engineering 37 (1994) 1897–1913.

[2] M. A. Crisfield, J. Shi, An energy conserving co-rotational procedure for non-linear dynamcis with finite elements, Nonlinear Dynamics 9 (1996) 37–52.

[3] U. Galvanetto, M. A. Crisfield, An energy-conserving co-rotational procedure for the dynamics of planar beam structures, International Journal for Numerical Methods in Engineering 39 (1996) 2265–2282.

[4] T.-N. Le, J.-M. Battini, M. Hjiaj, Efficient formulation for dynamics of corotational 2D beams, Computational Mechanics 39 (2011) 153–161.

[5] M. Iura, S. N. Atluri, Dynamic analysis of planar flexible beams with finite rotaions by using inertial and rotating frames, Computers and Structures 55 (1995) 453–462.

[6] K. M. Hsiao, J. Jang, Dynamic analysis of planar flexible mechanisms by co-rotational formulation, Computer Methods in Applied Mechanics and Engineering 87 (1991) 1–14.

[7] K. M. Hsiao, R. T.Yang, A co-rotational formulation for nonlinear dynamic analysis of curved euler beam, Computers and Structures 54 (1995) 1091–1097.

[8] K. Behdinan, M. C. Stylianou, B. Tabarrok, Co-rotational dynamic analysis of flexible beams, Computer Methods in Applied Mechanics and Engineering 154 (1998) 151–161.

[9] H. A. Elkaranshawy, M. A. Dokainish, Corotational finite element analysis of planar flexible multibody systems, Computers and Structures 54 (1995) 881–890.

[10] M. A. Crisfield, U. Galvanetto, G. Jelenić, Dynamics of 3-D co-rotational beams, Computational Mechanics 20 (1997) 507–519.

[11] T.-N. Le, J.-M. Battini, M. Hjiaj, Dynamics of 3D beam elements in a corotational context: A comparative study of established and new formulations, Finite Elements in Analysis and Design 61 (2012) 97–111.

[12] T.-N. Le, J.-M. Battini, M. Hjiaj, A consistent 3D corotational beam element for nonlinear dynamic analysis of flexible structures, Computer Methods in Applied Mechanics and Engineering 269 (2014) 538–565.

[13] T.-N. Le, J.-M. Battini, M. Hjiaj, Corotational formulation for nonlinear dynamics of beams with arbitrary thin-walled open cross-sections, Computers and Structures 134 (2014) 112–127.

[14] J. Salomon, A. A. Weiss, B. I. Wohlmuth, Energy-conserving algorithms for a corotational formulation, SIAM Journal on Numerical Analysis 46 (2008) 1842–1866.

[15] K. M. Hsiao, J. Y. Lin, W. Y. Lin, A consisten co-rotational finite element formulation for geometrically nonlinear dynamic analysis of 3-D beams, Computer Methods in Applied Mechanics and Engineering 169 (1999) 1–18.

[16] H. G. Zhong, M. A. Crisfield, An energy-conserving co-rotational procedure for the dynamics of shell structures, Engineering Computations 15 (1998) 552–576.

[17] F. S. Almeida, A. M. Awruch, Corotational nonlinear dynamic analysis of laminated composite shells, Finite Elements in Analysis and Design 47 (2011) 1131–1145.

[18] J. Yang, P. Xia, Corotational nonlinear dynamic analysis of thin-shell structures with finite rotations, AIAA Journal 53 (2015) 663–677.

[19] Y. Urthaler, J. N. Reddy, A corotational finite element formulation for the analysis of planar beams, International Journal for Numerical Methods in Biomedical Engineering 21 (2005) 553–570.

[20] C. Pacoste, A. Eriksson, Beam elements in instability problems, Computer Methods in Applied Mechanics and Engineering 144 (1997) 163–197.

[21] G. Garcea, A. Madeo, R. Casciaro, The implicit corotational method and its use in the derivation of nonlinear structural models for beams and plates, Journal of Mechanics of Materials and Structures 7 (2012) 509–538.

[22] J.-M. Battini, C. Pacoste, Co-rotational beam elements with warping effects in instability problems, Computer Methods in Applied Mechanics and Engineering 191 (2002) 1755–1789.

[23] J.-M. Battini, C. Pacoste, Plastic instability of beam structures using co-rotational elements, Computer Methods in Applied Mechanics and Engineering 191 (2002) 5811–5831.

[24] R. Alsafadie, M. Hjiaj, J.-M. Battini, Corotational mixed finite element formulation for thin-walled beams with generic cross-section, Computer Methods in Applied Mechanics and Engineering 199 (2010) 3197–3212.

[25] R. Alsafadie, J.-M. Battini, H. Somja, M. Hjiaj, Local formulation for elasto-plastic corotational thin-walled beams based on higher-order curvature terms, Finite Elements in Analysis and Design 47 (2011) 119–128.

[26] R. Alsafadie, J.-M. Battini, M. Hjiaj, Efficient local formulation for elasto-plastic corotational thin-walled beams, International Journal for Numerical Methods in Biomedical Engineering 27 (2011) 498–509.

[27] R. Alsafadie, J.-M. Battini, M. Hjiaj, Three-dimensional formulation of a mixed corotational thin-walled beam element incorporating shear and warping deformation, Thin-Walled Structures 49 (2011) 523–533.

[28] R. Alsafadie, M. H. H. Somja, J.-M. Battini, A comparative study of displacement and mixed-based corotational finite element formulations for elasto-plastic three-dimensional beam analysis, Engineering Computations 28 (2011) 939–982.

[29] G. Prathap, G. R. Bhashyam, Reduced integration and the shear-flexible beam element, International Journal for Numerical Methods in Engineering 18 (1982) 195–210.

[30] A. Ibrahimbegović, F. Frey, Finite element analysis of linear and non-linear planar deformations of elastic initially curved beams, International Journal for Numerical Methods in Engineering 36 (1993) 3239–3258.

[31] J. N. Reddy, An Introduction to the Finite Element Method, 2nd Edition, McGraw-Hill, New York, 1993.

[32] M. L. Day, T. Y. Yang, A mixed variational principle for finite element analysis, International Journal for Numerical Methods in Engineering 18 (1982) 1213–1230.

[33] R. L. Taylor, F. C. Filippou, A. Saritas, F. Auricchio, A mixed finite element method for beam and frame problems, Computational Mechanics 31 (2003) 192–203.

[34] P. K. V. V. Nukala, D. W. White, Variationally consistent state determination algorithms for nonlinear mixed beam finite elements, Computer Methods in Applied Mechanics and Engineering 193 (2004) 3647–3666.

[35] B. N. Almedar, D. W. White, Displacement, flexibility, and mixed beam-column finite element formuations for distributed plasticity analysis, Journal of Structural Engineering 131 (2005) 1811–1819.

[36] J. Korelc, P. Wriggers, Consistent gradient formulation for a stable enhanced strain method for large deformations, Engineering Computations 13 (1984) 103–123.

[37] P. Wriggers, J. Korelc, On enhanced strain methods for small and finite deformations of solids, Computational Mechanics 18 (1996) 413–428.

[38] J. C. Simo, F. Armero, Geometrically non-linear enhanced strain mixed methods and the method of incompatible modes, International Journal for Numerical Methods in Engineering 33 (1992) 1413–1449.

[39] E. P. Kasper, R. L. Taylor, A mixed-enhanced strain method. Part I: Geometrically linear problems, Computers and structures 75 (2000) 237–250.

[40] J. N. Reddy, On locking-free shear deformable beam finite elements, Computer Methods in Applied Mechanics and Engineering 149 (1997) 113–132.

[41] H. M. Hilber, T. J. R. Hughes, R. L. Taylor, Improved numerical dissipation for time integration algorithms in structural dynamics, Earthquake Engineering Strucuture Dynamic 5 (1977) 282–292.

[42] J. C. Simo, N. Tarnow, The discrete energy-momentum method. Conserving algorithms for nonlinear elastodynamics, Journal of Applied Mathematics and Physics 43 (1992) 757–792.

[43] M. Geradin, A. Cardona, Flexible Multibody Dynamics, A Finite Element Approach, John Wiley and Sons, 2001.

[44] J. C. Simo, N. Tarnow, M. Doblare, Non-linear dynamics of three-dimensional rods: exact energy and momentum conserving algorithms, International Journal for Numerical Methods in Engineering 38 (1995) 1431–1473.

[45] C. Sansour, T. L. Nguyen, M. Hjiaj, An energy-momentum method for in-plane geometrically exact euler-bernoulli beam dynamcis, International Journal for Numerical Methods in Engineering 102 (2015) 99–134.

[46] M. Gams, I. Planinc, M. Saje, Energy conserving time integration scheme for geometrically exact beam, Computer Methods in Applied Mechanics and Engineering 196 (2007) 2117–2129.

[47] I. Romero, F. Armero, An objective finite element approximation of the kinematics of geometrically exact rods and its use in the formulation of an energy-momentum conserving scheme in dynamics, International Journal for Numerical Methods in Engineering 54 (2002) 1683–1716.

[48] D. Kuhl, M. A. Crisfield, Energy-conserving and decaying algorithms in non-linear structural dynamics, International Journal for Numerical Methods in Engineering 45 (1999) 569–599.

[49] J. C. Simo, N. Tarnow, A new energy and momentum conserving algorithms for the non-linear dynamics of shells, International Journal for Numerical Methods in Engineering 37 (1994) 2527–254.

[50] C. Sansour, W. Wagner, P. Wriggers, J. Sansour, An energy-momentum integration scheme and enhanced strain finite elements for the non-linear dynamics of shells, International Journal of Non-linear Mechanics 37 (2002) 951–966.

[51] C. Sansour, P. Wriggers, J. Sansour, On the design of energy-momentum integration schemes for arbitrary continuum formulations. Applications to classical and chaotic motion of shells, International Journal for Numerical Methods in Engineering 60 (2004) 2419–2440.

[52] C. Sansour, P. Wriggers, J. Sansour, Nonlinear dynamics of shells: Theory, finite element formulation, and integration schemes, Nonlinear Dynamics 13 (1997) 279–305.

[53] B. Brank, L. Briseghella, N. Tonello, F. B. Damjanic, On non-linear dynamics of shells: Implementation of energy-momentum conserving algorithm for a finite rotation shell models, International Journal for Numerical Methods in Engineering 42 (1998) 409–442.

[54] D. Kuhl, E. Ramm, Generalized energy-momentum method for non-linear adaptive shell dynamics, Computer Methods in Applied Mechanics and Engineering 178 (1999) 343–366.

[55] L. Noels, L. Stainier, J. P. Ponthot, An energy-momentum conserving algorithm for non-linear hypoelastic constitutive models, International Journal for Numerical Methods in Engineering 59 (2004) 83–114.

[56] O. Gonzalez, Exact energy and momentum conserving algorithms for general models in nonlinear elasticity, Computer Methods in Applied Mechanics and Engineering 190 (2000) 1763–1783.

[57] I. Romero, An analysis of the stress formula for energy-momentum methods in nonlinear elastodynamics, Computational Mechanics 50 (2012) 603–610.

[58] P. Betsch, P. Steinmann, Conservation properties of a time FE method—part II: Time-stepping schemes for non-linear elastodynamics, International Journal for Numerical Methods in Engineering 50 (2001) 1931–1955.

[59] K.-J. Bathe, Conserving energy and momentum in nonlinear dynamics: A simple implicit time integration scheme, Computers and Structures 85 (2007) 437–445.

[60] N. M. Newmark, A method of computation for structural dynamics, Journal of the Enginneering Mechanics division ASCE 85 (1959) 67–94.

[61] A. Cardona, M. Geradin, A beam finite element non-linear theory with finite rotations, International Journal for Numerical Methods in Engineering 26 (1988) 2403–2438.

[62] J. C. Simo, L. Vu-Quoc, On the dynamics in space of rods undergoing large motions–a geometrically exact approach, Computer Methods in Applied Mechanics and Engineering 66 (1988) 125–161.

[63] J. Mäkinen, Critical study of Newmark-scheme on manifold of finite rotations, Computer Methods in Applied Mechanics and Engineering 191 (2001) 817–828.

[64] J. Chung, G. Hulbert, A predictor-corrector algorithm of the generalized-α Method for analysis of structural dynamics, Korean Society for Noise and Vibration Engineering 5 (2) (1995) 207–213.

[65] R. de. Borst, M. A. Crisfield, J. J. C. Remmers, C. V. Verhoosel, Non-linear finite element analysis of solids and structures, 2nd Edition, John Wiley and Sons, 2002.

Paper III:

Co-rotating flexible beam with generalized visco-plastic hinges for the nonlinear dynamics of frame structures under impacts

Manuscript.

Co-rotating flexible beam with generalized visco-plastic hinges for the nonlinear dynamics of frame structures under impacts

Sophy Chhang[a,b], Piseth Heng[a,b], Jean-Marc Battini[b], Mohammed Hjiaj[a,*], Samy Guezouli[a]

[a] *INSA Rennes, LGCGM/Structural Engineering Research Group, 20 avenue des Buttes de Cosmes, CS 70839, 35708 Rennes Cedex 7, France*
[b] *Department of Civil and Architectural Engineering, KTH Royal Institute of Technology, Stockholm, Sweden*

Abstract

In this paper, a co-rotational planar flexible beam element with generalized elasto-plastic hinges is extended to handled non-linear dynamics problems including impacts. To handle large displacement, the co-rotational formalism is adopted. The inelastic behavior of the frame structure is modelled either by distributed plasticity or by plastic hinge approach. In the later case, a family of symmetric and convex yield surfaces of super-elliptic shape is considered for the inelastic behavior. A condensation procedure is used to remove the internal degrees of freedom and to produce a two noded super-element that is compatible with the standard co-rotational approach. Strain effects have been considered by replacing the plastic flow rule with its visco-plasticity counterpart. In addition, impact loading is described by the Newton law in which a coefficient of restitution is used to accommodate energy loss. The equations of motion are rigorously derived using a set of differential measures and convex analysis tools. The response of the proposed formulation is compared against standard co-rotational based on linear Bernoulli/Timoshenko local formulation. It is shown that the proposed formulation is efficient, accurate and requires less elements.

Keywords: 2D co-rotational beams, Distributed plasticity approaches, Generalized elasto-plastic hinges, Strain rate effect, Impact loadings;

*Corresponding author
Email address: Mohammed.Hjiaj@insa-rennes.fr (Mohammed Hjiaj)

1. Introduction

Nowadays, structures should be designed to withstand extreme loadings induced by vehicle impact or explosion which may cause the resisting structure to undergo large displacement and substantial inelastic deformation. Subjected to impact or explosion loading, load carrying members of the building may fail due to the high intensity load produced by an impact or an explosion. The failure of such a local element can lead to the collapse of the entire structure or a disproportionately large part of it, called progressive collapse. The building must be designed to have sufficient robustness that is the state in which the structure has either adequate ductility or enough redundancy. Adequate ductility here is defined as the ability of the structural elements locally and directly affected to absorb energy corresponding to the load before failure; enough redundancy means the ability of the structure to redistribute the loads to the neighboring undamaged members.

In scenario-based design approach, a sudden column loss [1, 2, 3] is assumed and the response of the structure is analyzed. This method is rather unrealistic as it does not capture the nonlinear dynamic effect excited from the abnormal loading. Before the column collapses, it experiences large displacement and substantial plastic deformation. The column ductility also plays a role in absorbing the kinetic energy generated from the moving vehicle or the explosion. This interaction requires a full nonlinear dynamic and inelastic analysis of the whole structure including rigorous modeling of the impact interactions between the vehicle and the structure. Considering that 3D simulations and experimental tests require a considerable amount of time and resources, the problems have also been simplified to planar and fully nonlinear model with limited computational cost. The choice of finite element is essential in order to capture accurately both geometrical and material nonlinearities with minimal computational cost. In this context, the co-rotational method [4, 5, 6, 7, 8] is an attractive candidate thanks to its ability to combine accuracy with numerical efficiency. The main idea of the co-rotational formulation is to decompose the motion of the element into rigid body and pure deformational parts through the use of a local system which continuously rotates and translates with the element.

The inelastic behavior of framed structures can be modelled either with distributed

plasticity or plastic hinge approach. Although the distributed plasticity approach can accurately capture the inelastic behaviour of the structures, it is not convenient for practical usage. The reason is that it requires a large number of stress-strain sampling points through the cross-section and along the member length in order to accurately reproduce the plastic effects. This results in prohibitive computational time for nonlinear dynamic problems. In contrast to the distributed plasticity approach, the plastic-hinge approach requires fewer elements. For this reason, the plastic-hinge method is often preferred for practical use. In the past decades, many plastic hinge models [14, 15, 16, 17, 18, 19, 20, 21] have been proposed and enhanced in order to capture the inelastic behavior of framed structures. Lumped plasticity is one amongst of the developed plastic hinges approaches. The lumped plasticity method considers that plasticity is concentrated at specific cross-section located at the end of the members. This behaviour is modeled by means zeros plastic hinges in the form of nonlinear springs located at the member ends.

In the recent development, Heng et al. [22] proposed the generalized plastic-hinges method which is modelled by a combined axial and rotational spring. The plastification of the hinges follow the normality rule with a super-elliptic yield surface that accounts for the interaction between bending moment and normal force. Alhasawi et al. [23] proposed a two-node co-rotational flexible beam with generalized elasto-plastic hinges at the beam ends in static case.

It is well established that materials such as mild steel are highly sensitive to strain rate. Many experiments have shown that the yield stress increases substantially with the rate of straining affecting significantly the structure response. Therefore, this phenomena cannot be ignored especially for impact loadings. Several constitutive models have been proposed to reproduce the effect of strain-rate on the elasto-plastic response [24, 25, 26, 27, 28, 29]. Among these models, the elastic-visco-plastic model developed by Perzyna [26] has received much attention mainly due to its simplicity and its consistency with the classic theory of plasticity.

In this paper, a co-rotational planar flexible beam element with generalized elasto-visco-plastic hinges is developed. Strain effects have been considered by replacing the plastic flow rule with its visco-plasticity counterpart. Besides, a family of symmetric and convex yield surfaces of super-elliptic shape is considered for the inelastic behavior.

A condensation procedure is used to remove the internal degrees of freedom and to produce a two noded super-element that is compatible with the standard co-rotational approach. In addition, the elastic stiffness coefficients of the beam and the hinges are determined so that the total elastic stiffness of the element is conserved (see [30]). The predictions obtained from the generalized hinges are compared against the reference solution obtained using distributed plasticity (both Bernoulli and Timoshenko local visco-plastic beam formulations [31]).

For the impact analyses, the contact model is developed in a rigorous framework of non-smooth dynamics. The equations of motion are derived using a set of differential measures and convex analysis tools. Velocity jumps at impact instants are considered using the Newton's impact law by a means of the coefficient of restitution to account for possible energy losses during the collisions. The dynamic equations of motion are solved by using the energy-momentum conserving scheme developed by Chhang et al. [32, 33].

The outline of the paper is as follows. In the next section, the standard co-rotational beam formulation and the beam kinematic of the generalized hinges are described. The local formulation and the constitutive law for generalized elasto-visco-plastic hinges are presented in details in Section 3. In Section 4, the dynamical equations derived from the principle of virtual work and the energy-conserving scheme are presented. Section 5 is dedicated to the specific equations of motion for impact problem. In Section 6, two numerical examples are presented in order to assess the performances of the proposed method. Finally, conclusions are drawn in Section 7.

2. Co-rotational framework for planar beam elements

2.1. Standard co-rotational beam formulation

The central idea of the co-rotational formulism is to introduce a local coordinate system that continuously rotates and translates with a two-noded element. With respect to this moving frame, local deformational displacements $\bar{\boldsymbol{q}}$ are defined by extracting the rigid body movements from the global displacements $\boldsymbol{q}$. The local displacements are expressed as functions of the global ones, that is

$$\bar{\boldsymbol{q}} = \bar{\boldsymbol{q}}\left(\boldsymbol{q}\right) \tag{1}$$

The local displacement vector $\bar{\boldsymbol{q}}$ is used to compute the internal force vector $\boldsymbol{f}_l$ and the tangent stiffness matrix $\mathbf{k}_l$ in the local coordinates system. Note that $\boldsymbol{f}_l$ and $\mathbf{k}_l$ depend only on the definition of the local strains and not on the particular form of equation (1).

The transformation matrix $\mathbf{B}$ between the local and global displacements is defined by:

$$\delta\bar{\boldsymbol{q}} = \mathbf{B}\,\delta\boldsymbol{q} \tag{2}$$

and is obtained by differentiation of equation (1). The expression of the internal force vector $\boldsymbol{f}_g$ in the global coordinate system can be obtained by equating the internal virtual work in both the global and local coordinate systems, that is

$$\boldsymbol{f}_g = \mathbf{B}^{\mathrm{T}}\,\boldsymbol{f}_l \tag{3}$$

Equation (1), (2) and transformation (3) are explained in details in [31].

2.2. Co-rotational beam kinematic with generalized hinges

In this model, the structural member consists of three sub-elements: a standard flexible beam element and two generalized hinges that are modeled by a combination of axial and rotational springs, see Fig. 1. The elongation or shortening of the hinges occurs along the beam axis. The generalized hinges can be seen as finite element with zero initial length. By assembling these hinges with the beam element and by performing static condensation (see Section 3.1), a two node super-element (see Fig. 1) is obtained. This element is then incorporated into 'the co-rotational framework in order to account for geometrical nonlinearities. As a consequence, the local axial displacement $\bar{u}_1$ is equal to 0.

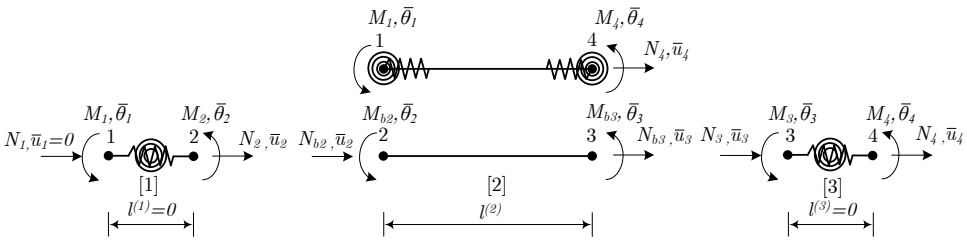

Figure 1: Local super-element.

The motion of the beam element (see Fig. 2) is decomposed in two parts. In a first step, a rigid body motion is defined by the global translation (u_1,w_1) of the node

1 as well as the rigid rotation α. This rigid motion defines a local coordinate system (x_l,z_l) which continuously translates and rotates with the element. In a second step, the element deformation is defined in the local coordinate system.

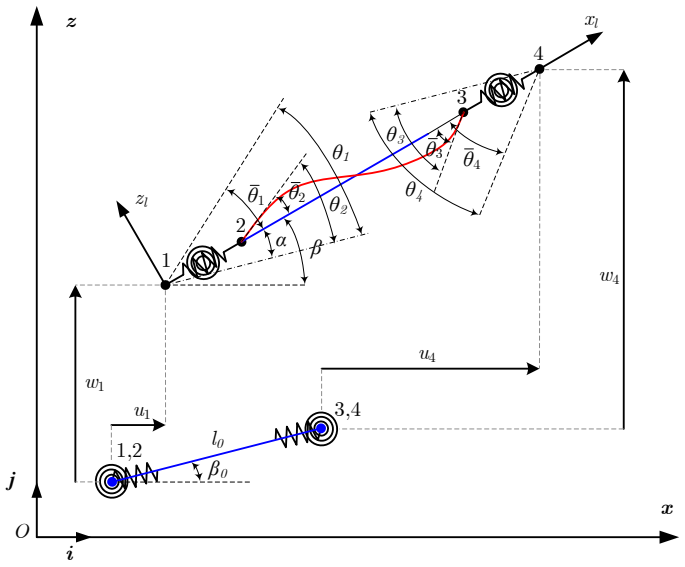

Figure 2: Beam kinematics.

The vectors of global and local displacements are respectively defined by

$$\begin{aligned} \boldsymbol{q} &= \left[\begin{array}{cccccc} u_1 & w_1 & \theta_1 & u_4 & w_4 & \theta_4 \end{array} \right]^{\mathrm{T}} \\ \bar{\boldsymbol{q}} &= \left[\begin{array}{ccc} \bar{u}_4 & \bar{\theta}_1 & \bar{\theta}_4 \end{array} \right]^{\mathrm{T}} \end{aligned} \tag{4}$$

The vectors of the local displacements of the standard beam is defined by

$$\bar{\boldsymbol{q}}_{sub} = \left[\begin{array}{cccc} \bar{u}_2 & \bar{\theta}_2 & \bar{u}_3 & \bar{\theta}_3 \end{array} \right]^{\mathrm{T}} \tag{5}$$

The components of $\bar{\boldsymbol{q}}$ are given by

$$\begin{aligned} \bar{u}_4 &= l - l_0 \\ \bar{\theta}_1 &= \theta_1 - \alpha = \theta_1 - \beta + \beta_0 \\ \bar{\theta}_4 &= \theta_4 - \alpha = \theta_4 - \beta + \beta_0 \end{aligned} \tag{6}$$

where l_0 and l denote the initial and current lengths of the element, respectively:

$$\begin{aligned} l_0 &= \sqrt{(x_4 - x_1)^2 + (z_4 - z_1)^2} \\ l &= \sqrt{(x_4 + u_4 - x_1 - u_1)^2 + (z_4 + w_4 - z_1 - w_1)^2} \end{aligned} \tag{7}$$

The current angle of the local system with respect to the global system is denoted as β and is given by

$$\begin{aligned} c = \cos\beta &= \frac{1}{l}\left(x_4 + u_4 - x_1 - u_1\right) \\ s = \sin\beta &= \frac{1}{l}\left(z_4 + w_4 - z_1 - w_1\right) \end{aligned} \tag{8}$$

3. Local element formulation for generalized elasto-visco-plastic hinges

The main objective of this paper is to assess the performances (accuracy, computing time) of the super-element by comparing its predictions against reliable reference solutions obtained from standard beam formulations using distributed visco-plasticity approach. To keep the paper self-contained, the major steps of the derivation are given.

3.1. Local tangent stiffness matrix of super beam element

The purpose of this sub-section is to define the local stiffness matrix $\mathbf{k}_l$ for the super beam element. The introduction of the hinges in the element member produces additional degree of freedoms exceeding the original ones of the co-rotational formulation. Therefore, the static condensation procedure is used to eliminate the internal nodes and their corresponding degree of freedoms.

The elastic stiffness matrix of the hinges is given by:

$$\mathbf{C}_t = \mathbf{C}_e = \begin{bmatrix} k_{\bar{u}} & 0 \\ 0 & k_{\bar{\theta}} \end{bmatrix} \tag{9}$$

In plasticity, the incremental stress-resultant for the first hinge (similar expression for the second hinge) is defined by

$$\begin{bmatrix} \Delta N_2 \\ \Delta M_2 \end{bmatrix} = \mathbf{C}_t \begin{bmatrix} \Delta\bar{u}_2 - \Delta\bar{u}_1 \\ \Delta\bar{\theta}_2 - \Delta\bar{\theta}_1 \end{bmatrix} = \begin{bmatrix} C_{11} & C_{12} \\ C_{21} & C_{22} \end{bmatrix} \begin{bmatrix} \Delta\bar{u}_2 - \Delta\bar{u}_1 \\ \Delta\bar{\theta}_2 - \Delta\bar{\theta}_1 \end{bmatrix} \tag{10}$$

where $C_{11} = \mathbf{C}_t(1,1)$,$C_{12} = \mathbf{C}_t(1,2)$, $C_{21} = \mathbf{C}_t(2,1)$ and $C_{22} = \mathbf{C}_t(2,2)$.

The incremental stress-resultants for the first hinge, the elastic beam and the second hinge are defined respectively:

$$\begin{bmatrix} \Delta M_1 \\ \Delta N_2 \\ \Delta M_2 \end{bmatrix} = \begin{bmatrix} C_{22} & -C_{21} & -C_{22} \\ -C_{12} & C_{11} & C_{12} \\ -C_{22} & C_{21} & C_{22} \end{bmatrix} \begin{bmatrix} \Delta\bar{\theta}_1 \\ \Delta\bar{u}_2 \\ \Delta\bar{\theta}_2 \end{bmatrix} \tag{11}$$

$$\begin{bmatrix} \Delta N_{b2} \\ \Delta M_{b2} \\ \Delta N_{b3} \\ \Delta M_{b3} \end{bmatrix} = \begin{bmatrix} k_{11} & 0 & -k_{11} & 0 \\ 0 & k_{22} & 0 & k_{23} \\ -k_{11} & 0 & k_{11} & 0 \\ 0 & k_{32} & 0 & k_{33} \end{bmatrix} \begin{bmatrix} \Delta \bar{u}_2 \\ \Delta \bar{\theta}_2 \\ \Delta \bar{u}_3 \\ \Delta \bar{\theta}_3 \end{bmatrix} \tag{12}$$

$$\begin{bmatrix} \Delta N_3 \\ \Delta M_3 \\ \Delta N_4 \\ \Delta M_4 \end{bmatrix} = \begin{bmatrix} C_{33} & C_{34} & -C_{33} & -C_{34} \\ C_{43} & C_{44} & -C_{43} & -C_{44} \\ -C_{33} & -C_{34} & C_{33} & C_{34} \\ -C_{43} & -C_{44} & C_{43} & C_{44} \end{bmatrix} \begin{bmatrix} \Delta \bar{u}_3 \\ \Delta \bar{\theta}_3 \\ \Delta \bar{u}_4 \\ \Delta \bar{\theta}_4 \end{bmatrix} \tag{13}$$

Moreover, the nodal equilibrium equations at the points 2 and 3 as shown in Fig. 1 are written by:

$$\begin{aligned} \Delta N_2 + \Delta N_{b2} &= 0 \\ \Delta M_2 + \Delta M_{b2} &= 0 \\ \Delta N_{b3} + \Delta N_3 &= 0 \\ \Delta M_{b3} + \Delta M_3 &= 0 \end{aligned} \tag{14}$$

By combining the Eqs.(11)-(13) with the previous equilibrium equations (Eqs.(14)), the following expression is obtained:

$$\begin{bmatrix} \Delta \boldsymbol{f}_l \\ \mathbf{0}_{4\times 1} \end{bmatrix} = \begin{bmatrix} \mathbf{k}_{hh} & \mathbf{k}_{hb} \\ \mathbf{k}_{bh} & \mathbf{k}_{bb} \end{bmatrix} \begin{bmatrix} \Delta \bar{\boldsymbol{q}} \\ \Delta \bar{\boldsymbol{q}}_{sub} \end{bmatrix} \tag{15}$$

with

$$\boldsymbol{f}_l = \begin{bmatrix} N_4 & M_1 & M_4 \end{bmatrix}^{\mathrm{T}} \tag{16}$$

$$\mathbf{k}_{hh} = \begin{bmatrix} C_{33} & 0 & C_{34} \\ 0 & C_{22} & 0 \\ C_{43} & 0 & C_{44} \end{bmatrix} \tag{17}$$

$$\mathbf{k}_{hb} = \mathbf{k}_{bh}^{\mathrm{T}} = - \begin{bmatrix} 0 & 0 & C_{33} & C_{34} \\ C_{21} & C_{22} & 0 & 0 \\ 0 & 0 & C_{43} & C_{44} \end{bmatrix} \tag{18}$$

$$\mathbf{k}_{bb} = \begin{bmatrix} k_{11}+C_{11} & C_{12} & -k_{11} & 0 \\ C_{21} & k_{22}+C_{22} & 0 & k_{23} \\ -k_{11} & 0 & k_{11}+C_{33} & C_{34} \\ 0 & k_{32} & C_{43} & k_{33}+C_{44} \end{bmatrix} \tag{19}$$

After the static condensation, the local internal force $\boldsymbol{f}_l$ and the local tangent stiffness matrix of the super-element $\mathbf{k}_l$ are given as:

$$\begin{aligned} \Delta \boldsymbol{f}_l &= \mathbf{k}_l \, \Delta \bar{\boldsymbol{q}} \\ \mathbf{k}_l &= \mathbf{k}_{hh} - \mathbf{k}_{bh}^{\mathrm{T}} \, \mathbf{k}_{bb}^{-1} \, \mathbf{k}_{bh} \end{aligned} \tag{20}$$

In elasticity, the local stiffness matrix $\mathbf{k}_l$ of the super beam element should be the local stiffness of the Bernoulli beam element:

$$\begin{bmatrix} \frac{EA}{l_0} & 0 & 0 \\ 0 & \frac{4\,EI}{l_0} & \frac{2\,EI}{l_0} \\ 0 & \frac{2\,EI}{l_0} & \frac{4\,EI}{l_0} \end{bmatrix} \tag{21}$$

To achieve that the elastic stiffness parameters of the hinges (see Eq.(9)) and the stiffness parameters of the elastic beam sub-element (see Eq.(12)) are taken as:

$$\begin{aligned} k_{\bar{u}} &= \varrho_n \frac{EA}{l_0} \\ k_{\bar{\theta}} &= \varrho_m \frac{EI}{l_0} \end{aligned} \tag{22}$$

$$\begin{aligned} k_{11} &= \varpi_1 \frac{EA}{l_0} \\ k_{22} = k_{33} &= \varpi_2 \frac{EI}{l_0} \\ k_{23} = k_{32} &= \varpi_3 \frac{EI}{l_0} \end{aligned} \tag{23}$$

By introducing Eqs.(22) and (23) in the second expression of Eqs.(20), the following relations are obtained:

$$\begin{aligned} \varpi_1 &= \left(1 - 2\,\varrho_n^{-1}\right)^{-1} \\ \varpi_2 &= \frac{4\,\varrho_m(\varrho_m - 3)}{\varrho_m^2 - 8\,\varrho_m + 12} \\ \varpi_3 &= \frac{2\,\varrho_m^2}{\varrho_m^2 - 8\,\varrho_m + 12} \end{aligned} \tag{24}$$

Hence the idea of the method is to choose the coefficients ϱ_n, ϱ_m of the hinges and then to calculate the coefficients $\varpi_1, \varpi_2, \varpi_3$ of the beam sub-element by using Eq.(24). By

doing this procedure, the choice of the elastic stiffness coefficients does not influence the results for generalized plastic-hinge formulation. Moreover, as shown in [30], their results are identical to the ones of the classical Bernoulli co-rotational beam element.

3.2. Constitutive law

The general plasticity theory is applied to the generalized elasto-visco-plastic hinges. The present model assumes that visco-plasticity is lumped into axial and rotational springs located at the end of flexible beam element. The elastic behavior of the generalized hinge is uncoupled whereas axial-moment interaction is considered in the visco-plastic range. The total generalized strain rate is decomposed into elastic and visco-plastic parts:

$$\dot{\mathbf{\Xi}} = \dot{\mathbf{\Xi}}^e + \dot{\mathbf{\Xi}}^p \tag{25}$$

where $\dot{\mathbf{\Xi}} = [\dot{u} \quad \dot{\bar{\theta}}]^{\mathrm{T}}$ are the axial and rotational strain rate. For an associated flow rule, the direction of the generalized visco-plastic strain rate vector, which based on the overstress concept, is given by the gradient to the yield function, with its magnitude given by the plastic multiplier rate $\dot{\lambda}$:

$$\dot{\mathbf{\Xi}}^p = \dot{\lambda} \frac{\partial \Phi}{\partial \mathbf{\Sigma}} \tag{26}$$

where $\mathbf{\Sigma} = [\, N, M \,]^{\mathrm{T}}$ is the generalized stress vector containing the bending and axial forces in the hinge. $\Phi(\Sigma)$ is a super-elliptic yield surface defined by:

$$\Phi(N, M) = \left(\left| \frac{M}{M^p} \right|^{\alpha} + \left| \frac{N}{N^p} \right|^{\beta} \right)^{\frac{1}{p}} - 1 \tag{27}$$

where α, β and p are the parameters of the yield surface shape. For example, the case of $\alpha = 1$, $\beta = 1.3$ and $p = 1$ corresponds to a yield surface of doubly symmetrical steel section.

In the case of visco-plasticity, the plastic multiplier $\dot{\lambda}$ is determined from the power function related to the visco-plastic behaviour of the material as:

$$\dot{\lambda} = \begin{cases} D^* \, \Phi^{\zeta}(\mathbf{\Sigma}) & \text{if} \quad \Phi(\mathbf{\Sigma}) \geq 0 \\ 0 & \text{if} \quad \Phi(\mathbf{\Sigma}) < 0 \end{cases} \tag{28}$$

where D^* and ζ are the drag stress and the viscosity exponent. The expression in Eq. (28) infers the loading and unloading conditions as following. $\Phi(\mathbf{\Sigma}) < 0$ corresponds to

the elastic domain, which leads to $\dot{\lambda} = 0$, and $\Phi(\boldsymbol{\Sigma}) \geq 0$ gives the over-stress resulting from the viscosity, which is the distance between the the current stress state and the boundary $\Phi = 0$.

In case of plasticity, the plastic multiplier $\dot{\lambda}$ is determined by the classical complementary conditions:

$$\dot{\lambda} \geq 0, \quad \Phi(N, M) \leq 0, \quad \dot{\lambda}\, \Phi(N, M) = 0 \tag{29}$$

3.3. Discrete constitutive equations

For the midpoint rule integration, the discrete system of equations of the stress-resultants read:

$$\boldsymbol{\Sigma}_{n+\frac{1}{2}} = \boldsymbol{\Sigma}_n + \frac{1}{2}\, \mathbf{C}_e\, (\Delta\boldsymbol{\Xi} - \Delta\boldsymbol{\Xi}^p) \tag{30}$$

By introducing the trial state as:

$$\boldsymbol{\Sigma}^{trial}_{n+\frac{1}{2}} = \boldsymbol{\Sigma}_n + \frac{1}{2}\, \mathbf{C}_e\, \Delta\boldsymbol{\Xi} \tag{31}$$

Eq. (30) becomes:

$$\boldsymbol{\Sigma}_{n+\frac{1}{2}} = \boldsymbol{\Sigma}^{trial}_{n+\frac{1}{2}} - \frac{1}{2}\, \mathbf{C}_e\, \Delta\boldsymbol{\Xi}^p \tag{32}$$

where the plastic strain at mid-point is given by

$$\boldsymbol{\Xi}^p_{n+\frac{1}{2}} = \boldsymbol{\Xi}^p_n + \frac{1}{2}\, \Delta\boldsymbol{\Xi}^p = \boldsymbol{\Xi}^p_n + \frac{1}{2}\, \Delta\lambda\, \left.\frac{\partial \Phi}{\partial \boldsymbol{\Sigma}}\right|_{n+\frac{1}{2}} \tag{33}$$

while the incremental plastic stain is defined by from expression (26) :

$$\Delta\boldsymbol{\Xi}^p = \Delta\lambda\, \left.\frac{\partial \Phi}{\partial \boldsymbol{\Sigma}}\right|_{n+\frac{1}{2}} \tag{34}$$

By using the latter expression, Eq. (32) can be written as

$$\boldsymbol{\Sigma}_{n+\frac{1}{2}} = \boldsymbol{\Sigma}^{trial}_{n+\frac{1}{2}} - \frac{1}{2}\, \mathbf{C}_e\, \Delta\lambda\, \left.\frac{\partial \Phi}{\partial \boldsymbol{\Sigma}}\right|_{n+\frac{1}{2}} \tag{35}$$

where the incremental plastic multiplier can be determined by using expression (29) as:

$$\Delta\lambda = \begin{cases} \Delta t\, D^*\, \Phi^{\zeta}\left(\boldsymbol{\Sigma}_{n+\frac{1}{2}}\right) & \text{if} \quad \Phi\left(\boldsymbol{\Sigma}_{n+\frac{1}{2}}\right) \geq 0 \\ 0 & \text{if} \quad \Phi\left(\boldsymbol{\Sigma}_{n+\frac{1}{2}}\right) < 0 \end{cases} \tag{36}$$

3.4. Consistent tangent operator

The tangent operator for the case of nonlinear yield surface requires the derivative of stress resultant vector $\mathbf{\Sigma}_{n+\frac{1}{2}}$ with respect to the deformation vector $\mathbf{\Xi}_{n+\frac{1}{2}}$. By using Eq. (35), the derivative of the stress resultant derive the $\mathbf{\Sigma}_{n+\frac{1}{2}}$ is:

$$\mathrm{d}\mathbf{\Sigma}_{n+\frac{1}{2}} = \mathrm{d}\mathbf{\Sigma}^{trial}_{n+\frac{1}{2}} - \frac{1}{2}\,\mathbf{C}_e\,\mathrm{d}\Delta\lambda\,\frac{\partial\Phi}{\partial\mathbf{\Sigma}}\bigg|_{n+\frac{1}{2}} - \frac{1}{2}\,\mathbf{C}_e\,\Delta\lambda\,\frac{\partial^2\Phi}{\partial\mathbf{\Sigma}^2}\bigg|_{n+\frac{1}{2}}\mathrm{d}\mathbf{\Sigma}_{n+\frac{1}{2}} \tag{37}$$

Rearranging the latter equation, it gives:

$$\mathrm{d}\mathbf{\Sigma}_{n+\frac{1}{2}} = \mathbf{H}^{-1}\left(\mathrm{d}\mathbf{\Sigma}^{trial}_{n+\frac{1}{2}} - \frac{1}{2}\,\mathbf{C}_e\,\mathrm{d}\Delta\lambda\,\frac{\partial\Phi}{\partial\mathbf{\Sigma}}\bigg|_{n+\frac{1}{2}}\right) \tag{38}$$

where the matrix $\mathbf{H}$ is given as:

$$\mathbf{H} = \mathbf{I} + \frac{1}{2}\,\mathbf{C}_e\,\Delta\lambda\frac{\partial^2\Phi}{\partial\mathbf{\Sigma}^2}\mathrm{d}\mathbf{\Sigma}_{n+\frac{1}{2}} \tag{39}$$

in which $\mathbf{I}$ is a 2×2 unit matrix. By taking derivative of Eq. (36), $\mathrm{d}\Delta\lambda$ is obtained as

$$\mathrm{d}\Delta\lambda = \Delta t\,D^*\zeta\,\Phi^{\zeta-1}\,\frac{\mathrm{d}\Phi}{\mathrm{d}\mathbf{\Sigma}}\bigg|^{\mathrm{T}}_{n+\frac{1}{2}}\mathrm{d}\mathbf{\Sigma}_{n+\frac{1}{2}} \tag{40}$$

Furthermore, the derivative of the yield surface is obtained from Eq. (27) as:

$$\mathrm{d}\Phi_{n+\frac{1}{2}} = \frac{\mathrm{d}\Phi}{\mathrm{d}\mathbf{\Sigma}}\bigg|^{\mathrm{T}}_{n+\frac{1}{2}}\mathrm{d}\mathbf{\Sigma}_{n+\frac{1}{2}} \tag{41}$$

By replacing Eq.(38) into the latter equation, $\mathrm{d}\Delta\lambda$ is given by:

$$\mathrm{d}\Delta\lambda = \left(1 + \frac{1}{2}\Delta t\,D^*\zeta\Phi^{\zeta-1}\,\frac{\mathrm{d}\Phi}{\mathrm{d}\mathbf{\Sigma}}\bigg|^{\mathrm{T}}_{n+\frac{1}{2}}\mathbf{H}^{-1}\mathbf{C}_e\,\frac{\partial\Phi}{\partial\mathbf{\Sigma}}\bigg|_{n+\frac{1}{2}}\right)^{-1}\left(\Delta t\,D^*\zeta\Phi^{\zeta-1}\,\frac{\mathrm{d}\Phi}{\mathrm{d}\mathbf{\Sigma}}\bigg|^{\mathrm{T}}_{n+\frac{1}{2}}\mathbf{H}^{-1}\mathrm{d}\mathbf{\Sigma}^{trial}_{n+\frac{1}{2}}\right) \tag{42}$$

Provided that

$$\mathbf{\Sigma}^{trial}_{n+\frac{1}{2}} = \mathbf{C}_e\,\Delta\mathbf{\Xi}_{n+\frac{1}{2}} \tag{43}$$

The consistent tangent operator for the visco-plasticity is then given by:

$$\mathbf{C}_t = \mathbf{H}^{-1}\mathbf{C}_e\left[\mathbf{I} - \frac{1}{2}\left(1 + \frac{1}{2}\Delta t\,D^*\zeta\Phi^{\zeta-1}\,\frac{\mathrm{d}\Phi}{\mathrm{d}\mathbf{\Sigma}}\bigg|^{\mathrm{T}}_{n+\frac{1}{2}}\mathbf{H}^{-1}\mathbf{C}_e\,\frac{\partial\Phi}{\partial\mathbf{\Sigma}}\bigg|_{n+\frac{1}{2}}\right)^{-1}\left(\Delta t\,D^*\zeta\Phi^{\zeta-1}\,\frac{\mathrm{d}\Phi}{\mathrm{d}\mathbf{\Sigma}}\bigg|_{n+\frac{1}{2}}\,\frac{\mathrm{d}\Phi}{\mathrm{d}\mathbf{\Sigma}}\bigg|^{\mathrm{T}}_{n+\frac{1}{2}}\mathbf{H}^{-1}\mathbf{C_e}\right)\right] \tag{44}$$

For the plastic case, the tangent operator $\mathbf{C}_t$ is derived from Eq. (44):

$$\mathbf{C}_t = \mathbf{H}^{-1}\mathbf{C}_e\left[\mathbf{I} - \frac{1}{2}\left(\frac{1}{2}\frac{\mathrm{d}\Phi}{\mathrm{d}\mathbf{\Sigma}}\bigg|^{\mathrm{T}}_{n+\frac{1}{2}}\mathbf{H}^{-1}\mathbf{C}_e\,\frac{\partial\Phi}{\partial\mathbf{\Sigma}}\bigg|_{n+\frac{1}{2}}\right)^{-1}\left(\frac{\partial\Phi}{\partial\mathbf{\Sigma}}\bigg|_{n+\frac{1}{2}}\,\frac{\mathrm{d}\Phi}{\mathrm{d}\mathbf{\Sigma}}\bigg|^{\mathrm{T}}_{n+\frac{1}{2}}\mathbf{H}^{-1}\mathbf{C}_e\right)\right] \tag{45}$$

4. Dynamic equations

4.1. Principle of virtual work

The principle of virtual work reads:

$$\int_{t_1}^{t_2} \left(\int_{l_0} \rho A \, \ddot{u}_G \, \delta u_G \, \mathrm{d}x + \int_{l_0} \rho A \, \ddot{w}_G \, \delta w_G \, \mathrm{d}x + \int_{l_0} \rho I \, \ddot{\theta}_G \, \delta\theta_G \, \mathrm{d}x + \delta \boldsymbol{q}^{\mathrm{T}} \, \boldsymbol{f}_g - \delta \boldsymbol{q}^{\mathrm{T}} \boldsymbol{P} \right) \mathrm{d}t = 0 \tag{46}$$

with I being the second moment of area of the cross-section and $\boldsymbol{P}$ the external force vector component of concentrated forces and moments at the nodes. The components u_G and w_G of the global displacements of the centroid G and the global rotation θ_G of the cross-section are approximated by a linear interpolation:

$$\begin{aligned} u_G &= \left(1 - \frac{x}{l_0}\right) u_1 + \frac{x}{l_0} u_4 \\ w_G &= \left(1 - \frac{x}{l_0}\right) w_1 + \frac{x}{l_0} w_4 \\ \theta_G &= \left(1 - \frac{x}{l_0}\right) \theta_1 + \frac{x}{l_0} \theta_4 \end{aligned} \tag{47}$$

Hence, the expression (46) can be written as:

$$\int_{t_1}^{t_2} \left(\int_{l_0} \delta \boldsymbol{q}^{\mathrm{T}} \mathbf{M} \, \ddot{\boldsymbol{q}} \, \mathrm{d}x + \delta \boldsymbol{q}^{\mathrm{T}} \, \mathbf{B}^{\mathrm{T}} \, \boldsymbol{f}_l - \delta \boldsymbol{q}^{\mathrm{T}} \boldsymbol{P} \right) \mathrm{d}t = 0 \tag{48}$$

where $\mathbf{M}$ is the constant mass matrix:

$$\mathbf{M} = \rho \, l_0 \begin{bmatrix} A/3 & 0 & 0 & A/6 & 0 & 0 \\ 0 & A/3 & 0 & 0 & A/6 & 0 \\ 0 & 0 & I/3 & 0 & 0 & I/6 \\ A/6 & 0 & 0 & A/3 & 0 & 0 \\ 0 & A/6 & 0 & 0 & A/3 & 0 \\ 0 & 0 & I/6 & 0 & 0 & I/3 \end{bmatrix} \tag{49}$$

4.2. Residual force vector and tangent matrix

The energy-momentum method [32, 33] in the context of co-rotational approach is used to solve the dynamical equation (Eq.(46)). The central idea of this method starts from the classical midpoint time integration:

$$\begin{aligned} \boldsymbol{q}_{n+\frac{1}{2}} &= \frac{\boldsymbol{q}_{n+1} + \boldsymbol{q}_n}{2} = \boldsymbol{q}_n + \frac{1}{2} \Delta \boldsymbol{q} \\ \dot{\boldsymbol{q}}_{n+\frac{1}{2}} &= \frac{\dot{\boldsymbol{q}}_{n+1} + \dot{\boldsymbol{q}}_n}{2} = \frac{\boldsymbol{q}_{n+1} - \boldsymbol{q}_n}{\Delta t} = \frac{\Delta \boldsymbol{q}}{\Delta t} \\ \ddot{\boldsymbol{q}}_{n+\frac{1}{2}} &= \frac{\ddot{\boldsymbol{q}}_{n+1} + \ddot{\boldsymbol{q}}_n}{2} = \frac{\dot{\boldsymbol{q}}_{n+1} - \dot{\boldsymbol{q}}_n}{\Delta t} = \frac{2}{\Delta t^2} \Delta \boldsymbol{q} - \frac{2}{\Delta t} \dot{\boldsymbol{q}}_n \end{aligned} \tag{50}$$

The main idea is to applied the midpoint rule to the strain fields. It takes the following generic form:

$$\begin{aligned} \int_{t_n}^{t_{n+1}} f(t)\,\mathrm{d}t &= f(t_{n+\frac{1}{2}})\,\Delta t = f_{n+\frac{1}{2}}\,\Delta t \\ f_{n+\frac{1}{2}} &= f_n + \frac{\Delta t}{2}\,\dot{f}_{n+\frac{1}{2}} \end{aligned} \tag{51}$$

The application of the midpoint rule Eq.(51) to Eq.(48) gives

$$\delta \boldsymbol{q}^{\mathrm{T}}_{n+\frac{1}{2}} \left(\mathbf{M}\,\ddot{\boldsymbol{q}}_{n+\frac{1}{2}} + \mathbf{B}^{\mathrm{T}}_{n+\frac{1}{2}} \boldsymbol{f}_{l\,n+\frac{1}{2}} - \boldsymbol{P}_{n+\frac{1}{2}} \right) = 0 \tag{52}$$

For any arbitrary $\delta \boldsymbol{q}^{\mathrm{T}}_{n+\frac{1}{2}}$, the residual force vector is defined as

$$\boldsymbol{f}_{R\,n+\frac{1}{2}} = \mathbf{M}\,\ddot{\boldsymbol{q}}_{n+\frac{1}{2}} + \mathbf{B}^{\mathrm{T}}_{n+\frac{1}{2}} \boldsymbol{f}_{l\,n+\frac{1}{2}} - \boldsymbol{P}_{n+\frac{1}{2}} = \mathbf{0} \tag{53}$$

The global tangent matrix is obtained by the derivation of the residual force vector $\boldsymbol{f}_{R\,n+\frac{1}{2}}$ respect to the global displacement vector $\boldsymbol{q}_{n+1}$:

$$\begin{aligned} \mathbf{K}_g =& \frac{2}{\Delta t^2}\mathbf{M} + \frac{1}{2}\,\mathbf{B}^{\mathrm{T}}_{n+\frac{1}{2}}\,\mathbf{k}_l \left(\mathbf{B}_{n+\frac{1}{2}} + \frac{1}{2}\,\mathbf{B}_{0\,n+\frac{1}{2}} \right) + \frac{\boldsymbol{z}_{n+\frac{1}{2}}\,\boldsymbol{z}^{\mathrm{T}}_{n+\frac{1}{2}}}{2\,l_{n+\frac{1}{2}}} N_{4\,n+\frac{1}{2}} \\ &+ \frac{\boldsymbol{r}_{n+\frac{1}{2}}\,\boldsymbol{z}^{\mathrm{T}}_{n+\frac{1}{2}} + \boldsymbol{z}_{n+\frac{1}{2}}\,\boldsymbol{r}^{\mathrm{T}}_{n+\frac{1}{2}}}{2\,l^2_{n+\frac{1}{2}}} \left(M_{1\,n+\frac{1}{2}} + M_{4\,n+\frac{1}{2}} \right) \end{aligned} \tag{54}$$

with $\mathbf{k}_l$ is the local tangent stiffness which is defined in Section 3 depending on the local beam theory. Besides, the remaining variables are:

$$\boldsymbol{r}_{n+\frac{1}{2}} = \left[\begin{array}{cccccc} -c_{n+\frac{1}{2}} & -s_{n+\frac{1}{2}} & 0 & c_{n+\frac{1}{2}} & s_{n+\frac{1}{2}} & 0 \end{array} \right]^{\mathrm{T}} \tag{55}$$

$$\boldsymbol{z}_{n+\frac{1}{2}} = \left[\begin{array}{cccccc} s_{n+\frac{1}{2}} & -c_{n+\frac{1}{2}} & 0 & -s_{n+\frac{1}{2}} & c_{n+\frac{1}{2}} & 0 \end{array} \right]^{\mathrm{T}} \tag{56}$$

$$\mathbf{B}_{0\,n+\frac{1}{2}} = \left[\begin{array}{c} \Delta \boldsymbol{q}^{\mathrm{T}} \left(\dfrac{\boldsymbol{z}_{n+\frac{1}{2}}\,\boldsymbol{z}^{\mathrm{T}}_{n+\frac{1}{2}}}{l_{n+\frac{1}{2}}} \right) \\ \Delta \boldsymbol{q}^{\mathrm{T}} \left(\dfrac{\boldsymbol{r}_{n+\frac{1}{2}}\,\boldsymbol{z}^{\mathrm{T}}_{n+\frac{1}{2}} + \boldsymbol{z}_{n+\frac{1}{2}}\,\boldsymbol{r}^{\mathrm{T}}_{n+\frac{1}{2}}}{l^2_{n+\frac{1}{2}}} \right) \\ \Delta \boldsymbol{q}^{\mathrm{T}} \left(\dfrac{\boldsymbol{r}_{n+\frac{1}{2}}\,\boldsymbol{z}^{\mathrm{T}}_{n+\frac{1}{2}} + \boldsymbol{z}_{n+\frac{1}{2}}\,\boldsymbol{r}^{\mathrm{T}}_{n+\frac{1}{2}}}{l^2_{n+\frac{1}{2}}} \right) \end{array} \right] \tag{57}$$

5. Non-smooth dynamics: impact loading

5.1. Contact model and constraint law

In this contact model, we consider an impact between a rigid point mass m_c and a nodal mass m_i of the beam element (Fig. 3). The motions of the masses are constrained

by the contact conditions without penetration and adhesion conditions. These contact conditions at position level can be summarized by the so-called Signorini's force law:

$$g_N \geq 0, \quad \lambda_N \geq 0, \quad g_N \, \lambda_N = 0 \tag{58}$$

where $g_N = q_i - x_c$ is the gap function between the positions of mass m_c and m_i. λ_N corresponds to the force exerted $F_{i \to c}$ by mass m_i on mass m_c. In reverse, the force exerted $F_{c \to i}$ by mass m_c on mass m_i is defined as $-\lambda_N$ according to Newton's third laws.

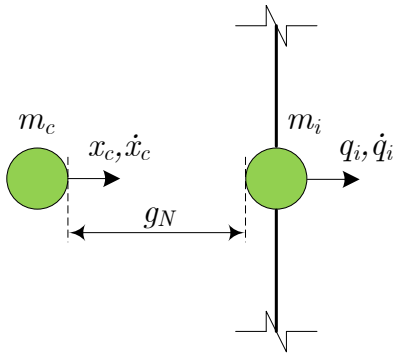

Figure 3: Contact model.

These laws do not consider the properties of the collision's contact. Newton introduced the coefficient of restitution ϵ in order to accommodate the energy dissipation during collision. By inserting Newton's impact law, the constraint law at the velocity level can be written as

$$\xi_N \geq 0, \quad -\Lambda_N \leq 0 \quad \xi_N \, \Lambda_N = 0 \tag{59}$$

where Λ is the percussion force and $\xi_N = \gamma_N^+ + \epsilon \, \gamma_N^-$ where $\gamma_N = \dot{q}_i - \dot{x}_c$ is the relative velocity. The superscript $(-)$ and $(+)$ are referred to the state before and after impact respectively.

5.2. Equations of motion

Depending on the value of the gap g_N, the equation of motion are defined for two cases: open contact ($g_N > 0$) and closed contact ($g_N = 0$). The equations of motion of the open contact are

$$m_c \, \ddot{x}_{c \, n+\frac{1}{2}} = 0 \tag{60}$$

$$\mathbf{M} \, \ddot{\boldsymbol{q}}_{n+\frac{1}{2}} + \boldsymbol{f}_{g \, n+\frac{1}{2}} = \mathbf{0} \tag{61}$$

while the external force vector $\boldsymbol{P}$ is not considered in the impact.

When the impact occurs, the velocity may jump at the time instances. At those times the velocity is not differentiable and the contact force is impulsive. In [34], Moreau proposed a set of differentiable measures in which an equation of motion is combined together. Thus, one does not have to write separately the equation of smooth part and impact part of the closed contact. The equation of the closed contact is now written as

$$m_c \left(\dot{x}_{c\,n+1} - \dot{x}_{c\,n}\right) = -P_N \tag{62}$$

$$\mathbf{M} \left(\dot{\boldsymbol{q}}_{n+1} - \dot{\boldsymbol{q}}_n\right) + \boldsymbol{f}_{g\,n+\frac{1}{2}} \Delta t = P_N \boldsymbol{I_1} \tag{63}$$

$$\xi_N = \gamma_{N\,n+1} + \epsilon\, \gamma_{N\,n} \geq 0 \tag{64}$$

where $\boldsymbol{I}_1$ is the unit vector corresponding to the impact node and P_N is the percussion force resulting from the integration of the differential measure of the contact force:

$$\int_{t_n}^{t_{n+1}} \mathrm{d}\Lambda_N = \int_{t_n}^{t_{n+1}} \left[\lambda_N \,\mathrm{d}t + \left(\Lambda_N^+ - \Lambda_N^-\right) \,\mathrm{d}\eta\right] = P_N \tag{65}$$

In order to solve Eqs.(62)-(64), the following methodology is used. First, the percussion force P_N is assumed to be zero, then Eqs.(62) and (64) are solved for the unknown displacements. If $\xi > 0$, the prediction of no percussion force is true. Otherwise, if $\xi < 0$, then the contact force exists and has a positive value. In such case, the following equations are solved for the unknown displacements and the contact force:

$$m_c \left(\dot{x}_{c\,n+1} - \dot{x}_{c\,n}\right) = -P_N \tag{66}$$

$$\mathbf{M} \left(\dot{\boldsymbol{q}}_{n+1} - \dot{\boldsymbol{q}}_n\right) + \boldsymbol{f}_{g\,n+\frac{1}{2}} \Delta t = P_N \boldsymbol{I_1} \tag{67}$$

$$\xi_N = \gamma_{N\,n+1} + \epsilon\, \gamma_{N\,n} = 0 \tag{68}$$

Equation (68) can be written as:

$$\dot{x}_{c\,n+1} = \dot{q}_{i\,n+1} + \epsilon \left(\dot{q}_{i\,n} - \dot{x}_{c\,n}\right) \tag{69}$$

By replacing the latter equation into Eq. (66), it gives after some manipulations:

$$m_c \left[\dot{q}_{i\,n+1} + \epsilon\, \dot{q}_{i\,n} - (\epsilon + 1)\dot{x}_{c\,n}\right] = -P_N \tag{70}$$

By replacing one more time Eq. (70) into Eq. 67, only one final equation is given:

$$\mathbf{M} \left(\dot{\boldsymbol{q}}_{n+1} - \dot{\boldsymbol{q}}_n\right) + \boldsymbol{f}_{g\,n+\frac{1}{2}} \Delta t = -m_c \left[\dot{q}_{i\,n+1} + \epsilon\, \dot{q}_{i\,n} - (\epsilon + 1)\dot{x}_{c\,n}\right] \boldsymbol{I_1} \tag{71}$$

6. Numerical examples

The purpose of these examples presented in this section is to show the ability of the proposed model in capturing the response of frame structures subjected to impact loadings.

6.1. Example 1

Three steel frames is depicted in Fig. 4. The column of each structure is subjected to a mass m at the position A with the initial velocities v_0. The parameter of the member are: the density $\rho = 7850$ kg/m^3, Young modulus $E = 210$ GPa, the yield stress $\sigma_y = 355$ MPa and the coefficient of poisson $\nu = 0.3$. The yield function of the generalized hinges for the square section is $\Phi(N, M) = |M/M^p|^{1.05} + |N/N^p|^2 - 1$. The time step for the analysis is $\Delta t = 10^{-5}$.

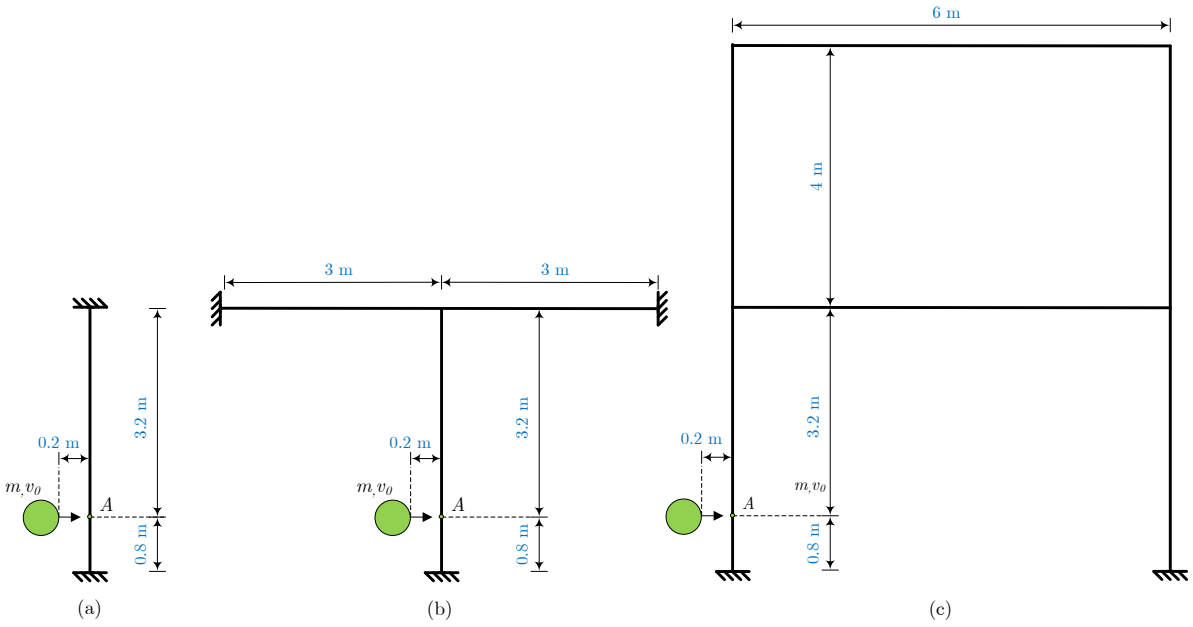

Figure 4: Geometry of the frames with the impact loadings

Regarding to the element discretization, the size of the element is 0.1 m for the distributed plasticity models. For the generalize hinges, one element is taken for each member except for the impacted column when two elements have been considered. Figures 5 and 6 shows the evolution of the maximum horizontal and vertical displacements of the impacted column, respectively, for the initial velocity of 30 m/s for the frame *c*.

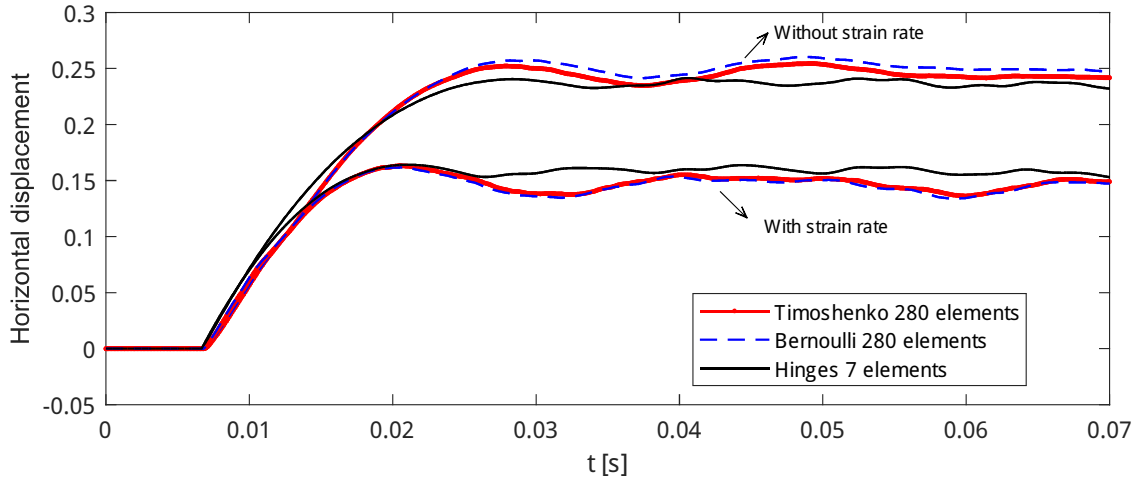

Figure 5: Ex1: Evolution of the maximum horizontal displacement [m] of the impacted column of frame c with $v_0 = 30$ m/s.

For the elasto-perfectly plastic case, the result obtained with the generalized plastic-hinges are in good agreement comparing to the ones obtained with the two fiber models. Furthermore, the series of calculation on the maximum displacement of the column under the impact are summarized in Table 1. The discrepancies between Timoshenko and Bernoulli fiber models are small and it does not exceed 3%. Otherwise, the maximum difference between the generalized elasto-plastic hinges and the distributed plasticity models are about 11% which is still acceptable in the fact that the generalized hinges model used only few number of elements.

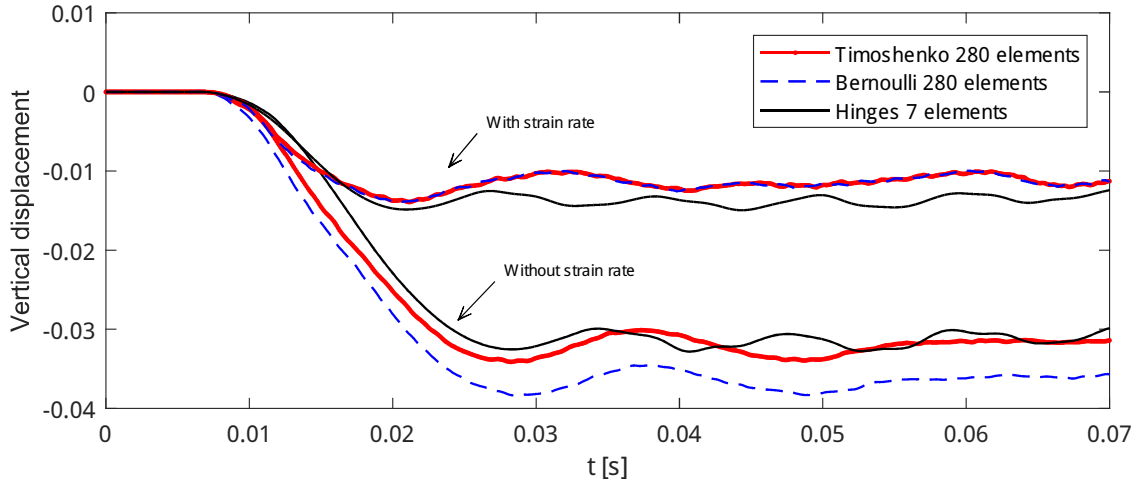

Figure 6: Ex1: Evolution of the maximum vertical displacement [m] of the impacted column of frame c with $v_0 = 30$ m/s.

Table 1: Ex1: Elasto-perfectly plasticity model: maximum displacement on the impacted column: Mass of vehicle 1500 kg, square section 20 cm, $\epsilon = 0$.

	Timoshenko	Bernoulli	Hinges
Frame a ($v_0 = 20$ m/s)	0.1085	0.1074	0.1030
Frame a ($v_0 = 30$ m/s)	0.1905	0.1909	0.1907
Frame a ($v_0 = 40$ m/s)	0.2718	0.2728	0.2739
Frame b ($v_0 = 20$ m/s)	0.1261	0.1232	0.1118
Frame b ($v_0 = 30$ m/s)	0.2454	0.2493	0.2351
Frame b ($v_0 = 40$ m/s)	0.3940	0.3994	0.3883
Frame c ($v_0 = 20$ m/s)	0.1200	0.1226	0.1125
Frame c ($v_0 = 30$ m/s)	0.2521	0.2579	0.2414
Frame c ($v_0 = 40$ m/s)	0.4136	0.4253	0.4086

Table 2: Ex1: Elasto-visco-plasticity model: displacement maximum on the impacted column: Mass of vehicle 1500 kg, square section 20 cm, $\epsilon = 0$.

	Timoshenko	Bernoulli	Hinges
Frame a ($v_0 = 20$ m/s)	0.0804	0.0780	0.0763
Frame a ($v_0 = 30$ m/s)	0.1402	0.1367	0.1469
Frame a ($v_0 = 40$ m/s)	0.2011	0.1982	0.2228
Frame b ($v_0 = 20$ m/s)	0.0854	0.0856	0.0799
Frame b ($v_0 = 30$ m/s)	0.1645	0.1625	0.1625
Frame b ($v_0 = 40$ m/s)	0.2659	0.2638	0.2685
Frame c ($v_0 = 20$ m/s)	0.0853	0.0840	0.0806
Frame c ($v_0 = 30$ m/s)	0.1644	0.1635	0.1641
Frame c ($v_0 = 40$ m/s)	0.2718	0.2714	0.2743

Regarding to the study on the strain effect, $\zeta = 5$ and $D = 40.4$ s^{-1} are material constant for the mild steel [35] which are employed for the fibre models whereas $\zeta = 5$ and $D^* = 2.025 \times 10^8$ s^{-1} are used for the hinges. Table 2 shows the maximum displacement of the impacted column for each frame and initial velocities. The discrepancies between the two fiber models are only 3% which indicate that the shear effect of Timoshenko model does not influence the outcome of the displacements. With the appropriate selected value of D^* (2.025×10^8 in this case), this model can reproduce the correct results and the evolution of the displacements (see Figures 5 and 6) with the overall maximum different of 11%.

Another series of calculation (see Table 3) have been made for testing the value D^* above if it can be used for other mass (3000 kg in this case) or the coefficient of restitution (0.5 in the case). With the same value D^*, the maximum different of the displacement does not exceed 10%. It can be concluded that this value can be used for the application of the steel structure with the square section.

Table 3: Ex1: Elasto-visco-plasticity model: displacement maximum on the impacted column: Mass of vehicle 3000 kg, square section 25 cm, $\epsilon = 0.5$.

	Timoshenko	Bernoulli	Hinges
Frame a ($v_0 = 20$ m/s)	0.0842	0.0819	0.0761
Frame a ($v_0 = 30$ m/s)	0.1525	0.1495	0.1524
Frame a ($v_0 = 40$ m/s)	0.2240	0.2196	0.2389
Frame b ($v_0 = 20$ m/s)	0.0876	0.0869	0.0787
Frame b ($v_0 = 30$ m/s)	0.1697	0.1700	0.1630
Frame b ($v_0 = 40$ m/s)	0.2743	0.2746	0.2714
Frame c ($v_0 = 20$ m/s)	0.0860	0.0854	0.0793
Frame c ($v_0 = 30$ m/s)	0.1685	0.1700	0.1641
Frame c ($v_0 = 40$ m/s)	0.2775	0.2803	0.2765

6.2. Example 2

Only frame c illustrated in Fig. 4 are used in this example. The material characteristics and the discretization remains the same. The section of all member is HEB240. The radius fillet for this sections is not taking account. The characteristic of the section are: area of the cross-section 0.0102 m^2, the inertia moment $1.0893 \times 10^{-4}\,\mathrm{m}^4$, the axial resistant $N^p = 3628.1\,\mathrm{kN}$ and the bending resistance $M^p = 360.66\,\mathrm{kNm}$. The yield function of the generalized hinges is $\Phi(N, M) = |M/M^p|^{1.05} + |N/N^p|^{1.3} - 1$. The mass of the vehicle is 1500 kg. The coefficient of the restitution ϵ is 0.5. The time step for the analysis is $\Delta t = 10^{-5}$. For the study of strain rate effect, the value $\zeta = 5$ and $D = 40.4\ \mathrm{s}^{-1}$ is used for the fibre models whereas $\zeta = 5$ and $D^* = 2.025 \times 10^7\ \mathrm{s}^{-1}$ are used for the hinges.

Figures 7 and 8 shows the evolution of the maximum horizontal and vertical displacements of the impacted column with and without strain effects, respectively. The evolution of the displacements for both directions are very similar. Tables 4 and 5 show the maximum displacement of the impacted column for frame c. The results show that the maximum difference between the Timoshenko and Bernoulli fiber models does not exceed 5.6% for both case studies. In addition, the response of the displacements obtained from the generalized elasto-plastic hinges differs to Timoshenko model about 6% and to Bernoulli model about 12% in maximum. With the value of $D^* = 2.025 \times 10^7$,

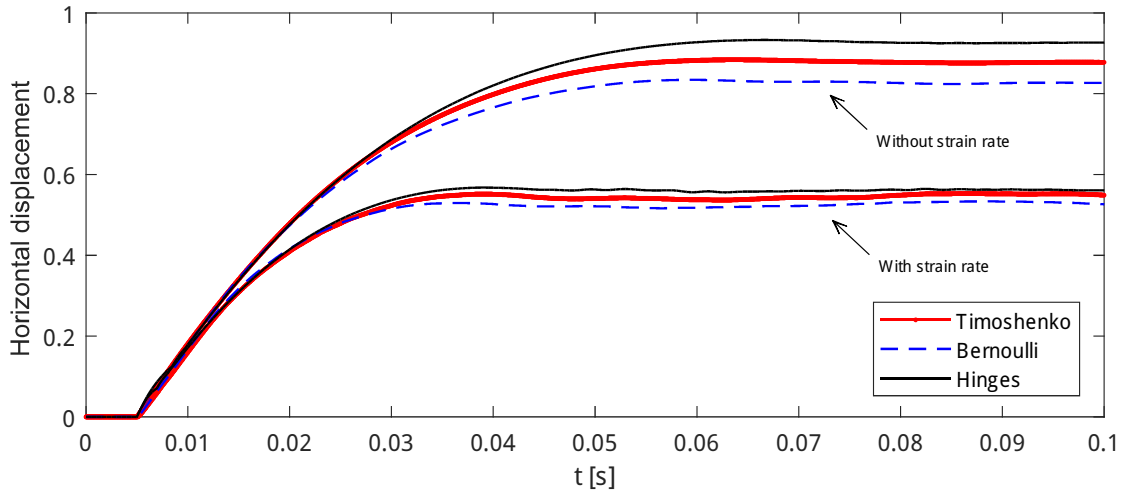

Figure 7: Ex2: Evolution of the maximum horizontal displacement [m] of the impacted column of frame c with $v_0 = 40$ m/s.

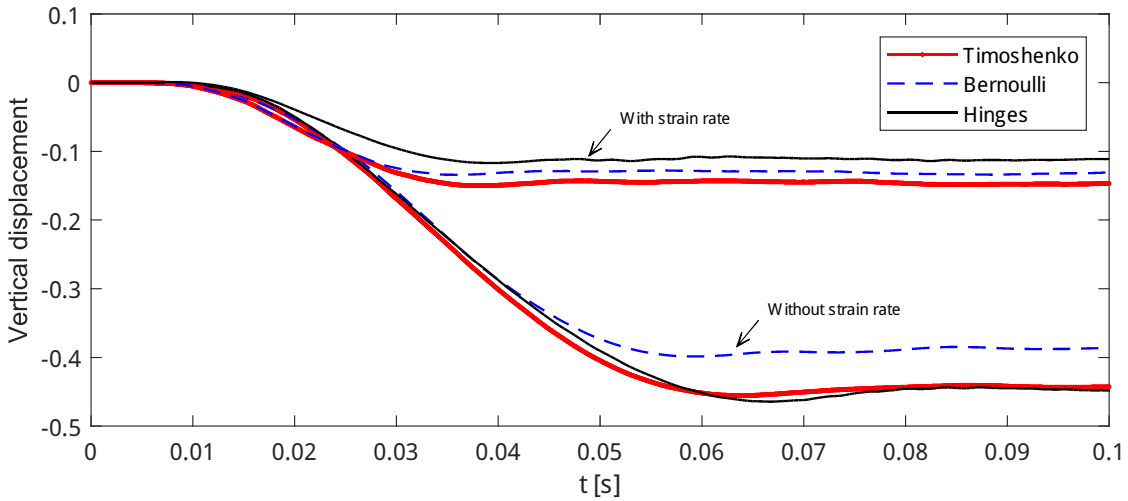

Figure 8: Ex2: Evolution of the maximum vertical displacement [m] of the impacted column of frame c with $v_0 = 40$ m/s.

the generalized hinges model is able to capture the correct response of the structures.

Table 4: Ex2: Elasto-perfectly plastic model: maximum displacement on the impacted column

	Timoshenko	Bernoulli	Hinges
Frame c ($v_0 = 20$ m/s)	0.2550	0.2536	0.2557
Frame c ($v_0 = 30$ m/s)	0.5433	0.5339	0.5707
Frame c ($v_0 = 40$ m/s)	0.8840	0.8345	0.9331

Table 5: Ex2: Elasto-visco-plastic model: maximum displacement on the impacted column

	Timoshenko	Bernoulli	Hinges
Frame c ($v_0 = 20$ m/s)	0.1621	0.1580	0.1533
Frame c ($v_0 = 30$ m/s)	0.3506	0.3211	0.3300
Frame c ($v_0 = 40$ m/s)	0.5528	0.5296	0.5675

7. Conclusion

In this paper, a co-rotational planar flexible beam element with generalized elasto-plastic hinges is extended to handled non-linear dynamics problems including impacts. Strain effects have been considered by replacing the plastic flow rule with its visco-plasticity counterpart. A family of symmetric and convex yield surfaces of super-elliptic shape is consider the behaviour of the hinges. A condensation procedure is used to remove the internal degree of freedom and to produce a two noded super-element that fit the standard co-rotational appraoch. Besides, the dynamical equations of motion are solved by using a scheme that conserves the energy in case of elasticity. The predictions obtained from the generalized hinges are compared against the reference solution obtained using distributed plasticity. Both Bernoulli and Timoshenko local beam formulations are employed for the distributed plasticity approach.

The responses of the three formulations have been compared against each other for the impact problems. The numerical examples show that the distribute plasticity beam elements accurately predict the response of the structures and are employed as the reference solution by taking lot of number of elements. The effects of the shear deformation in both elasto-plastic and visco-elasto-plastic ranges is not significant in the impact problem. Besides, the generalized hinges beam element is able to reproduce

with a good accuracy with only a few elements by comparing with the reference of the two plastic zone models. The introduction of the strain rate in the constitutive law shows that the frame deformed less due to the hardening of the material.

Acknowledgements

The first and the fourth authors gratefully acknowledge financial support by the European Commission (Research Fund for Coal and Steel) through the project RobustImpact under grant agreement RFSR-CT-2012-00029 and the financial support of the region of Brittany (France) through the ARED funding scheme.

Appendix A. Distributed plasticity approach

In this section, the tangent stiffness matrix $\mathbf{k}_l$ and the consistent tangent operator of local element formulations for both Bernoulli and Timoshenko are derived. The details for both linear Bernoulli and Timoshenko local plastic beam formulations are presented in [31].

The tangent stiffness matrix is obtained by taking the differentiation of the internal force vector $\boldsymbol{f}_l$:

$$\mathbf{k}_l = \int_{l_0} \mathbf{N}_e^{\mathrm{T}}\, \hat{\mathbf{k}}\, \mathbf{N}_e \, \mathrm{d}x \tag{A.1}$$

where the cross-section tangent stiffness matrix $\hat{\mathbf{k}}$ is calculated by taking the variations of the cross-section constitutive relation (Eq. (A.1)):

$$\hat{\mathbf{k}} = \int_A \mathbf{A}^{\mathrm{T}}\, \mathbf{C_t}\, \mathbf{A} \, \mathrm{d}A \tag{A.2}$$

A.1. Bernoulli formulation

The vector $\boldsymbol{A}$ is defined by:

$$\boldsymbol{A} = \begin{bmatrix} 1 & -z \end{bmatrix}^{\mathrm{T}} \tag{A.3}$$

The matrix $\mathbf{N}_e$ relates the variation of the cross-section deformation to the variation of the local displacement degree of freedoms:

$$\mathbf{N}_e = \begin{bmatrix} \frac{1}{l_0} & 0 & 0 \\ 0 & \frac{6\,x}{l_0^2} - \frac{4}{l_0} & \frac{6\,x}{l_0^2} - \frac{2}{l_0} \end{bmatrix} \tag{A.4}$$

If the behaviour is elastic, $\mathbf{C}_t = \mathbf{C}_e = E$. Otherwise, $\mathbf{C}_t = 0$ for elasto-perfectly plastic. For the visco-plasticity, $\mathbf{C}_t$ is given by:

$$\mathbf{C}_t = H^{-1}\,E\,\left[1 - \frac{1}{2}\left(1 + \frac{1}{2}\frac{\Delta t\,D\zeta}{\sigma_y^{\zeta}}\Phi^{\zeta-1}\,\frac{\mathrm{d}\Phi}{\mathrm{d}\sigma}\bigg|_{n+\frac{1}{2}}^{\mathrm{T}} H^{-1}E\,\frac{\partial\Phi}{\partial\sigma}\bigg|_{n+\frac{1}{2}}\right)^{-1} \left(\frac{\Delta t\,D\zeta}{\sigma_y^{\zeta}}\Phi^{\zeta-1}\,\frac{\mathrm{d}\Phi}{\mathrm{d}\sigma}\bigg|_{n+\frac{1}{2}}\,\frac{\mathrm{d}\Phi}{\mathrm{d}\sigma}\bigg|_{n+\frac{1}{2}}^{\mathrm{T}} H^{-1}E\right)\right] \tag{A.5}$$

with

$$H = 1 + \frac{1}{2}E\,\Delta\lambda\,\frac{\partial^2\Phi}{\partial\sigma^2}\,\mathrm{d}\sigma_{n+\frac{1}{2}} \tag{A.6}$$

The yield surface Φ is given by a power function of Cowper-Symonds-Bonder type [35, 36]. D and ζ are material constants; for mild steel, $\zeta = 5$ and $D = 40.4$ s^{-1} according to Cowper and Symonds [35] and for aluminum alloys, $\zeta = 4$ and $D = 6500$ s^{-1} according to Bonder and Symonds [36].

A.2. Timoshenko formulation

The matrix $\mathbf{A}_t$ is defined by

$$\mathbf{A}_t = \begin{bmatrix} 1 & -z & 0 \\ 0 & 0 & 1 \end{bmatrix} \tag{A.7}$$

The matrix $\mathbf{N}_e$ is defined by

$$\mathbf{N}_e = \begin{bmatrix} \frac{1}{l_0} & 0 & 0 \\ 0 & -\frac{1}{l_0} & \frac{1}{l_0} \\ 0 & -\left(1 - \frac{x}{l_0}\right) & -\frac{x}{l_0} \end{bmatrix} \tag{A.8}$$

In elastic case, the stiffness matrix $\mathbf{C}_t$ is defined by:

$$\mathbf{C}_t = \mathbf{C}_e = \begin{bmatrix} E & 0 \\ 0 & G \end{bmatrix} \tag{A.9}$$

with G being the shear modulus of the material.

For the visco-plasticity, the tangent operator is defined by:

$$\mathbf{C}_t = \mathbf{H}^{-1}\mathbf{C}_e\left[\mathbf{I} - \frac{1}{2}\left(1 + \frac{1}{2}\frac{\Delta t\,D\zeta}{\sigma_y^{\zeta}}\Phi^{\zeta-1}\,\frac{\mathrm{d}\Phi}{\mathrm{d}\boldsymbol{\Sigma}}\bigg|_{n+\frac{1}{2}}^{\mathrm{T}} \mathbf{H}^{-1}\mathbf{C}_e\,\frac{\partial\Phi}{\partial\boldsymbol{\Sigma}}\bigg|_{n+\frac{1}{2}}\right)^{-1} \left(\frac{\Delta t\,D\zeta}{\sigma_y^{\zeta}}\Phi^{\zeta-1}\,\frac{\mathrm{d}\Phi}{\mathrm{d}\boldsymbol{\Sigma}}\bigg|_{n+\frac{1}{2}}\,\frac{\mathrm{d}\Phi}{\mathrm{d}\boldsymbol{\Sigma}}\bigg|_{n+\frac{1}{2}}^{\mathrm{T}} \mathbf{H}^{-1}\mathbf{C_e}\right)\right] \tag{A.10}$$

with $\mathbf{\Sigma} = [\sigma \quad \tau]^{\mathrm{T}}$.

The tangent operator for plasticity case is given by:

$$\mathbf{C}_t = \mathbf{H}^{-1}\mathbf{C}_e \left[\mathbf{I} - \frac{1}{2} \left(\frac{1}{2} \frac{\mathrm{d}\Phi}{\mathrm{d}\mathbf{\Sigma}}\bigg|_{n+\frac{1}{2}}^{\mathrm{T}} \mathbf{H}^{-1}\mathbf{C}_e \frac{\partial \Phi}{\partial \mathbf{\Sigma}}\bigg|_{n+\frac{1}{2}} \right)^{-1} \left(\frac{\partial \Phi}{\partial \mathbf{\Sigma}}\bigg|_{n+\frac{1}{2}} \frac{\mathrm{d}\Phi}{\mathrm{d}\mathbf{\Sigma}}\bigg|_{n+\frac{1}{2}}^{\mathrm{T}} \mathbf{H}^{-1}\mathbf{C}_e \right) \right] \tag{A.11}$$

with

$$\mathbf{H} = \mathbf{I} + \frac{1}{2}\mathbf{C}_e \, \Delta\lambda \, \frac{\partial^2 \Phi}{\partial \mathbf{\Sigma}^2} \, \mathrm{d}\mathbf{\Sigma}_{n+\frac{1}{2}} \tag{A.12}$$

References

[1] B.A. Izzuddin, A.G. Vlassis, A.Y. Elghazouli, D.A. Nethercot. Progressive collapse of multi-storey buildings due to sudden column loss Part I: Simplified assessment framework. *Eng Struct* 2008; 30(5): 1308–1318.

[2] L. Comeliau, B. Rossi, J-F. Demonceau. Robustness of steel and composite buildings suffering the dynamic loss of a column. *Struct Eng Int* 2012; 22(3):323-329.

[3] J-F. Demonceau. Steel and composite building frames: sway response under conventional loading and development of membrane effects in beams further to an exceptional action. PhD thesis, University of Liege 2008.

[4] R. Alsafadie, M. Hjiaj, J.-M. Battini. Corotational mixed finite element formulation for thin-walled beams with generic cross-section. *Comput Methods Appl Mech Eng* 2010;199:3197-3212.

[5] R. Alsafadie, J.-M. Battini, H. Somja, M. Hjiaj. Local formulation for elasto-plastic corotational thin-walled beams based on higher-order curvature terms. *Finite Elem Anal Des* 2011;47:119-128.

[6] M.A. Crisfield, J. Shi. A co-rotational element/time-integration strategy for non-linear dynamics. *Int J Numer Methods Eng* 1994;37:1897-1913.

[7] T.-N. Le, J.-M. Battini, M. Hjiaj. Efficient formulation for dynamics of corotational 2D beams. *Comp Mech* 2011;48:153-161.

[8] T.-N. Le, J.-M. Battini, M. Hjiaj. A consistent 3D corotational beam element for nonlinear dynamic analysis of flexible structures. *Comput Methods Appl Mech Eng* 2014;269:538-565.

[9] C.M. Forley, S. Vinnakota. Inelastic behavior of multistory partially restrained steel frames. Part I. *J Struct Eng* 1999;125:854-861.

[10] S.E. Kim, D.H. Lee. Second-order distributed plasticity analysis of space steel frames. *Eng Struct* 2002;24:735-744.

[11] P. Avery, M. Mahendran. Distributed plasticity analysis of steel frame structures comprising non-compact sections. *Eng Struct* 2000;22:901-919.

[12] J.R. Liew, H. Chen. Explosion and fire analysis of steel frames using fiber element approach. *J Struct Eng* 2004;130:991-1000.

[13] P.C. Nguyen, N.T. Doan, C. Ngo-Huu, S.E. Kim. Nonlinear inelastic response history analysis of steel frame structures using plastic-zone method. *Thin Wall Struct* 2014;85:220-233.

[14] J.R. Liew, D.W. White, W.F. Chen. Second-order refined plastic-hinge analysis for frame design. Part I. *J Struct Eng* 1993;119:3196-3216.

[15] J.R. Liew, D.W. White, W.F. Chen. Notional-load plastic-hinge method for frame design. *J Struct Eng* 1994;120:1434-1454.

[16] M.R. Attalla, G.G. Deierlein, W. McGuire. Spread of plasticity: quasi-plastic-hinge approach. *J Struct Eng* 1994;120:2451-2473.

[17] W.S. King, W.F. Chen. Practical second-order inelastic analysis of semirigid frames. *J Struct Eng* 1994;120:2156-2175.

[18] C.Y. Yau, S.L. Chan. Inelastic and stability analysis of flexibly connected steel frames by springs-in-series model. *J Struct Eng* 1994;120:2803-2819.

[19] R.D. Ziemian, W. McGuire. Modified tangent modulus approach, a contribution to plastic hinge analysis. *J Struct Eng* 2002;128:1301-1307.

[20] C. Ngo-Huu, S.E. Kim, J.R. Oh. Nonlinear analysis of space steel frames using fiber plastic hinge concept. *Eng Struct* 2007;29:649-657.

[21] T.N. Doan-Ngoc, X.L. Dang, Q.T. Chu, R.J. Balling, C. Ngo-Huu. Second-order plastic-hinge analysis of planar steel frames using corotational beam-column element. *J Const Steel Res* 2016;121:413-426.

[22] P. Heng, M. Hjiaj, J.-M. Battini, A. Limam. A simplified model for nonlinear dynamic analysis of steel column subjected to impact. *Int J Nonlin Mech* 2016;86:37-54.

[23] A. Alhasawi, P. Heng, M. Hjiaj,S. Guezouli, J.-M. Battini. Co-rotational planar beam element with generalized elasto-plastic hinges. *Eng Struct* 2017;154:188-205.

[24] L.E. Malver. The propagation of longitudinal waves of plastic deformation in a bar of material exhibiting a strain rate effect. *J Appl Mech, ASME* 1951;18:203-208.

[25] S.R. Bonder, P.S. Symonds. Plastic deformation in impact and impulsive loading of beams. *Proceedings of the second Symposium on Naval Structural Mechanics*. Rhode Island, USA, 488-500.

[26] P. Perzyna. Fundamental problems in viscoplasticity. *Adv Appl Mech* 1966;9:243-377.

[27] R.C. Shieh. Large displacement matrix analysis of elastic/viscoplastic, plane frame structure. *J Eng Ind, ASME* 1975;97:1238-1244.

[28] K.C. Chang, K. Sugiura, G.C. Lee. Rate-sentitive analysis of framed structured Parts I: model formulation and verification. *J Eng Mech, ASCE* 1989;115:465-474.

[29] B.A. Izzudin, Q. Fang. Rate-sentitive analysis of framed structured Parts I: model formulation and verification. *Struct Eng Mech* 1997;5:221-237.

[30] S. Chhang, M. Hjiaj, J.-M. Battini, C. Sansour. Nonlinear dynamic analaysis of framed structures with an energy-momentum conserving co-rotational formulation: generalized plastic hinge model vs distributed plasticity approach. *Proceeding in 16th European conference on Earthquake Enginnering, Greece* 2018.

[31] J.-M. Battini. Co-rotational beam element in instability problems. *Doctoral dissertation KTH,* 2002.

[32] S. Chhang, C. Sansour, M. Hjiaj, J.-M. Battini. An energy-momentum co-rotational formulation for nonlinear dynamics of planar beams. *Comput Struct* 2017;187:50-63.

[33] S. Chhang, J.-M. Battini, M. Hjiaj. Energy-momentum method for co-rotational plane beams: A comparative study of shear flexible formulations. *Finite Elem Anal Des* 2017;134:41-54.

[34] J.J. Moreau. Unilateral contact and dry friction in finite freedom dynamics. *In Nonsmooth Mechanics and Applications* 1988;1-82.

[35] G. Cowper, P. Symonds. Strain hardening and strain rate effects in the impact loading of cantilever Beams. *No. TR-C11-28, Brown University Providence Ri* 1957.

[36] S. Bonder, P. Symonds. Experimental and theoretical investigation of the plastic deformation of cantilever beams Subjected to impulsive loadings. *J Appl Mech* 1962;29:719-728.

Paper IV:

Energy-conserving scheme of geometrically exact Euler-Bernoulli spatial beam in nonlinear dynamics

Manuscript.

Energy-conserving scheme of geometrically exact Euler-Bernoulli spatial beam in nonlinear dynamics

Sophy Chhang[a,b], Carlo Sansour[a], Mohammed Hjiaj[a,*], Jean-Marc Battini[b]

[a] *INSA Rennes, LGCGM, Université Bretagne Loire, Rennes, France*
[b] *Department of Civil and Architectural Engineering, KTH Royal Institute of Technology, Stockholm, Sweden*

Abstract

While the linear beam theory is generally based on the Euler-Bernoulli hypothesis, which neglects shear deformations, a generalisation to the non-linear large deformation regime is usually based on the Timoshenko assumption which considers shear deformations. The formulation of a 3D Euler-Bernoulli beam has been significantly delayed and only recently it did attract the attention of few researchers. The main reason lies in the challenging complexities met once an attempt to develop such a theory is undertaken. Though, such a formulation would be very useful in cases such as biomechanics, very large systems or when ill-conditioning becomes a dominant issue. This is especially true in the case of dynamics. The main obstacle in defining a three-dimensional Euler-Bernoulli beam theory lies in the fact that there is no natural way of defining a base system at the deformed configuration. Such a system exists at the reference configuration by definition. To define strain measures, we need to be able to characterise the deformation of these base vectors into the current configuration. In this paper, we provide a novel methodology to do so leading to the development of a spatial rod formulation which incorporates the Euler-Bernoulli assumption. The approach makes use of Gram-Schmidt orthogonalisation process coupled to a one-parametric rotation. The latter completes the description of the torsional cross sectional rotation and overcomes the non-uniqueness of the Gram-Schmidt procedure.

Furthermore, the formulation is extended to the dynamical case and a stable, energy conserving time-stepping algorithm is presented as well. The time integration scheme extends previously developed energy-conserving time stepping algorithms, which is in-

*Corresponding author
Email address: Mohammed.Hjiaj@insa-rennes.fr (Mohammed Hjiaj)

dependent of the non-linear complexities involved in the geometric description of the deformation at hand. Many examples of large spatial deformations confirm the power of the formulation and the integration method presented.
Keywords: Nonlinear dynamics, Euler-Bernoulli beam, 3D Geometrically exact beam, Total Lagrangian, Energy-conserving scheme.

1. Introduction

Flexible beam elements can be found in different areas of engineering practice. For some applications, such as large deployable space-structures, wind turbines propellers, offshore platforms or structures under extreme loading, beam structures could undergo large deformations as well. In addition to industrial applications, in many areas in biology and biomechanics researchers are resorting to slender beam theories as a powerful modelling tool as well.

While the linear beam theory is generally based on the Euler-Bernoulli hypothesis, which neglects shear deformations, a generalisation to the non-linear large deformation regime is usually based on the Timoshenko assumption which considers shear deformations. The main reason is that the kinematic description of the deformation of the beam cross section is straightforward under the latter assumption and very complex under the former. Indeed, the modelling of the non-linear static and dynamic behaviour of beams has been successfully carried out using concepts which incorporate three-parametric rotation tensors while exhibiting shear strains. The specific assumptions, details and parameterisations may differ but the outcomes are very much similar: Argyris et al. [1], Bathe and Balourchi [2], Simo and Vu-Quoc [3], Cardona and Géradin [4], Pimento and Yojo [5], Bauchau et al. [6] Ibrahimbegović [7, 8], Gruttmann et al. [9], Zupan and Saje [10], Sansour and Wagner [11], Kapania and Lie [12], Mata et al. [13], Zupan et al. [14], Zhong et al. [15]. and Li et al [16].

The extension of Euler-Bernoulli assumption to the non-linear large deformation regime is far more challenging. A spatial Euler-Bernoulli-based beam formulation has the advantage of being displacement-based with only three degrees of freedom, along with additional degrees of freedom to describe the torsional behaviour. This is useful in the simulation of very large structures, where the number of degrees of freedom could be very high, or when the slenderness is high rendering the numerical models ill-posed,

e.g. already at moderate slenderness rates, shear deformable beam theories exhibit locking in the framework of finite elements. Also, the complexities of rotations and their update could be avoided.

In the planar case, the desired extension has been successfully carried out for both the static and dynamic cases (Nanakorn and Vu [17], Armero and Valverde [18], Sansour et al. [19]). In contrast, the general three-dimensional case finds itself faced with multiple problems which prevented its development and so hindered possible applications. This is especially true within the context of dynamics. In this paper, we take the challenge and provide a three dimensional formulation for an Euler-Bernoulli-based beam theory.

The main obstacle in defining a three-dimensional Euler-Bernoulli beam theory lies in the fact that there is no natural way of defining a base system at the deformed configuration. Such a system exists at the reference configuration by definition. To define strain measures we need to be able to characterise the deformation of these base vectors into the current configuration. Beam formulations, which consider shear, make use of a rotation tensor to define the current configuration of these vectors. In an Euler-Bernoulli beam, their final position cannot be defined directly. Some recent attempts can be found in the literature where the problem has been successfully solved via different strategies which result in replacing two rotation parameters by expressions which relate to the displacements of the centre line resulting in 4 parametric beam formulations. Three of those parameters are either displacements or rotations, while the fourth parameter captures the cross sectional torsional rotation or the stretch of the centre line, respectively. The reader is referred to Pai [20], Zhoa and Ren [21], Greco and Cuomo [22], Bauer et al. [23], Meier [24] for a complete details on the issue. We mention also Shabana et al. [25, 26] who used the absolute nodal position and slope degree of freedom instead of angles to define the orientation of the element.

In this paper, we present an alternative and direct approach to realise the objective of developing an Euler-Bernoulli-based three-dimensional beam theory. In the present approach, we start by the following two facts. Based on the Euler-Bernoulli assumption, the only information available is that 1) the base vectors will stay normal to each other after the deformation and 2) the central line is well defined by means of a displacement vector and the only vector which changes length is that tangent to the central line. We

will present two approaches to define the position of the deformed base system in a way consistent with the overarching Euler-Bernoulli assumption. In a first approach, we resolve the issue by resorting to the following idea. Given the tangent vector at the base line (centre line), which is available through a standard differentiating process, we construct an orthogonal base system by means of a Gram-Schmidt process. This base system is then rotated to the final deformed one by means of a rotation tensor, the rotation vector of which is parallel to the tangent vector at the deformed configuration. Hence, this rotation is only one-parametric. The rotation defines an angle which is a degree of freedom of the system. Indeed, it contributes to the definition of the torsional motion of the cross section, though it does not describe it completely as parts of this torsional rotation are captured by means of the orthogonalisation process. However, since the orthogonal base system constructed by means of the Gram-Schmidt process is not unique, the rotation angle is not unique as well. Though, the final configuration of the base vectors is unique and so the resulting strain measures are unique and objective providing us with an access to a complete Euler-Bernoulli three-dimensional beam theory.

In a second approach, it will be shown as to how the rotation tensor can be defined based on first and second derivatives of the displacement vector of the centre line, together along a one parametric rotation. While this second approach is presented, it is not going to be implemented as we restrict the numerical implementation to the first approach.

A further important objective of this paper is to provide a corresponding formulation for the dynamics of such beams and the design of a time integration scheme to capture the large overall motion in the context of long term dynamics. The latter requires a stable time stepping method which renders standard time integration schemes as inappropriate. Indeed, it is well known that stability of the time integration scheme relates to its capacity to conserve energy, in case of Hamiltonian systems (Simo and Tarnow [27]). Examples of special design of energy-conservation schemes which suite certain specific formulations are plenty in the literature (Gonzalez [28], Betsch and Steinmann [29], Laursen and Meng [30], Bottasso et al. [31], Brank [32], Romero and Armero [33], Ibrahimbegović and Mamouri [34], Noels et al. [35], Bathe [36], Gams et al. [37], Krenk [38], Chhang et al. [39, 40]).

The design of energy conservation is not straightforward and depends very much on the involved non-linearities in the formulation at hand. In fact the Euler-Bernoulli hypothesis, due to its coupling of the cross sectional deformation to the deformation of the central line, does provide us with highly complex non-linear expressions for bending as well as for the kinetic energy, which involve second derivatives of the displacement field. A general methodology for the systematic construction of energy-conserving schemes has been proposed by Sansour et al. [41, 42] and successfully applied to different shell and rod formulations in [43], [19]. The methodology is based on the realisation that geometric and material non-linearities have to be treated differently. The complexities of the geometric non-linearities can be circumvented by resorting to strain velocities to provide, by means of integration, the expressions for the strain measures themselves. The expressions for the strain velocities, by definition, are linear in the velocities of the degrees of freedom of the system; the displacements in the case of the present beam formulation. This is a powerful statement which makes energy-conservation accessible no matter how complex the geometric non-linearities, meaning the expressions of the strain-displacement relations, may be. This methodology will be applied to the present formulation and it proves itself again as powerful.

The paper is organised as follows. In the next section, we present the beam kinematics in the three-dimensional case and show how to implement the Euler-Bernoulli assumption. An alternative approach to the same objective is presented as well. In Section 3, Hamilton's principle is applied to generate the field equations, followed by the finite element formulation in Section 4. The time integration scheme is discussed in full in Section 5, followed by several examples presented in Section 6. The paper concludes in Section 7.

2. Beam kinematics and strains

2.1. Beam kinematics

Let $\mathcal{B} \subset \mathbb{R}^3$, where $\mathcal{B}$ defines a reference configuration of a material body. The map $\varphi(t) : \mathcal{B} \to \mathbb{R}^3$ is an embedding depending on a time-like parameter $t \in \mathbb{R}$. Hence, $\varphi_0 = \varphi\,(t = t_0)$ defines a reference configuration which enables the identification of the material points. Then, for the reference position $\boldsymbol{X} \in \mathcal{B}$ and the deformed position $\boldsymbol{x} \in \mathcal{B}_t$, we have: $\boldsymbol{x}(t) = \varphi(\boldsymbol{X}, t)$ and $\boldsymbol{X}(t) = \varphi^{-1}(\boldsymbol{x}, t)$. We introduce the Cartesian

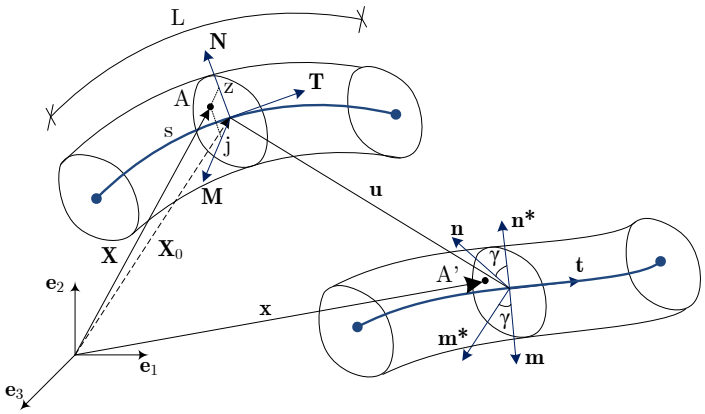

Figure 1: Beam kinematics.

basis vectors $\boldsymbol{e}_i$, $i = 1, 2, 3$. As shown in Figure 1, all centre points of the rod cross sections define the centre line, which we assume to be smooth. We consider an arc length parametrisation of this line with the arc length L at the reference configuration denoted as $s \in [0, L] \subset \mathbb{R}$. Therefore, a curvilinear coordinate system, which we consider to be convected, is described by the triple (s, z, j) for any material point in the cross-section.

Let $\boldsymbol{X}_0$ be the position of the center line at the reference configuration and we have:

$$\boldsymbol{X}(s, z, j) = \boldsymbol{X}_0(s) + z\,\boldsymbol{N}(s) + j\,\boldsymbol{M}(s) \tag{1}$$

We define the unit tangent vector $\boldsymbol{T} = \partial \boldsymbol{X}_0/\partial s|_{j=z=0}$. Similarly, we introduce the vectors: $\boldsymbol{T}_1 = \partial \boldsymbol{X}/\partial s$, $\boldsymbol{N} = \partial \boldsymbol{X}/\partial z$ and $\boldsymbol{M} = \partial \boldsymbol{X}/\partial j$. Hence, the triple $(\boldsymbol{T}_1, \boldsymbol{N}, \boldsymbol{M})$ defines a local curvilinear basis for the reference configuration. The corresponding contravariant-based vectors are then given by $\left(\boldsymbol{T}^1, \boldsymbol{N}, \boldsymbol{M}\right)$ with $\boldsymbol{T}^1 = \boldsymbol{T}_1/\left|\boldsymbol{T}_1\right|^2$. In the latter expression, $|\bullet|$ denotes the norm of a vector.

The corresponding tangent vectors at the deformed configuration are defined as $(\boldsymbol{g}, \boldsymbol{n}, \boldsymbol{m})$ with $\boldsymbol{g}_0 = \boldsymbol{t} = \boldsymbol{g}|_{z=j=0}$, $\boldsymbol{g} = \partial \boldsymbol{x}/\partial s$ and both $\boldsymbol{n}$ and $\boldsymbol{m}$ are the normal vectors of the cross-section. From Figure 1, the position $\boldsymbol{x}$ of point A' at the deformed configuration is then defined as :

$$\boldsymbol{x}(s, z, j) = \boldsymbol{X}_0(s) + \boldsymbol{u}(s) + z\,\boldsymbol{n}(s) + j\,\boldsymbol{m}(s) \tag{2}$$

where $\boldsymbol{u}(s)$ is the displacement vector of the center line. From the above expression,

we derive:

$$\boldsymbol{g} = \boldsymbol{x}_{,s} = \boldsymbol{X}_{0,s} + \boldsymbol{u}_{,s} + z\,\boldsymbol{n}_{,s} + j\,\boldsymbol{m}_{,s} \tag{3}$$

and the unit tangent vector $\boldsymbol{t}$ is given by:

$$\boldsymbol{t} = \frac{\boldsymbol{X}_{0,s} + \boldsymbol{u}_{,s}}{|\boldsymbol{X}_{0,s} + \boldsymbol{u}_{,s}|} \tag{4}$$

where a comma denotes the derivative.

Two choices for the normal vectors of cross-sections in the deformed configuration are discussed in the following section.

2.1.1. First approach

By the definition of the Gram-Schmidt process, the normal vector $\boldsymbol{n}^*$ in the deformed configuration can be constructed based on the deformed unit tangent vector $\boldsymbol{t}$ and one of the normal vectors ($\boldsymbol{N}$ or $\boldsymbol{M}$) in the reference configuration. By doing this, the orthogonality of the $\boldsymbol{n}^*$ and $\boldsymbol{t}$ is exactly met. Therefore, the normal vector $\boldsymbol{n}^*$ is defined as:

$$\boldsymbol{n}^* = \frac{\boldsymbol{N} - (\boldsymbol{N}\cdot\boldsymbol{t})\;\boldsymbol{t}}{|\boldsymbol{N} - (\boldsymbol{N}\cdot\boldsymbol{t})\;\boldsymbol{t}|} \quad Or \quad \boldsymbol{n}^* = \frac{\boldsymbol{M} - (\boldsymbol{M}\cdot\boldsymbol{t})\;\boldsymbol{t}}{|\boldsymbol{M} - (\boldsymbol{M}\cdot\boldsymbol{t})\;\boldsymbol{t}|} \tag{5}$$

where a dot denotes the scalar product of vectors.

This base system is then rotated to the final deformed one by means of a rotation tensor $\mathbf{R}_1$, the rotation vector of which is parallel to the tangent vector at the deformed configuration. Hence, this rotation is only one-parametric γ. The rotation defines an angle which is a degree of freedom of the system. Indeed, it contributes to the definition of the torsional motion of the cross section, though it does not describe it completely as parts of this torsional rotation are captured by means of the orthogonalisation process.

The rotation tensor $\mathbf{R}_1$ is defined with the help exponential map as follow (Choquet-Bruhat et al. [48]; Dubrovin et al. [49]).

$$\mathbf{R}_1 = \mathbf{I} + \sin\gamma\,\underline{\boldsymbol{\Gamma}}_t + (1-\cos\gamma)\,\underline{\boldsymbol{\Gamma}}_t\,\underline{\boldsymbol{\Gamma}}_t \tag{6}$$

where $\underline{\boldsymbol{\Gamma}}_t$ denotes a skew-symmetric matrix of the vector $\boldsymbol{t}$:

$$\underline{\boldsymbol{\Gamma}}_t = \begin{bmatrix} 0 & -t(3) & t(2) \\ t(3) & 0 & -t(1) \\ -t(2) & t(1) & 0 \end{bmatrix} \tag{7}$$

Therefore, the final normal vector $\boldsymbol{n}$ in the deformed configuration is given as

$$\boldsymbol{n} = \mathbf{R}_1 \, \boldsymbol{n}^* \tag{8}$$

Since we adopt the Euler-Bernoulli assumption, the remaining normal vector $\boldsymbol{m}$ stays normal to other vectors ($\boldsymbol{n}$, $\boldsymbol{t}$) after the deformation and hence is defined by:

$$\boldsymbol{m} = \boldsymbol{t} \times \boldsymbol{n} \tag{9}$$

where $\times$ denotes the cross product of two vectors.

2.1.2. Second approach

In a second approach, the rotation tensor will be defined based on first and second derivatives of the displacement vector of the centre line, together along a one parametric rotation γ. The total rotation matrix is obtained by a multiplication of two rotation matrix:

$$\mathbf{R} = \mathbf{R}_1 \left(\gamma \, \boldsymbol{t}\right) \mathbf{R}_2 \left(\boldsymbol{w}\right) \tag{10}$$

where the rotation tensor $\mathbf{R}_1$ is already defined in the first approach. $\boldsymbol{w}$ is the rotation vector of $\mathbf{R}_2$ which is computed from the following expression:

$$\boldsymbol{T} \cdot \boldsymbol{t} = |\boldsymbol{T}||\boldsymbol{t}| \cos\alpha = \cos\alpha \tag{11}$$

$$\boldsymbol{T} \times \boldsymbol{t} = |\boldsymbol{T}||\boldsymbol{t}| \sin\alpha \frac{\boldsymbol{w}}{|\boldsymbol{w}|} = \frac{\sin\alpha}{\alpha} \boldsymbol{w} \tag{12}$$

with α being the angle between the vectors $\boldsymbol{T}$ and $\boldsymbol{t}$. It yields:

$$\boldsymbol{w} = \frac{\alpha}{\sin\alpha} \left(\boldsymbol{T} \times \boldsymbol{t}\right) \tag{13}$$

The rotation tensor $\mathbf{R}_2$ is given as:

$$\begin{aligned} \mathbf{R}_2 &= \mathbf{I} + \frac{\sin\alpha}{\alpha} \underline{\boldsymbol{\Gamma}}_w + \frac{1-\cos\alpha}{\alpha^2} \underline{\boldsymbol{\Gamma}}_w \underline{\boldsymbol{\Gamma}}_w \\ &= \mathbf{I} + \underline{\boldsymbol{\Gamma}}_v + \frac{1}{1+\boldsymbol{T}\cdot\boldsymbol{t}} \underline{\boldsymbol{\Gamma}}_v \underline{\boldsymbol{\Gamma}}_v \end{aligned} \tag{14}$$

where $\underline{\boldsymbol{\Gamma}}_w$ denotes a skew-symmetric matrix of the vector $\boldsymbol{w}$ and $\underline{\boldsymbol{\Gamma}}_v$ a skew-symmetric matrix of the vector $\boldsymbol{v} = \boldsymbol{T} \times \boldsymbol{t}$.

Finally, the normal vectors in the deformed configuration are then given by:

$$\boldsymbol{n} = \mathbf{R} \, \boldsymbol{N} \tag{15}$$

$$\boldsymbol{m} = \mathbf{R} \, \boldsymbol{M} \tag{16}$$

2.2. Strains

Based on the above beam kinematics, the deformation gradient can be written down in the curvilinear bases system as:

$$\mathbf{F} = \boldsymbol{g} \otimes \boldsymbol{T}^1 + \boldsymbol{n} \otimes \boldsymbol{N} + \boldsymbol{m} \otimes \boldsymbol{M} \tag{17}$$

The right Cauchy deformation tensor is defined as $\mathbf{F}^{\mathrm{T}}\mathbf{F}$, which gives under the matrix form:

$$\mathbf{C} = \begin{bmatrix} \boldsymbol{g} \cdot \boldsymbol{g} & \boldsymbol{g} \cdot \boldsymbol{n} & \boldsymbol{g} \cdot \boldsymbol{m} \\ \boldsymbol{g} \cdot \boldsymbol{n} & 1 & 0 \\ \boldsymbol{g} \cdot \boldsymbol{m} & 0 & 1 \end{bmatrix} \tag{18}$$

Then, we can compute the Green strain tensor by $\mathbf{E} = \frac{1}{2}(\mathbf{C} - \mathbf{I})$ as

$$\mathbf{E} = \begin{bmatrix} E_{11} & E_{12} & E_{13} \\ E_{12} & 0 & 0 \\ E_{13} & 0 & 0 \end{bmatrix} \tag{19}$$

The non-trivial components of the Green tensor are written as

$$E_{11} = \varepsilon_{11} + z\,\kappa_1 + j\,\kappa_2 \tag{20}$$

$$E_{12} = \frac{1}{2}\, j\,\kappa_{12} \tag{21}$$

$$E_{13} = \frac{1}{2}\, z\,\kappa_{13} \tag{22}$$

where ε_{11} denotes as the axial strain, κ_1, κ_2 as the curvature of the direction z and j respectively, κ_{12} and κ_{13} as the torsion of the cross-section. These strains are given after some algebraic simplifications such as the condition of normality and the neglected terms of z^2 and j^2 (the thickness of the beam is small compared to its length):

$$\begin{aligned} \varepsilon_{11} &\approx \boldsymbol{X}_{0,s} \cdot \boldsymbol{u}_{,s} + \frac{1}{2}\boldsymbol{u}_{,s} \cdot \boldsymbol{u}_{,s} \\ \kappa_1 &= (\boldsymbol{X}_{0,s} + \boldsymbol{u}_{,s}) \cdot \boldsymbol{n}_{,s} - \boldsymbol{X}_{0,s} \cdot \boldsymbol{N}_{,s} \\ \kappa_2 &= (\boldsymbol{X}_{0,s} + \boldsymbol{u}_{,s}) \cdot \boldsymbol{m}_{,s} - \boldsymbol{X}_{0,s} \cdot \boldsymbol{M}_{,s} \\ \kappa_{12} &= \boldsymbol{n} \cdot \boldsymbol{m}_{,s} - \boldsymbol{N} \cdot \boldsymbol{M}_{,s} \\ \kappa_{13} &= \boldsymbol{n}_{,s} \cdot \boldsymbol{m} - \boldsymbol{N}_{,s} \cdot \boldsymbol{M} \end{aligned} \tag{23}$$

Moreover, $\kappa_{12} = -\kappa_{13}$ are equal to each other in magnitude because we have the following condition of normality $(\boldsymbol{m} \cdot \boldsymbol{n} - \boldsymbol{M} \cdot \boldsymbol{N})_{,s} = 0$.

3. Principle of virtual work and field equations

3.1. Principle of virtual work

The principle of virtual work in dynamics is given by:

$$\int_{t_1}^{t_2} \left(\int_V \rho\, \ddot{\boldsymbol{x}} \cdot \delta \boldsymbol{x}\, \mathrm{d}V + \int_V E\, E_{11}\, \delta E_{11}\, \mathrm{d}V + \int_V \frac{2E}{1+\nu}\, E_{12}\, \delta E_{12}\, \mathrm{d}V \right.$$
$$\left. + \int_V \frac{2E}{1+\nu}\, E_{13}\, \delta E_{13}\, \mathrm{d}V - \int_L \boldsymbol{p}(s) \cdot \delta \boldsymbol{u}\, \mathrm{d}s - \sum_{i=1}^{N} \boldsymbol{P}_i \cdot \delta \boldsymbol{u}_i - \sum_{j=1}^{M} \boldsymbol{M}_j \cdot \delta \boldsymbol{\theta}_j \right) \mathrm{d}t = 0 \tag{24}$$

Equation (24) is further developed to produce

$$\int_{t_1}^{t_2} \left(\int_L \rho A\, \ddot{\boldsymbol{u}} \cdot \delta \boldsymbol{u}\, \mathrm{d}s + \int_L \rho I_z\, \ddot{\boldsymbol{n}} \cdot \delta \boldsymbol{n}\, \mathrm{d}s + \int_L \rho I_j\, \ddot{\boldsymbol{m}} \cdot \delta \boldsymbol{m}\, \mathrm{d}s \right.$$
$$+ \int_L EA\, \varepsilon_{11}\, \delta \varepsilon_{11}\, \mathrm{d}s + \int_L EI_z\, \kappa_1\, \delta \kappa_1\, \mathrm{d}s + \int_L EI_j\, \kappa_2\, \delta \kappa_2\, \mathrm{d}s + \int_L GI_j\, \kappa_{12}\, \delta \kappa_{12}\, \mathrm{d}s$$
$$\left. + \int_L GI_z\, \kappa_{13}\, \delta \kappa_{13}\, \mathrm{d}s - \int_L \boldsymbol{p}(s) \cdot \delta \boldsymbol{u}\, \mathrm{d}s - \sum_{i=1}^{N} \boldsymbol{P}_i \cdot \delta \boldsymbol{u}_i - \sum_{j=1}^{M} \boldsymbol{M}_j \cdot \delta \boldsymbol{\theta}_j \right) \mathrm{d}t = 0 \tag{25}$$

where V is the volume of the beam, L its length, ρ the density of the material, A the area of the cross section and I_z and I_j moment of inertia. E is young module of the material and G shear modulus with the coefficient of Poisson ν. $\boldsymbol{P}_i$, $i = 1, 2, ..., N$ are concentrated forces and $\boldsymbol{p}$ is a distributed external force. $\boldsymbol{M}_i$, $i = 1, 2, ..., M$ and $\boldsymbol{\theta}_j$ are the concentrated external moments and the corresponding rotational angles, respectively.

Since $\kappa_{12} = -\kappa_{13}$, the terms related to torsion can be combined together into a single term:

$$\int_L GI_j\, \kappa_{12}\, \delta \kappa_{12}\, \mathrm{d}s + \int_L GI_z\, \kappa_{13}\, \delta \kappa_{13}\, \mathrm{d}s = \int_L G\,(I_j + I_z)\, \kappa_{12}\, \delta \kappa_{12}\, \mathrm{d}s = \int_L GJ\, \kappa_{12}\, \delta \kappa_{12}\, \mathrm{d}s \tag{26}$$

Indeed, the torsional constant J equal to $I_j + I_z$ is only valid for circular section. However, for an arbitrary cross-section, the actual Saint-Venant torsional constant J should be adopted instead of the terms $I_j + I_z$.

Therefore, Equation (25) can be rewritten as

$$\int_{t_1}^{t_2} \Bigg(\int_L \rho A\, \ddot{\boldsymbol{u}} \cdot \delta \boldsymbol{u}\, \mathrm{d}s + \int_L \rho I_z\, \ddot{\boldsymbol{n}} \cdot \delta \boldsymbol{n}\, \mathrm{d}s + \int_L \rho I_j\, \ddot{\boldsymbol{m}} \cdot \delta \boldsymbol{m}\, \mathrm{d}s + \int_L EA\ \varepsilon_{11}\, \delta\varepsilon_{11}\, \mathrm{d}s + \int_L EI_z\, \kappa_1\, \delta\kappa_1\, \mathrm{d}s + \int_L EI_j\, \kappa_2\, \delta\kappa_2\, \mathrm{d}s + \int_L GJ\, \kappa_{12}\, \delta\kappa_{12}\, \mathrm{d}s - \int_L \boldsymbol{p}(s) \cdot \delta \boldsymbol{u}\ \mathrm{d}s - \sum_{i=1}^{N} \boldsymbol{P}_i \cdot \delta \boldsymbol{u}_i - \sum_{j=1}^{M} \boldsymbol{M}_j \cdot \delta \boldsymbol{\theta}_j \Bigg)\ \mathrm{d}t = 0 \tag{27}$$

What remains to be determined in (25) is the variation $\delta\boldsymbol{\theta}$. The variation of $\delta\boldsymbol{\theta}$ is given as:

$$\delta\boldsymbol{\theta} = \delta\boldsymbol{\theta}_{\parallel} + \delta\boldsymbol{\theta}_{\perp} = (\boldsymbol{m} \cdot \delta\boldsymbol{n})\, \boldsymbol{t} + \boldsymbol{t} \times \delta\boldsymbol{t} \tag{28}$$

One can show that the aforementioned statement entails certain conservation properties. The total energy is defined by:

$$\mathsf{E} = \mathsf{K} + \mathsf{U}_{int} + \mathsf{U}_{ext} \tag{29}$$

with:

$$\mathsf{K} = \frac{1}{2} \int_L \rho A\, \dot{\boldsymbol{u}} \cdot \dot{\boldsymbol{u}}\, \mathrm{d}s + \frac{1}{2} \int_L \rho I_z\, \dot{\boldsymbol{n}} \cdot \dot{\boldsymbol{n}}\, \mathrm{d}s + \frac{1}{2} \int_L \rho I_j\, \dot{\boldsymbol{m}} \cdot \dot{\boldsymbol{m}}\, \mathrm{d}s \tag{30}$$

$$\mathsf{U}_{int} = \frac{1}{2} \int_L EA\ \varepsilon_{11}^2\, \mathrm{d}s + \frac{1}{2} \int_L EI_z\, \kappa_1^2\, \mathrm{d}s + \frac{1}{2} \int_L EI_j\, \kappa_2^2\, \mathrm{d}s + \frac{1}{2} \int_L GJ\, \kappa_{12}^2\, \mathrm{d}s \tag{31}$$

$$\mathsf{U}_{ext} = \int_L \boldsymbol{p}(s) \cdot \boldsymbol{u}\, \mathrm{d}s + \sum_{i=1}^{N} \boldsymbol{P}_i \cdot \boldsymbol{u}_i + \sum_{j=1}^{M} \boldsymbol{M}_j \cdot \delta\boldsymbol{\theta}_j \tag{32}$$

The linear momentum is defined by

$$\mathsf{L} = \int_V \rho\, \dot{\boldsymbol{x}}\, \mathrm{d}V = \int_L \int_A \rho\ (\dot{\boldsymbol{u}} + z\, \dot{\boldsymbol{n}} + j\, \dot{\boldsymbol{m}})\ \mathrm{d}A\, \mathrm{d}L = \int_L \rho A\, \dot{\boldsymbol{u}}\, \mathrm{d}s \tag{33}$$

and the angular momentum defined by

$$\begin{aligned} \mathsf{J} &= \int_V \rho\, \boldsymbol{x} \times \dot{\boldsymbol{x}}\, \mathrm{d}V \\ &= \int_L \rho A\ (\boldsymbol{X}_0 + \boldsymbol{u}) \times \dot{\boldsymbol{u}}\, \mathrm{d}s + \int_L \rho I_z\, (\boldsymbol{n} \times \dot{\boldsymbol{n}})\, \mathrm{d}s + \int_L \rho I_j\, (\boldsymbol{m} \times \dot{\boldsymbol{m}})\, \mathrm{d}s \end{aligned} \tag{34}$$

Functional (27) is equivalent to the statements:

$$\frac{D}{Dt}\mathsf{L} = \int_L \boldsymbol{p}(s)\cdot\delta\boldsymbol{u}\;\mathrm{d}s + \sum_{i=1}^{N}\boldsymbol{P}_i \tag{35}$$

$$\frac{D}{Dt}\mathsf{J} = \int_L \boldsymbol{x}_0(s)\times\boldsymbol{p}(s)\,\mathrm{d}s + \sum_{i=1}^{N}\boldsymbol{x}_0(s)\times\boldsymbol{P}_i + \sum_{j=1}^{M}\boldsymbol{M}_j \tag{36}$$

From the aforementioned equations, we entail the conservation properties:

$$\mathsf{L} = \mathsf{constant}, \quad \text{for vanishing loading} \tag{37}$$

$$\mathsf{J} = \mathsf{constant}, \quad \text{for vanishing moments} \tag{38}$$

Likewise, one can derive that the total energy of the system $\mathsf{E} = \mathsf{K} + \mathsf{U}_{int} + \mathsf{U}_{ext}$, which coincides in most cases with the Hamilitonian, is constant if damping is disregarded. It gives: $\mathsf{E} = \mathsf{K} + \mathsf{U}_{int} + \mathsf{U}_{ext} = \mathsf{constant}$.

3.2. Field equations

In order to obtain the field equations, we start from functional (27):

$$\begin{aligned}
&\int_L \rho A\,\ddot{\boldsymbol{u}}\cdot\delta\boldsymbol{u}\,\mathrm{d}s + \int_L \rho I_z\left[\left(\frac{\partial\boldsymbol{n}}{\partial\boldsymbol{u}_{,s}}\right)^{\mathrm{T}}\ddot{\boldsymbol{n}}\cdot\delta\boldsymbol{u}_{,s} + \ddot{\boldsymbol{n}}\cdot\frac{\partial\boldsymbol{n}}{\partial\gamma}\delta\gamma\right]\mathrm{d}s\\
&+\int_L \rho I_j\left[\left(\frac{\partial\boldsymbol{m}}{\partial\boldsymbol{u}_{,s}}\right)^{\mathrm{T}}\ddot{\boldsymbol{m}}\cdot\delta\boldsymbol{u}_{,s} + \ddot{\boldsymbol{m}}\cdot\frac{\partial\boldsymbol{m}}{\partial\gamma}\delta\gamma\right]\mathrm{d}s + \int_L EA\left(\varepsilon_{11}\frac{\partial\varepsilon_{11}}{\partial\boldsymbol{u}_{,s}}\right)\delta\boldsymbol{u}_{,s}\,\mathrm{d}s\\
&+\int_L EI_z\left(\kappa_1\frac{\partial\kappa_1}{\partial\boldsymbol{u}_{,\boldsymbol{s}}}\delta\boldsymbol{u}_{,\boldsymbol{s}} + \kappa_1\frac{\partial\kappa_1}{\partial\boldsymbol{u}_{,\boldsymbol{ss}}}\delta\boldsymbol{u}_{,\boldsymbol{ss}} + \kappa_1\frac{\partial\kappa_1}{\partial\gamma}\delta\gamma + \kappa_1\frac{\partial\kappa_1}{\partial\gamma_{,s}}\delta\gamma_{,s}\right)\mathrm{d}s\\
&+\int_L EI_j\left(\kappa_2\frac{\partial\kappa_2}{\partial\boldsymbol{u}_{,\boldsymbol{s}}}\delta\boldsymbol{u}_{,\boldsymbol{s}} + \kappa_2\frac{\partial\kappa_2}{\partial\boldsymbol{u}_{,\boldsymbol{ss}}}\delta\boldsymbol{u}_{,\boldsymbol{ss}} + \kappa_2\frac{\partial\kappa_2}{\partial\gamma}\delta\gamma + \kappa_2\frac{\partial\kappa_2}{\partial\gamma_{,s}}\delta\gamma_{,s}\right)\mathrm{d}s\\
&+\int_L GJ\left(\kappa_{12}\frac{\partial\kappa_{12}}{\partial\boldsymbol{u}_{,\boldsymbol{s}}}\delta\boldsymbol{u}_{,\boldsymbol{s}} + \kappa_{12}\frac{\partial\kappa_{12}}{\partial\boldsymbol{u}_{,\boldsymbol{ss}}}\delta\boldsymbol{u}_{,\boldsymbol{ss}} + \kappa_{12}\frac{\partial\kappa_{12}}{\partial\gamma}\delta\gamma + \kappa_{12}\frac{\partial\kappa_{12}}{\partial\gamma_{,s}}\delta\gamma_{,s}\right)\mathrm{d}s\\
&-\int_L \boldsymbol{p}(s)\cdot\delta\boldsymbol{u}\,\mathrm{d}s - \sum_{i=1}^{N}\boldsymbol{P}_i\cdot\delta\boldsymbol{u}_i - \sum_{j=1}^{M}\boldsymbol{M}_j\cdot\delta\boldsymbol{\theta}_j = 0
\end{aligned} \tag{39}$$

We use the following identities for determine the field equations:

$$\square\cdot\frac{\partial\square}{\partial\bigcirc_{,s}}\delta\bigcirc_{,s} = \left(\square\cdot\frac{\partial\square}{\partial\bigcirc_{,s}}\delta\bigcirc\right)_{,s} - \left(\square\cdot\frac{\partial\square}{\partial\bigcirc_{,s}}\right)_{,s}\cdot\delta\bigcirc \tag{40}$$

$$\begin{aligned}
\square\frac{\partial\square}{\partial\bigcirc_{,ss}}\cdot\delta\bigcirc_{,ss} = &\left(\square\frac{\partial\square}{\partial\bigcirc_{,ss}}\cdot\delta\bigcirc_{,s}\right)_{,s} - \left(\left(\square\frac{\partial\square}{\partial\bigcirc_{,ss}}\right)_{,s}\cdot\delta\bigcirc\right)_{,s}\\
&+\left(\square\frac{\partial\square}{\partial\bigcirc_{,ss}}\right)_{,ss}\cdot\delta\bigcirc
\end{aligned} \tag{41}$$

where $\square$ and $\bigcirc$ represent any variable vectors.

By using Gauss's theorem above and with the help of Eq. (40) and Eq. (41), Eq. (39) can be rewritten as

$$\begin{aligned}
&\int_L \Bigg(\rho A\, \ddot{\boldsymbol{u}} - \rho I_z \left[\left(\frac{\partial \boldsymbol{n}}{\partial \boldsymbol{u}_{,s}} \right)^{\mathrm{T}} \ddot{\boldsymbol{n}} \right]_{,s} - \rho I_j \left[\left(\frac{\partial \boldsymbol{m}}{\partial \boldsymbol{u}_{,s}} \right)^{\mathrm{T}} \ddot{\boldsymbol{m}} \right]_{,s} - EA \left(\varepsilon_{11} \frac{\partial \varepsilon_{11}}{\partial \boldsymbol{u}_{,s}} \right)_{,s} \\
&- EI_z \left(\kappa_1 \frac{\partial \kappa_1}{\partial \boldsymbol{u}_{,\boldsymbol{s}}} \right)_{,s} - EI_j \left(\kappa_2 \frac{\partial \kappa_2}{\partial \boldsymbol{u}_{,\boldsymbol{s}}} \right)_{,s} - GJ \left(\kappa_{12} \frac{\partial \kappa_{12}}{\partial \boldsymbol{u}_{,\boldsymbol{s}}} \right)_{,s} \\
&+ EI_z \left(\kappa_1 \frac{\partial \kappa_1}{\partial \boldsymbol{u}_{,\boldsymbol{ss}}} \right)_{,ss} + EI_j \left(\kappa_2 \frac{\partial \kappa_2}{\partial \boldsymbol{u}_{,\boldsymbol{ss}}} \right)_{,ss} + GJ \left(\kappa_{12} \frac{\partial \kappa_{12}}{\partial \boldsymbol{u}_{,\boldsymbol{ss}}} \right)_{,ss} - \boldsymbol{p}(s) \Bigg) \cdot \delta \boldsymbol{u}\, \mathrm{d}s \\
&+ \Bigg(\rho I_z \left(\frac{\partial \boldsymbol{n}}{\partial \boldsymbol{u}_{,s}} \right)^{\mathrm{T}} \ddot{\boldsymbol{n}} + \rho I_j \left(\frac{\partial \boldsymbol{m}}{\partial \boldsymbol{u}_{,s}} \right)^{\mathrm{T}} \ddot{\boldsymbol{m}} + EA\, \varepsilon_{11} \frac{\partial \varepsilon_{11}}{\partial \boldsymbol{u}_{,s}} + EI_z\, \kappa_1 \frac{\partial \kappa_1}{\partial \boldsymbol{u}_{,\boldsymbol{s}}} + EI_j\, \kappa_2 \frac{\partial \kappa_2}{\partial \boldsymbol{u}_{,\boldsymbol{s}}} \\
&+ GJ\, \kappa_{12} \frac{\partial \kappa_{12}}{\partial \boldsymbol{u}_{,\boldsymbol{s}}} - EI_z \left(\kappa_1 \frac{\partial \kappa_1}{\partial \boldsymbol{u}_{,\boldsymbol{ss}}} \right)_{,s} - EI_j \left(\kappa_2 \frac{\partial \kappa_2}{\partial \boldsymbol{u}_{,\boldsymbol{ss}}} \right)_{,s} \\
&- GJ \left(\kappa_{12} \frac{\partial \kappa_{12}}{\partial \boldsymbol{u}_{,\boldsymbol{ss}}} \right)_{,s} - \boldsymbol{P}_i \Bigg) \cdot \delta \boldsymbol{u} \Bigg|_{Boundary} \\
&+ \left(EI_z\, \kappa_1 \frac{\partial \kappa_1}{\partial \boldsymbol{u}_{,\boldsymbol{ss}}} + EI_j\, \kappa_2 \frac{\partial \kappa_2}{\partial \boldsymbol{u}_{,\boldsymbol{ss}}} + GJ\, \kappa_{12} \frac{\partial \kappa_{12}}{\partial \boldsymbol{u}_{,\boldsymbol{ss}}} - \sum_{j=1}^{M} \boldsymbol{M}_j \cdot \frac{\partial \boldsymbol{\theta}_j}{\partial \boldsymbol{u}_{,s}} \right) \cdot \delta \boldsymbol{u}_{,s} \Bigg|_{Boundary} \\
&+ \int_L \Bigg(\rho I_z\, \ddot{\boldsymbol{n}} \cdot \frac{\partial \boldsymbol{n}}{\partial \gamma} + \rho I_j\, \ddot{\boldsymbol{m}} \cdot \frac{\partial \boldsymbol{m}}{\partial \gamma} + EI_z\, \kappa_1 \frac{\partial \kappa_1}{\partial \gamma} + EI_j\, \kappa_2 \frac{\partial \kappa_2}{\partial \gamma} + GJ\, \kappa_{12} \frac{\partial \kappa_{12}}{\partial \gamma} \\
&- EI_z \left(\kappa_1 \frac{\partial \kappa_1}{\partial \gamma_{,s}} \right)_{,s} - EI_j \left(\kappa_2 \frac{\partial \kappa_2}{\partial \gamma_{,s}} \right)_{,s} - GJ \left(\kappa_{12} \frac{\partial \kappa_{12}}{\partial \gamma_{,s}} \right)_{,s} \Bigg) \cdot \delta \gamma\, \mathrm{d}s \\
&+ \left(EI_z\, \kappa_1 \frac{\partial \kappa_1}{\partial \gamma} + EI_j\, \kappa_2 \frac{\partial \kappa_2}{\partial \gamma} + GJ\, \kappa_{12} \frac{\partial \kappa_{12}}{\partial \gamma} - \sum_{j=1}^{M} \boldsymbol{M}_j \cdot \frac{\partial \boldsymbol{\theta}_j}{\partial \gamma} \right) \cdot \delta \gamma \Bigg|_{Boundary} = 0 \quad (42)
\end{aligned}$$

Because the variations $\delta \boldsymbol{u}, \delta \boldsymbol{u}_{,s}, \delta \gamma$, are arbitrary, two Euler-Lagrange equations are obtained:

$$\begin{aligned}
&\rho A\, \ddot{\boldsymbol{u}} - \rho I_z \left[\left(\frac{\partial \boldsymbol{n}}{\partial \boldsymbol{u}_{,s}} \right)^{\mathrm{T}} \ddot{\boldsymbol{n}} \right]_{,s} - \rho I_j \left[\left(\frac{\partial \boldsymbol{m}}{\partial \boldsymbol{u}_{,s}} \right)^{\mathrm{T}} \ddot{\boldsymbol{m}} \right]_{,s} - EA \left(\varepsilon_{11} \frac{\partial \varepsilon_{11}}{\partial \boldsymbol{u}_{,s}} \right)_{,s} \\
&- EI_z \left(\kappa_1 \frac{\partial \kappa_1}{\partial \boldsymbol{u}_{,\boldsymbol{s}}} \right)_{,s} - EI_j \left(\kappa_2 \frac{\partial \kappa_2}{\partial \boldsymbol{u}_{,\boldsymbol{s}}} \right)_{,s} - GJ \left(\kappa_{12} \frac{\partial \kappa_{12}}{\partial \boldsymbol{u}_{,\boldsymbol{s}}} \right)_{,s} \\
&+ EI_z \left(\kappa_1 \frac{\partial \kappa_1}{\partial \boldsymbol{u}_{,\boldsymbol{ss}}} \right)_{,ss} + EI_j \left(\kappa_2 \frac{\partial \kappa_2}{\partial \boldsymbol{u}_{,\boldsymbol{ss}}} \right)_{,ss} + GJ\, \kappa_{12} \left(\frac{\partial \kappa_{12}}{\partial \boldsymbol{u}_{,\boldsymbol{ss}}} \right)_{,ss} = \boldsymbol{p}(s) \quad (43)
\end{aligned}$$

$$\begin{aligned}
&\rho I_z\, \ddot{\boldsymbol{n}} \cdot \frac{\partial \boldsymbol{n}}{\partial \gamma} + \rho I_j\, \ddot{\boldsymbol{m}} \cdot \frac{\partial \boldsymbol{m}}{\partial \gamma} + EI_z\, \kappa_1 \frac{\partial \kappa_1}{\partial \gamma} + EI_j\, \kappa_2 \frac{\partial \kappa_2}{\partial \gamma} + GJ\, \kappa_{12} \frac{\partial \kappa_{12}}{\partial \gamma} \\
&-EI_z \left(\kappa_1 \frac{\partial \kappa_1}{\partial \gamma_{,s}} \right)_{,s} - EI_j \left(\kappa_2 \frac{\partial \kappa_2}{\partial \gamma_{,s}} \right)_{,s} - GJ \left(\kappa_{12} \frac{\partial \kappa_{12}}{\partial \gamma_{,s}} \right)_{,s} = 0 \quad (44)
\end{aligned}$$

following with the three boundary conditions:

$$\left(\rho I_z \left(\frac{\partial \boldsymbol{n}}{\partial \boldsymbol{u}_{,s}} \right)^{\mathrm{T}} \ddot{\boldsymbol{n}} + \rho I_j \left(\frac{\partial \boldsymbol{m}}{\partial \boldsymbol{u}_{,s}} \right)^{\mathrm{T}} \ddot{\boldsymbol{m}} + EA\, \varepsilon_{11} \frac{\partial \varepsilon_{11}}{\partial \boldsymbol{u}_{,s}} + EI_z\, \kappa_1 \frac{\partial \kappa_1}{\partial \boldsymbol{u}_{,s}} + EI_j\, \kappa_2 \frac{\partial \kappa_2}{\partial \boldsymbol{u}_{,s}} \right.$$
$$+ GJ\, \kappa_{12} \frac{\partial \kappa_{12}}{\partial \boldsymbol{u}_{,s}} - EI_z \left(\kappa_1 \frac{\partial \kappa_1}{\partial \boldsymbol{u}_{,ss}} \right)_{,s} - EI_j \left(\kappa_2 \frac{\partial \kappa_2}{\partial \boldsymbol{u}_{,ss}} \right)_{,s}$$
$$\left. - GJ \left(\kappa_{12} \frac{\partial \kappa_{12}}{\partial \boldsymbol{u}_{,ss}} \right)_{,s} \right) \Bigg|_0^L = \boldsymbol{P}_i|_0^L \tag{45}$$

$$\left(EI_z\, \kappa_1 \frac{\partial \kappa_1}{\partial \boldsymbol{u}_{,ss}} + EI_z\, \kappa_2 \frac{\partial \kappa_2}{\partial \boldsymbol{u}_{,ss}} + GJ\, \kappa_{12} \frac{\partial \kappa_{12}}{\partial \boldsymbol{u}_{,ss}} \right) \Bigg|_0^L = \sum_{j=1}^{M} \boldsymbol{M}_j \cdot \frac{\partial \boldsymbol{\theta}_j}{\partial \boldsymbol{u}_{,s}} \Bigg|_0^L \tag{46}$$

$$\left(EI_z\, \kappa_1 \frac{\partial \kappa_1}{\partial \gamma} + EI_j\, \kappa_2 \frac{\partial \kappa_2}{\partial \gamma} + GJ\, \kappa_{12} \frac{\partial \kappa_{12}}{\partial \gamma} \right) \Bigg|_0^L = \sum_{j=1}^{M} \boldsymbol{M}_j \cdot \frac{\partial \boldsymbol{\theta}_j}{\partial \gamma} \Bigg|_0^L \tag{47}$$

4. Finite element discretization

Given the fact that the second derivatives are presented in functional (27) (a result of the Bernoulli hypothesis), the finite element formulation must exhibit continuous first derivatives. Hence, we resort within a finite element context by using the cubic Hermite interpolation function. Consider a 3D curved beam element of arc length L with two nodes (I, II) at the end; see Figure 2. At each node, the degrees of freedom for the displacement fields are u_1, u_2, u_3, u_1', u_2', u_3' which describe respectively three displacements and their derivatives. For the torsional fields, the degrees of freedom are γ and γ'. The interpolations at the element level read:

$$\boldsymbol{u} = \mathcal{N}\, \boldsymbol{q} \tag{48}$$

$$\boldsymbol{u}_{,s} = \mathcal{N}_{,s}\, \boldsymbol{q} \tag{49}$$

$$\boldsymbol{u}_{,ss} = \mathcal{N}_{,ss}\, \boldsymbol{q} \tag{50}$$

$$\gamma = \mathcal{H}\, \boldsymbol{q} \tag{51}$$

$$\gamma_{,s} = \mathcal{H}_{,s}\, \boldsymbol{q} \tag{52}$$

where

$$\mathcal{N} = \begin{bmatrix} N_1 & 0 & 0 & 0 & N_2 & 0 & 0 & 0 & N_3 & 0 & 0 & 0 & N_4 & 0 & 0 & 0 \\ 0 & N_1 & 0 & 0 & 0 & N_2 & 0 & 0 & 0 & N_3 & 0 & 0 & 0 & N_4 & 0 & 0 \\ 0 & 0 & N_1 & 0 & 0 & 0 & N_2 & 0 & 0 & 0 & N_3 & 0 & 0 & 0 & N_4 & 0 \end{bmatrix} \tag{53}$$

$$\mathcal{H} = \begin{bmatrix} 0 & 0 & 0 & N_1 & 0 & 0 & 0 & N_2 & 0 & 0 & 0 & N_3 & 0 & 0 & 0 & N_4 \end{bmatrix} \tag{54}$$

where $\boldsymbol{q}$,denotes the global degrees of freedom, given as

$$\boldsymbol{q} = \begin{bmatrix} u_1^I & u_2^I & u_3^I & \gamma^I & u_1'^I & u_2'^I & u_3'^I & \gamma'^I & u_1^{II} & u_2^{II} & u_3^{II} & \gamma^{II} & u_1'^{II} & u_2'^{II} & u_3'^{II} & \gamma'^{II} \end{bmatrix}^{\mathrm{T}} \tag{55}$$

and the interpolations functions are defined by

$$N_1 = \frac{\xi^3}{4} - \frac{3\xi}{4} + \frac{1}{2} \tag{56}$$

$$N_2 = \frac{L\xi^3}{8} - \frac{L\xi^2}{8} - \frac{L\xi}{8} + \frac{L}{8} \tag{57}$$

$$N_3 = -\frac{\xi^3}{4} + \frac{3\xi}{4} + \frac{1}{2} \tag{58}$$

$$N_4 = \frac{L\xi^3}{8} + \frac{L\xi^2}{8} - \frac{L\xi}{8} - \frac{L}{8} \tag{59}$$

with $\xi = [-1, 1]$.

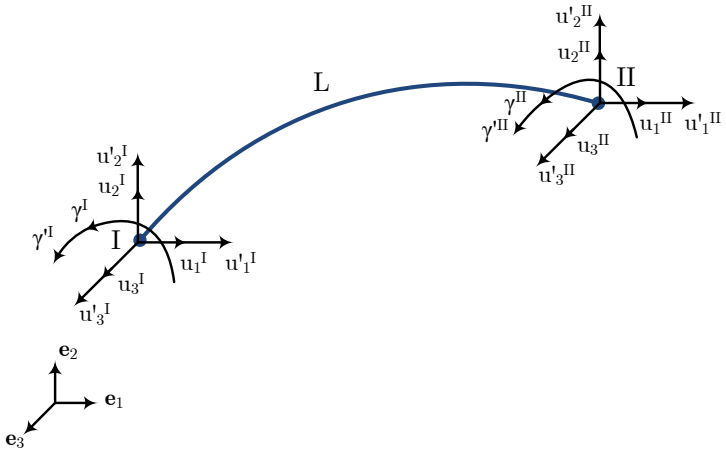

Figure 2: A 3D Beam element.

5. Time integration scheme

5.1. Energy-momentum method

The Newmark method [45], is the most widely used in the implicit time stepping method. It is said to be unconditionally stable in linear analyses but it suffers severe

shortcomings in nonlinear dynamics [27, 46]. It is known that the energy-momentum method ensures the conservation of the linear and angular momenta, and the total energy which improves the stability of the algorithm. Therefore, we aim to develop the energy-momentum method for the geometrically exact 3D Euler-Bernoulli beam where we follow the idea developed by Sansour et al. [41, 42].

The starting point comes from the standard midpoint rule:

$$\boldsymbol{q}_{n+\frac{1}{2}} = \frac{\boldsymbol{q}_n + \boldsymbol{q}_{n+1}}{2} = \boldsymbol{q}_n + \frac{1}{2}\,\Delta\boldsymbol{q} \tag{60}$$

$$\dot{\boldsymbol{q}}_{n+\frac{1}{2}} = \frac{\boldsymbol{q}_{n+1} - \boldsymbol{q}_n}{\Delta t} = \frac{2\Delta\boldsymbol{q}}{\Delta t} - \dot{\boldsymbol{q}}_n \tag{61}$$

$$\ddot{\boldsymbol{q}}_{n+\frac{1}{2}} = \frac{\dot{\boldsymbol{q}}_{n+1} - \dot{\boldsymbol{q}}_n}{\Delta t} = \frac{2\Delta\boldsymbol{q}}{\Delta t^2} - \frac{2\dot{\boldsymbol{q}}_n}{\Delta t} \tag{62}$$

The midpoint rule applied to any variable $\boldsymbol{f}$ gives

$$\int_{t_1}^{t_2} \boldsymbol{f}\,\mathrm{d}t \approx \boldsymbol{f}_{n+\frac{1}{2}}\Delta t \tag{63}$$

Equation (27) leads to

$$\begin{aligned}
&\int_L \rho A\,\ddot{\boldsymbol{u}}_{n+\frac{1}{2}} \cdot \delta\boldsymbol{u}_{n+\frac{1}{2}}\mathrm{d}s + \int_L \rho I_z\,\ddot{\boldsymbol{n}}_{n+\frac{1}{2}} \cdot \delta\boldsymbol{n}_{n+\frac{1}{2}}\mathrm{d}s + \int_L \rho I_j\,\ddot{\boldsymbol{m}}_{n+\frac{1}{2}} \cdot \delta\boldsymbol{m}_{n+\frac{1}{2}}\mathrm{d}s \\
&+ \int_L EA\;\varepsilon_{11\,n+\frac{1}{2}}\,\delta\varepsilon_{11\,n+\frac{1}{2}}\mathrm{d}s + \int_L EI_z\,\kappa_{1\,n+\frac{1}{2}}\,\delta\kappa_{1\,n+\frac{1}{2}}\mathrm{d}s + \int_L EI_j\,\kappa_{2\,n+\frac{1}{2}}\,\delta\kappa_{2\,n+\frac{1}{2}}\mathrm{d}s \\
&+ \int_L GJ\,\kappa_{12\,n+\frac{1}{2}}\,\delta\kappa_{12\,n+\frac{1}{2}}\mathrm{d}s - \int_L \boldsymbol{p}(s) \cdot \delta\boldsymbol{u}_{n+\frac{1}{2}}\,\mathrm{d}s - \sum_{i=1}^{N} \boldsymbol{P}_i \cdot \delta\boldsymbol{u}_{n+\frac{1}{2}} - \sum_{j=1}^{M} \boldsymbol{M}_j \cdot \delta\boldsymbol{\theta}_j = 0
\end{aligned} \tag{64}$$

By taking the variation $\delta\boldsymbol{q}^{\mathrm{T}}_{n+\frac{1}{2}}$ from Eq. (64), the equation of motion is obtained as:

$$\begin{aligned}
&\int_L \rho A \left(\frac{\partial \boldsymbol{u}_{n+\frac{1}{2}}}{\partial \boldsymbol{q}_{n+\frac{1}{2}}}\right)^{\mathrm{T}} \ddot{\boldsymbol{u}}_{n+\frac{1}{2}}\,\mathrm{d}s + \int_L \rho I_z \left(\frac{\partial \boldsymbol{n}_{n+\frac{1}{2}}}{\partial \boldsymbol{q}_{n+\frac{1}{2}}}\right)^{\mathrm{T}} \ddot{\boldsymbol{n}}_{n+\frac{1}{2}}\,\mathrm{d}s + \int_L \rho I_j \left(\frac{\partial \boldsymbol{m}_{n+\frac{1}{2}}}{\partial \boldsymbol{q}_{n+\frac{1}{2}}}\right)^{\mathrm{T}} \ddot{\boldsymbol{m}}_{n+\frac{1}{2}}\,\mathrm{d}s \\
&+ \int_L EA\;\varepsilon_{11\,n+\frac{1}{2}} \left(\frac{\partial \varepsilon_{11\,n+\frac{1}{2}}}{\partial \boldsymbol{q}}\right)^{\mathrm{T}} \mathrm{d}s + \int_L EI_z\,\kappa_{1\,n+\frac{1}{2}} \left(\frac{\partial \kappa_{1\,n+\frac{1}{2}}}{\partial \boldsymbol{q}}\right)^{\mathrm{T}} \mathrm{d}s + \int_L EI_j\,\kappa_{2\,n+\frac{1}{2}} \left(\frac{\partial \kappa_{2\,n+\frac{1}{2}}}{\partial \boldsymbol{q}}\right)^{\mathrm{T}} \mathrm{d}s \\
&+ \int_L GJ\,\kappa_{12\,n+\frac{1}{2}} \left(\frac{\partial \kappa_{12\,n+\frac{1}{2}}}{\partial \boldsymbol{q}}\right)^{\mathrm{T}} \mathrm{d}s - \int_L \left(\frac{\partial \boldsymbol{u}_{n+\frac{1}{2}}}{\partial \boldsymbol{q}_{n+\frac{1}{2}}}\right)^{\mathrm{T}} \boldsymbol{p}(s)\,\mathrm{d}s - \left(\frac{\partial \boldsymbol{u}_{n+\frac{1}{2}}}{\partial \boldsymbol{q}_{n+\frac{1}{2}}}\right)^{\mathrm{T}} \cdot \sum_{i=1}^{N} \boldsymbol{P}_i \\
&- \left(\frac{\partial \boldsymbol{\theta}_{j\,n+\frac{1}{2}}}{\partial \boldsymbol{q}_{n+\frac{1}{2}}}\right)^{\mathrm{T}} \cdot \sum_{j=1}^{M} \boldsymbol{M}_j = \boldsymbol{0}
\end{aligned} \tag{65}$$

The key step is to employ strain velocity fields to define the strain fields in replacement of Equations (23). These equations are used to merely define the strain velocity

fields. The same concept is applied for the kinematic velocity fields of Equations (8) and (9). One has

$$
\begin{aligned}
\dot{\varepsilon}_{11\,n+\frac{1}{2}} &= \left(\boldsymbol{X}_{0,s} + \boldsymbol{u}_{,s\,n+\frac{1}{2}}\right) \cdot \dot{\boldsymbol{u}}_{,s\,n+\frac{1}{2}} \\
\dot{\kappa}_{1\,n+\frac{1}{2}} &= \dot{\boldsymbol{u}}_{,s\,n+\frac{1}{2}} \cdot \boldsymbol{n}_{,s\,n+\frac{1}{2}} + \left(\boldsymbol{X}_{0,s} + \boldsymbol{u}_{,s\,n+\frac{1}{2}}\right) \cdot \dot{\boldsymbol{n}}_{,s\,n+\frac{1}{2}} \\
\dot{\kappa}_{2\,n+\frac{1}{2}} &= \dot{\boldsymbol{u}}_{,s\,n+\frac{1}{2}} \cdot \boldsymbol{m}_{,s\,n+\frac{1}{2}} + \left(\boldsymbol{X}_{0,s} + \boldsymbol{u}_{,s\,n+\frac{1}{2}}\right) \dot{\boldsymbol{m}}_{,s\,n+\frac{1}{2}} \\
\dot{\kappa}_{12,n+\frac{1}{2}} &= \dot{\boldsymbol{n}}_{n+\frac{1}{2}} \cdot \boldsymbol{m}_{,s\,n+\frac{1}{2}} + \boldsymbol{n}_{n+\frac{1}{2}} \cdot \dot{\boldsymbol{m}}_{,s\,n+\frac{1}{2}} \\
\dot{\boldsymbol{n}}_{n+\frac{1}{2}} &= \frac{\partial \boldsymbol{n}}{\partial \boldsymbol{u}_{,s}}\, \dot{\boldsymbol{u}}_{,s\,n+\frac{1}{2}} + \frac{\partial \boldsymbol{n}}{\partial \gamma}\, \dot{\gamma}_{n+\frac{1}{2}} \\
\dot{\boldsymbol{m}}_{n+\frac{1}{2}} &= \frac{\partial \boldsymbol{m}}{\partial \boldsymbol{u}_{,s}}\, \dot{\boldsymbol{u}}_{,s\,n+\frac{1}{2}} + \frac{\partial \boldsymbol{m}}{\partial \gamma}\, \dot{\gamma}_{n+\frac{1}{2}}
\end{aligned}
\tag{66}
$$

Given the strain and kinematic fields at time n and computing quantities of Eqs. (66) at time $n+\frac{1}{2}$ from $\boldsymbol{q}_{n+\frac{1}{2}}$, the same fields at time $n+\frac{1}{2}$ are then defined as follows:

$$
\begin{aligned}
\varepsilon_{11\,n+\frac{1}{2}} &= \varepsilon_{11\,n} + \frac{1}{2}\Delta t\, \dot{\varepsilon}_{11\,n+\frac{1}{2}} \\
\kappa_{1\,n+\frac{1}{2}} &= \kappa_{1\,n} + \frac{1}{2}\Delta t\, \dot{\kappa}_{1\,n+\frac{1}{2}} \\
\kappa_{2\,n+\frac{1}{2}} &= \kappa_{2\,n} + \frac{1}{2}\Delta t\, \dot{\kappa}_{2\,n+\frac{1}{2}} \\
\kappa_{12\,n+\frac{1}{2}} &= \kappa_{12\,n} + \frac{1}{2}\Delta t\, \dot{\kappa}_{12\,n+\frac{1}{2}} \\
\ddot{\boldsymbol{n}}_{n+\frac{1}{2}} &= \frac{2}{\Delta t}\dot{\boldsymbol{n}}_{n+\frac{1}{2}} - \frac{2}{\Delta t}\dot{\boldsymbol{n}}_{n} \\
\ddot{\boldsymbol{m}}_{n+\frac{1}{2}} &= \frac{2}{\Delta t}\dot{\boldsymbol{m}}_{n+\frac{1}{2}} - \frac{2}{\Delta t}\dot{\boldsymbol{m}}_{n}
\end{aligned}
\tag{67}
$$

It should be noted that the complexities of the geometric non-linearities can be circumvented by resorting to strain velocities to provide, by means of integration, the expressions for the strain measures themselves. The expressions for the strain velocities, by definition, are linear in the velocities of the degrees of freedom of the system; the displacements as in the case of the present beam formulation. This is a powerful method which makes energy-conservation accessible no matter how complex the geometric non-linearities.

5.2. Proof of the conservation of total energy

To prove the aforementioned statement, we take the scalar product of Equation (43) with $\dot{\boldsymbol{u}}_{n+\frac{1}{2}}$, the multiplication of Equation (44) with $\dot{\gamma}_{n+\frac{1}{2}}$. The following expressions are obtained:

$$
\begin{aligned}
&\rho A\, \ddot{\boldsymbol{u}}_{n+\frac{1}{2}} \cdot \dot{\boldsymbol{u}}_{n+\frac{1}{2}} - \rho I_z \left[\left(\frac{\partial \boldsymbol{n}}{\partial \boldsymbol{u}_{,s}} \right)^{\mathrm{T}} \ddot{\boldsymbol{n}}_{n+\frac{1}{2}} \right]_{,s} \cdot \dot{\boldsymbol{u}}_{n+\frac{1}{2}} - \rho I_j \left[\left(\frac{\partial \boldsymbol{m}}{\partial \boldsymbol{u}_{,s}} \right)^{\mathrm{T}} \ddot{\boldsymbol{m}}_{n+\frac{1}{2}} \right]_{,s} \cdot \dot{\boldsymbol{u}}_{n+\frac{1}{2}} \\
&- EA \left(\varepsilon_{11\, n+\frac{1}{2}} \frac{\partial \varepsilon_{11}}{\partial \boldsymbol{u}_{,s}} \right)_{,s} \cdot \dot{\boldsymbol{u}}_{n+\frac{1}{2}} - EI_z \left(\kappa_{1\, n+\frac{1}{2}} \frac{\partial \kappa_1}{\partial \boldsymbol{u}_{,\boldsymbol{s}}} \right)_{,s} \cdot \dot{\boldsymbol{u}}_{n+\frac{1}{2}} - EI_j \left(\kappa_{2\, n+\frac{1}{2}} \frac{\partial \kappa_2}{\partial \boldsymbol{u}_{,\boldsymbol{s}}} \right)_{,s} \cdot \dot{\boldsymbol{u}}_{n+\frac{1}{2}} \\
&- GJ \left(\kappa_{12\, n+\frac{1}{2}} \frac{\partial \kappa_{12}}{\partial \boldsymbol{u}_{,\boldsymbol{s}}} \right)_{,s} \cdot \dot{\boldsymbol{u}}_{n+\frac{1}{2}} + EI_z \left(\kappa_{1\, n+\frac{1}{2}} \frac{\partial \kappa_1}{\partial \boldsymbol{u}_{,\boldsymbol{ss}}} \right)_{,ss} \cdot \dot{\boldsymbol{u}}_{n+\frac{1}{2}} + EI_j \left(\kappa_{2\, n+\frac{1}{2}} \frac{\partial \kappa_2}{\partial \boldsymbol{u}_{,\boldsymbol{ss}}} \right)_{,ss} \cdot \dot{\boldsymbol{u}}_{n+\frac{1}{2}} \\
&+ GJ \left(\kappa_{12\, n+\frac{1}{2}} \frac{\partial \kappa_{12}}{\partial \boldsymbol{u}_{,\boldsymbol{ss}}} \right)_{,ss} \cdot \dot{\boldsymbol{u}}_{n+\frac{1}{2}} = \boldsymbol{p}(s) \cdot \dot{\boldsymbol{u}}_{n+\frac{1}{2}}
\end{aligned} \tag{68}
$$

$$
\begin{aligned}
&\rho I_z\, \ddot{\boldsymbol{n}}_{n+\frac{1}{2}} \cdot \frac{\partial \boldsymbol{n}}{\partial \gamma}\, \dot{\gamma}_{n+\frac{1}{2}} + \rho I_j\, \ddot{\boldsymbol{m}}_{n+\frac{1}{2}} \frac{\partial \boldsymbol{m}}{\partial \gamma}\, \dot{\gamma}_{n+\frac{1}{2}} + EI_z\, \kappa_{1\, n+\frac{1}{2}} \frac{\partial \kappa_1}{\partial \gamma}\, \dot{\gamma}_{n+\frac{1}{2}} + EI_j\, \kappa_{2\, n+\frac{1}{2}} \frac{\partial \kappa_2}{\partial \gamma}\, \dot{\gamma}_{n+\frac{1}{2}} \\
&+ GJ\, \kappa_{12\, n+\frac{1}{2}} \frac{\partial \kappa_{12}}{\partial \gamma}\, \dot{\gamma}_{n+\frac{1}{2}} - EI_z \left(\kappa_{1\, n+\frac{1}{2}} \frac{\partial \kappa_1}{\partial \gamma_{,s}} \right)_{,s} \dot{\gamma}_{n+\frac{1}{2}} - EI_j \left(\kappa_{2\, n+\frac{1}{2}} \frac{\partial \kappa_2}{\partial \gamma_{,s}} \right)_{,s} \dot{\gamma}_{n+\frac{1}{2}} \\
&- GJ \left(\kappa_{12\, n+\frac{1}{2}} \frac{\partial \kappa_{12}}{\partial \gamma_{,s}} \right)_{,s} \dot{\gamma}_{n+\frac{1}{2}} = 0
\end{aligned} \tag{69}
$$

For the boundary equations, we take the scalar product of Equation ((45)) $\dot{\boldsymbol{u}}_{n+\frac{1}{2}}$, Equation (46) with $\dot{\boldsymbol{u}}_{,s,n+\frac{1}{2}}$ and the multiplication of Equation (47) with $\dot{\gamma}_{n+\frac{1}{2}}$ are given as

$$
\begin{aligned}
&\Bigg(\rho I_z \left(\frac{\partial \boldsymbol{n}}{\partial \boldsymbol{u}_{,s}} \right)^{\mathrm{T}} \ddot{\boldsymbol{n}}_{n+\frac{1}{2}} \cdot \dot{\boldsymbol{u}}_{n+\frac{1}{2}} + \rho I_j \left(\frac{\partial \boldsymbol{m}}{\partial \boldsymbol{u}_{,s}} \right)^{\mathrm{T}} \ddot{\boldsymbol{m}}_{n+\frac{1}{2}} \cdot \dot{\boldsymbol{u}}_{n+\frac{1}{2}} + EA\, \varepsilon_{11\, n+\frac{1}{2}} \frac{\partial \varepsilon_{11}}{\partial \boldsymbol{u}_{,s}} \cdot \dot{\boldsymbol{u}}_{n+\frac{1}{2}} \\
&+ EI_z\, \kappa_{1\, n+\frac{1}{2}} \frac{\partial \kappa_1}{\partial \boldsymbol{u}_{,\boldsymbol{s}}} \cdot \dot{\boldsymbol{u}}_{n+\frac{1}{2}} + EI_j\, \kappa_{2\, n+\frac{1}{2}} \frac{\partial \kappa_2}{\partial \boldsymbol{u}_{,\boldsymbol{s}}} \cdot \dot{\boldsymbol{u}}_{n+\frac{1}{2}} + GJ\, \kappa_{12\, n+\frac{1}{2}} \frac{\partial \kappa_{12}}{\partial \boldsymbol{u}_{,\boldsymbol{s}}} \cdot \dot{\boldsymbol{u}}_{n+\frac{1}{2}} \\
&- EI_z \left(\kappa_{1\, n+\frac{1}{2}} \frac{\partial \kappa_1}{\partial \boldsymbol{u}_{,\boldsymbol{ss}}} \right)_{,s} \cdot \dot{\boldsymbol{u}}_{n+\frac{1}{2}} - EI_j \left(\kappa_{2\, n+\frac{1}{2}} \frac{\partial \kappa_2}{\partial \boldsymbol{u}_{,\boldsymbol{ss}}} \right)_{,s} \cdot \dot{\boldsymbol{u}}_{n+\frac{1}{2}} \\
&- GJ \left(\kappa_{12\, n+\frac{1}{2}} \frac{\partial \kappa_{12}}{\partial \boldsymbol{u}_{,\boldsymbol{ss}}} \right)_{,s} \cdot \dot{\boldsymbol{u}}_{n+\frac{1}{2}} \Bigg) \Bigg|_0^L = \boldsymbol{P}_i \cdot \dot{\boldsymbol{u}}_{n+\frac{1}{2}} \Big|_0^L
\end{aligned} \tag{70}
$$

$$
\begin{aligned}
&\left(EI_z\, \kappa_{1\, n+\frac{1}{2}} \frac{\partial \kappa_1}{\partial \boldsymbol{u}_{,\boldsymbol{ss}}} \cdot \dot{\boldsymbol{u}}_{,s\, n+\frac{1}{2}} + EI_z\, \kappa_{2\, n+\frac{1}{2}} \frac{\partial \kappa_2}{\partial \boldsymbol{u}_{,\boldsymbol{ss}}} \cdot \dot{\boldsymbol{u}}_{,s\, n+\frac{1}{2}} + GJ\, \kappa_{12\, n+\frac{1}{2}} \frac{\partial \kappa_{12}}{\partial \boldsymbol{u}_{,\boldsymbol{ss}}} \cdot \dot{\boldsymbol{u}}_{,s\, n+\frac{1}{2}} \right) \Bigg|_0^L \\
&= \sum_{j=1}^{M} \boldsymbol{M}_j \cdot \frac{\partial \boldsymbol{\theta}_j}{\partial \boldsymbol{u}_{,s}} \cdot \dot{\boldsymbol{u}}_{,s\, n+\frac{1}{2}} \Bigg|_0^L
\end{aligned} \tag{71}
$$

$$
\begin{aligned}
&\left(EI_z\, \kappa_{1\, n+\frac{1}{2}} \frac{\partial \kappa_1}{\partial \gamma}\, \dot{\gamma}_{n+\frac{1}{2}} + EI_j\, \kappa_{2\, n+\frac{1}{2}} \frac{\partial \kappa_2}{\partial \gamma}\, \dot{\gamma}_{n+\frac{1}{2}} + GJ\, \kappa_{12\, n+\frac{1}{2}} \frac{\partial \kappa_{12}}{\partial \gamma}\, \dot{\gamma}_{n+\frac{1}{2}} \right) \Bigg|_0^L \\
&= \sum_{j=1}^{M} \boldsymbol{M}_j \cdot \frac{\partial \boldsymbol{\theta}_j}{\partial \gamma}\, \dot{\gamma}_{n+\frac{1}{2}} \Bigg|_0^L
\end{aligned} \tag{72}
$$

The subsequent application of Gauss's theorem with the boundary conditions (70), (71), (72) results in

$$
\begin{aligned}
&\int_L \rho A\, \ddot{\boldsymbol{u}}_{n+\frac{1}{2}} \cdot \dot{\boldsymbol{u}}_{n+\frac{1}{2}} \mathrm{d}s + \int_L \rho I_z \left[\left(\frac{\partial \boldsymbol{n}}{\partial \boldsymbol{u}_{,s}} \right)^{\mathrm{T}} \ddot{\boldsymbol{n}}_{n+\frac{1}{2}} \cdot \dot{\boldsymbol{u}}_{,s\, n+\frac{1}{2}} + \ddot{\boldsymbol{n}}_{n+\frac{1}{2}} \cdot \frac{\partial \boldsymbol{n}}{\partial \gamma} \dot{\gamma}_{n+\frac{1}{2}} \right] \mathrm{d}s \\
&+ \int_L \rho I_j \left[\left(\frac{\partial \boldsymbol{m}}{\partial \boldsymbol{u}_{,s}} \right)^{\mathrm{T}} \ddot{\boldsymbol{m}}_{n+\frac{1}{2}} \cdot \dot{\boldsymbol{u}}_{,s\, n+\frac{1}{2}} + \ddot{\boldsymbol{m}}_{n+\frac{1}{2}} \cdot \frac{\partial \boldsymbol{m}}{\partial \gamma} \dot{\gamma}_{n+\frac{1}{2}} \right] \mathrm{d}s + \int_L EA\, \varepsilon_{11\, n+\frac{1}{2}} \frac{\partial \varepsilon_{11}}{\partial \boldsymbol{u}_{,s}} \dot{\boldsymbol{u}}_{,s\, n+\frac{1}{2}} \mathrm{d}s \\
&+ \int_L EI_z \left(\kappa_{1\, n+\frac{1}{2}} \frac{\partial \kappa_1}{\partial \boldsymbol{u}_{,\boldsymbol{s}}} \cdot \dot{\boldsymbol{u}}_{,s\, n+\frac{1}{2}} + \kappa_{1\, n+\frac{1}{2}} \frac{\partial \kappa_1}{\partial \boldsymbol{u}_{,\boldsymbol{ss}}} \dot{\boldsymbol{u}}_{,ss\, n+\frac{1}{2}} + \kappa_{1,n+\frac{1}{2}} \frac{\partial \kappa_1}{\partial \gamma} \dot{\gamma}_{n+\frac{1}{2}} + \kappa_{1,n+\frac{1}{2}} \frac{\partial \kappa_1}{\partial \gamma_{,s}} \dot{\gamma}_{,s\, n+\frac{1}{2}} \right) \mathrm{d}s \\
&+ \int_L EI_j \left(\kappa_{2\, n+\frac{1}{2}} \frac{\partial \kappa_2}{\partial \boldsymbol{u}_{,\boldsymbol{s}}} \cdot \dot{\boldsymbol{u}}_{,s\, n+\frac{1}{2}} + \kappa_{2\, n+\frac{1}{2}} \frac{\partial \kappa_2}{\partial \boldsymbol{u}_{,\boldsymbol{ss}}} \dot{\boldsymbol{u}}_{,ss\, n+\frac{1}{2}} + \kappa_{2,n+\frac{1}{2}} \frac{\partial \kappa_2}{\partial \gamma} \dot{\gamma}_{n+\frac{1}{2}} + \kappa_{2,n+\frac{1}{2}} \frac{\partial \kappa_2}{\partial \gamma_{,s}} \dot{\gamma}_{,s\, n+\frac{1}{2}} \right) \mathrm{d}s \\
&+ \int_L GJ \left(\kappa_{12\, n+\frac{1}{2}} \frac{\partial \kappa_{12}}{\partial \boldsymbol{u}_{,\boldsymbol{s}}} \cdot \dot{\boldsymbol{u}}_{,s\, n+\frac{1}{2}} + \kappa_{12\, n+\frac{1}{2}} \frac{\partial \kappa_{12}}{\partial \boldsymbol{u}_{,\boldsymbol{ss}}} \dot{\boldsymbol{u}}_{,ss\, n+\frac{1}{2}} + \kappa_{12\, n+\frac{1}{2}} \frac{\partial \kappa_{12}}{\partial \gamma} \dot{\gamma}_{n+\frac{1}{2}} + \kappa_{12\, n+\frac{1}{2}} \frac{\partial \kappa_{12}}{\partial \gamma_{,s}} \dot{\gamma}_{,s\, n+\frac{1}{2}} \right) \mathrm{d}s \\
&= \int_L \boldsymbol{p}(s) \cdot \dot{\boldsymbol{u}}_{n+\frac{1}{2}}\, \mathrm{d}s + \sum_{i=1}^{N} \boldsymbol{P}_i \cdot \dot{\boldsymbol{u}}_{n+\frac{1}{2}} + \sum_{j=1}^{M} \boldsymbol{M}_j \cdot \left(\frac{\partial \boldsymbol{\theta}_j}{\partial \boldsymbol{u}_{,s}} \cdot \dot{\boldsymbol{u}}_{,s\, n+\frac{1}{2}} + \frac{\partial \boldsymbol{\theta}_j}{\partial \gamma}\, \dot{\gamma}_{n+\frac{1}{2}} \right)
\end{aligned}
\tag{73}
$$

By using equations (66), the previous equation is rewritten as

$$
\begin{aligned}
&\int_L \rho A\, \ddot{\boldsymbol{u}}_{n+\frac{1}{2}} \cdot \dot{\boldsymbol{u}}_{n+\frac{1}{2}}\, \mathrm{d}s + \int_L \rho I_z\, \ddot{\boldsymbol{n}}_{n+\frac{1}{2}} \cdot \dot{\boldsymbol{n}}_{n+\frac{1}{2}}\, \mathrm{d}s + \int_L \rho I_j\, \ddot{\boldsymbol{m}}_{n+\frac{1}{2}} \cdot \dot{\boldsymbol{m}}_{n+\frac{1}{2}}\, \mathrm{d}s \\
&+ \int_L EA\, \varepsilon_{11\, n+\frac{1}{2}}\, \dot{\varepsilon}_{11\, n+\frac{1}{2}}\, \mathrm{d}s + \int_L EI_z\, \kappa_{1\, n+\frac{1}{2}}\, \cdot \dot{\kappa}_{1\, n+\frac{1}{2}}\, \mathrm{d}s + \int_L EI_j\, \kappa_{2\, n+\frac{1}{2}}\, \cdot \dot{\kappa}_{2\, n+\frac{1}{2}}\, \mathrm{d}s \\
&+ \int_L GJ\, \kappa_{12\, n+\frac{1}{2}}\, \cdot \dot{\kappa}_{12\, n+\frac{1}{2}}\, \mathrm{d}s = \int_L \boldsymbol{p}(s) \cdot \dot{\boldsymbol{u}}_{n+\frac{1}{2}}\, \mathrm{d}s + \sum_{i=1}^{N} \boldsymbol{P}_i \cdot \dot{\boldsymbol{u}}_{n+\frac{1}{2}} + \sum_{j=1}^{M} \boldsymbol{M}_j \cdot \dot{\boldsymbol{\theta}}_{j,n+\frac{1}{2}}
\end{aligned}
\tag{74}
$$

which, with the use of the midpoint rule, is equivalent to

$$
\begin{aligned}
&\int_L \rho A\, \frac{\dot{\boldsymbol{u}}_{n+1} - \dot{\boldsymbol{u}}_n}{\Delta t} \cdot \frac{\dot{\boldsymbol{u}}_{n+1} + \dot{\boldsymbol{u}}_n}{2}\, \mathrm{d}s + \int_L \rho I_z\, \frac{\dot{\boldsymbol{n}}_{n+1} - \dot{\boldsymbol{n}}_n}{\Delta t} \cdot \frac{\dot{\boldsymbol{n}}_{n+1} + \dot{\boldsymbol{n}}_n}{2}\, \mathrm{d}s \\
&+ \int_L \rho I_j\, \frac{\dot{\boldsymbol{m}}_{n+1} - \dot{\boldsymbol{m}}_n}{\Delta t} \cdot \frac{\dot{\boldsymbol{m}}_{n+1} + \dot{\boldsymbol{m}}_n}{2}\, \mathrm{d}s + \int_L EA\, \frac{\varepsilon_{11\, n+1} + \varepsilon_{11\, n}}{2}\, \frac{\varepsilon_{11\, n+1} - \varepsilon_{11\, n}}{\Delta t}\, \mathrm{d}s \\
&+ \int_L EI_z\, \frac{\kappa_{1\, n+1} + \kappa_{1\, n}}{2}\, \frac{\kappa_{1\, n+1} - \kappa_{1\, n}}{\Delta t}\, \mathrm{d}s + \int_L EI_j\, \frac{\kappa_{2\, n+1} + \kappa_{2\, n}}{2}\, \frac{\kappa_{2\, n+1} - \kappa_{2\, n}}{\Delta t}\, \mathrm{d}s \\
&+ \int_L GJ\, \frac{\kappa_{12\, n+1} + \kappa_{12\, n}}{2}\, \frac{\kappa_{12\, n+1} - \kappa_{12\, n}}{\Delta t}\, \mathrm{d}s \\
&= \int_L \boldsymbol{p}(s) \cdot \frac{\boldsymbol{u}_{n+1} - \boldsymbol{u}_n}{\Delta t}\, \mathrm{d}s + \sum_{i=1}^{N} \boldsymbol{P}_i \cdot \frac{\boldsymbol{u}_{i\, n+1} - \boldsymbol{u}_{i\, n}}{\Delta t} + \sum_{j=1}^{M} \boldsymbol{M}_j \cdot \frac{\boldsymbol{\theta}_{j\, n+1} - \boldsymbol{\theta}_{j\, n}}{\Delta t}
\end{aligned}
\tag{75}
$$

The last equation finally simplifies to

$$\frac{1}{2}\int_L \rho A\,\left(\dot{\boldsymbol{u}}_{n+1}^2-\dot{\boldsymbol{u}}_n^2\right)\,\mathrm{d}s+\frac{1}{2}\int_L \rho I_z\,\left(\dot{\boldsymbol{n}}_{n+1}^2-\dot{\boldsymbol{n}}_n^2\right)\,\mathrm{d}s+\frac{1}{2}\int_L \rho I_j\,\left(\dot{\boldsymbol{m}}_{n+1}^2-\dot{\boldsymbol{m}}_n^2\right)\,\mathrm{d}s$$
$$+\frac{1}{2}\int_L EA\,\left(\varepsilon_{11\,n+1}^2-\varepsilon_{11\,n}^2\right)\,\mathrm{d}s+\frac{1}{2}\int_L EI_z\,\left(\kappa_{1\,n+1}^2-\kappa_{1\,n}^2\right)\,\mathrm{d}s+\frac{1}{2}\int_L EI_j\,\left(\kappa_{2\,n+1}^2-\kappa_{2\,n}^2\right)\,\mathrm{d}s$$
$$+\frac{1}{2}\int_L GJ\,\left(\kappa_{12\,n+1}^2-\kappa_{12\,n}^2\right)\,\mathrm{d}s=\int_L \boldsymbol{p}(s)\cdot(\boldsymbol{u}_{n+1}-\boldsymbol{u}_n)\,\mathrm{d}s+\sum_{i=1}^{N}\boldsymbol{P}_i\cdot(\boldsymbol{u}_{i\,n+1}-\boldsymbol{u}_{i\,n})$$
$$+\sum_{j=1}^{M}\boldsymbol{M}_j\cdot(\boldsymbol{\theta}_{j\,n+1}-\boldsymbol{\theta}_{j\,n}) \tag{76}$$

Assuming that the external loading is conservative, Equation (5.2) is equivalent to:

$$[\mathsf{K}+\mathsf{U}_{int}+\mathsf{U}_{ext}]_{n+1}=[\mathsf{K}+\mathsf{U}_{int}+\mathsf{U}_{ext}]_n \tag{77}$$

which proves the conservation of the total energy.

5.3. Proof of the conservation of linear momentum

To prove the conservation of linear momentum, we start by integrating field equation (43) , which provides us with the statement,

$$\int_L \rho A\,\ddot{\boldsymbol{u}}\,\mathrm{d}s-\int_L\left(\rho I_z\left[\left(\frac{\partial\boldsymbol{n}}{\partial\boldsymbol{u}_{,s}}\right)^{\mathrm{T}}\ddot{\boldsymbol{n}}\right]_{,s}+\rho I_j\left[\left(\frac{\partial\boldsymbol{m}}{\partial\boldsymbol{u}_{,s}}\right)^{\mathrm{T}}\ddot{\boldsymbol{m}}\right]_{,s}+EA\,\left(\varepsilon_{11}\,\frac{\partial\varepsilon_{11}}{\partial\boldsymbol{u}_{,s}}\right)_{,s}\right.$$
$$+EI_z\,\left(\kappa_1\frac{\partial\kappa_1}{\partial\boldsymbol{u}_{,\boldsymbol{s}}}\right)_{,s}+EI_j\,\left(\kappa_2\frac{\partial\kappa_2}{\partial\boldsymbol{u}_{,\boldsymbol{s}}}\right)_{,s}+GJ\,\kappa_{12}\,\left(\frac{\partial\kappa_{12}}{\partial\boldsymbol{u}_{,\boldsymbol{s}}}\right)_{,s}$$
$$\left.-\,EI_z\,\left(\kappa_1\frac{\partial\kappa_1}{\partial\boldsymbol{u}_{,\boldsymbol{ss}}}\right)_{,ss}-EI_j\,\left(\kappa_2\frac{\partial\kappa_2}{\partial\boldsymbol{u}_{,\boldsymbol{ss}}}\right)_{,ss}-GI_j\,\left(\kappa_{12}\frac{\partial\kappa_{12}}{\partial\boldsymbol{u}_{,\boldsymbol{ss}}}\right)_{,ss}\right)\,\mathrm{d}s=\int_L\boldsymbol{p}(s)\,\mathrm{d}s \tag{78}$$

The subsequent application of Gauss's theorem results in

$$\int_L \rho A\,\ddot{\boldsymbol{u}}\,\mathrm{d}s-\left(\rho I_z\,\left(\frac{\partial\boldsymbol{n}}{\partial\boldsymbol{u}_{,s}}\right)^{\mathrm{T}}\ddot{\boldsymbol{n}}+\rho I_j\,\left(\frac{\partial\boldsymbol{m}}{\partial\boldsymbol{u}_{,s}}\right)^{\mathrm{T}}\ddot{\boldsymbol{m}}+EA\,\varepsilon_{11}\,\frac{\partial\varepsilon_{11}}{\partial\boldsymbol{u}_{,s}}\right.$$
$$+EI_z\,\kappa_1\,\frac{\partial\kappa_1}{\partial\boldsymbol{u}_{,\boldsymbol{s}}}+EI_j\,\kappa_2\,\frac{\partial\kappa_2}{\partial\boldsymbol{u}_{,\boldsymbol{s}}}+GJ\,\kappa_{12}\,\frac{\partial\kappa_{12}}{\partial\boldsymbol{u}_{,\boldsymbol{s}}}$$
$$\left.-\,EI_z\,\kappa_1\,\frac{\partial\kappa_1}{\partial\boldsymbol{u}_{,\boldsymbol{ss}}}-EI_j\,\kappa_2\,\frac{\partial\kappa_2}{\partial\boldsymbol{u}_{,\boldsymbol{ss}}}-GJ\,\kappa_{12}\,\frac{\partial\kappa_{12}}{\partial\boldsymbol{u}_{,\boldsymbol{ss}}}\right)\Bigg|_0^L=\int_L\boldsymbol{p}(s)\,\mathrm{d}s \tag{79}$$

The boundary condition (45) appears in the equation (79) which yields the general linear momentum equation:

$$\int_L \rho A\,\ddot{\boldsymbol{u}}_{n+\frac{1}{2}}\,\mathrm{d}s=\int_L\boldsymbol{p}(s)\,\mathrm{d}s+\sum_{i=1}^{N}\boldsymbol{P}_i \tag{80}$$

which indicates that in the case of vanishing external forces and by applying the mid-point rule provides with the statement, we get:

$$\int_L \rho A \, \frac{\dot{\boldsymbol{u}}_{n+1} - \dot{\boldsymbol{u}}_n}{\Delta t} \, \mathrm{d}s = \mathbf{0} \tag{81}$$

leading to

$$\int_L \rho A \, \left(\dot{\boldsymbol{u}}_{n+1} - \dot{\boldsymbol{u}}_n\right) \, \mathrm{d}s = \mathbf{0} \tag{82}$$

which reveals in Equation (33):

$$\mathsf{L}_{n+1} = \mathsf{L}_n \tag{83}$$

Hence, the conservation of linear momentum is now proven.

6. Numerical examples

In this section, four numerical examples are presented. The first purpose is to assess the efficiency and the accuracy of the proposed formulation considering both straight and curved beams. Moreover, we compare the predictions of our model against the numerical results obtained from Abaqus software considering a large number of elements. We also compare the responses of the displacement of the first example by the cubic co-rotational formulation by Le et al. [47]. Both compared formulations are performed with only the straight beam element. The second purpose is to show that the proposed algorithm conserves the total energy of the system and remain stable even if a very large number of time steps are applied. The last purpose is to verify if this new formulation conserves also the linear and angular momenta in the absence of applied external loads.

6.1. Example 1: Shallow arch

A circular shallow arch clamped at both ends is considered [47] in this example. The shallow arc has a span of $L = 20$ m with a uniform square cross-section of $b = 0.25$ m (see Fig. 3). The radius R of the arch is equal to 20 m with $\Phi = 30^o$. The arch is subjected to a vertical force F_y and to an out-of-plane sinusoidal force F_z (see Fig. 4). The circular frequency of F_z is $w = 10$ rad/s. The arch has a modulus of elasticity E

= 210 GPa, and a Poisson ratio $\nu = 0.3$. The mass per unit volume ρ is 7850 kg/m^3. The time step is chosen as $\Delta t = 10^{-4}$ s.

This example is suitable for showing the efficiency of the new curved Bernoulli beam element. Only 12 elements are used to perform the analysis whereas the reference solution is obtained with 21 elements. We also compare the response of displacements with cubic co-rotational formulation [47] by using the HHT-α method while the value of α is taken -0.05. The same scheme has been considered for Abaqus simulation. The time histories of the displacements are depicted in Figs. 5, 6 and 7. It can be observed that, with only 12 elements, the results obtained with the proposed formulation are in very good agreement with the reference solution and the cubic co-rotational approach. As shown in Fig. 8, the proposed algorithm conserves the energy for one million time steps. This indicates that the stability of the system has been achieved.

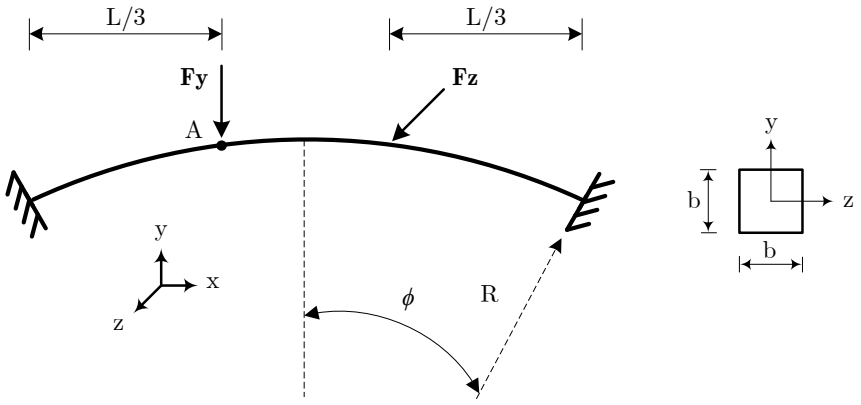

Figure 3: Shallow arch - Geometrical data.

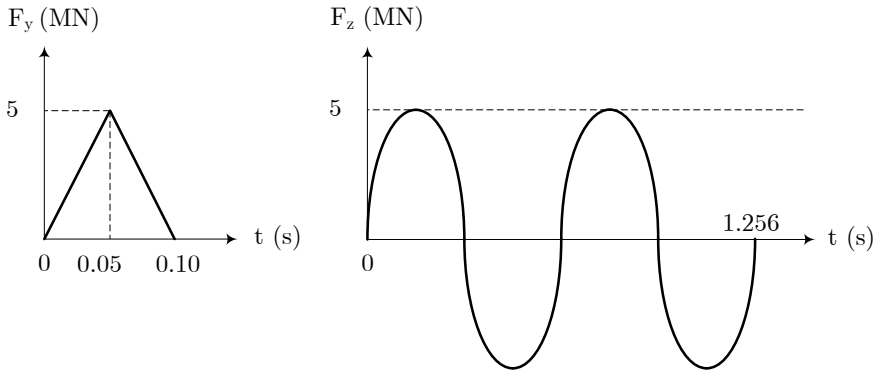

Figure 4: Shallow arch - Loading history.

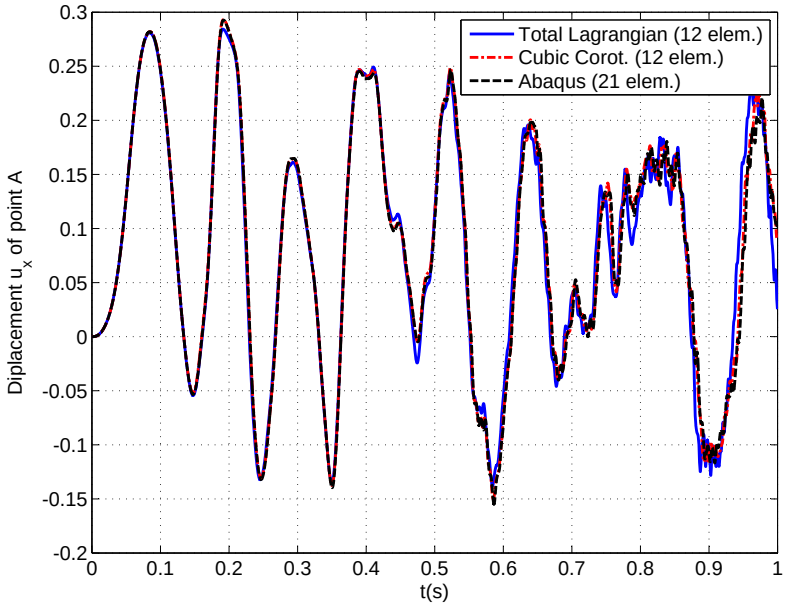

Figure 5: Shallow arch - Displacement u_x(m) of point A.

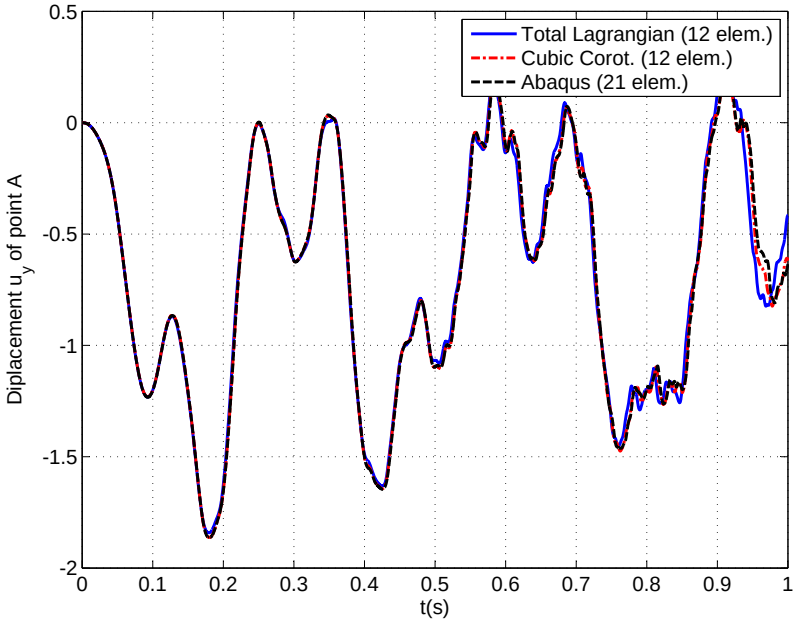

Figure 6: Shallow arch - Displacement u_y(m) of point A.

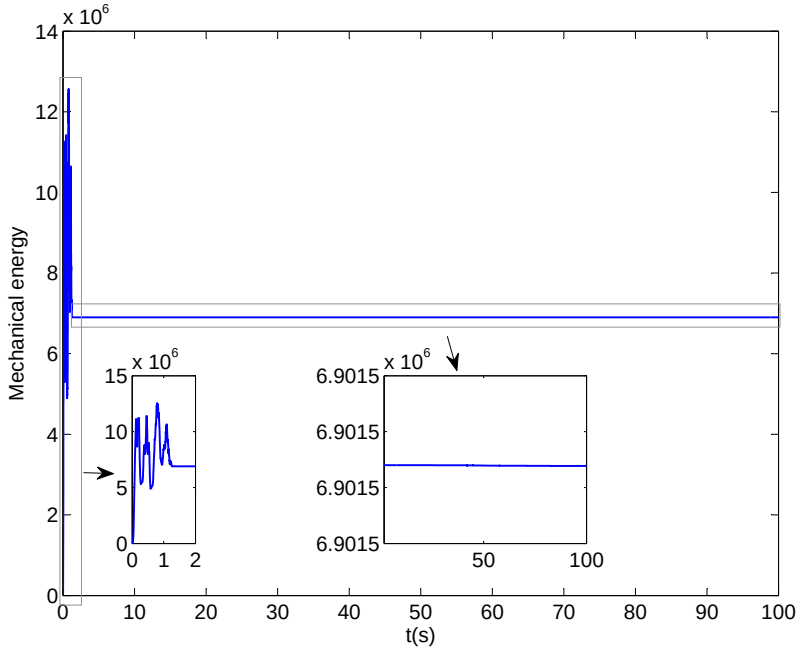

Figure 8: Shallow arch - Time evolution of the energy.

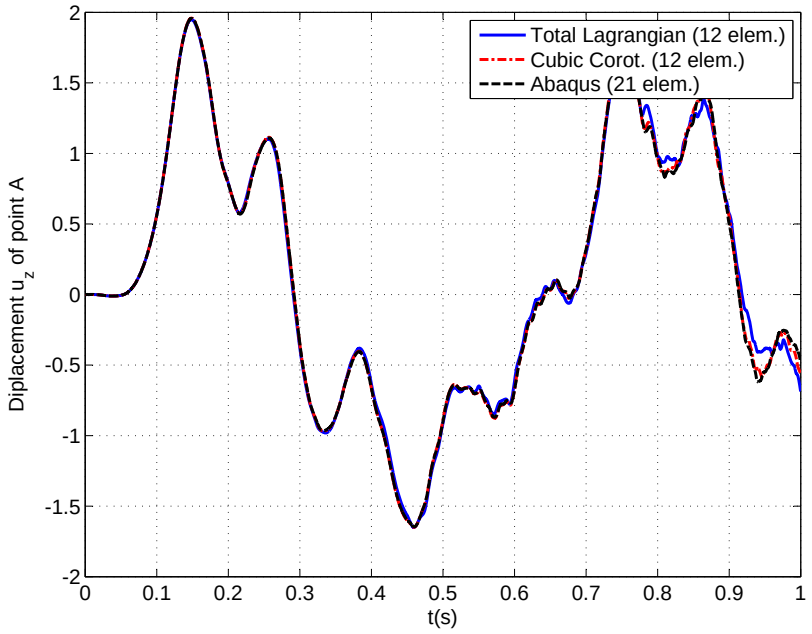

Figure 7: Shallow arch - Displacement u_z(m) of point A.

6.2. Example 2: Roorda-Koiter frame

Roorda-Koiter frame is considered [47] in this example. In this problem, the connection between the column and the beam is not an easy task to solve because it requires nonlinear constraint equation. One possible solution for maintaining the continuity of

this connection is to introduce a small radius R of 0.25 m, see Fig. 9. This frame has a uniform rectangular cross-section and is subjected to two out-of-plane forces. Both applied forces follow the pattern of a hat function as shown in Fig. 10. The length of the beam L is 12 m, the width of the beam 0.3 m and the depth of the beam 0.2 m. The Young modulus E of the frame is 210 GPa and the Poisson's ratio $\nu = 0.3$. The mass per unit volume ρ is 7850 kg/m^3. The time step size is taken $t = 10^{-4}$ s.

The reference solution, obtained with 22 elements (11 elements per member), and the results obtained with the proposed formulation with 10 elements (4 straight beam elements and 1 curved beam per member) are shown in Figs. 11, 12 and 13. It can be observed that with only 10 elements, the new total Lagrangian formulation gives results that are in good agreement with the reference solution. Additionally, we can show again in Fig. 14 the conservation of the energy for one million time steps after the external loads vanish.

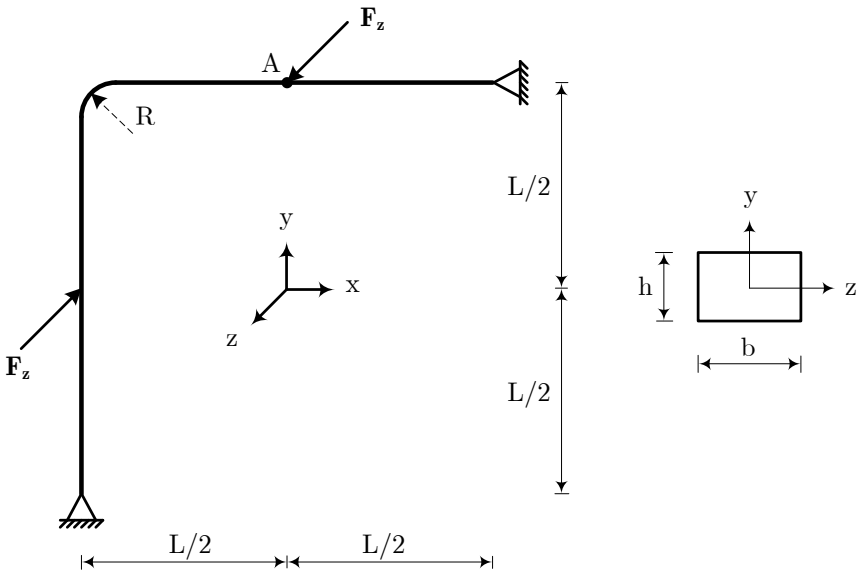

Figure 9: Roorda-Koiter frame - Geometrical data.

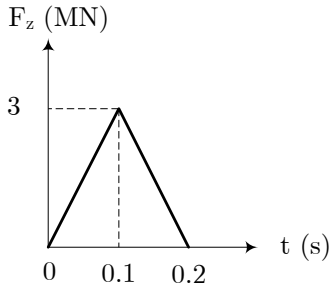

Figure 10: Roorda-Koiter frame - Loading history.

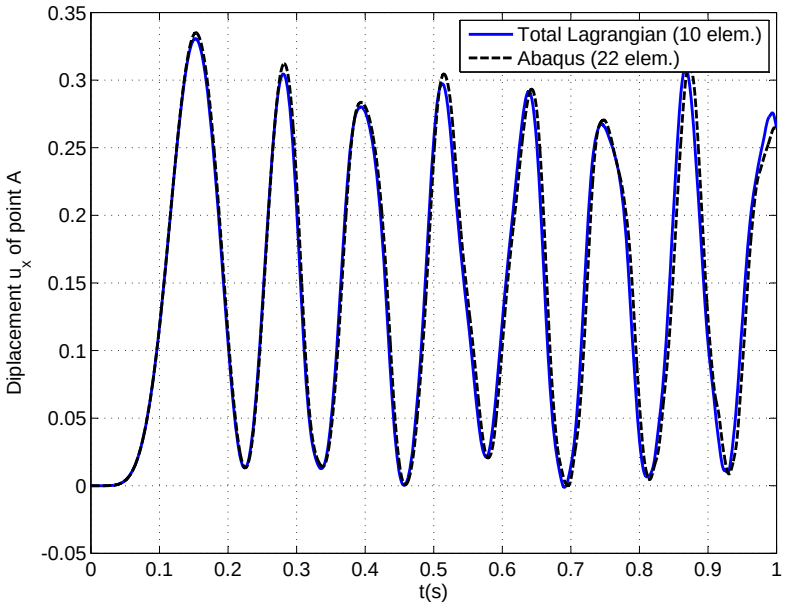

Figure 11: Roorda-Koiter frame - Displacement u_x of point A.

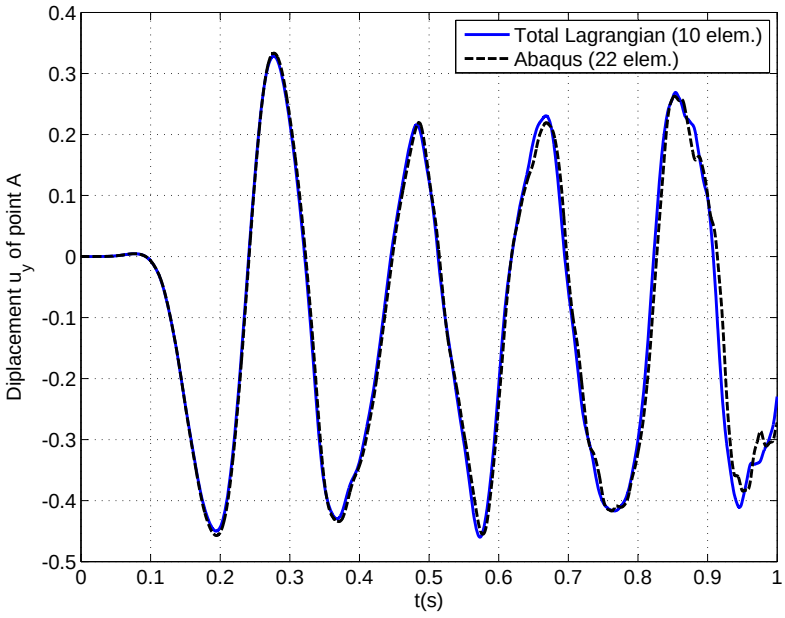

Figure 12: Roorda-Koiter - Displacement u_y of point A.

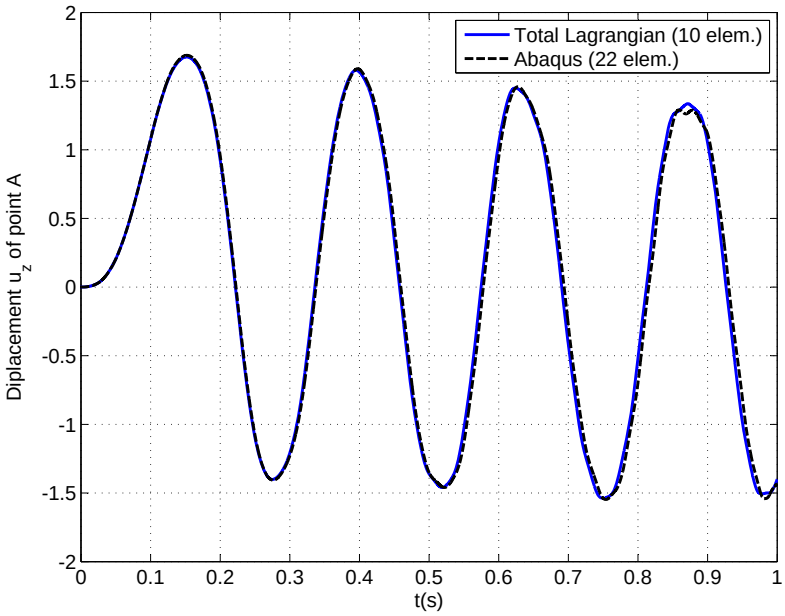

Figure 13: Roorda-Koiter - Displacement u_z of point A.

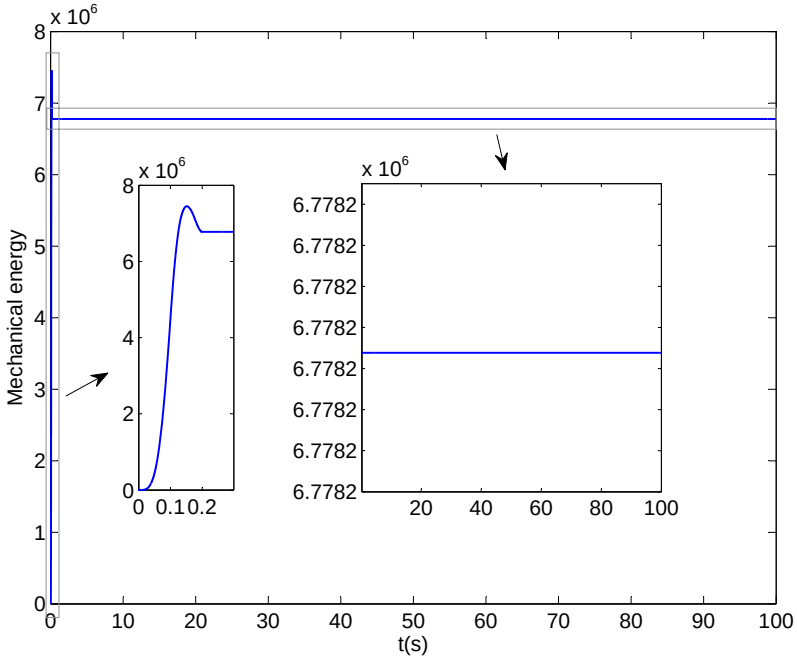

Figure 14: Roorda-Koiter - Time evolution of the energy.

6.3. Example 3: Right-angle cantilever beam subject to out-of-plane loading

The right-angle cantilever beam [3, 7, 44, 20] is subjected to an out-of-plane concentrated load applied at the elbow (see Fig. 15 and 16). The radius R is 0.25 m, the length of the beam L is 10 m, the width of the beam 0.2 m and the depth of the beam 0.4 m. The Young modulus E of the frame is 210 GPa and the Poisson's ratio $\nu = 0.3$. The mass per unit volume ρ is 7850 kg/m^3. The time step size is taken $t = 10^{-4}$ s.

The reference solution, obtained with 22 elements (11 elements per member), and the displacement responses obtained with 10 elements (4 straight beam elements and 1 curved beam per member) are shown in Figs. 17, 18 and 19. It can be observed that with only 10 elements, the proposed formulation approach gives results that are in good agreement with the reference solution. As shown in Fig. 20, the new algorithm preserves the conservation of the energy for one million time steps after vanishing of the external loads at 0.2 s.

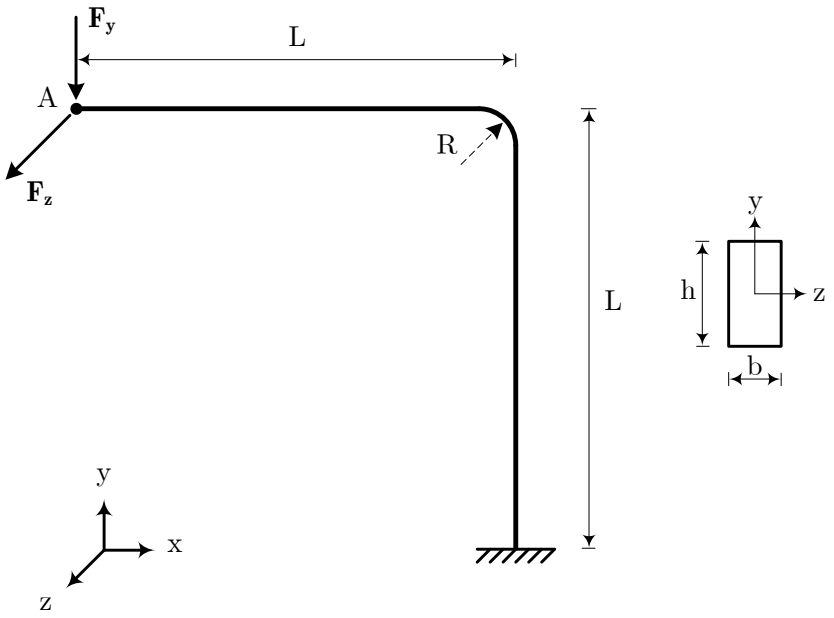

Figure 15: Right-angle cantilever beam - Geometrical data.

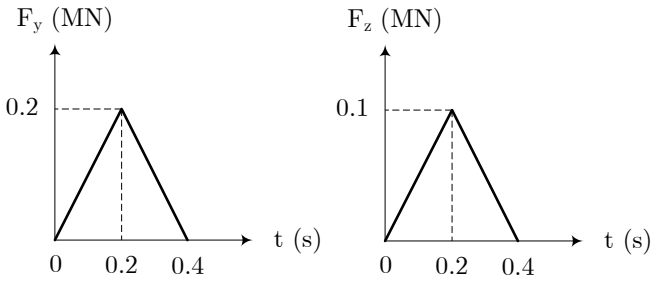

Figure 16: Right-angle cantilever beam - Loading history.

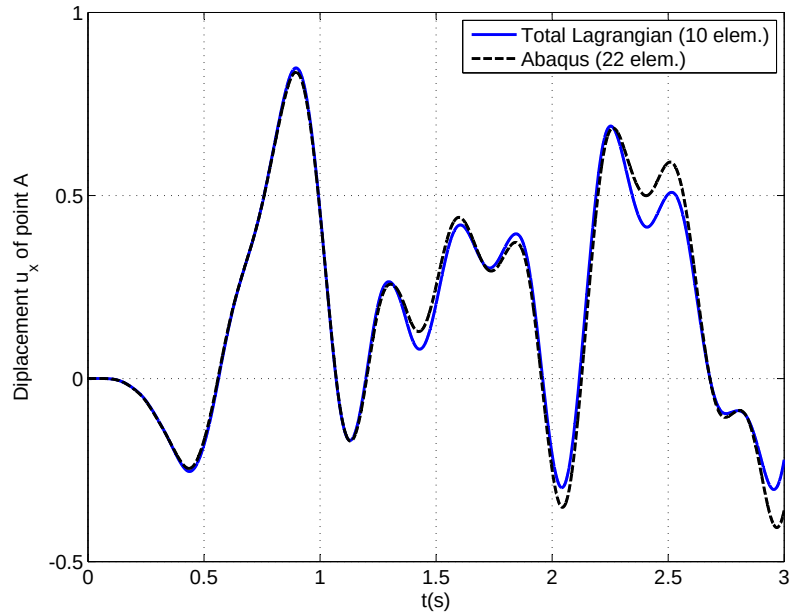

Figure 17: Right-angle cantilever beam - Displacement u_x of point A.

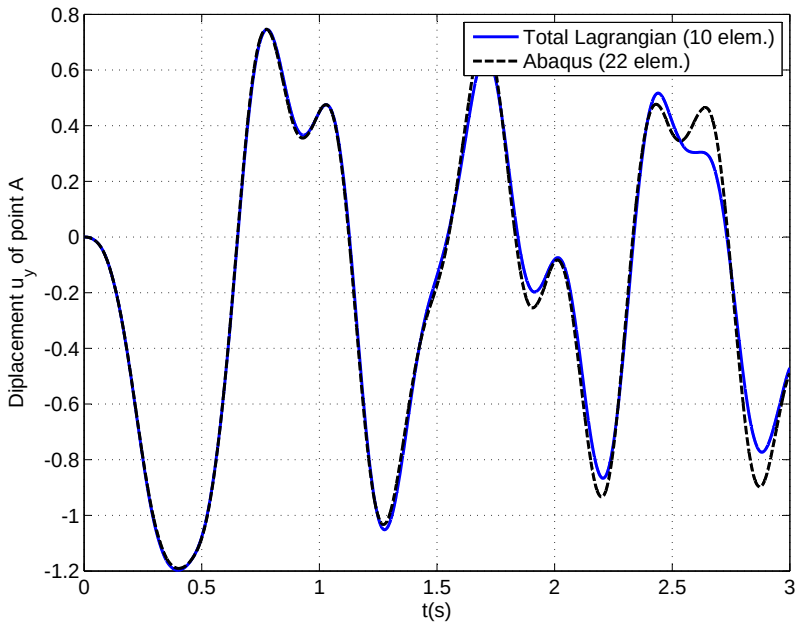

Figure 18: Right-angle cantilever beam - Displacement u_y of point A.

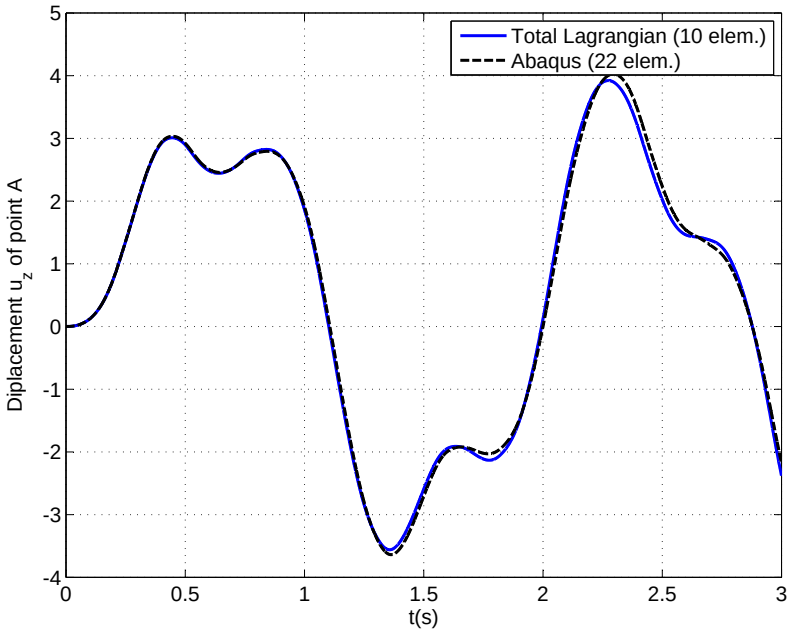

Figure 19: Right-angle cantilever beam - Displacement u_z of point A.

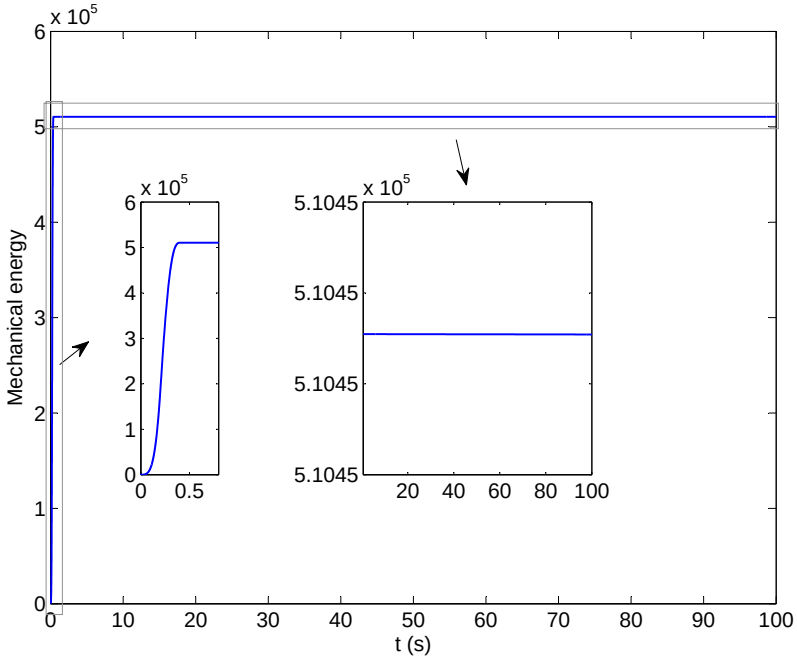

Figure 20: Right-angle cantilever beam - Time evolution of the energy.

6.4. Example 4: Free beam undergoing a large overall motion

The last example focuses on the conservation of energy and momenta. The problem was analysed in the plane case in ([3, 37]). The current loadings as shown in Fig. 22 are different from the original problems. The beam is subjected to an horizontal force

F_y and to an out-of-plane force F_z. The geometrical data of the beam are the length of $L = 10$ m and a uniform cross-section of $b = 0.2$ m. The beam has a modulus of elasticity $E = 210$ GPa and a Poisson ratio $\nu = 0.3$. The mass per unit volume is 7850 kg/m^3. Ten elements have been used to perform the calculation. The time step is chosen as $\Delta t = 10^{-4}$ s.

Fig. 23 shows the time history of the displacement in the direction u_z in which the beam moves in a very long distance about 31528 m.

Figs. 24, 25 and 26 show respectively the time histories of the energy, the linear momentum and the angular momentum. The fluctuation relative error for the energy is only 3.75×10^{-8} after vanishing the external load. It proved again that the formulation conserves the energy in case of free fly beam. Besides, for the linear momentum, the fluctuation relative errors are 2.16×10^{-6}, 5×10^{-8} and 5×10^{-8} for L_x, L_y and L_z respectively. At last, the fluctuation relative errors for the angular momentum are 2.42×10^{-4}, 4.80×10^{-8} and 4.80×10^{-8} for J_x, J_y and J_z respectively. It can be concluded that the new total Lagrangian formulation preserves as well linear and angular momenta for a million time steps of the duration 100s.

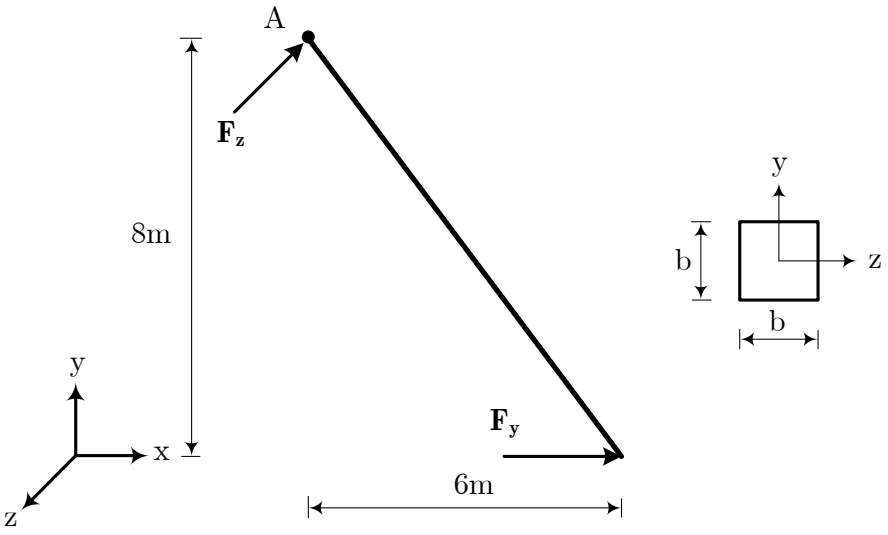

Figure 21: Free beam - Geometrical data.

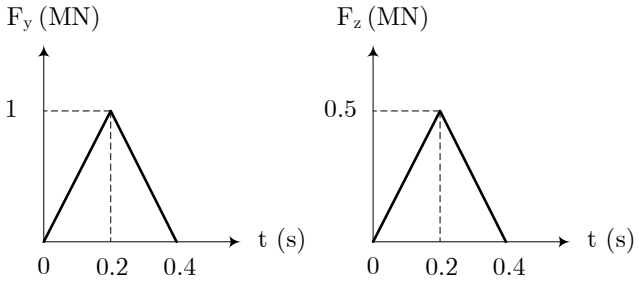

Figure 22: Free beam - Loading history.

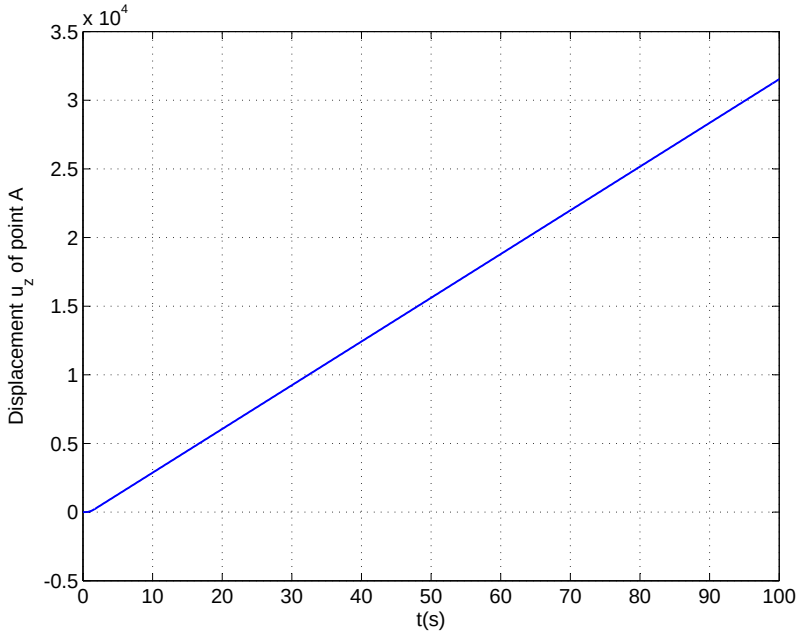

Figure 23: Free beam - Displacement u_z of point A.

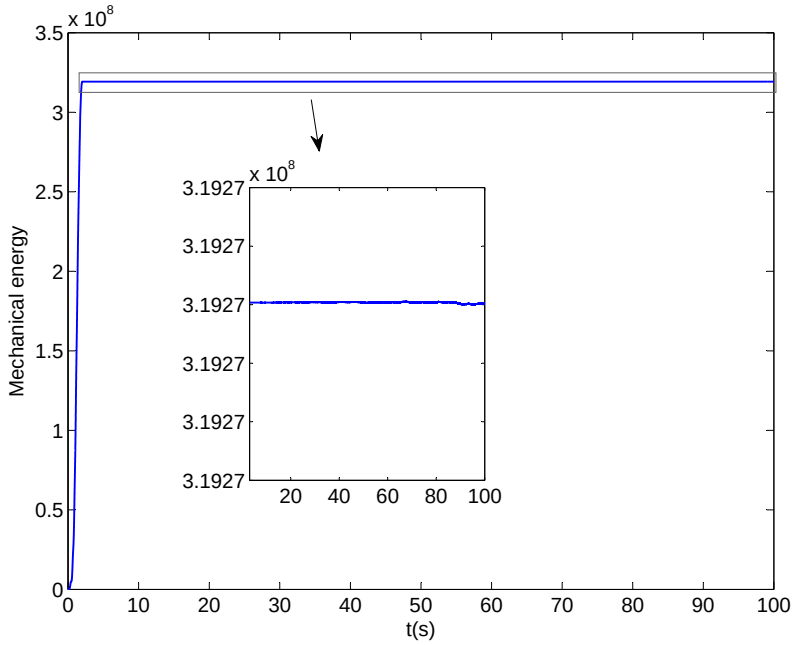

Figure 24: Free beam - Time evolution of the energy.

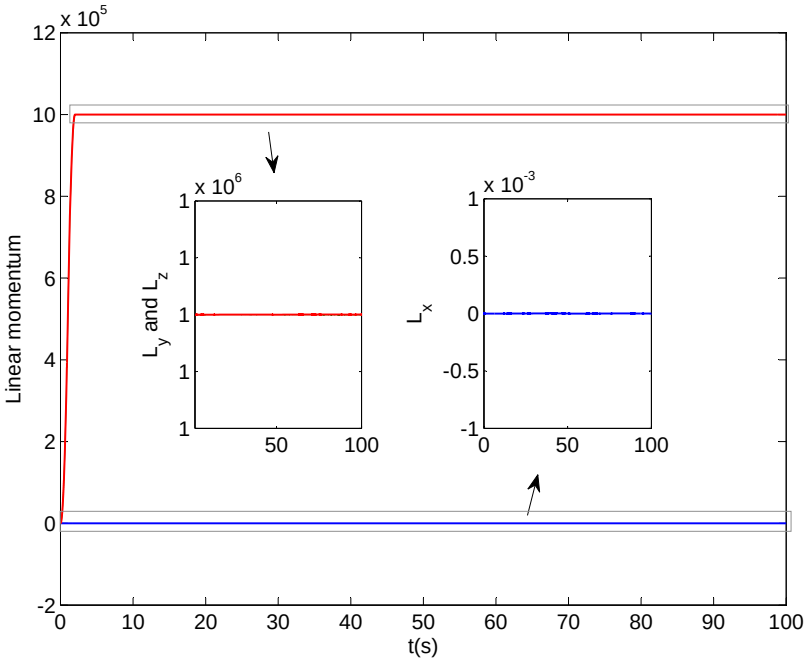

Figure 25: Free beam - Time evolution of the linear momentum.

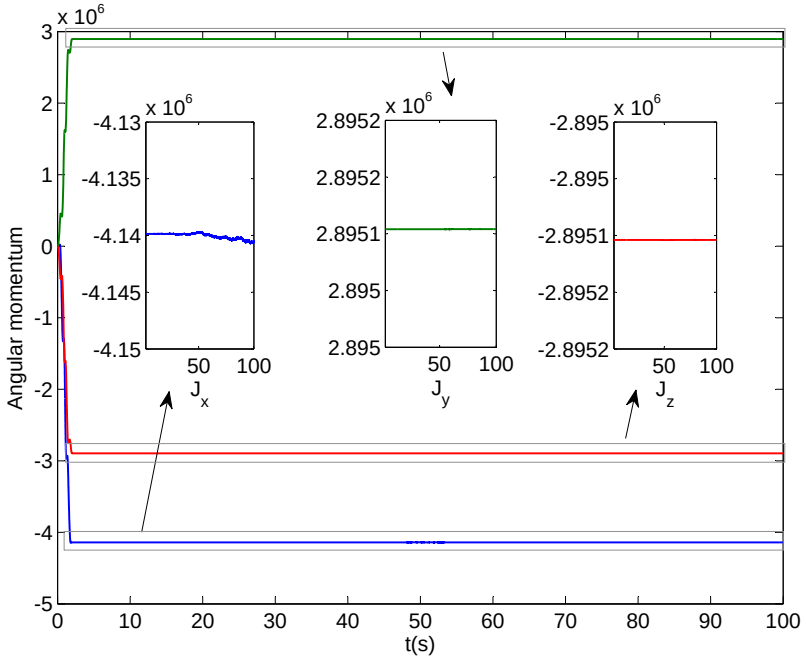

Figure 26: Free beam - Time evolution of the angular momentum.

7. Conclusion

An energy-conserving scheme for geometrically exact Euler-Bernoulli 3D curved beam dynamics is presented. In this paper, we provide a novel methodology to do so leading to the development of a spatial rod formulation which incorporates the Euler-Bernoulli assumption. The approach makes use of Gram-Schmidt orthogonalisation process coupled to a one-parametric rotation. The latter completes the description of the torsional cross sectional rotation and overcomes the non-uniqueness of the Gram-Schmidt procedure. The formulation is extended to the dynamical case and a stable, energy-conserving time-stepping algorithm is presented. The time integration scheme extends previously developed energy-conserving time stepping algorithms, which is independent of the non-linear complexities involved in the geometric description of the deformation at hand. The numerical results have shown a high level of accuracy compared to the benchmark reference solutions of Abaqus and the solution of the cubic co-rotational formulation. Finally, the proposed algorithm conserves the energy and momenta which guarantees the stability for the long-term dynamic analysis.

Acknowledgement

The first and the third authors gratefully acknowledge financial support by the European Commission (Research Fund for Coal and Steel) through the project RobustImpact under grant agreement RFSR-CT-2012-00029 and the financial support of the region of Brittany (France) through the ARED funding scheme.

References

[1] J.H. Argyris, H. Balmer, J.St. Doltsinis, P.C. Dunne, M. Hasse, M. Kleiber, G.A. Malejannakis, H.-P. Meljnek, M. Müller, and D.W. Scharpf. Finite element method-the natural approach. Comput. Methods Appl. Mech. Engrg. 17-18(Part I) (1979) 1–106.

[2] K.-J. Bathe, S. Bolourchi. Large displacement analysis of three-dimensional beam structures. Int. J. Numer. Methods Engrg. 14 (1979) 961–986.

[3] J.C. Simo, L. Vu-Quoc. On the dynamics in space of rods undergoing large motions - a geometrically exact approach. Comput. Methods Appl. Mech. Engrg. 66 (1988) 125–161.

[4] A. Cardona, M. Géradin. A beam finite element non-linear theory with finite rotations. Int. J. Numer. Methods Engrg. 26 (1988) 2403–2438.

[5] P.M. Pimento, T. Yojo. Geometrically exact analysis of spatial frames. Appl. Mech. Rev. 46 (1993) 118–128.

[6] O.A. Bauchau, G. Damilano, N.J. Theron. Numerical integration of non-linear elastic multi-body systems. Int. J. Numer. Methods Engrg. 38 (1995) 2727–2751.

[7] A. Ibrahmibegović. On finite element implementation of geometrically nonlinear Reissner's beam theory: Three-dimensional curved beam element. Comput. Methods Appl. Mech. Engrg. 122 (1995) 11–26.

[8] A. Ibrahmibegović. On the choice of finite rotation parameters. Comput. Methods Appl. Mech. Engrg. 149 (1997) 49–71.

[9] F. Gruttmannm, R. Sauer, W. Wagner. Theory and numerics of three-dimensional beams with elastoplastic material behaviour. Int. J. Numer. Methods Engrg. 48 (2000) 1675–1702.

[10] D. Zupan, M. Saje. Finite-element formulation of geometrically exact three-dimensional beam theories based on interpolation of strain mesures. Comput. Methods Appl. Mech. Engrg. 192 (2003) 5209–5248.

[11] C. Sansour, W. Wagner. Mutliplicative update of the rotation tensor in the finite element analysis of rods and shells - a path independent appraoch. Comput. Mech. 31 (2003) 153-162.

[12] R. Kapania, J. Li. A formulation and implementation of geometrically exact curved beam elements incorporating finite strains and finite rotations. Comput. Mech. 30 (2003) 444-459.

[13] P. Mata, S. Oller, A.H. Barbat. Static analysis of beam structures under nonlinear geometric and constitutive behavior. Comput. Methods Appl. Mech. Engrg. 196 (2007) 4458-4478.

[14] E. Zupan, M. Saje, D. Zupan. Quaternion-based dynamics of geometrically nonlinear spatial beams using the Runge-Kutta method. Finite Elem. Anal. Des. 54 (2012) 48–60.

[15] H. Zhong, R. Zhang, N. Xiao. A quaternion-based weak form quadrature element formulation for spatial geometrically exact beams. Arch. Appl. Mech. 84 (2014) 1825–1840.

[16] W. Li, H. Ma, W. Gao. Geoemtrically exact curved beam element using interal force field defined in deformed configuration. Int. J. Non-linear Mech. 89 (2017) 116-126.

[17] P. Nanakorn, L.N.Vu. A 2D field-consistent beam element for large displacement analysis using the total Lagrangian formulation. Finite Elem. Anal. Des. 134 (2017) 41–54.

[18] F. Armero, J. Valverde. Invariant Hermitian finite elements for thin Kirchhoff rods. I: The linear plane case. Comput. Methods Appl. Mech. Engrg. 213-216:427457, 2012.

[19] C. Sansour, T.L. Nguyen, M. Hjiaj. An energy-momentum method for in-plane geometrically exact Euler-Bernoulli beam dynamcis. Int. J. Numer. Methods Engrg. 102 (2015) 99–134.

[20] F.P. Pai. Geometrically exact beam theory without Euler angles. Int. J. Solids Struct. 48 (2011) 3075–3090.

[21] Z. Zhao, G. Ren. A quaternion-based formulation of EulerBernoulli beam without singularity. Nonlinear Dyn. 67 (2012) :1825-1835

[22] L. Greco, M. Cuomo. B-Spline interpolation of Kirchhoff-Love space rods. Comput. Methods Appl. Mech. Engrg. 256 (2013) 251-269.

[23] A.M. Bauer, M. Breitenberger, B. Philipp, R. Wchner, K.-U. Bletzinger. Nonlinear isogeometric spatial Bernoulli beam. Comput. Methods Appl. Mech. Engrg. 303 (2016) 101-127.

[24] C. Meier, A. Popp, W.A. Wall. Geometrically exact finite element formulations for slender beams: Kirchhoff–love theory versus Simo-Reissner theory. Arch. Comp. Methods Engrg. (2017) 1–81.

[25] A.A. Shabana, H.A. Hussien, J.L.Escalona. Application of the absolute nodal coordinate formulation of large rotation and large deformation problems. J. Mech. Des. 120 (1998) 188–195.

[26] A.A. Shabana, R.Y. Yakoub. Three dimensional absolute nodal coordinate formulation for beam theory: Theory. J. Mech. Des. 123 (2000) 606–613.

[27] J.C. Simo , N. Tarnow. The discrete energy-momentum method. Conserving algorithms for nonlinear elastodynamics. J. Appl. Math. Phys. 43 (1992) 757–792.

[28] O. Gonzalez. Exact energy and momentum conserving algorithms for general models in nonlinear elasticity. Comput. Methods Appl. Mech. Engrg. 2000 (190) 1763–1783.

[29] P. Betsch, P. Steinmann. Conservation properties of a time FE method—part II: Time-stepping schemes for non-linear elastodynamics. Int. J. Numer. Methods Engrg. 2001 (50) 1931–1955.

[30] T.A. Laursen , X.N. Meng. A new solution procedure for application of energy-conserving algorithms to general constitutive models in nonlinear elastodynamics. Comput. Methods Appl. Mech. Engrg. 190 (2001) 6309–6322.

[31] L.C. Bottasso, O.A. Bauchau, J.-Y. Choi. An energy decaying scheme for nonlinear dynamics of shells. Comput. Methods Appl. Mech. Engrg. 191 (2002) 3099–3121.

[32] B. Brank. An energy conserving non-linear dynamic finite element formulation for flexible composite laminates. Comput. Struct. 80 (2002) 677–689.

[33] I. Romero, F. Armero. An objective finite element approximation of the kinematics of geometrically exact rods and its use in the formulation of an energy–momentum conserving scheme in dynamics. Int. J. Numer. Methods Engrg. 54 (2002) 1683–1716.

[34] Ibrahimbegović, S. Mamouri. Energy-conserving and decaying implicit time-steppping scheme for nonlinear dynamics of three-dimenisonal beams undergoing finite rotations. Comput. Methods Appl. Mech. Engrg. 191 (2002) 4241–4258.

[35] L. Noels, L. Stainier, J.P. Ponthot. An energy-momentum conserving algorithm for non-linear hypoelastic constitutive models. Int. J. Numer. Methods Engrg. 2004 (59) 83–114.

[36] K.-J. Bathe. Conserving energy and momentum in nonlinear dynamics: A simple implicit time integration scheme. Comput. Struct. 85 (2007) 437–445.

[37] M. Gams, I. Planinc, M. Saje. Energy conserving time integration scheme for geometrically exact beam. Comput. Methods Appl. Mech. Engrg. 196 (2007) 2117–2129.

[38] S. Krenk. Global energy-momentum-based time integration in nonlinear dynamics. Int. J. Numer. Methods Engrg. 100(2014) 458–476.

[39] S. Chhang, C. Sansour, M. Hjiaj, J.-M. Battini. An energy-momentum co-rotational formulation for nonlinear dynamcis of planar beams. Comput. Struct. 187 (2017) 50–63.

[40] S. Chhang, J.-M. Battini, M. Hjiaj. Energy-momentum method for co-rotational planar beams: A comparative study of shear flexible formulations. Finite Elem. Anal. Des. 134 (2017) 41–54.

[41] C. Sansour, P. Wriggers, J. Sansour. Nonlinear dynamics of shells: theory, finite element formulation, and integration schemes. Nonlinear Dyn. 13 (1997) 279–305.

[42] C. Sansour, W. Wagner, P. Wriggers, J. Sansour. An energy momentum integration scheme and enhanced strain finite elements for the non-linear dynamics of shells. Int. J. Non-linear Mech. 37 (2002) 951–966.

[43] C. Sansour, P. Wriggers, J. Sansour. On the design of energy-momentum integration schemes for arbitrary continuum formulations. Applications to classical and chaotic motion of shells. Int. J. Numer. Methods Engrg. 60 (2004) 2419–2440.

[44] J. Mäkinen. Total Lagrangian Reissner's goemetrically exact beam element without singularities. Int. J. Numer. Methods Engrg. 70 (2007) 1009–1048.

[45] Newmark NM. A method of computation for structural dynamics. J. Eng. Mech. division ASCE 85 (1959) 67–94.

[46] A. Cardona, M. Géradin. Time integration of the equations of motion in mechanism analysis. Comp. Struct. 33 (1989) 801–820.

[47] T.-N. Le, J.-M. Battini, M. Hjiaj. A consistent 3D corotational beam element for nonlinear dynamic analysis of flexible structures. Comput. Methods Appl. Mech. Engrg. 269 (2014) 538–565.

[48] Y. Choquet-Bruhat, C. DeWitt-Morette, M. Dillard-Bleick. Analysis, Manifolds and Physics Part I. North-Holland, Amsterdam.

[49] B.A. Dubrovin, A.T. Fomenko, S.P. Novikov. Modern Geometry-Methods and Applications I. Springer-Verlag, New York.

INSA de RENNES
Service des Formations

AVIS DU JURY SUR LA REPRODUCTION DE LA THESE SOUTENUE

Titre de la thèse:
Energy-momentum conserving time-stepping algorithms for nonlinear dynamics of planar and spatial Euler-Bernoulli/Timoshenko beams

Nom Prénom de l'auteur : CHHANG SOPHY

Membres du jury :
- Monsieur BATOU Anas
- Monsieur BOYER Frédéric
- Monsieur KOUHIA Reijo
- Monsieur HJIAJ Mohammed
- Monsieur BRÜLS Olivier
- Monsieur DE SAXCE Géry
- Monsieur BATTINI Jean-Marc
- Madame BOUVIER Salima

Président du jury : Salima BOUVIER

Date de la soutenance : 11 Décembre 2018

Reproduction de la these soutenue

☒ Thèse pouvant être reproduite en l'état
☐ Thèse pouvant être reproduite après corrections suggérées

Fait à Rennes, le 11 Décembre 2018

Signature du président de jury

PR Salima BOUVIER

Le Directeur,

M'hamed DRISSI

UNIVERSITE BRETAGNE SCIENCES LOIRE POUR L'INGENIEUR

INSA RENNES

Titre : Algorithmes d'intégration conservatifs de l'analyse dynamique non-linéaire des poutres planes et spatiales d'Euler-Bernoulli/Timoshenko

Mots clés : Dynamique non-linéaire, Schémas d'intégration conservatifs, Poutre co-rotationelle 2D, Poutre spatiale d'Euler-Bernoulli géométriquement exacte, Impact

Résumé : Dans la première partie de la thèse, les schémas d'intégration conservatifs sont appliqués aux poutres co-rotationnelles 2D. Les cinématiques d'Euler-Bernoulli et de Timoshenko sont abordées. Ces formulations produisent des expressions de l'énergie interne et l'énergie cinétique complexe et fortement non-linéaires. L'idée centrale de l'algorithme consiste à définir, par intégration, le champ des déformations en fin de pas à partir du champ de vitesses de déformations et non à partir du champ des déplacements au travers de la relation déplacement-déformation. La même technique est appliquée aux termes d'inerties. Ensuite, une poutre co-rotationnelle plane avec rotules généralisées élasto-(visco)-plastiques aux extrémités est développée et comparée au modèle fibre avec le même comportement pour des problèmes d'impact. Des exemples numériques montrent que les effets de la vitesse de déformation influencent sensiblement la réponse de la structure.

Dans la seconde partie de cette thèse, une théorie de poutre spatiale d'Euler-Bernoulli géométriquement exacte est développée. Le principal défi dans la construction d'une telle théorie réside dans le fait qu'il n'existe aucun moyen naturel de définir un trièdre orthonormé dans la configuration déformée. Une nouvelle méthodologie permettant de définir ce trièdre et par conséquent de développer une théorie de poutre spatiale en incorporant l'hypothèse d'Euler-Bernoulli est fournie. Cette approche utilise le processus d'orthogonalisation de Gram-Schmidt couplé avec un paramètre rotation qui complète la description cinématique et décrit la rotation associée à la torsion. Ce processus permet de surmonter le caractère non-unique de la procédure de Gram-Schmidt. La formulation est étendue au cas dynamique et un schéma intégration temporelle conservant l'énergie est également développé. De nombreux exemples démontrent l'efficacité de cette formulation.

Title : Energy-momentum conserving time-stepping algorithms for nonlinear dynamics of planar and spatial Euler-Bernoulli/Timoshenko beams

Keywords : Nonlinear Dynamics, Energy-momentum conserving scheme, 2D co-rotational beam, Geometrically exact 3D Euler-Bernoulli beam, impact.

Abstract : In the first part of the thesis, energy-momentum conserving algorithms are designed for planar co-rotational beams. Both Euler-Bernoulli and Timoshenko kinematics are addressed. These formulations provide us with highly complex non-linear expressions for the internal energy as well as for the kinetic energy which involve second derivatives of the displacement field. The main idea of the algorithm is to circumvent the complexities of the geometric non-linearities by resorting to strain velocities to provide, by means of integration, the expressions for the strain measures themselves. Similarly, the same strategy is applied to the highly nonlinear inertia terms. Next, 2D elasto-(visco)-plastic fiber co-rotational beams element and a planar co-rotational beam with generalized elasto-(visco)-plastic hinges at beam ends have been developed and compared against each other for impact problems.

In the second part of this thesis, a geometrically exact 3D Euler-Bernoulli beam theory is developed. The main challenge in defining a three-dimensional Euler-Bernoulli beam theory lies in the fact that there is no natural way of defining a base system at the deformed configuration. A novel methodology to do so leading to the development of a spatial rod formulation which incorporates the Euler-Bernoulli assumption is provided. The approach makes use of Gram-Schmidt orthogonalisation process coupled to a one-parametric rotation to complete the description of the torsional cross sectional rotation and overcomes the non-uniqueness of the Gram-Schmidt procedure. Furthermore, the formulation is extended to the dynamical case and a stable, energy conserving time-stepping algorithm is developed as well. Many examples confirm the power of the formulation and the integration method presented.